SYNTHESIS, PHOTOPHYSICAL STUDIES AND CHEMICAL SENSOR APPLICATIONS OF LUMINESCENT CARBON DOTS

A Thesis submitted

in partial fulfillment for the Degree of

Doctor of Philosophy

by

Manjunatha Ganiga

Department of Chemistry

INDIAN INSTITUTE OF SPACE SCIENCE AND TECHNOLOGY

THIRUVANANTHAPURAM

MAY 2018

To my beloved Guru, Mother, Father, Sister and Friends…

CERTIFICATE

This is to certify that the thesis entitled **Synthesis, Photophysical Studies and Chemical Sensor Applications of Luminescent Carbon Dots** submitted by **Manjunatha Ganiga** to the Indian Institute of Space Science and Technology Thiruvananthapuram, in partial fulfilment for the award of the degree of **Doctor of Philosophy** is a *bona fide* record of research work carried out by him under my supervision. The contents of this Thesis, in full or in parts, have not been submitted to any other Institution or University for the award of any degree or diploma.

Dr. Jobin Cyriac
Supervisor
Associate Professor
Department of Chemistry

Counter signature of the HOD with seal

Thiruvananthapuram
May 2018

DECLARATION

I declare that this thesis entitled **Synthesis, Photophysical Studies and Chemical Sensor Applications of Luminescent Carbon Dots** submitted in partial fulfilment of the degree of **Doctor of Philosophy** is a record of original work carried out by me under the supervision of Dr. Jobin Cyriac, and has not formed the basis for the award of any other degree or diploma, in this or any other Institution or University. In keeping with the ethical practice of reporting scientific information, due acknowledgments have been made wherever the finding of others have been cited.

Manjunatha Ganiga
SC13D001

Thiruvananthapuram-695 547
May 2018

ACKNOWLEDGEMENTS

Completion of this doctoral dissertation would not have possible without the support of several people. Firstly, my deepest gratitude to my research supervisor, Dr. Jobin Cyriac, Associate Professor, Department of Chemistry for his constant support, valuable guidance and consistent encouragement. I consider it as a great opportunity to pursue my research work under his guidance and to learn from his research expertise. He cared so much about my work, and responded to my questions and queries so promptly.

My sincere thanks to Dr. V. K. Dadhwal, Director, IIST for providing research facilities during the tenure of my work. I would also like to thank Professor Kuruvilla Joseph, Dean, Student Activities and Dr. Nirmala Rachael James, HOD, Department of Chemistry for their constant support. My heartfelt thanks to the IIST for the financial support.

My doctoral committee guided me through all these years. I thank all my doctoral committee members, Dr. Benny K George, Dr. Edamana Prasad, Dr. Vinesh Vijayan, Dr. K. Prabhakaran, Dr. Rakesh Kumar Singh for their critical comments. I also thank all faculty members of the Department of Chemistry for their valuable guidance which enabled the successful completion of the research work.

I am deeply indebted to all my colleagues and staffs of Department of Chemistry, without them the thesis would not have come to a successful completion. My sincere thanks to my colleague Neema P. M. for her kind help and encouragement. I deeply acknowledge my senior colleagues Dr. Mohammed Mukthar Ali, Dr. Raneesh Konnola, Dr. Narasimman Rajaraman, Dr. Jalaja K, Dr. Kavitha M. K., for their strong motivation and helping me in the initial phase of my research. I also acknowledge my colleagues, Devi Renuka K, Meegle S Mathew, Reshma R, Aswathi R, Rakesh R, Sujith Vijayan, Arya Nair, Saisree, Yogesh choudhary, Haritha H, BDS Deeraj, Roymon Joseph, Vidhya Raj and Linsha V. I appreciate staff members Jayasree L, Jayasree Dinesh, Rehana, Bindu P C, Remya

T, Mr. Loveson Albert and Mr. Sreekumaran Nair for helping me in every possible way.

I deeply acknowledge IIT Madras, STIC CUSAT, Amrita Cochin and VSSC Thiruvananthapuram for the characterization studies. My sincere thanks also to Nisha Balachandran and Bhuvana Raj for helping me in sample characterization.

Finally, I express my deep sense of gratitude to my mother, my late father and my sister for their affection, encouragement and inspiration during my research tenure.

(Manjunatha Ganiga)

ABSTRACT

Over past two decades, there has been an intense focus to understand and to extend the technological boundaries of carbon-based nanomaterials such as graphene, carbon nanotubes, fullerene, graphene quantum dots, and carbon dots (CDs). Among these, due to their bright fluorescence, tuneable luminescence, facile synthetic routes, CDs have captivated the attention of fluorescence community. CDs can overcome the toxicity associated with semiconductor-based fluorescence quantum dots (QDs) and photobleaching tendency of organic fluorescent dyes. There has been an enormous number of publications emphasizing both fundamentals and technological aspects of CDs. Despite there is an excellent progress, the fundamentals of photophysics are not evident in CDs. The predominance in blue emission and the weak solubility in the non-polar environment are the various aspects needs to be addressed. Although there was a substantial number of applications, where CDs have scrutinized, there is still room for exploration. We have synthesised a range of CDs, studied the photophysical properties and demonstrated its chemical sensor applications for the detection of biological, environmental and industrially significant molecules/ions. The studies conducted using various CDs given in this Thesis is briefed below.

Ammonia is an important industrial gas and it has a biological and environmental significance. A fluorescent-based probe, which operates via Forster Resonance Energy Transfer (FRET) mechanism explored for the ammonia detection in gaseous as well as the liquid state using CDs as a fluorophore. The CDs, derived from carbonizing acetic acid and sodium rhodizonate was used as the sensor system. CDs acted as a signal transducer and sodium rhodizonate as an analyte-specific molecule. Both solution and vapor phase detection of ammonia was performed. Excited state energy transfer (FRET) from CDs to sodium rhodizonate was activated when ammonia was present in the sensor solution. The detection limit of the current sensor system was 3 ppm. Selectivity was demonstrated using oxides of nitrogen and common organic solvents.

A nitrogen-rich carbon dots (NCDs) having broad emission covering a substantial portion of visible regions (nearly white light) of the electromagnetic spectrum was synthesized using ethylenediamine as carbon and nitrogen precursor. An attempt to understand the broad emission from NCDs was performed by interacting with Cu^{2+}. The detailed spectroscopic and microscopic studies reveal that the broad, steady-state photoluminescence emission of NCDs originates from the direct recombination of excitons (higher energy) as well as due to the involvement of defect states (lower energy). A selective fluorescence platform for the detection of Cu^{2+} using NCDs was also accomplished. The detection limit was 10 µM and the dynamic range was 10 µM – 0.4 mM.

A hydrothermal synthetic route for a bright blue emitting silicon passivated carbon dots gel (SiCDs gel) was accomplished using an aminosilane precursor. A detailed microscopic, spectroscopic, rheological and surface area analysis confirms that the CDs attached to the polymeric backbone. Nitrogen adsorption studies shows that the gel has high nitrogen adsorption tendency, approximately two orders of magnitude higher than that of the conventional CDs. A fluorescence sensor for

Ag^+ ions using SiCDs gel, which operates via the formation of Ag nanoparticles on the SiCDs gel surface, was demonstrated. The luminescence of CDs was quenched by Ag nanoparticles formed on the surface, which was proportional to the concentration of Ag^+ ions. The sensor shows high selectivity towards Ag^+ with a sensitivity and dynamic range of 85 nM and 0.4 µM – 0.1 M, respectively.

Hydrothermal synthesis of sulfur and nitrogen doped carbon dots referred as 'SNCDs' was achieved using glutathione as a single precursor of carbon and dopants. The reason behind atypical fluorescence emission profile of SNCDs, showing both excitation dependency and independency unfolded by comprehensive pH-dependent fluorescence studies. Based on the results, a complete energy level diagram of SNCDs was proposed. Further, SNCDs was utilized for selective detection of Cr(VI), which operates via both FRET and inner filter effect (IFE).

CDs having high solubility in non-polar environment referred as 'organophilic CDs (OCDs)' was synthesized using cyclohexane as a precursor and dispersion media. Spectroscopic studies revealed the presence of non-polar functional groups at the OCDs surface. OCDs was then utilized for nitroaromatics sensing. The fluorophore was found to be highly sensitive to trinitrophenol (TNP), compared to the other nitroaromatics, in turn opening up the possibility of detection of potent explosives and environmental pollutants. An attempt to understand the mechanism of fluorescence quenching of OCDs by nitroaromatics was made. OCDs' emission was quenched by primary inner filter effect (IFE), which happens by the absorption of nitroaromatics at the excitation wavelength of OCDs, against commonly observed electron transfer mechanisms.

We envisage that the studies presented here would be highly useful in understanding the properties of CDs in depth and to extend its technological realms by encouraging the possibility of various synthetic routes and applications.

TABLE OF CONTENTS

LIST OF TABLES

LIST OF FIGURES

ABBREVIATIONS

AFM	Atomic force microscopy
APTES	3-aminopropyltriethoxysilane
ATR	Attenuated total internal reflection
CDs	Carbon dots
CIE	Commission Internationale de l'eclairage
CNTs	Carbon nanotubes
DNP	Dinitrophenol
DNT	Dinitrotoluene
DPC	Diphenylcarbazide
EDA	Ethylenediamine
FRET	Forster Resonance Energy Transfer
FTIR	Fourier transform infrared spectroscopy
GO	Graphene oxide
GQDs	Graphene quantum dots
HFCNs	Hollow fluorescent carbon nanoparticles
IFE	Inner filter effect
LED	Light emitting diodes
NAs	Nitroaromatics
NB	Nitrobenzene
NCDs	Nitrogen rich carbon dots
NMR	Nuclear magnetic resonance
OCDs	Organophilic carbon dots
PA	Picric acid
PET	Photoinduced electron transfer
PL	Photoluminescence
PVA	Poly-(vinyl alcohol)
QDs	Quantum dots
QY	Quantum yield
RGO	Reduced graphene oxide

SiCDs gel	Silicon passivated carbon dots gel
SNCDs	Sulphur and nitrogen doped carbon dots
TCSPC	Time-correlated single-photon counting
TEM	Transmission electron microscopy
TGA	Thermo gravimetric analyser
TLC	Thin layer chromatography
TNP	Trinitrophenol
TNT	Trinitrotoluene
XPS	X-ray photoelectron spectroscopy

NOTATIONS

Φ	Quantum yield
E	FRET efficiency
R_0	FRET distance
К	Orientation factor
J_{DA}	Spectral overlap
η	Refractive index
ε	Molar absorption coefficient
A	Absorbance
I	Intensity
λ	Wavelength
τ	Lifetime
χ^2	CHSQ2
T	Temperature
t	Time
G’	Elastic modulus
G”	Viscous modulus
σ	Standard deviation of blank
k	Slope
F	Fluorescence intensity
C	Concentration

CHAPTER 1

INTRODUCTION

This chapter gives a brief insight into the key properties of carbon dots (CDs), which made them an attractive candidate to scrutinize in many application domains ranging from energy conversion to sensors. The pros and cons of CDs compared to other carbon-based nanomaterials and analogues photoluminescent materials has been discussed. Further, various synthetic routes adopted for synthesizing CDs were also highlighted. The chapter also describes the state of the art photoluminescent sensing strategies for small molecule detection and its general mechanistic pathways.

1.1. Luminescent carbon dots

After the serendipitous discovery of CDs while purifying the single-walled carbon nanotubes by electrophoresis (X. Xu et al., 2004), this material occupied the leading position in the family of emerging photoluminescence (PL) materials. The feeble cytotoxicity, excellent biocompatibility, facile synthetic methods and favourable circumstances for the post-functionalization are the attractions in CDs. These are the zero-dimensional carbon-based nanomaterials in which sp^2 hybridized carbon core containing a plethora of surface functional groups, predominantly carboxyl, and hydroxyl functional groups. The size of the nanodots typically falls below 10 nm is accountable for quantum confinement and leading to the molecule like energy states. A simple pictorial representation of the structure of CDs is given in Figure 1.1. Understanding the fundamental aspects of CDs is important to unfold the aforementioned technological utilities of this luminescent carbon nanostructures (Gao, Du, Zhuang, & Chen, 2016; H. Li, Kang, Liu, & Lee, 2012; Lim, Shen, & Gao, 2015).

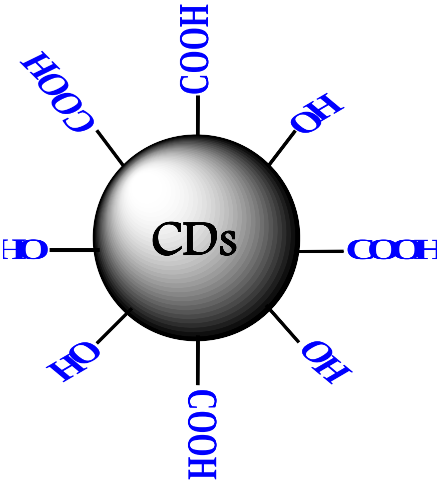

Figure 1.1. Schematic representation of CDs.

Compared to luminescent semiconductor-based quantum dots (QDs) and organic dyes, CDs stands high in terms of its feeble cytotoxicity and biocompatibility, which made them an excellent candidate of choice for bioimaging and contrasting agent. The capacity of CDs to exchange its energy/electron, its propensity for post-functionalization, large surface area, and facile synthetic strategies transformed them as a splendid candidate for light-emitting materials, energy storage/conversion, and sensor-based applications. Even though CDs possesses several advantages, there are key challenges, which needs attention. The PL quantum yield (QY), which is one of the key properties of fluorescent-based materials is feeble in the CDs. There have been several successful attempts to enhance the QY of CDs using surface passivation and doping. However, to transform this material from the laboratory to real-world applications require effective strategies. The mechanism of PL, which is hypothesized to be stemmed from radiative recombination of excitons, emissive traps, small sp^2 clusters encapsulated within sp^3 domains, zigzag and armchair edges, etc. is still no clear. Owing to the presence of polar surface functional groups, the solubility of CDs in non-polar organic solvents is weak and hence hinders the post-functionalization and amalgamation of non-polar molecules with CDs. The following discussion describes the state of the art synthetic strategies, surface structure and morphology, key properties and challenges in the field of CDs (Georgakilas, Perman, Tucek, & Zboril, 2015; R. Wang, Lu, Tang, & Xu, 2017; Y. Wang & Hu, 2014).

1.1.1. Synthetic routes

As in the case of any nanomaterials, general approaches for the synthesis of CDs include ‘top-down’ and ‘bottom-up’ strategies (H. Li et al., 2012; X. Li, Zhao, & Pan, 2016; Y. Wang & Hu, 2014). In the ‘top-down’ approach, 2D carbon nanomaterials such as graphene, carbon nanotubes, fullerene, etc. are disintegrated into smaller zero-dimensional CDs. An atom by atom construction using the suitable carbon precursor is accomplished for the synthesis of CDs in ‘bottom-up’ approach. Some important synthetic approaches are discussed below.

1.1.1.1. Microwave-assisted synthesis

The microwave assisted synthesis involves the disintegration of a suitable carbon source under microwave irradiation. This method is advantageous in terms of its rapidity and large-scale synthesis (Chae et al., 2017; López et al., 2015). Wang et al. reported a ‘green approach’ for the synthesis of CDs by irradiating eggshell membrane ashes in NaOH solution using microwave radiation (Q. Wang, Liu, Zhang, & Lv, 2012). The synthesis was completed in 5 minutes with a blue emitting CDs of 14% QY. Following pathways were hypothesized for the formation of CDs: (a) breaking down of eggshell membrane ashes into tiny pieces (b) polymerization and growth (c) oxidation followed by the surface passivation.

Microwave-assisted synthesis of CDs from citric acid and ethylenediamine was achieved within 5 min (He et al., 2015). The formation of CDs was based on the condensation followed by the carbonization of citric acid and ethylenediamine (Figure 1.2). Here the reaction was carried out in a sealed vessel placed in a microwave digestion furnace having controllable temperature and pressure. A microwave-assisted pyrolysis of citric acid and 4,7,10-trioxa-1,13-tridecanediamine (TTDDA), which functioned as an A_3 and B_2 poly-amidation type monomer used for the preparation of CDs was shown by Choi et al. CDs were formed in gram level within 5 minutes. Because of the surface passivation by TTDDA fluorescence QY of 29% was acheived (J.-L. Xu et al., 2017). Using carbohydrates (glycerol, glycol, glucose, sucrose, etc.) as a source for carbon in the presence of small amount of an inorganic ion (Na^+, Ca^{2+}, Al^{3+}, Cl^-, SO_4^{2-}, PO_4^{3-})

resulted in CDs within a few minutes. Colour tuneability was an interesting property found in these CDs (Xiaohui Wang, Qu, Xu, Ren, & Qu, 2011).

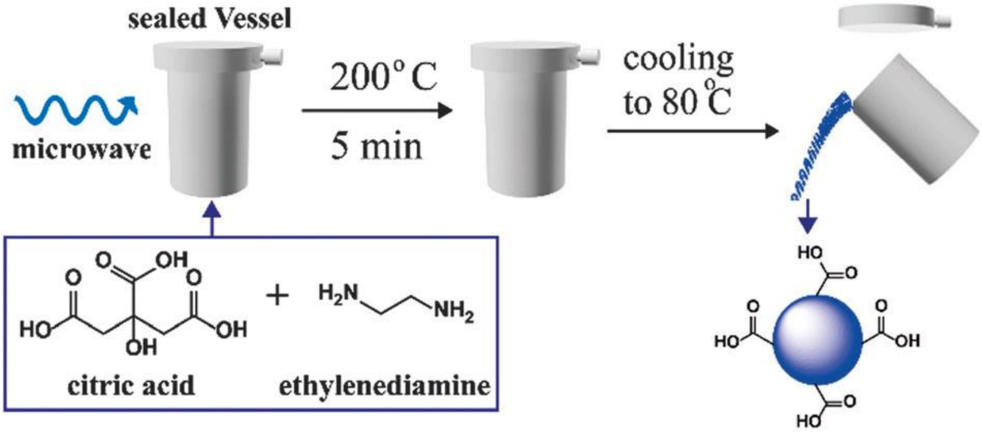

Figure 1.2. Synthesis of CDs via microwave-assisted reaction with controllable temperature and pressure.

1.1.1.2. Hydrothermal synthesis

Known for its eco-friendliness and easiness, the hydrothermal strategy has emerged as one of the most useful ways to realize CDs. In this procedure, a suitable carbon precursor in the aqueous medium is treated at an elevated temperature for a specified duration of time. So far, myriad of precursors, including natural and laboratory chemicals have been exploited for the synthesis of CDs via hydrothermal routes (Qu, Wang, Ren, & Qu, 2013; Xuefei Wang, Cheng, Yu, & Yu, 2017). For example, nitrogen doped CDs were synthesized by subjecting ammonium citrate under hydrothermal conditions at 160 ^{0}C for 6 h (Yang et al., 2014). X-ray photoelectron spectra (XPS) analysis confirmed the presence of nitrogen as C-N and N-H.

CDs exhibiting excitation independent emission response was prepared by a hydrothermal synthetic route using sodium citrate and polyacrylamide (Y. Liu, Zhou, Yuan, & Wu, 2017). In another study, authors utilized hydrothermal methods to synthesize CDs-graphitic carbon nitride (g-C_3N_4) composite using ascorbic acid as a carbon precursor. Here, an aqueous solution of ascorbic acid is introduced into autoclave along with g-C_3N_4 bulk and the resulting dispersion was heated at 180 °C for 4 h to obtain CDs-g-C_3N_4 composite. (X. Wang et al., 2017).

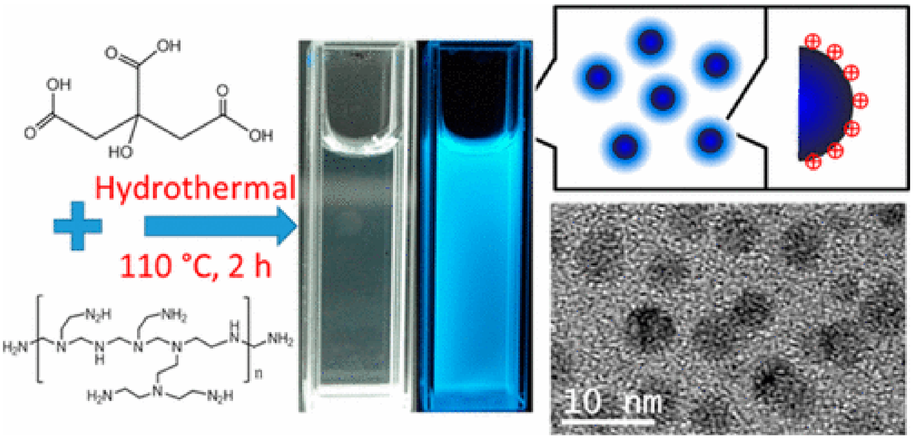

Figure 1.3. Hydrothermal synthesis of CDs using citric acid and PEI. TEM image of the CDs is also shown.

A blue luminescent CDs with 50% QY has been synthesized hydrothermally using citric acid and polyethyleneimine (PEI) (J.-Y. Li et al., 2017). The reaction was carried out at a relatively low temperature (110 ^{o}C) and moderate reaction time (2 h) (Figure 1.3). Synthesis of multicolor emitting CDs was demonstrated by the simple refluxing of an aqueous solution of L-cysteine and D-(+)-galactose in the presence of NaOH at 80 ^{o}C for 24 h (T.-Y. Wang, Chen, Wang, Tan, & Liao, 2017). The color of the resulting CDs can be tuned by changing the concentration of precursors. One step synthesis of boronic acid functionalized CDs was shown by hydrothermal reaction of phenylboronic acid at 160 °C for 8 h (Shen & Xia, 2014). There are plenty of examples of CDs prepared from natural resources. For example, hydrothermal treatment of orange peels at 180 °C shows the formation of CDs (Prasannan & Imae, 2013).

1.1.1.3. Electrochemical synthesis

Size uniformity of nanomaterials is of utmost importance both for fundamental studies as well for many technological domains. In this regard, the electrochemical route for CDs is significance because of its ability to control the size by tuning the applied voltage. A bottom-up route for CDs by NaOH assisted direct electrochemical carbonization of ethanol was demonstrated by Li et al. (Figure 1.4) (H. Li, Ming, et al., 2011). The experiment was performed by electrochemical reaction of a basic solution of ethanol using Pt rods, both as an anode and cathode with a current intensity in the range 200–260 mA/cm^2. The QY of the CDs is found to be 4% with a multicolor emission covering the visible range and the size range of 3-7 nm (Figure 1.4). The electrochemical route to CDs using glycine (C.-I. Wang, Wu, Periasamy, & Chang, 2014) and sodium citrate and urea were reported. (Hou, Lu, Deng, Li, & Zhang, 2015)

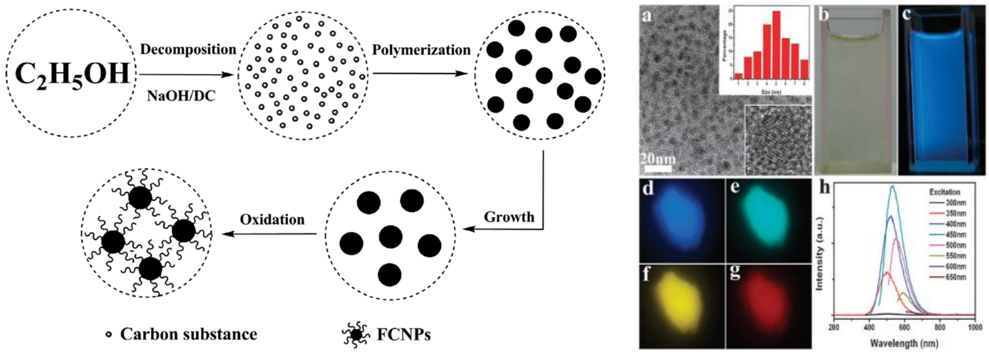

Figure 1.4. Electrochemical synthesis of CDs, corresponding TEM image and the multicolor emission from CDs.

A top-down approach in which electrochemical cutting of graphite using ultrapure water as the electrolyte has been used to produce large-scale, high-quality CDs (Ming et al., 2012). Graphite rods were used as both anode and cathode and inserted in ultrapure water and applied the static potential of 15-60 V using a DC power supply. After 2 h, graphite rod from anode has corroded, and the dark-yellow solution contains graphite oxide, graphite particles and CDs.

1.1.1.4. Plasma-assisted synthesis

Powered by inherently produced charged ions (electrons and cations) and excited neutral species, the plasma induced synthesis of nanomaterials was attractive due to its rapidity and large-scale production. Wang and co-workers demonstrated the fabrication of egg-derived fluorescent CDs by plasma-induced pyrolysis process (J. Wang, Wang, & Chen, 2012). Another representative work uses acrylamide as a carbon source (Figure 1.5) (C.-X. Li, Yu, Wang, & Chen, 2013). Good amphiphilicity with high solubility in many organic and aqueous solvents, high resistance to acids and bases, good fluorescence QY (in the order of 10%) are some of the reported advantages of these CDs.

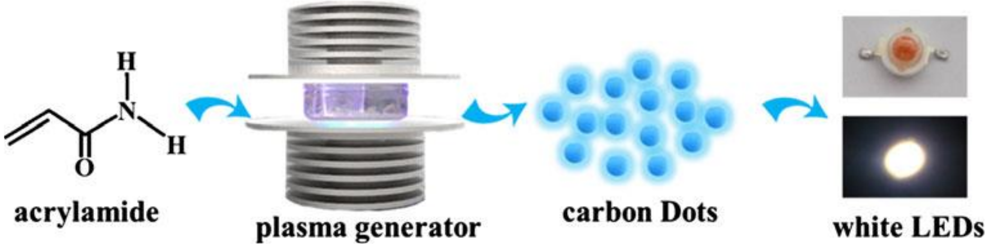

Figure 1.5. Synthesis of CDs using plasma irradiation and the photograph of the fabricated LED.

1.1.1.5. Ultrasonic synthetic routes

Compared to conventional methods for the synthesis of nanomaterials, utilization of high-intensity ultrasound offers a facile, versatile synthetic route (Bang & Suslick, 2010). The cavitation and nebulization are the primary physical phenomena associated with ultrasound synthesis. Acoustic cavitation (formation, growth, and implosive collapse of bubbles in a liquid) creates extreme conditions inside the collapsing bubble and serves as the origin of most sonochemical phenomena in liquids or liquid-solid slurries. Representative examples are the CDs derived from polyamide resin & ethylenediamine (Dang, Huang, Zhang, Wang, & Chen, 2016) and glucose & aqueous ammonia (Z. Ma, Ming, Huang, Liu, & Kang, 2012). The alkali or acid assisted sonochemical reaction of glucose, interestingly, resulted in the CDs with emission range from visible to NIR region (H. Li, He, et al., 2011). Typical reaction time used for these syntheses were in a few hours.

1.1.1.6. Chemical oxidation

Preparation of CDs via chemical oxidation of a carbon precursors using strong oxidizing agents was proven to be the effective way to generate fluorescent carbon nanomaterials. The oxidizing agents used here will either cut the 2D carbon materials into CDs by introducing surface functional groups such as epoxy, hydroxyl, and carboxyl groups in a typical top-down approach or by carbonizing and subsequent functionalization of smaller carbon precursors to introduce sp^2 hybridized core with oxygen-containing surface functional groups. Chemical oxidation of three traditional carbon sources viz. coal activated carbon, wood activated carbon and coconut activated carbon successfully turned into CDs (Qiao et al., 2010). All three carbon sources were treated with nitric acid to obtain the CDs and the subsequent passivation of as obtained CDs was accomplished using amine-terminated compounds. Starch was oxidized using H_2O_2 after it was digested under high pressure. The oxidation reaction was conducted in the ultrasonic environment (Yan et al., 2015).

A chemical oxidation route in which P_2O_5 was exploited as dehydration/oxidation of acetic acid for the easy and large-scale production of CDs (Figure 1.6) (Fang et al., 2012). The CDs were formed very quickly by simply mixing acetic acid, water and P_2O_5. The authors designated this CDs as hollow fluorescent carbon nanoparticles (HFCNs). The reaction may proceed via initial generation of a large amount of heat due to the exothermic reaction between P_2O_5 and water; this heat is then utilized for the evaporation and the subsequent carbonization of acetic acid. The emission of these HFCNs was excitation independent, reasoned as the resonance energy transfer from small-sized nanodomains to larger ones, led to the green emission of HFCNs at all excitation wavelengths.

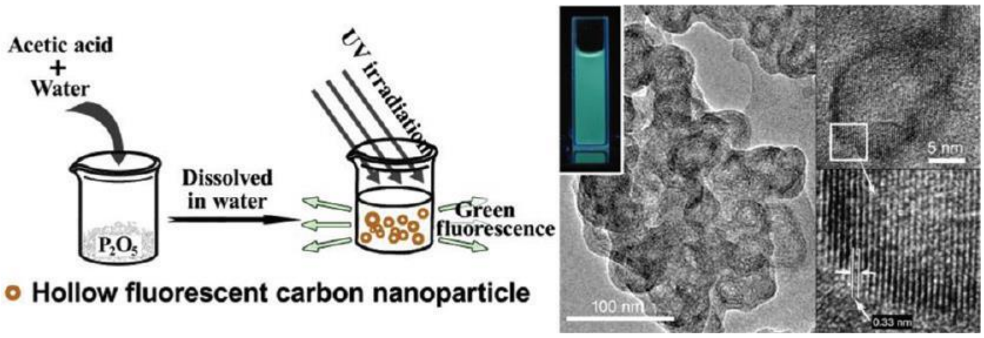

Figure 1.6. Schematic representation of the synthesis of HFCNs using acetic acid, P_2O_5, and water.

1.1.1.7. Pyrolysis

Simple pyrolysis of the carbon precursor also will lead to the formation of CDs. Many of the CDs prepared using pyrolysis shows very high QY, nearly 40%. Pan et al. demonstrated the synthesis of CDs by one step pyrolysis ethylenediamine-tetraacetic acid salts at 400 ^{0}C (Pan et al., 2010). A systematic study has been conducted in the temperature range 200- 400 ^{0}C using citric acid and ethylenediamine to understand the CDs formation mechanism (Krysmann, Kelarakis, Dallas, & Giannelis, 2012). Briefly, lower pyrolysis temperature favors the formation of highly emitting condensation product, whereas higher pyrolysis temperature is required for the generation of CDs.

1.1.1.8. Supported/Templated synthesis

Achieving homogeneous size nanomaterial is a challenge. In this respect, use of templates or supports for the synthesis of nanomaterials has been reported (Baker & Baker, 2010; Kwon, Lee, Do, Joo, & Rhee, 2014). The carbon precursors are pyrolyzed after embedding them in a suitable solid matrix, most commonly SiO_2, zeolites, etc. and subsequent removal of the solid supports after the carbonization leads to the homogeneous size distribution.

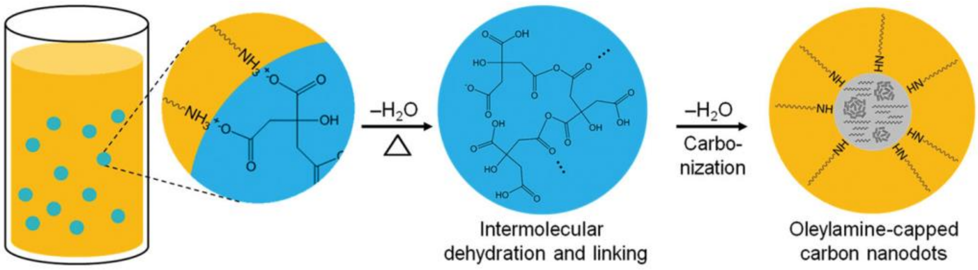

Figure 1.7. Schematic of size-controlled soft template synthetic route for oleylamine capped CDs.

A highly size controllable soft template method for the synthesis of oleylamine-capped CDs were reported (Kwon et al., 2014). Initially, an emulsion was formed by a vigorous agitation of the mixture of oil and water. The water droplet, which contains citric acid (carbon source for CDs) was stabilized by oleylamine (emulsifier). Upon heating the emulsion, polymer-like intermediate was formed due to the condensation of citric acid molecules. These intermediates were then carbonized and simultaneously capped by oleylamine molecules to give the organic-soluble CDs (Figure 1.7).

1.1.1.9. Laser irradiation

Laser irradiation technique to synthesize CDs offers fast, controlled and easy preparative routes. The carbonisation and aromatisation of the precursor were done using a focused beam of an intense laser. The irradiation of toluene using Nd YAG laser (H. Yu, Li, Zeng, & Lu, 2016) of characterestics; 1064 nm, pulse rate: 10 Hz, pulse width: 8 ns, beam diameter: 8 mm resulted in a well defined CDs. It was observed that the size of the CDs obtained and hence its PL output could be controlled by changing the input laser fluence. For instance, CDs of size, 2.0–3.9 nm, 3.0–10.0 nm, 10.0–17.2 nm and 13.0–20.5 nm was obtained when the laser fluence were 100, 200, 300 and 350 mJ per pulse, respectively. Nd YAG lasers of other wavelengths; 532 and 355 nm were also used for the preparation of CDs.

1.1.2. Structure and Properties

The following section describes the key properties of CDs such as optical properties, cytotoxicity, biocompatibility, and stability. The structure of CDs explained using various spectroscopic and microscopic tools, and the structure and property relationship has been highlighted.

1.1.2.1. UV-visible absorption

CDs possesses strong absorption bands in the UV region due to the absorption from sp^2 hybridized core (π–π*) and from the surface functional groups (n–π*), with a tail extending to visible and NIR region of the electromagnetic spectrum. Blue emitting excitation independent CDs (BCDs) and full-color fluorescent CDs (FCDs) prepared through the mild one-pot process from chloroform and diethylamine had distinct UV-visible absorption features (Nie et al., 2014). The BCDs exhibited absorption peaks at 228 and 282 nm, respectively due to π–π* (C=C from the core) and n–π* (from C=O) transitions. On the other hand, FCDs, which contains C=N group at the core had exhibited absorption features at 300 and 421 nm, respectively assigned to π–π* (C=N from the core) and n–π* (from C=O) transitions. CDs synthesised via electrochemical (H. Li, Ming, et al., 2011), hydrothermal (L. Wang & Zhou, 2014) and microwave-assisted (Huang et al., 2014) routes displayed similar absorption features at 240-300 nm range, assigned to the absorption from aromatic π system or n–π* transition of C=O.

1.1.2.2. Photoluminescence and its origin

The most captivating property of CDs compared to its other carbon nanomaterial counterparts such as carbon nanotubes (CNTs) and graphene oxide (GO) is its bright photoluminescence emission, covering UV, visible and NIR region of the electromagnetic spectrum. Unlike semiconductor QDs and organic dyes, most of the reported CDs emission can be tuned by merely changing the excitation wavelength. The PL in CDs is surmised to be originated from quantum confinement, presence of zig-zag states, emissive traps, sp^2 nanodomains embedded in sp^3 matrix, presence of aromatic moieties and from the surface functional groups (Baker & Baker, 2010; R. Wang et al., 2017; Y. Wang & Hu, 2014).

Although there are several reports on the origin of PL in CDs, it is still blurry owing to the complexity associated with CDs structure, which depends on synthetic conditions and the nature of the precursors used. The quantum yield, which represents the luminescence brightness of a fluorophore is low compared to semiconductor QDs and organic dyes. Although, excitation-dependent emission is commonly displayed by CDs, the intensity of the emission at higher wavelengths (>500 nm) is low. Most of the CDs found to possess dominant emission in blue region of the electromagnetic spectrum.

The blue emitting excitation dependent CDs were transformed to full-color excitation independent CDs by heating with chloroform and diethylamine at different time intervals ((Nie et al., 2014) (Figure 1.8). Due to the incorporation of nitrogen atoms into the sp^2 hybridized core, additional energy levels are introduced and is responsible for the red shift in the emission. Supporting this argument, it was shown that nitrogen and sulfur co-doped CDs, synthesized by hydrothermal treatment of citric acid and L-cysteine, manifested the high QY of 73% and the emission was excitation independent (Dong et al., 2013). Elimination of the energy levels introduced by O-states and enhancing the N-states by the co-operative effect from doped N and S atoms could be the reason for excitation independent emission.

There are a few reports specific to the synthesis of long wavelength emitting CDs. For instance, yellow emitting (approx. 550 nm) CDs (Datta, Qi, Zboril, & Giannelis, 2016; T. H. Kim et al., 2016) and red emitting (600 nm) CDs were successfully prepared (Ding et al., 2017).

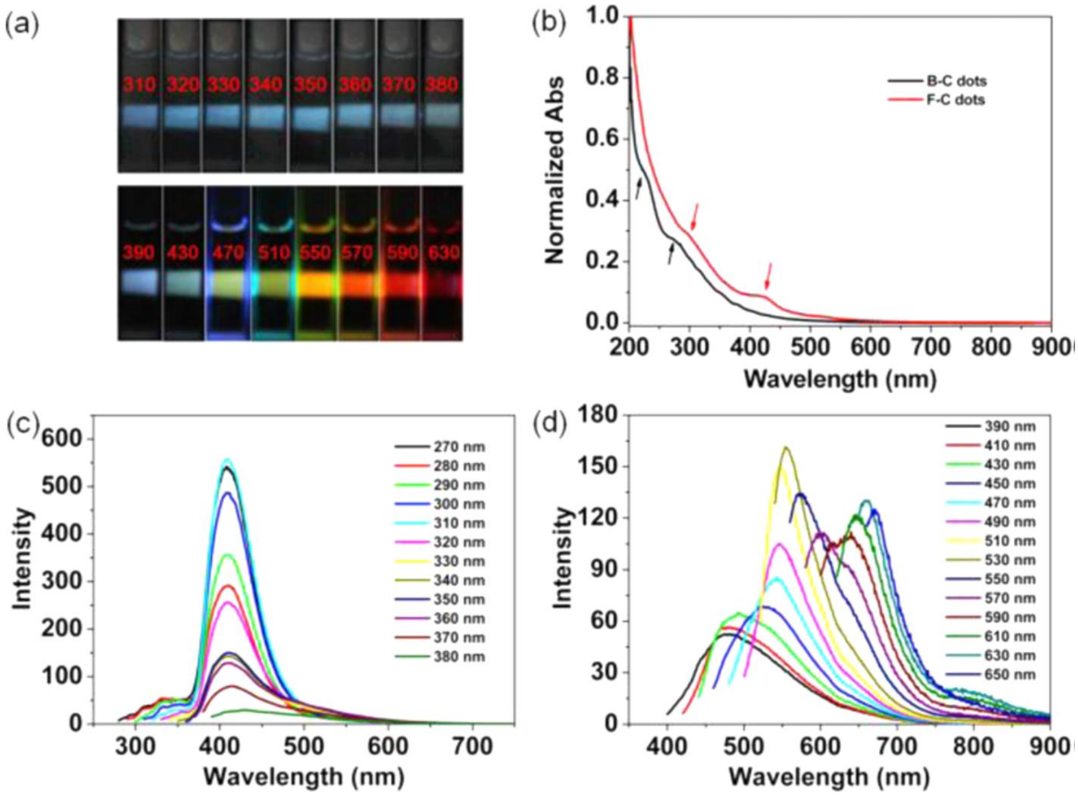

Figure 1.8. (a) Photographs under UV lamp showing blue emitting and full color emitting CDs, (b) corresponding UV-visible absorption spectra, and (c) and (d) fluorescence emission spectra at different excitation wavelengths of B-C dots and F-C dots, respectively.

Jiang et al. prepared green, blue and red emitting CDs at single excitation wavelength by solvothermal reaction of ortho, meta and para phenylenediamine isomers (Figure 1.9) (K. Jiang et al., 2015). The difference in the particle size and nitrogen content was reasoned for the alteration in the PL emission of these CDs. CDs obtained by electrooxidation of graphite in aqueous solution exhibited size dependent PL. Here, the CDs with an average diameter of 1.9 nm was blue fluorescent, whereas those having average diameter of 3.2 nm has emitted yellow light (Q.-L. Zhao et al., 2008). The microwave assisted synthesis of blue emitting (by carbonizing polyethylenimine alone) and wavelength tuneable CDs (by carbonizing polyethylenimine and glutaraldehyde in different ratios) demonstrated excitation-dependent emission (Hongying Liu, He, Jiang, & Zhu, 2015). Although, these CDs showed polydispersity, authors attributed the excitation-dependent behavior to the oxygen-related surface states. Another type of excitation-dependent emission were reported was due to the resonance energy transfer from smaller CDs to larger ones (Fang et al., 2012). Apart from these, many CDs show excitation dependent emission. (Bourlinos et al., 2012; Kozák et al., 2013; C. Liu et al., 2011).

Figure 1.9. Blue, green and red emission from CDs prepared using three isomers viz., ortho, meta and para isomers of phenelynediamine, respectively.

The majority of CDs shows excitation-dependent emission, there are a few cases in which excitation independent CDs have been reported. Most of these cases were attributed to the uniformity in size and surface structures (D. Chen et al., 2017; Wen & Yin, 2016; X. Yang et al., 2017).

1.1.2.2.1. pH-dependent luminescence

Most of the CDs show pH-dependent fluorescence. Influence of pH on the PL intensity of CDs could mainly be attributed to the existence of acidic/basic functional groups on the CDs surface (Pan et al., 2010; Qian et al., 2014). The emission wavelength of ascorbic acid derived CDs was red-shifted to 550 nm from 441 when the pH was changed from 2.32 to 12.00, attributed to the change in the π–π^* and n–π^* electronic transitions (Jia, Li, & Wang, 2012). CDs hyperbranched with polyethyleneimine (PEI) as a surface passivation agent exhibited nearly 5 fold enhancement in the emission intensity when the pH decreased from 11 to 3. The pH sensitivity of CDs to the external environment arises from surface passivation with PEI, which has basic/acidic sites to tune the PL by solution pH (C. Wang, Xu, & Zhang, 2015).

1.1.2.2.2. Quantum yield

Quantum yield (QY), the measure of fluorescence of material is an important parameter and judgemental regarding its technological usage. Unfortunately, CDs generally exhibit feeble QY as compared to the semiconductor QDs or organic dyes especially at the higher wavelength region (<500 nm) (Bourlinos et al., 2008; Fang et al., 2012; Y. Liu et al., 2016; Qian et al., 2014; Y. Wang & Hu, 2014; Q.-L. Zhao et al., 2008). As a result, there were several attempts to enhance the QY of CDs, most commonly by doping the heteroatom/s and by surface passivation using nitrogen-containing moieties (Park, Yoo, Lim, Kwon, & Rhee, 2016).

Green fluorescent N and B doped CDs (Jahan, Mansoor, Naz, Lei, & Kanwal, 2013) had an initial QY of 11.44%. After surface passivation with amine functionality, QY has raised to 23.71%. Surface passivating agents containing primary amine groups such as polyethyleneimine had proven to be effective probably due to the formation of amide linkage with surface carboxyl groups. The CDs incorporated into polyvinyl alcohol had shown enhanced luminescence emission with a QY as high as 61% (Z. C. Jiang et al., 2016). In another report, S-doped and N and S co-doped CDs, the former has shown QY 5.5% whereas latter had a QY 54.4%. The large increase in the QY in N and S co-doped CDs was attributed to the presence of C=N and C–N bonds in the form of polyaromatic structures, which are considered to be the key factors in amplifying the QY (Ding, Wei, & Xiong, 2014). Si containing functional groups were another passivating agent utilised for improving the QY. In one such report, the QY of around 47% has been demonstrated for an organosilane functionalized CDs, obtained by the pyrolysis of anhydrous citric acid in N -(β -aminoethyl)- γ -aminopropyl methyldimethoxy silane (F. Wang, Xie, Zhang, Liu, & Zhang, 2011). Apart from lab chemicals, CDs from natural sources, shows good QY owing to the abundant hetero atoms in it. For example, CDs prepared by hydrothermal treatment of egg white has shown high QY of 61% (Ding et al., 2014).

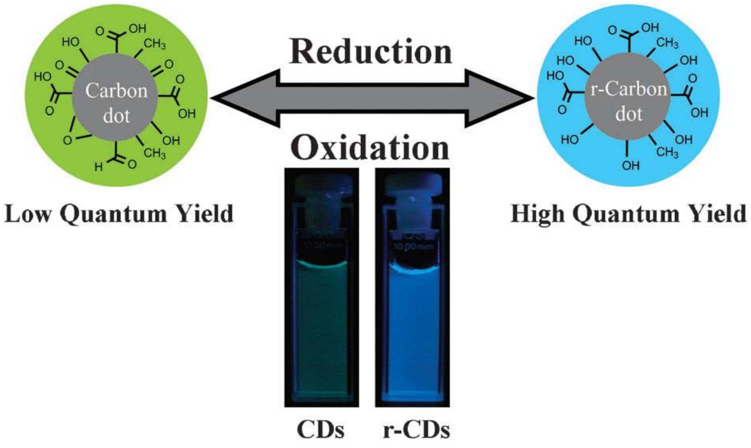

Figure 1.10. Demonstration of quantum yield enhancement of CDs after the reduction with $NaBH_4$.

In a seminal report by Zheng et al. demonstrated that the QY of CDs could be enhanced significantly by reducing with $NaBH_4$ (Zheng et al., 2011). The CDs obtained from an oxidative clipping of graphite with QY 2% has been shown to enhance its QY to 24% after the reduction with $NaBH_4$, along with a blue shift in the wavelength from 520 to 450 nm. Authors attribute these to the increased number of electron donating surface hydroxyl groups owing to the reduction of epoxy and C=O group in the original CDs (Figure 1.10).

1.1.2.2.3. Upconversion luminescence

Use of long wavelength radiations such as NIR and IR have significantly increased in the field of bioimaging and chemotherapeutic applications due to the minimal tissue damage, depth of penetration and feeble auto-fluorescence (Pansare, Hejazi, Faenza, & Prud’homme, 2012). One way to employ long wavelength radiation is to exploit upconversion luminescence in which fluorophores absorb two or more photons of lower energy and fluoresce at the high energy radiations or undergoes anti-Stokes luminescence. Many efforts are being put towards the synthesis of CDs having high upconversion throughput (Jia et al., 2012; Pansare et al., 2012; Salinas-Castillo et al., 2013).

1.1.2.2.4. Origin of photoluminescence

As already mentioned, the existence of broad, excitation-dependent emission and the dramatic amplification of QY upon surface passivation and doping has been a hot topic of debate. Many are attributing the origin of photoluminescence in CDs to the complex structure of CDs regarding the size of the core and nature of surface/edge states. These factors differ according to the synthetic strategies, dispersion media, and nature of doping, to name a few.

A comprehensive steady-state and time-resolved fluorescence studies have been performed to unfold the multi-emission observed in citric acid derived CDs. The emission below 400 nm was stemmed from carbon core whereas higher wavelength emission (above 400 nm) originated from surface states. An additional band which can be explained by molecule like state was observed when the above CDs were functionalized with an amine group. There is an electron transfer from core to surface states and vice-versa involving –COOH and –NH_2 groups at the surface, which strongly affect the luminescence output from CDs (Pansare et al., 2012).

Luminescence of CDs can be tuned by altering the oxygen-containing functional groups at the surface (Ding, Yu, Wei, & Xiong, 2016; L. Wang et al., 2014) and unlike semiconductor QDs, the energy gap is not influenced by the size of the CDs (Figure 1.11). Controversially, the shift in the emission could be due to the change in the size of CDs and the excitation-dependent emission is not an intrinsic property of CDs (Vinci et al., 2013).

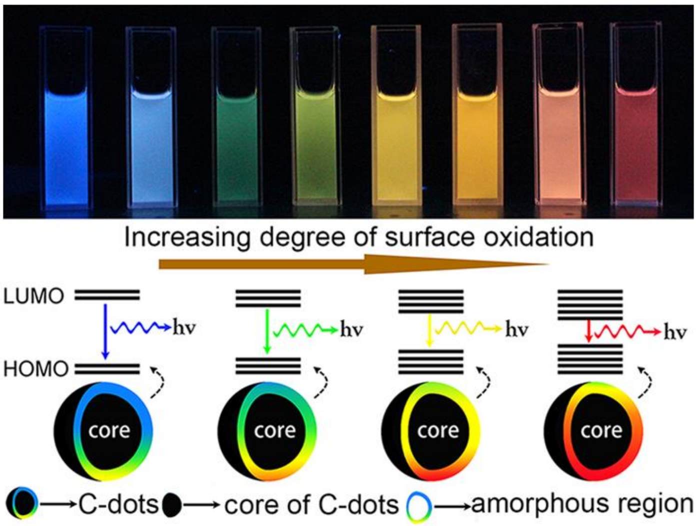

Figure 1.11. Schematic illustration red-shifted emission of CDs with increasing surface functional groups. CDs were prepared by hydrothermal reaction of urea and p-

phenylenediamine. Various fractions were separated using silica column chromatography. A gradual red shift in emission peaks from 440 to 645 nm was observed.

A model CD system made by fine-tuned concentrations of polycyclic aromatic hydrocarbon (PAH) embedded in a polymer described the origin of large Stokes shift and excitation-dependent emission response in CDs (Figure 1.12) (Fu et al., 2015). The self-trapping of exciton in the PAH network was responsible for the observed large Stokes shift whereas the excitation dependence emission originates from the selective excitation of PAH having slightly different energy levels and subsequent energy transfer between them. Calculations show that graphitic nitrogen atoms in CDs is doing the effect and shift the emission peak by altering the energy levels (Sarkar et al., 2016). However, the pyridinic and pyrrolic nitrogen atoms have no appreciable influence on the energy levels of CDs.

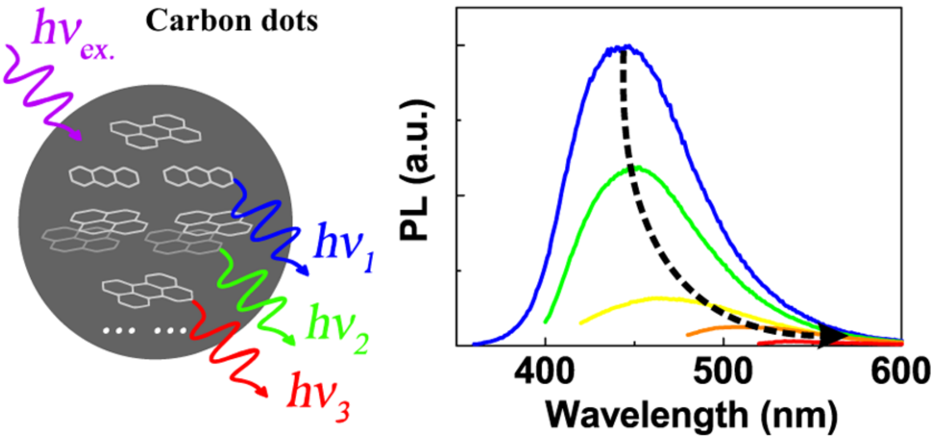

Figure 1.12. Origin of PL in CDs unveiled using PAH-polymer matrix model system.

There are reports implies the red shift in emission to the size of the graphitic core as well as to the improved surface carboxyl groups (Hola et al., 2014). A detailed investigation of CDs prepared by the oxidation of carbon fibers in nitric acid revealed that both size and surface states are crucial in determining the position of the emission band in CDs (Bao, Liu, Zhang, & Pang, 2015). On the other hand, Khan et al. argue that multicolor emission from CDs is not from any quantum confinement but due to the presence of ensemble of emissive states (Hsu, Chen, & Chang, 2016; Khan, Gupta, Verma, & Nandi, 2015).

1.1.2.3. Cytotoxicity and biocompatibility

Low cytotoxicity and biocompatibility are the key features of CDs made them an attractive candidate among the cluster of fluorescent nanomaterials (Q.-L. Zhao et al., 2008). In a noted study, three types of CDs viz. blue, green and red emitting, derived from phenylenediamine isomers were evaluated for cytotoxicity using a standard MTT assay with MCF-7 cells (K. Jiang et al., 2015). Over 90% cell viability was observed even after the incubation of CDs having concentrations ranging from 10 to 50 mgmL^{-1} for 24 h. Cellular imaging capability of these CDs were evaluated (Figure 1.13). Comparable biocompatibility was reported in the case of gold-CDs (GCDs) composite material as well (Lingyang Zhang et al., 2016). It was found that when the concentration of GCDs was less than 833 μg/mL, GCDs shown no toxicity towards cells. At higher concentration, GCDs start to show a little inhibition effect on normal cells, but cancer cell has no adverse effect.

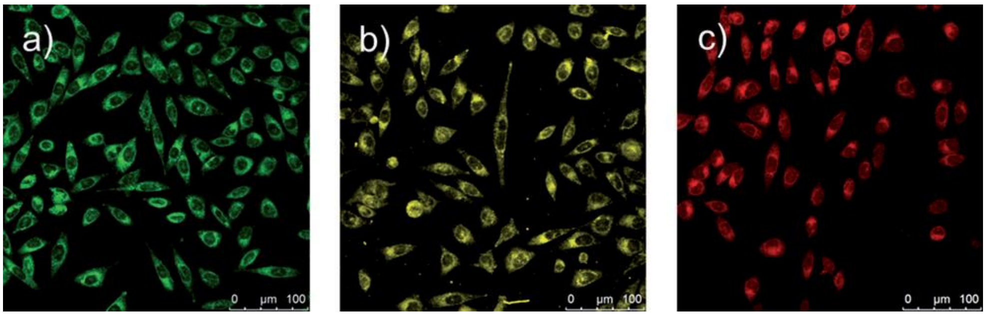

Figure 1.13. Confocal fluorescence images recorded by staining MCF-7 cells at 405 nm laser excitation using three different CDs (a, b and c) prepared by phenylenediamine isomers.

Polyethylene glycol (PEG)-derived CDs@SiO$_2$, prepared by growing the CDs inside mesoporous silica followed by capping with PEG molecules had depicted enhanced biocompatibility. The biocompatibility studies were carried out by incubating CDs@SiO$_2$-PEG with HeLa cells followed by MTT assay. The results indicate that most of the cells were intact after the specified duration of time, reflecting the non-cytotoxicity of CDs towards the cell (Lai, Hsiao, Peng, & Chou, 2012). Histidine derived CDs was tested for its toxicity by labeling AD-293 (human embryonic kidney) cells (Huang et al., 2014). The AD-293 cells were cultured in the medium with different concentrations of CDs for 24 h. The cell viability, tested using MTT assay, was almost 100%, even when the concentration of CDs was kept

2000 μg/mL after 24 h. These studies indicate that the CDs are biocompatible and impart only low toxicity and hence can be utilized for biological applications.

1.1.2.4. Electroluminescence

The luminescence output from the material because of the electrical energy input is referred as electroluminescence. Highly conjugated organic molecules and cadmium based semiconductor quantum dots have been extensively scrutinized for this purpose. Though many reports hypothesized the electroluminescence from CDs, there are only handful of reports in which LEDs have been fabricated using the CDs.

Wang et al. constructed LED by exploiting the white light emission from CDs (F. Wang, Chen, Liu, & Ma, 2011). A maximum external quantum efficiency achieved was 0.083% at a current density of 5 mA/cm^2. The device fabrication was accomplished by placing CDs between hole-transport and an electron-transport layers. Another interesting work demonstrated the fabrication of CDs based light emitting diodes in which switching of electroluminescence output was accomplished by tuning injection current density and device structure (X. Zhang et al., 2013). By varying the injection current density/applied voltage various color output such as blue, cyan, magenta and white was observed as demonstrated in Figure 1.14. A multi-color band gap fluorescent CDs was used as an active emission layer in monochrome electroluminescent LEDs with stable emission that can vary from blue to red without the usage of hole transport layer (F. Yuan et al., 2017). The maximum luminance (I_{max}) was observed for blue LEDs (136 cd m^{-2}), found to be the best performing CDs based monochrome electroluminescent LEDs. A white LED (WLEDs) with a Commission International d’Eclairage (CIE) color coordinate at (0.30, 0.33) were fabricated by using the CDs blended poly(N-vinyl carbazole) (PVK) as an emissive layer. The I_{max} and current efficiency (η_c) values for WLED was found to be comparable to semiconductor-based LEDs.

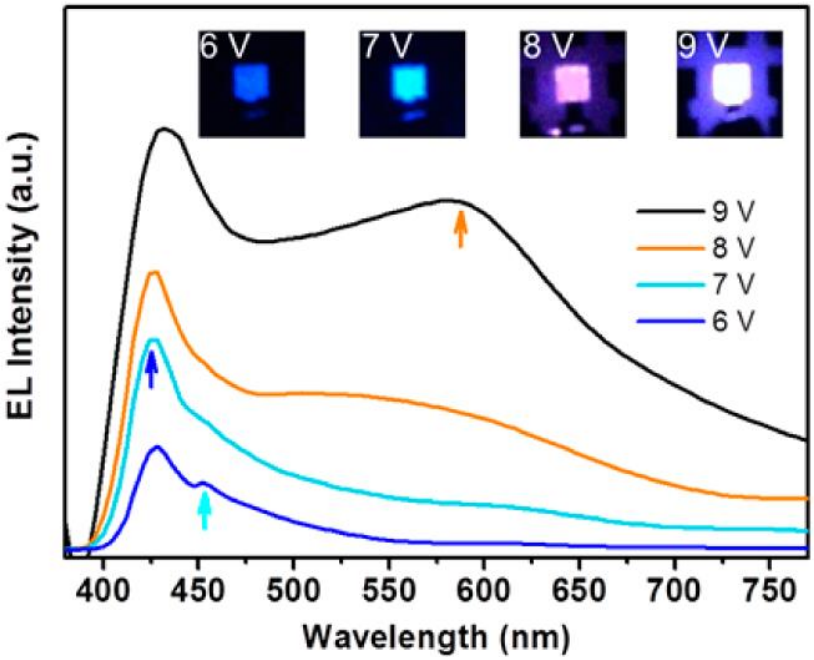

Figure 1.14. EL spectra and true color photographs of blue, cyan, magenta, and white emissions.

1.1.2.5. Energy transfer and redox properties

The excellent electron accepting and transferring ability of CDs are demonstrated in many studies. Here, we enlist some of the reports. Photoinduced electron transfer from CDs to the singly occupied molecular orbital of nitroxide radical led to the PL quenching (Lin et al., 2012). The same CDs can accept electrons from organic amines such as triethylamine. The electron transferability of two different types of nitrogen-containing CDs (NCDs) to nickel(II)phthalocyanine complex were compared (Barman, Jana, Bhattacharyya, & Patra, 2014). The P doped NCDs and B doped NCDs were used for this study. Due to the high electron density in P doped NCDs, the electron transfer ability of CDs to phthalocyanine was enhanced whereas opposite effect was observed in case of boron co-doped N-CDs (Figure 1.15).

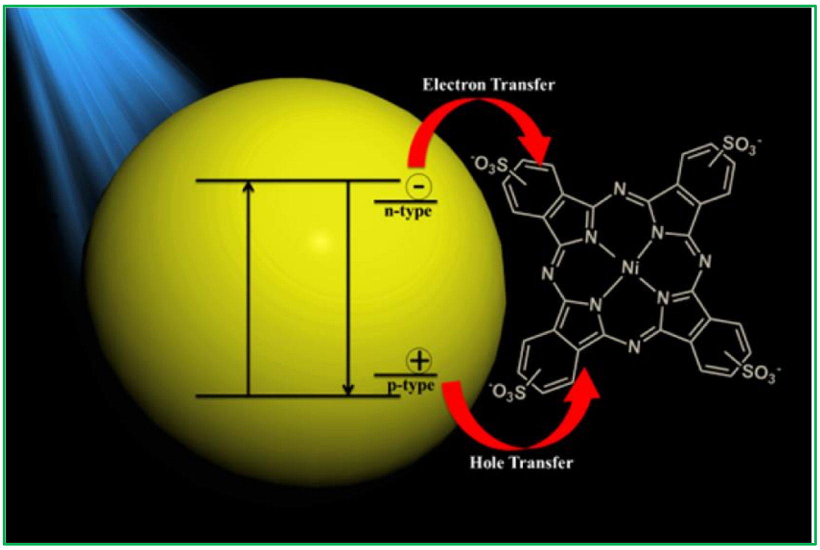

Figure 1.15. Schematic of electron transfer between CDs and nickel(II)phthalocyanine complex.

Surface passivation can alter the electron transfer ability. Amine passivated of CDs-Ru(III) system transfer electron to a model quinone drug more effectively compared to un-passivated CDs. The electron transfer occurs via both dynamic and static quenching pathways (Sau, Bera, Mondal, Satpati, & Basu, 2016). It was shown that the surface modification of NCDs with different thiophene containing groups improve its electron transfer efficiency to the fullerene derivative and resulted in luminescence quenching of CDs (Privitera et al., 2016). The electron transfer from amine functionalized CDs to chloroplast was reported. The study was intended to understand the ability of CDs to take part in photosynthesis and related events (Chandra et al., 2014). Another study shows that the aggregated nanostructures of α-cyclodextrin functionalized CDs could act as an efficient donor to methyl viologen acceptor (Mondal & Purkayastha, 2016).

Like electron transfer, the energy transfer tendency of CDs also been exploited in the sensors, catalysis, energy harvesting, etc. The energy transfer between CDs and variously sized silver nanoparticles (AgNPs) have been investigated (Prajapati, Bhattacharya, & Mukherjee, 2016). The energy transfer from CDs to AgNPs increased with increase in the size of the nanoparticles. This variation could be due to the enhanced spectral overlap and decreased separation distance. A FRET type energy transfer was reported in the case chitosan derived CDs to nitroaromatics (Z. Liang, Kang, Payne, Wang, & Sun, 2016). In another study, Suzuki et al. demonstrated that CDs could transfer its excited state energy to ZnO nanoparticles and hence can modulate the luminescence of latter. The dipole interactions between ZnO and CDs and the formation of surface defects in inorganic oxide structure was reasoned for the efficient energy transfer between CDs and ZnO nanoparticles (Suzuki et al., 2015).

1.1.2.6. Morphology and Crystallinity

In general, the CDs are quasi-spherical dots having the size usually falls below 10 nm. (Figure 1.16) The thickness of CDs was found to be equivalent to few graphene layers (around 1-5 layers). Compared to other allotropes of carbon such as GQDs, GO, CNT and fullerenes, CDs manifest poor crystallinity. This could be mainly due to the presence of plenty of defects introduced by surface functional groups and a lesser amount of sp^2 hybridized core (Hu, Yang, Tian, & Yu, 2015). The extend of crystallinity in CDs is comparable to that of graphene oxide. X-ray diffraction (XRD) pattern of CDs derived from chitosan has a 2θ value of 22.48°. This is like that of graphite lattice spacing, attributed to the highly disordered carbon lattice (Xin Liu, Pang, Xu, & Zhang, 2016). Further, Raman spectra depicted relatively strong D band at 1378 cm^{-1} and G band at 1580 cm^{-1} with I_D/I_G ratio 1.15, indicating the poor crystalline nature.

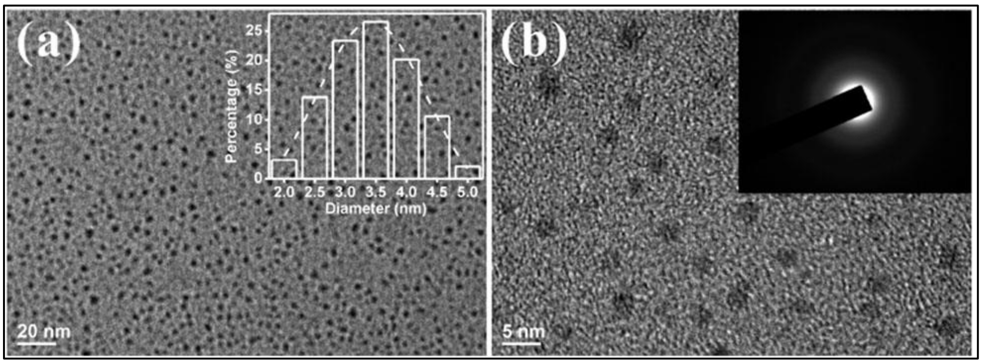

Figure 1.16. (a) TEM and (b) HRTEM images of CDs prepared by carbonization of citric acid. Inset showing (a) size distribution and (b) selected area electron diffraction (SAED) pattern of CDs (Hu et al., 2015).

1.1.2.7. Stability

Compared to its organic counterparts, such as fluorescent dyes, CDs manifested high photostability, thermal stability, and tolerance to pH. These aspects are important as the random fluctuation in the PL intensity under various physical or chemical environment leads to false results in fluorescence-based imaging or sensing. Many CDs manifests good photostability towards the irradiation of UV light (a few hundred mW power) for several hours (Yingbo Liu, Zhou, Li, Deng, & Zhang, 2017) and tolerance to a wide range of pH (Ren et al., 2014).

1.1.2.8. CDs verses GQDs

The difference between CDs and graphene quantum dots GQDs is not much clear and many consider GQDs as a kind of CDs. A few differences can be drawn between CDs and GQDs are as follows. Since GQDs are most often produced from graphene-based starting materials or the rigid synthetic chemistry of graphene-like smaller polycyclic aromatic hydrocarbon molecules, they possess graphene lattice in the core irrespective of the size of QDs. Hence, GQDs composed of sp^2 hybridized carbon core and are crystalline. GQDs have lateral dimensions less than 100 nm in single-, double- and few- (3 to <10) layers. On the other hand, CDs are generally prepared by carbonizing lab chemicals and naturally available sources with size below 10 nm. And hence CDs are mostly amorphous although the synthesis of many crystalline CDs is reported.

1.1.3. CDs as Fluorescent Sensors

This section highlights the recent developments in the fluorescent sensing scaffolds concocted using CDs as a signaling agent. The class of analytes includes metal ions, biomolecules, water contaminants and hazardous chemical species.

1.1.3.1.Detection of Metal Ions

Metal ions, although not all, undoubtedly play a vital role in biological activities such as in enzymatic catalysis, bio-molecular transportation, stabilizing the protein configuration, cleavage and replication of DNA and RNA strand, etc. Hence their imbalance unambiguously causes severe damage and sometimes even fatal. However, the presence of heavy metal ions such as Cd(II), Hg(II), Cr(VI), etc. in the body may cause acute damage. It is of utmost importance to detect these metal ions with high sensitivity and selectivity. Alongside, a large mass of metal ions is discarding into the water bodies by industries, which cause damage to the ecological system. There have been several attempts to construct luminescent-based metal ion sensors using environmentally benign and cheap CDs as fluorescence indicators (Baker & Baker, 2010; Gao et al., 2016; Liao, Cheng, & Zhou, 2016; Ruedas-Rama, Walters, Orte, & Hall, 2012; Shi, Lu, Yan, & Ma, 2013). Some representative work in this area is mentioned below.

A sensitive fluorescent detection of Hg^{2+}, exploiting the selective binding of Hg^{2+} to thymine bases of deoxyribonucleic acid has been successfully demonstrated using DNA functionalized CDs and MoS_2 nanosheets (Srinivasan, Subramanian, Murugan, & Dinakaran, 2016). MoS_2 nanosheet quenches the blue emission of DNA functionalized CDs in the first step which was then turned on by Hg^{2+}. The sensitivity of the probe was ~1 nM. Detection of Ag^+ ions was achieved using a green luminescence of CDs synthesized from ethylene glycol (Gao et al., 2015). The mechanism was attributed to the reduction of Ag^+ to silver nanoclusters by CDs. A yellow emitting CDs prepared via microwave-assisted route shows its capability of screening Cr^{6+} (Z. Xu et al., 2015). The quenching response during the detection was associated a wavelength shift (blue-shift).

A selective detection strategy for Fe^{3+} ions was demonstrated using N and P co-doped CDs derived from adenosinetriphosphate (ATP) as a precursor. The formation of Fe-O-P bonds formed between Fe^{3+} and the N and P co-doped CDs was surmised to be responsible for the selective quenching of CDs emission by Fe^{3+} ions (Shangguan et al., 2017). This sensor was successfully applied for the detection of Fe^{3+} in human blood serum and living cells

1.1.3.2.Detection of biomolecules

Many bio-events can be assessed by the precise quantification and qualification of biomolecules. Detection of amino acids, sugars, carbohydrates, vitamins, proteins, enzymes, DNA, etc. is falling under this category. Plenty of CDs demonstrated its ability to detect a diverse number of biomolecules.

Fluorescent detection of biothiols such as cysteine, homocysteine, and glutathione has been shown using CDs (L. Zhou, Lin, Huang, Ren, & Qu, 2012). The detection involves two steps. PL of CDs was quenched by Hg^{2+} by electron transfer mechanism, and in the second step, fluorescence was ‘turned-on’ by biothiols via the selective removal of Hg^{2+} through the formation of Hg^{2+}–S bond. A one step, straightforward, non-enzymatic blood glucose assay by using boronic acid functionalized CDs was demonstrated by Shen et al. (Shen & Xia, 2014). Due to the selective binding of glucose molecules to surface-bound boronic acid groups, the luminescence intensity of CDs was linearly quenched and is used to assess the blood glucose level (Figure 1.17).

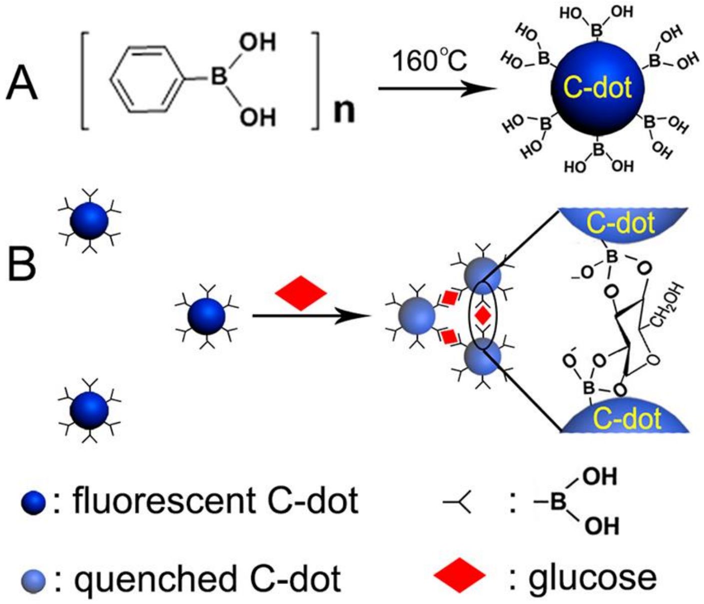

Figure 1.17. Schematic representation of blood glucose sensing using boronic acid functionalized CDs.

Apart from these, detection of glutathione (Cai et al., 2015), glucosamine (Das & Mohapatra, 2017), hyaluronidase (W. Yang et al., 2017), ascorbic acid (AA) (L. Li et al., 2015), alkaline phosphatase (ALP) activity (Qian et al., 2015), etc. are reported. All strategies exploited the specific interaction between the surface functional group of CDs and the analyte molecule.

1.1.3.3.Detection of explosives and pesticides

Explosives and pesticides are lethal to humanity (Germain & Knapp, 2009). Selective detection of many of these compounds is challenging owing to the similarity in chemical structure and physical properties. Analytical tools such as mass spectrometry, atomic spectrometry, absorption spectroscopy and fluorescence spectroscopy are usually employed for this purpose. CDs are being demonstrated as potential fluorescence based approach for the detection of explosives/pesticides molecules (H. Li et al., 2016).

Zhang et al. show a multidimensional sensing approach for TNT using nitrogen-rich CDs (Lingling Zhang, Han, Zhu, Zhai, & Dong, 2015). The amino functionalized CDs was selectively quenched by TNT via electron transfer pathway, which is used for establishing fluorescence sensing platform for TNT. The CDs doped with rare earth metal ion terbium (Tb-CDs) was used as both signaling and recognition part for the detection of a potential nitro-explosive called as trinitrophenol (TNP) (B. B. Chen, Liu, Zou, & Huang, 2016). The limit of detection (LOD) of this sensor system was 200 nM. Another detection strategy employed for the same molecule used B and N co-doped CDs (BN-CDs) (Sadhanala & Nanda, 2015). The strong quenching of BN-CDs emission by TNP was attributed to the static quenching route induced by the electrostatic interaction between BN-CDs and TNP. The detection limit of this method was 10 nM. Apart from fluorescence-based sensors, electrochemical detection of TNP using CDs was also demonstrated. A film made using conducting CDs and polypyrrole (PPy) nanocomposite was used for the electrochemical detection (Pal, Sk, & Chattopadhyay, 2016).

1.2. Methods in Fluorescence-based Sensors

Compared to electrochemical and mass spectrometry-based sensors, optical sensors are superior in terms of their ease of handling and non-invasive nature. Because of high sensitivity and versatility, fluorescence-based optical sensors are preferred when compared to absorption based optical sensors. Ability to recognize the analyte of interest is a key aspect of any sensor and in fluorescence sensors, it is realized by tagging a target-specific molecule to the fluorophore. Fluorescence sensors for diverse number analytes; environmental, biological and industrial significance have been established in recent years. We now discuss the various approaches used in fluorescence sensors and their mechanism.

1.2.1. General approaches to fluorescence sensing

Fluorescence-based sensors can be broadly categorized as intensity and lifetime based sensors. The variation in the PL intensity of fluorophore in the presence of analyte is monitoring in the first case whereas alteration in the excited state lifetime of a fluorophore is followed in the second case.

1.2.1.1. Intensity-based fluorescence sensors

Here the emission intensity of a fluorophore at a specific wavelength is tracked concerning the concentration of the analyte molecule. The PL intensity of the fluorophore may increase (Turn on) or decrease (Turn off) or there can be a simultaneous on-off at two different wavelengths (ratiometric) when encounters with an analyte molecule.

1.2.1.1.1. Turn-off fluorescent sensors

Several of these category sensors are already discussed in the previous sections. The turn-off may be due to electron transfer by ground state complexation as in the case of Cu^{2+} detection using lysozyme stabilized Au nanoclusters (Shanmugaraj & Ilanchelian, 2016). The red emission from nanoclusters was quenched by Cu^{2+} due to its selective binding by lysozyme molecules. Similar quenching pathway was operated for Fe^{3+} ions using nitrogen-doped CDs synthesized by hydrothermal carbonization of Prunus avium fruit extract (Edison et al., 2016). The Fe^{3+} formed a complex with phenolic hydroxyl groups present on the CDs.

The alternative channel of turn-off is the excited state electron transfer. One example is the detection of vancomycin using glutathione capped CdTe QDs. The pathway was confirmed by time-resolved fluorescence techniques (W. Liang et al., 2015). A fluorescence quenching based melamine sensor using GQDs as a fluorophore in the presence of mercury operate on the principle of electron transfer (dynamic quenching) from GQDs to Hg^{2+}, assisted by melamine (Figure 1.18) (Sun, Wu, Gao, Ren, & Qu, 2013). A Eu(III)-based metal-organic framework was exploited for the simultaneous detection of Fe^{3+} and picric acid (PA). Both these analytes were able to quench the emission of the fluorophore by combined dynamic and collisional quenching mechanisms (X.-H. Zhou et al., 2013).

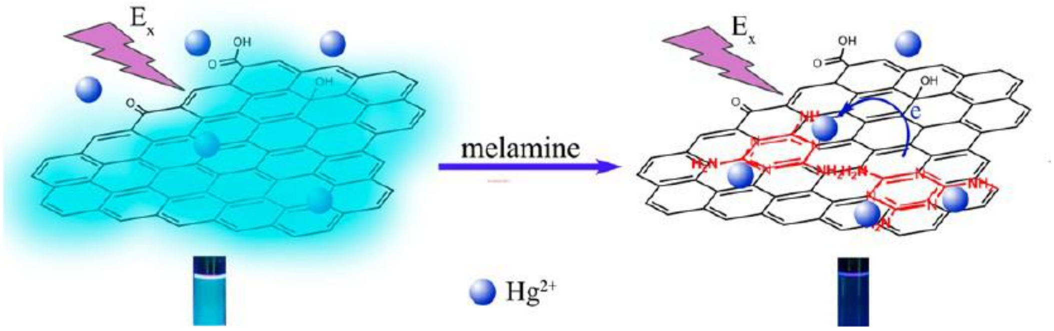

Figure 1.18. Schematic representation of melamine sensor using GQDs in the presence of Hg^{2+}.

1.2.1.1.2. Turn-on fluorescent sensors

Turn-on fluorescence probes are more selective as compared to turn-off fluorescent sensors. Liu and co-workers designed perylene tetracarboxylic diimide fluorophore for the turn-on fluorescence sensing of Zn^{2+} and Cd^{2+} at pH 6.0-7.0 and 9.0, respectively. The ability of the sensor to discriminate and detect these two metal ions by simply adjusting the pH of the medium is the captivating feature of this sensor (Xiangjun Liu et al., 2013). A graphitic phase C_3N_4 nanosheet-MnO_2 composite was demonstrated for the selective turn-on fluorescence detection of glutathione in aqueous solution as well as in living cells. The luminescence was restored due to the reduction of MnO_2 to Mn^{2+} by glutathione thereby breaking the FRET dyad between the nanosheet and MnO_2 (X.-L. Zhang et al., 2014). Turn-on fluorescence sensors based on QDs was also demonstrated for the detection of H_2O_2 (Lan et al., 2015), thioctic acid (Tan, Li, Zhang, Shen, & Yang, 2015), alkaline phosphatase (Haijian Liu, Li, Xia, & Ren, 2017) and many more.

1.2.1.1.3. Simultaneous turn-off and turn-on based fluorescent sensors

There is a growing interest among the scientific community to develop a single sensor capable of detecting two or more analytes (Singla et al., 2015; Q. Wang et al., 2015). The PL intensity of the fluorophore can be switched-off or switched-on by employing different analytes. For instance, a turn off-on fluorescent sensor for anticancer drugs and DNA was established using CdTe QDs as a fluorophore (D. Zhao, Li, Yang, & He, 2014). In the first step, the fluorescence emission of CdTe QDs was quenched by the addition of platinum anticancer drugs via the PET. The recovery was achieved using DNA, which links covalently with Pt anticancer drugs and thereby removing the PET.

1.2.1.1.4. Ratiometric fluorescent sensors

Single wavelength modulation type sensors may be influenced by variation in the assay environment. On the contrary, ratiometric fluorescent sensors, which tracks the emission of two different wavelengths can effectively eliminate the environmental effects to some extent and hence provides an inbuilt correction (Gui et al., 2012; F. Ma, Sun, Zhang, & Wang, 2015; Sinha, Chowdhury, & Ghosh, 2016). For example, a ratiometric picric acid (PA) sensor was constructed using squaraine dye connected to the dansylamide ring bearing electron acceptor and donor groups, respectively. Upon the addition of PA, the 684 nm emission of the probe was decreased whereas a new emission at 644 nm emerged. This gives an opportunity to measure the emission intensity the ratio of which was found to be proportional to the concentration of PA (Sinha et al., 2016).

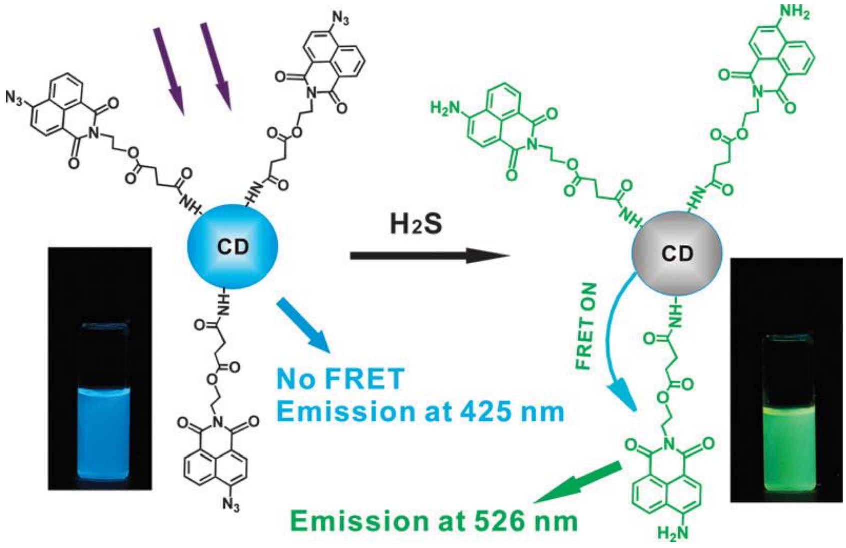

Figure 1.19. Schematic of a ratiometric FRET-based sensor for H_2S.

Yu and co-workers developed a FRET based novel ratiometric fluorescence sensor towards H_2S by using CDs (energy donor), which is covalently connected to naphthalimide-azide (energy acceptor) (C. Yu, Li, Zeng, Zheng, & Wu, 2013). Here, the blue emission from CDs is unquenched in the first step due to the lack transfer of energy from CDs to naphthalimide-azide, whereas in the subsequent step, owing to the conversion of azide group to amine group in the naphthalimide-azide by H_2S, FRET become effective and hence blue emission from CDs quenched and a green emission from naphthalimide moiety is observed, which in turn serving as a ratiometric sensor for H_2S (Figure 1.19).

1.2.1.2. Fluorescence lifetime-based sensors

The fluorescence sensors, which works on the modulation of its lifetime is comparably less in number. This is because lifetime based sensors are time-consuming and costly. None the less, as the fluorescence lifetime is independent of the concentration of the fluorophore. Hence, lifetime-based sensors are highly advantageous when the local concentration of the fluorophore alters due to washout or photobleaching and hence affecting the intensity based measurements. This is particularly useful in cell imaging using fluorescence microscope, where the local concentration of the probe in each part of the cell is not known. Further, intensity-based sensors may suffer from the drifts of the optoelectronic system (lamps and detectors), whereas lifetime is independent of these factors (McCranor et al., 2014; Peng et al., 2010; Tantama, Hung, & Yellen, 2011).

1.2.2. Mechanism of fluorescence sensing

The mechanism of fluorescence sensing involves energy transfer, electron transfer and in few cases inner filter effect based pathways. The discussion in this section focusses on highlighting the key aspects of these mechanisms.

1.2.2.1. Energy transfer

In case of energy transfer governed sensing, FRET is most often encountered compared to Dexter type energy transfer (Clare, Carl, Igor, & James, 2015; L. Yuan, Lin, Zheng, & Zhu, 2013). FRET is a non-radiative energy transfer process from excited state fluorophore referred as ‘donor’ to ground state quencher ‘acceptor’ (A schematic representation of FRET process is given in Figure 1.20). Dexter mechanism involves the electron exchange between the excited state donor and ground state acceptor. The excited electron from the donor moves to the LUMO of the acceptor, then transfer of an electron back to the ground state of the donor. Both

FRET and Dexter mechanisms require the spectral overlap between the donor and acceptor. The later operates at smaller distances (<1.5 nm) and does not need any specific dipole orientation.

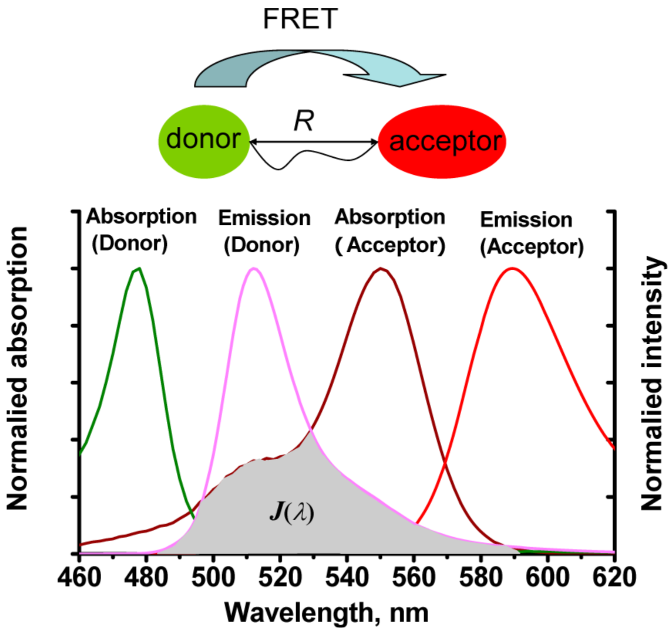

Figure 1.20. Representation of FRET. J(λ) represents spectral overlap.

Experimentally the presence of FRET mechanism can be ascertained. If the acceptor is an emitter, there is a concomitant increase in its emission intensity when the donor is being quenched. This is the direct evidence for the existence of FRET. But care should be taken that, the direct excitation of acceptor does not happen at the excitation wavelength of the donor. On the other hand, if acceptor is a non-emitter, the excited electrons of the acceptor joins the ground state hole by non-radiative pathway and hence decrease donor’s emission. The time-resolved analysis can be performed to authenticate the existence of FRET. Donor’s lifetime will be unambiguously decreased during the FRET because it is an excited state energy transfer process.

There are essentially three criteria for an efficient FRET process. Primarily, there should be a matching of donor’s emission and acceptor’s absorption. Secondly, donor and acceptor molecules should be at proximity. This can be accomplished by establishing a dipole-dipole, electrostatic or a covalent interaction between donor and acceptor. Finally, donor and acceptor must exhibit a suitable dipole orientation. Efficiency of a FRET process; $\mathrm{E} = \frac{R_0^6}{[R_0^6 + R^6]}$

Where, R_0 is the distance between donor and acceptor when E is 50%. R^2 is the distance between donor and acceptor. R_0 is proportional to the donor's QY, the integral of the spectral overlap between the donor emission and acceptor absorbance (I), and the relative orientation of the dipoles of the donor and acceptor (κ_p) and inversely proportional to the refractive index of the material (n_D), as shown below:

$$R_0 = 0.211[\kappa^2 n^{-4} \emptyset_D J_{DA}]^{1/6} \text{ (In A°)}$$

Where, n is the refractive index, Φ_D is the quantum yield of the donor, κ denotes the average squared orientational part of a dipole-dipole interaction (it is typically assumed $\kappa^2 = 2/3$ for common organic fluorophores provided that both partners are freely moveable and thus randomly oriented), and J_{DA} expresses the degree of spectral overlap between the donor emission and the acceptor absorption, which is given by, $J_{DA} = \int_0^\infty I_D(\lambda)\varepsilon_A(\lambda)\lambda^4 \, d\lambda$

Where, $I_D(\lambda)$ is the donor normalized fluorescence emission spectrum, $\varepsilon_A(\lambda)$ is the acceptor molar absorption coefficient, and λ is the wavelength. Further, the efficiency of the FRET process can also be found out experimentally using steady state and time-resolved analysis. The steady-state FRET efficiency (E_{SS}) is given by, $E_{SS} = \frac{\phi_{DA}}{\phi_D}$

Where, ϕ_{DA} is the quantum yield of the donor in the presence of acceptor and ϕ_D is the donor alone quantum yield. The quantum yield of the fluorophore can be measured using following general equation: $\phi_c = \frac{\phi_o I_c A_0 \eta_c^2}{I_0 A_c \eta_0^2}$

Where ϕ_0 and ϕ_c are the photoluminescence quantum yield of the standard and the sample. I_0 and I_c are the integrated emission intensity of the standard and sample. A_0 and A_c are the absorbances of the standard and sample. η_0 and η_c are the refractive index of the standard and the sample solutions, respectively.

The time-resolved FRET efficiency (E_{TR}) can be calculated using the lifetime of the donor in the absence and presence of acceptor, which is: $E_{TR} = \frac{\tau_{DA}}{\tau_D}$

Where τ_{DA} is the donor's lifetime in the presence of an acceptor and τ_D is the donor alone lifetime.

Modulation of FRET efficiency is the key to most of the FRET-based sensing strategies. This is commonly done in two ways. By altering the distance between donor and acceptor; i.e. by distance-dependent FRET or by changing the spectral overlap between donor and acceptor (Dennis, Rhee, Sotto, Dublin, & Bao, 2012; Dinda, Gupta, Shaw, Sadhu, & Saha, 2014; Y. Kim, Jang, & Lee, 2015; Loo et al., 2016; Moquin et al., 2013; Xiang & Tang, 2017; S. Xu et al., 2014).

1.2.2.2. Collisional and static quenching

There is a number of probes designed which operates on the principle of electron transfer mechanisms, particularly via collisional (also referred as dynamic quenching) and static quenching. Both quenchings have been widely studied as fundamental phenomena as well as in numerous applications such as biochemical, biomedical, environmental and safety and industrial domains. Here we highlight the key features of collisional and static quenching phenomena.

In *collisional quenching*, the photo-excited fluorophore interacts with ground state quencher and the electron transfer between these two leads to the quenching of fluorophore's emission. In other words, fluorophore is back to the ground state without the emission. On the contrary, binding of fluorophore and quencher in the ground state leads to the formation of a non-fluorescent complex is referred as *static quenching*. Hence, a collisional quenching relies on the extent of diffusion of fluorophore and quencher in addition to the lifetime of the fluorophore. Strong molecular interactions such as electrostatic and π–π interactions, which can form ground state molecular complex is necessitated for the static quenching (Germain & Knapp, 2009; Schibilla, Stegemann, Strassert, Rizzo, & Ravoo, 2016; Shanmugaraju & Mukherjee, 2015; Song et al., 2014).

There are several ways to distinguish static and collisional quenching. Absorption spectra of the fluorophore in the presence of quencher is a useful tool.

As the collisional quenching is an excited state process, the absorption spectra of fluorophore are unlikely to change. In contrast, ground state complex formation is expected to result in a variation in absorption spectra of the fluorophore. Temperature-dependent steady-state fluorescence spectra is the another method to understand the nature of electron transfer quenching mechanisms. Since collisional quenching is a diffusion controlled process, the extent of quenching is expected to increase with an increase in temperature as quencher can diffuse quickly at elevated temperature. Whereas the ground state complex between fluorophore and quencher can be destroyed at elevated temperatures and the emission will decrease with temperature rising. Time-resolved fluorescence analysis is commonly used for understanding the mechanism of electron transfer based quenching. As stated above, collisional quenching is an excited state process whereas static quenching happens at ground state. Hence fluorophore's lifetime is anticipated to decrease due to the emergence of a new non-radiative component in the denominator of the following equation.

$$\tau = \frac{1}{\Gamma + k_{nr} + k_q}$$

Where τ is the lifetime, Γ is the emissive rate, k_{nr} is the rate constant for non-radiative process and k_q is the rate constant due to quenching.

On the other hand, static quenching is not accompanied by the alteration of the lifetime of the fluorophore. This is because static quenching only removes some of the fluorophores by forming non-fluorescent ground state complex without affecting the excited state lifetime.

Both collisional and static quenching is characterized by the well-known Stern-Volmer equation.

$$\frac{F_0}{F} = 1 + K_{sv}[Q]$$

Where F_0 and F are the fluorescence intensity of fluorophore in the absence and presence of a quencher. Q is the concentration of the quencher and K_{sv} is the

Stern-Volmer quenching constant. Stern-Volmer equation can be expressed separately for collisional and dynamic quenching,

For collisional quenching,

$$\frac{F_0}{F} = 1 + K_D[Q]$$

For static quenching,

$$\frac{F_0}{F} = 1 + K_S[Q]$$

Here K_D and K_S are the Stern-Volmer quenching constant for collisional/dynamic and static quenching, respectively.

From the above equation, the plot of F_0/F versus concentration of quencher is a straight line with slope K_{sv} if either of the quenching mechanisms operates. On the contrary, if both quenching mechanisms are involved then the plot of F_0/F versus concentration of quencher is an upward curve pointing towards y-axis. In such cases, one can separate dynamic and static quenching contribution by plotting τ_0/τ versus concentration of quencher, where τ_0 and τ are fluorophore's lifetime in the absence and presence of a quencher. This plot will be a straight line, and the slope of the graph gives the contribution from dynamic quenching as it only changes the lifetime of the fluorophore (Figure 1.21).

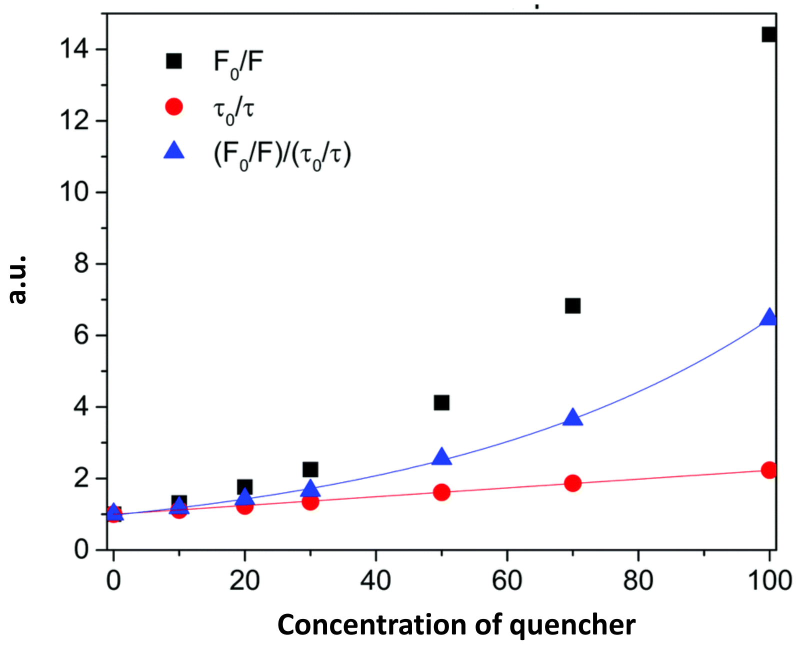

Figure 1.21. Plot representing the involvement of both dynamic and static mechanisms toward quenching of fluorescence.

1.2.2.3. Inner Filter Effect

Although less exploited and less selective, fluorescence sensors based on inner filter effect (IFE) mechanisms also exist, which does not demand any molecular interactions as in cases above. IFE happens due to the absorption of excitation or emitted light by the absorber (G. Li et al., 2016). This results in the decrease of emission of fluorophore because of the absorption of a part of excited or emitted light. The IFE based fluorescent sensors are constructed by altering the absorption of the absorber at the excitation or emission wavelengths, which in turn alters the fluorescence intensity and can be finally correlated to the concentration of target analyte.

1.3. Objective and Scope of the Work

For fluorescence based applications, it is very importance to choose the fluorophore having high numbers of merits. Most of nanomaterial based fluorophore used in recent times for the fluorescent based applications are semiconductor QDs and metal nanoclusters, which possess high toxicity, low photostability and excessive cost. CDs are advantageous in many of these aspects, though with many challenges, which should be addressed to extend the technological possibilities of CDs as fluorophore.

Another less explored aspect of CDs is its photo physics. Luminescence origin in CDs is unclear although many groups have proposed various hypothesis about the same. To extend the technological possibilities of CDs it is of paramount importance to understand its photophysical properties in detail. Synthesis of CDs through novel routes and tuning the size and property of the core and surface functional groups will be highly useful to extend the applications of CDs. Further, enhancing the quantum yield of CDs is also important as it is found to be relatively low for CDs which hinder their practical significance.

Despite, CDs synthesis of CDs in solid and liquid form is largely shown, CDs in its gel form is very rare. Hence, exploring the ways to realize CDs in gel form is also significant as it is advantageous and demanded for several purposes.

Considering excellent properties of CDs, we attempted to address some of the challenges and explore the use of CDs. We identify the specific objectives of present research as

- To explore an easy, rapid and eco-friendly synthetic routes for CDs and heteroatom doped CDs with variety of surface functional groups and polarity
- To attain CDs in gel form
- Tune the functional groups on the CDs' surface and hence its solubility
- Enhance the quantum yield of CDs by passivation and doping
- Understand the origin of fluorescence in CDs using fluorescence lifetime analysis, steady state fluorescence excitation and emission analysis, etc.
- Establish luminescence based chemical sensors based on CDs to screen some relevant molecules/ions.

The work presented in this report is useful in terms of the fundamental understanding of CDs and related materials and also we hope that it may open up variuos technological possibilities.

1.4. Organization of the Thesis

The thesis describes the synthesis, characterization, photophysical behaviour and some sensor applications of CDs. The thesis is organized as follows:

Chapter 1 elaborates the literature review on various synthetic routes for CDs, its general properties and its fluorescent based sensor applications. The mechanisms of fluorescence quenching and general approaches to fluorescence sensing with a few representative examples are highlighted.

Chapter 2 demonstrates a FRET based highly selective sensing of ammonia in both solution and gaseous states using CDs synthesized by the carbonization of acetic acid.

Chapter 3 details on the synthesis of a nearly white light emitting NCDs, their application as selective Cu^{2+} sensor and the luminescence origin in NCDs. An energy level diagram for NCDs is proposed based on a detailed study.

Chapter 4 describes on the synthesis of SiCDs gel via hydrothermal route using APTES as a precursor. The application of SiCDs gel in the selective sensing of Ag^{+} is also demonstrated here.

Chapter 5 highlights the synthesis of highly emitting SNCDs by hydrothermal carbonization of glutathione as a source of carbon as well as S and N. The luminescence origin in SNCDs, energy level diagram and a fluorescence based sensing strategy for Cr(VI) is detailed in this chapter.

Chapter 6 outlines the synthesis of organophilic CDs, using cyclohexane as a carbon source. A detailed characterization of OCDs, its application in the selective screening of nitroaromatics and the mechanism of luminescence quenching is discussed in detail.

Chapter 7 summarizes the conclusions drawn from the present thesis and highlights on the future scope of the work.

CHAPTER 2

FRET BASED AMMONIA SENSOR USING CARBON DOTS

This chapter describes the fluorescence sensing of Ammonia in solution as well as vapor phase using a sensor dyad, which consists of CDs and sodium rhodizonate. Here, a greenish blue fluorescence emitting CDs acts as fluorescence signaling agent and sodium rhodizonate as target specific molecule. The mechanism of the sensor relies on the fact that the excited state energy transfer (FRET) from CDs to sodium rhodizonate will be activated only when ammonia encounters sensor system, in turn quenching the luminescence of CDs, which can be utilized to correlate the amount of ammonia. The sensor shows high selectivity towards ammonia over oxides of nitrogen and common organic solvents.

2.1. Introduction

Detection and quantification of ammonia are crucial for environmental, industrial, and biomedical purposes (Dai et al., 2013; Timmer, Olthuis, & Berg, 2005). Several methods, including amperometric (Crowley, O'Malley, Morrin, Smyth, & Killard, 2008; Cui et al., 2013), fluorimetric (Takagai et al., 2010; Widmer et al., 2014) and colorimetric (Courbat, Briand, Damon-Lacoste, Wöllenstein, & de Rooij, 2009; Pandey, Goswami, & Nanda, 2013), have been used for detecting ammonia in solution and in vapour phases. Early amperometry-based methods for the detection of ammonia employed metal oxides, more commonly tin oxide-based sensors, in which the output resistance varied with ammonia exposure (Chandra Sekhar, Manu, Govindaraj, & Rao, 2007).Recently, more attention has been paid to the development of amperometric sensors using carbon-based nanomaterials, such as graphene and carbon nanotubes, as well as conducting polymers such as polyaniline (Bekyarova et al., 2004; S. Chen & Sun, 2013; Paglia et al., 2014). For example, an amperometric sensor comprising a multi-walled carbon nanotube electrostatically bonded to silver nanocrystals shows enhanced sensitivity compared with sensors comprising carbon nanotube alone (Cui et al., 2012). Although amperometric-based ammonia sensors are the most studied and offer high sensitivity, but suffers from low selectivity. Furthermore, moisture and volatile organic compounds strongly interfere. The requirement of high operating temperatures and cumbersome sensor design are other disadvantages of these methods (Chandra Sekhar et al., 2007; Sahm, Oprea, Bârsan, & Weimar, 2007; Shimizu et al., 2009).

Fluorescence sensors offer relatively higher sensitivity, easier design strategies, lower cost, and higher portability (Basabe-Desmonts, Reinhoudt, & Crego-Calama, 2007). Fluorometric systems have been successfully used for sensing gaseous analyte molecules. A selective fluorescence 'turn-on' sensing strategy for detecting ammonia has been demonstrated with rigid metal-organic frameworks and some fluorophores incorporated as a ligand (Shustova, Cozzolino, Reineke, Baldo, & Dincă, 2013). In another study, fluorophores, such as fluorescein and acridine orange, over cross-linked acrylic ester micro-particles were used for detecting ammonia vapor (Takagai et al., 2010).

When the proximity between a donor and an acceptor, having sufficient spectral overlap, is of <10 nm, the Förster (fluorescence) resonance energy transfer (FRET) process can be achieved. The FRET-based sensing strategy is applied in diverse fields, including cellular imaging (Piljic & Schultz, 2008), single molecule spectroscopy (Roy, Hohng, & Ha, 2008), DNA hybridization, (G. Jiang et al., 2009) and small molecule detection (L. Yuan et al., 2013). A few groups have used the FRET-based fluorescence strategy for detecting ammonia in the gaseous as well as liquid phases. For instance, in a fluorescence sensor, the addition of ammonia enhanced the FRET between coumarin (donor) and fluorescein (acceptor) because of the deprotonation of fluorescein, thereby leading to an improved spectral overlap (Widmer et al., 2014Widmer et al., 2014). Mader et al. designed a FRET-based sensor, in which upconverted luminescence intensity of the nanoparticle decreased because of energy transfer between the nanoparticle and phenol red in the presence of ammonia (Mader & Wolfbeis, 2010).

Here, we present a highly sensitive and selective fluorescence sensing platform for detecting ammonia in the solution and vapor phases by using sodium rhodizonate as an analyte-specific molecule and CDs as the signal transducer. The mechanism of sensing scaffold depends on the fact that excited state energy transfer (FRET) from CDs to sodium rhodizonate will be triggered once ammonia is introduced into the sensor solution (a solution containing 3 mL of CDs and 600 μL of 1 mM sodium rhodizonate is referred as 'sensor solution'). Subsequently, the fluorescence of CDs will be efficiently quenched; the quenching can be used for sensing ammonia.

Furthermore, the sensor solution adsorbed over cotton fibers is used for detecting ammonia from the vapor phase. We found this platform to be highly sensitive, respond linearly to ammonia concentration, and reversible after passing HCl gas. The sensor system was highly selective towards ammonia over the oxidizing gases such as NOx, allowing its use for biological and industrial purposes, where discriminating ammonia from oxidizing gases is highly desirable. Low cost, fast response, high selectivity, linear response, and good reversibility make the sensor extremely appealing.

2.2. Experimental Section

2.2.1. Reagents and Materials

Phosphorous pentoxide (P_2O_5), copper turnings, and quinine sulfate were purchased from Sigma Aldrich, India. Acetic acid, nitric acid, and ammonia solution were supplied by Merck Specialties, India, and sodium rhodizonate was obtained from Otto Chemicals, India. All aqueous solutions were prepared using double distilled water.

2.2.2. Instrumentation

UV-visible absorption spectra were recorded using Carry-100 double beam UV-visible spectrophotometer. Infrared (IR) spectroscopy studies were conducted using a Spectrum 100T Perkin-Elmer FT-IR spectrometer. Attenuated total internal reflection (ATR) mode was used for recording the IR spectra. Number of scans were fixed at 32. Before collecting IR spectra, samples were lyophilized for 2 days at -30 °C, the solid samples were then used for IR spectral analysis. Hydrodynamic diameter and zeta potential of CDs were recorded using Zetasizer Nano ZS (Malvern Instruments). Transmission electron microscopy (TEM) images were obtained using a JEOL 3010 UHR instrument. Here, dilute solution of CDs was drop-casted over the carbon coated grid, dried under vacuum and then used for TEM analysis. All fluorescence measurements were performed using the Fluoro Max-4C Spectrofluorometer (Horiba Instruments, USA). The excitation wavelength was fixed at 400 nm with an integration time of 0.1 s. Both excitation and emission slit widths were kept at 5 nm. QY of CDs, CDs-rhodizonate, and CDs-rhodizonate-NH_3 solutions were calculated using quinine sulfate as standard (reference QY- 0.54). Time-resolved fluorescence measurements were performed using time-correlated single-photon counting (360 nm excitation wavelength by using a picosecond diode laser, with 10.5 nm excitation bandpass and 9.5 nm emission bandpass; Horiba Instruments). Before recording the decay profile of the sample, prompt decay was carried out using dispersed milk powder in water. The obtained decay curves of the sample were then fitted using ‘data analysis’ software. The best fit was ensured by keeping the χ^2 value of the fit as minimum as possible (ca. 1). Thermogravimetric analysis (TGA) was conducted using TA instruments Q50. Heating rate was maintained at 10 °C/min in an inert (N_2) atmosphere. Photostability experiments were performed using a UV light source (360 nm, power: 8 W). In a typical experiment, sample solutions were irradiated with UV light for a specified time interval and the fluorescence spectra of the irradiated samples were subsequently recorded.

2.2.3. Preparation of CDs

Carbon nanoparticles having a green fluorescence were prepared according to a previous report (Fang et al., 2012). In short, a solution containing glacial acetic acid (1 mL) and water (80 μL) was rapidly added to 2.5 g of P_2O_5 in a 25 mL beaker without stirring, and the reaction mixture was cooled to room temperature. The dark brown solution containing CDs was then collected by dispersing in distilled water and centrifuged, and the clear supernatant solution was used in this study.

2.2.4. Sensor solution and generation of oxides of nitrogen

The pH of the purified solution was 3. The sensor solution was prepared by mixing 3 mL of CDs and 600 µL of 1 mM sodium rhodizonate. Oxides of nitrogen (NO_2 and NO) were generated by slowly adding concentrated HNO_3 into a conical flask containing copper turnings. The evolved reddish-brown gas was then introduced onto the cotton fibers coated with the sensor solution.

2.2.5. Calculation of QY and FRET efficiency

Quantum yield of the donor (CDs) in the absence and the presence of the acceptor is calculated by using quinine sulfate as a standard (literature quantum yield of the quinine sulfate, φ_o= 0.54 at 350 nm).

(a) In the absence of the acceptor (CDs alone): $\varphi_D = 0.0528$

(b) In the presence of the acceptor (CDs-Rhodizonate-NH_3): $\varphi_{DA} = 0.032$

FRET efficiency (E) has been calculated using steady-state fluorescence data by, $E = 1- (\varphi_{DA/}\ \varphi_D)$. Where φ_D = Donor (carbon dot) alone quantum yield, φ_{DA} = Donor QY in the presence of acceptor (sodium rhodizonate and ammonia).

$$E = 1-(0.032/0.0528)$$

$$E = 0.40$$

2.3. Results and Discussion

2.3.1. Characterization of CDs

TEM analysis showed that the average size distribution of the CDs is around 3-4 nm (Figure 2.1. UV-visible spectrum (Figure 2.2. (A)) of the CDs confirmed the presence of C=C and C=O groups as electronic absorption bands were observed at 250 nm and 300 nm, which are ascribed to the $\pi-\pi^*$ and $n-\pi^*$ transitions of the C=C core and C=O surface groups, respectively (Fang et al., 2012).

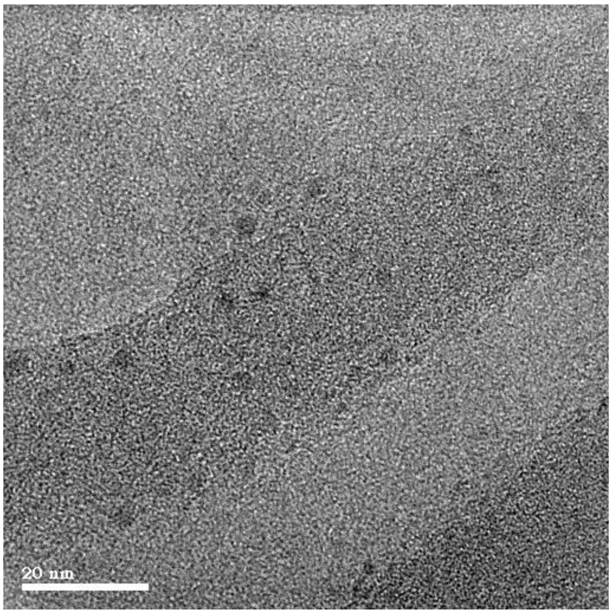

Figure 2.1. TEM image of CDs prepared from acetic acid.

The PL emission of CDs at 400 nm excitation is shown in Figure 2.2. (A), depicting the strong greenish-blue emission centered at 490 nm (the photograph under UV light is shown in the inset). The quantum yield of purified CDs, calculated using quinine sulfate as a standard (QY_{ref} = 0.54), was 5.28%. The large full width at half maximum (FWHM) in the PL spectrum was attributed to the presence of multi-emissive states arising from the emission of the core and surface groups or due to the presence of surface defects (H. Li, Kang, Liu, & Lee, 2012; P. Yu, Wen, Toh, & Tang, 2012). The presence of multi-emissive states was further confirmed by fluorescence lifetime measurements (discussed later).

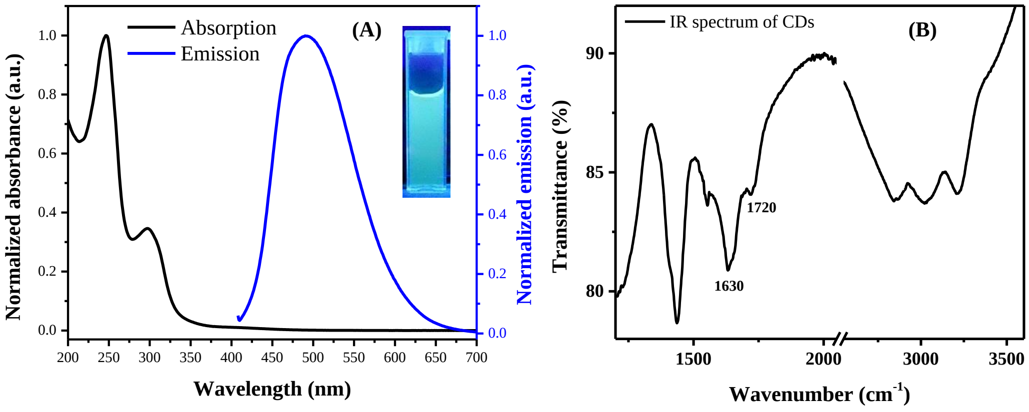

Figure 2.2. (A) Absorption (black trace) and emission (blue trace) spectra of CDs, inset showing the photograph of CDs under UV light. (B) IR spectrum of CDs.

The IR spectrum of the purified CDs showed characteristic vibrations at 1720 cm^{-1} and 1630 cm^{-1}, supporting the presence of surface carboxyl groups and sp^2-hybridised carbon core, respectively (Figure 2.2 (B)).

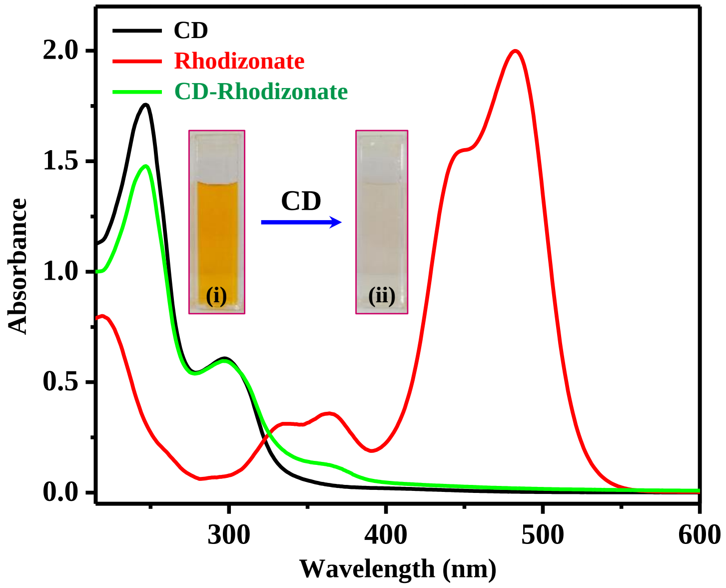

Figure 2.3. UV-visible spectra of CDs (black), sodium rhodizonate (red), and CDs with sodium rhodizonate (green). Inset: Photograph of sodium rhodizonate solution before (i) and after (ii) the addition of CDs.

Compared with that of pure acetic acid, a strong band appeared at 1630 cm^{-1}, which corresponded to the sp^2 C=C stretching vibration; reflected the successful carbonization of acetic acid by P_2O_5 and water. This was further confirmed by the presence of aromatic C-H stretching at 3021 cm^{-1}. The band centered around 3200 cm^{-1} was due to the stretching vibrations of surface -OH groups (Guo, Wang, Shao, & Jiang, 2013). A zeta potential value of +10.3 mV in water suggested dispersion stability because of the presence of numerous surface -COOH groups in the CDs (Z. L. Wu et al., 2013; C. Yu, Li, Zeng, Zheng, & Wu, 2013).

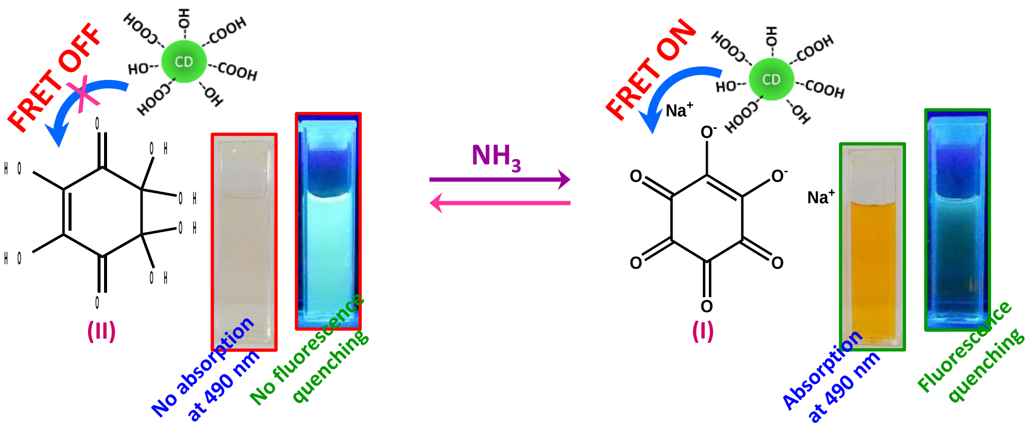

Figure 2.4. Schematic representation of the FRET-based sensing of Ammonia.

2.3.2. Interaction between CDs and sodium rhodizonate

UV-visible spectra of the aqueous solution of sodium rhodizonate (I) with and without CDs are shown in Figure 2.3. Pure sodium rhodizonate exhibited characteristic visible absorption bands at 445 nm and 485 nm (red trace) (Bettermann, Dasting, & Wolff, 1997). However, the sensor solution, composed of CDs and sodium rhodizonate, lacked these features. The addition of sodium rhodizonate (I) to CDs having plenty of surface -COOH groups (at pH = 3) resulted in the formation of a colorless dihydrate form of rhodizonate (rhodizonate (II); Figure 2.4). The protonation and subsequent dehydration of rhodizonate (I) resulted in the formation of rhodizonate (II) structure with absorption at 365 nm (blue trace). A similar structural change has been reported previously in which rhodizonate (II) was found at a lower pH (Heller & Williams, 1970). These observations confirm that sodium rhodizonate is present as rhodizonate dihydrate form (II) in our sensor solution. Also n–π* absorption band at 290 nm corresponding to the surface –COOH group of CDs was red-shifted to 300 nm after the introduction of rhodizonate (I). This is attributed to the conversion of –COOH group of CDs to carboxylate anion (Figure 2.4), which lead to the stabilization of π* orbital due to the weakening of π bond. However, no appreciable change was observed in the emission behavior of CDs with the addition of sodium rhodizonate, implying the absence of excited state energy transfer between CDs and rhodizonate (II).

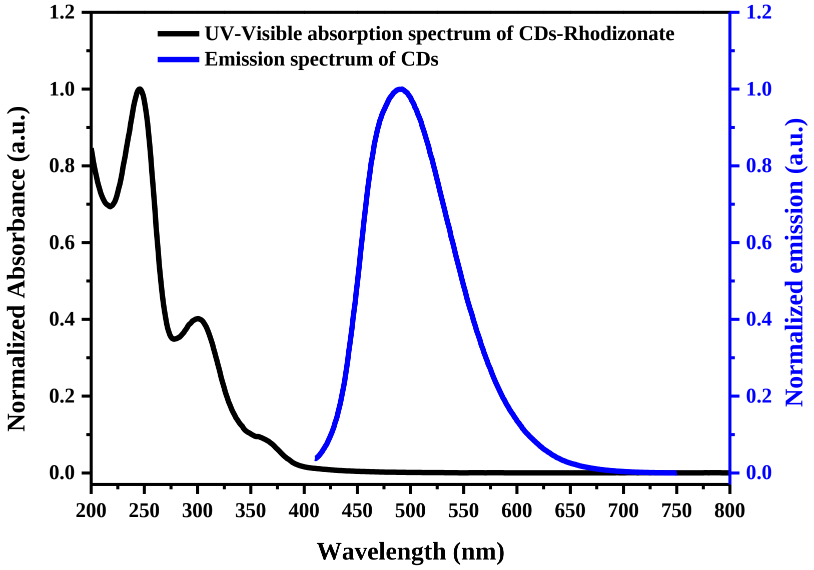

Figure 2.5. The absorption spectrum of rhodizonate II (black trace, structure II is formed in CDs+rhodizonate solution) and emission spectrum of CDs. (blue trace). There is no spectral overlap between the two molecular species.

This can be ascribed to the lack of spectral overlap between the two molecular species (absorption spectrum of rhodizonate (II) and emission spectrum of CDs) as shown in Figure 2.5. The steady-state fluorescence spectra of CDs with and without sodium rhodizonate which was excited at 400 nm are shown in Figure 2.6. The PL spectra were recorded at an excitation wavelength of 400 nm to avoid the inner filter effect.

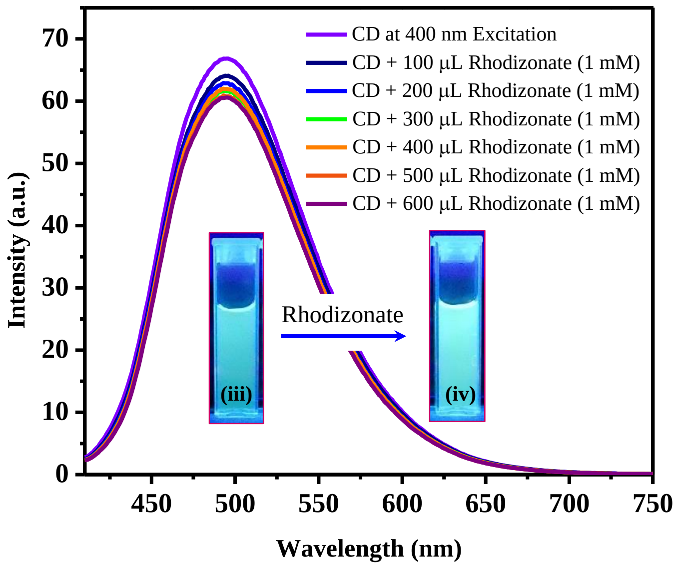

Figure 2.6. PL spectra of CDs with and without sodium rhodizonate recorded at an excitation wavelength of 400 nm. Inset: Photographs of CDs under UV light in the absence (iii) and presence (iv) of sodium rhodizonate.

2.3.3. Ammonia Sensor: Solution-phase

Aqueous ammonia was introduced at various concentrations to the sensor solution, comprising CDs and rhodizonate (II). The fluorescence of CDs decreased concomitantly, as clearly seen in Figure 2.7.

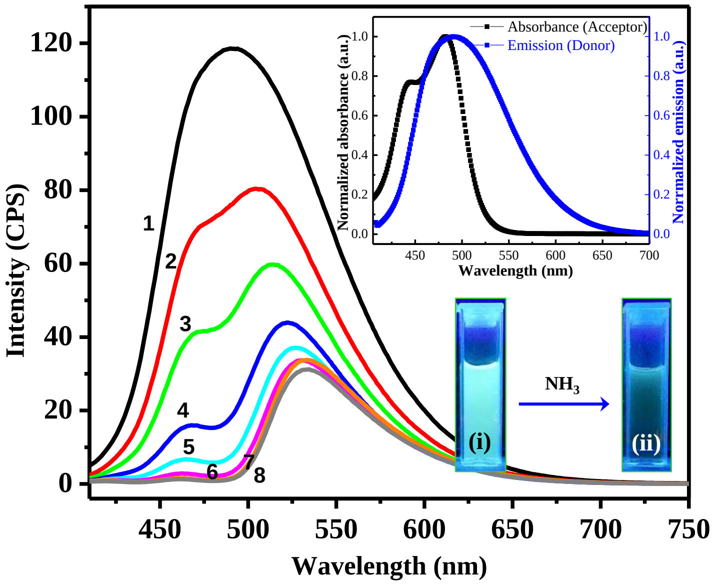

Figure 2.7. The PL spectra of the sensor solution with the addition of ammonia at various concentrations recorded at an excitation wavelength of 400 nm. The numbers 1–8 depict 0, 50, 100, 150, 200, 250, 300, and 350 ppm of ammonia, respectively. Photograph no. 1

and 8 taken under UV light are denoted as (i) and (ii), respectively. The spectral overlap between donor's emission and acceptor's absorption is shown in the inset.

The reduction in the fluorescence intensity of CDs was proportional to the amount of ammonia being introduced, allowing the quantification of ammonia present in the solution. The fluorescence quenching of CDs was associated with a red shift and decreased FWHM (Figure 2.7). This can be ascribed to the selective quenching of blue emitting states of CDs by resonance energy transfer. Only the blue region of the CDs emission spectrum had a spectral overlap with the absorption spectrum of the acceptor (inset of Figure 2.7). This provides an indirect evidence for the presence of FRET between the donor (CDs) and acceptor (sodium rhodizonate). Efficiency of the FRET process calculated using steady-state fluorescence data was 40% (see experimental section). The photograph shown in Figure 2.7 depicts a clear change in the fluorescence of the sensor solution with the addition of ammonia, allowing visual detection, under a UV light. As shown in Figure 2.4, the addition of ammonia deprotonates rhodizonate (II) to rhodizonate (I). This argument is supported by the UV-visible spectrum of the sensor solution treated with ammonia (Figure 2.8). The absorption bands at 445 and 485 nm, which were attributed to rhodizonate (I), were appeared after the addition of ammonia to the sensor solution. These absorption bands had a strong spectral overlap with the emission spectrum of CDs (inset of Figure 2.7). Hence, FRET can be presumed between the CDs (donor) and the in situ generated sodium rhodizonate (acceptor), which is responsible for quenching the CDs emission when ammonia is introduced.

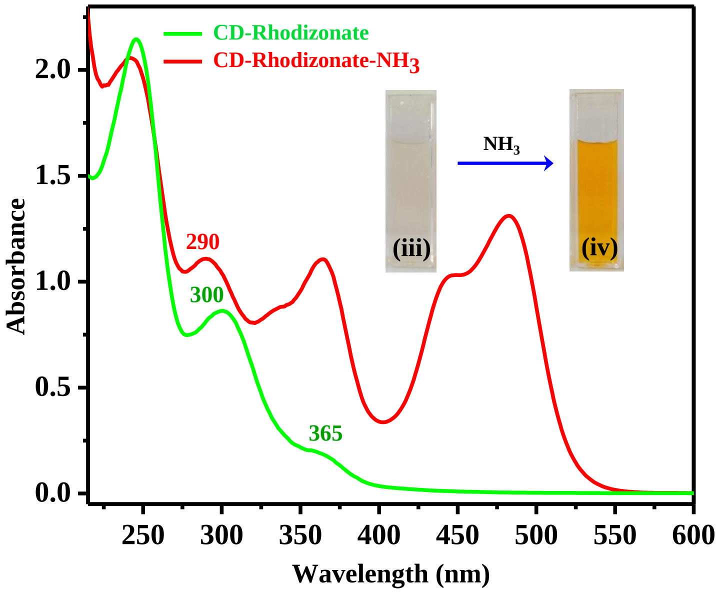

Figure 2.8. UV-visible spectra of the sensor solution with and without ammonia. Corresponding visible light photographs are given as insets (i) and (ii).

In addition to spectral overlap, FRET demands the participating molecules to be in proximity, essentially <10 nm. The absorption bands at 445 and 485 nm corresponding to sodium rhodizonate (structure I) restored with the addition of ammonia (Figure 2.8, red trace). Here, the structure I containing C=O as well as enolate anion interact with –COOH and -OH groups of CDs through hydrogen bonding (Nakahara & Sanada, 1995). As discussed in the preceding section, absorption of CDs at 300 nm was ascribed to the n-π* transition of surface carbonyl groups. When ammonia was introduced to the sensor solution, this peak was strongly blue shifted to 290 nm (Figure 2.8). Blueshift in the n-π* transition of the carbonyl group was due to the stabilization of the non-bonding 'n' orbital because of strong hydrogen bonding interaction (Taylor, 1982). This resulted in an increase in the energy gap between 'n' and π* orbitals of the carbonyl group and hence the blue shift in absorption, which corroborates the presence of the hydrogen bonding interaction between the CDs and in situ generated sodium rhodizonate.

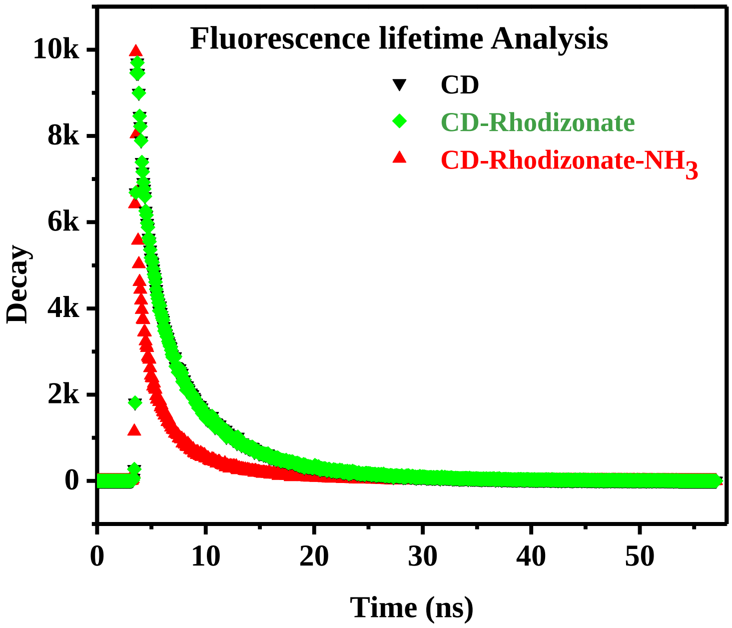

Figure 2.9. Time-resolved fluorescence spectra of CDs (green trace), sensor solution (CDs–rhodizonate) (black trace), and CDs–rhodizonate–ammonia (red trace). The excitation wavelength was 400 nm using the picosecond diode laser) and emission collection was at 500 nm.

The lifetime of the donor's excitation decreases when the donor molecule is engaged in the energy transfer process. Hence, fluorescence lifetime measurement can provide a strong, direct evidence for the presence of the excited state energy transfer process. The time-resolved fluorescence measurements presented in Figure 2.9 and the data given in Table 2.1, clearly depict the presence of the FRET process between the CDs (donor) and rhodizonate (acceptor). Lifetime of the CDs solution alone and in sensor solution is triexponential with an average lifetime of 6.8 ns. Instead, lifetime of CDs after the addition of ammonia to the sensor solution is a 4-exponential fit with an average lifetime of 5.9 ns. The substantial decrease in lifetime of the donor (CDs) after the addition of the analyte strongly supports the presence of an excited state energy transfer process. From Table 2.1, we can see the emergence of an ultrafast component having a lifetime of 0.03 ns. This short-lived component majorly originates from the energy transfer from CDs to rhodizonate (I) because the exchange of the virtual photon for energy transfer is a kinetically faster process (Xu, Zhang, Shi, & Zhu, 2013).

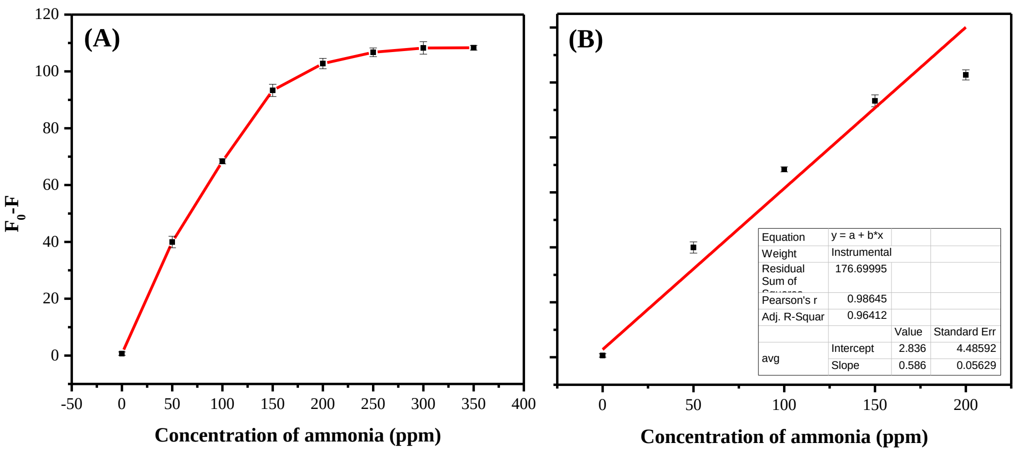

Figure 2.10. (A) and (B) Calibration graph showing the response of sensor system to the various concentration of ammonia.

A calibration graph was drawn with F_0-F (where F_0 and F are the fluorescence intensity at 470 nm before and after the addition of ammonia, respectively) as the ordinate and ammonia concentration along abscissa Figure 2.10. A linear relationship between the extent of PL quenching (F_0–F) and ammonia concentration was observed ($R^2 = 0.9641$) between 0 to 200 ppm (Figure 2.10 (B)). The detection limit calculated using $3xS_{bl}/k$ was 3 ppm, where S_{bl} was the standard deviation for the blank signal and k was the slope of the plot.

Table 2.1. Time-resolved fluorescence data of the FRET donor and donor–acceptor system. Here ‘a’ and ‘τ’ are the amplitude and lifetime respectively and <τ> is an average lifetime calculated using the formula, $<\tau> = \Sigma a*\tau^2 / \Sigma a*\tau$ (ns)

System	τ_1 (ns)	a_1	τ_2 (ns)	a_2	τ_3 (ns)	a_3	τ_4 (ns)	a_4	χ^2	$<\tau>$
CDs	2.41	0.34	7.54	0.60	0.32	0.06	-	-	1.3	6.8
CDs–Rhodizonate	2.43	0.34	7.6	0.59	0.34	0.06			1.2	6.8
CDs–Rhodizonate –NH_3	2.62	0.43	0.56	0.116	7.45	0.34	0.03	10.3	1.0	5.9

2.3.4. Ammonia Sensor: Gaseous phase

Gaseous phase detection of ammonia is crucial in many industries. Here, we demonstrated an efficient method for rapidly detecting ammonia vapors by using our sensor solution adsorbed on a cotton substrate (we will refer to the sensor solution-coated cotton substrate as ‘sensor wool’). For this purpose, we prepared a cylindrical-shaped cotton wool with approximately 3 cm height and 1 cm diameter (Figure 2.11). The shape was selected to ease fluorescence measurements. Low cost, easy availability, and importantly, lack of fluorescent background are the advantages of using cotton in the present study. The cotton wool was immersed in the sensor solution for 1 min, followed by vacuum drying to remove the excess solvent. The sensor wool was then exposed to various ammonia concentrations, and the fluorescence spectra were eventually recorded. similar to the solution phase sensor, this gaseous phase sensor showed a detection limit of 3 ppm. The fluorescence emission of CDs decreased as ammonia concentration increased (Figure 2.11). A rough conclusion could be achieved by observing the sensor wool under UV lamp immediately after the ammonia exposure. The probe has a quick response towards ammonia vapour and the detection can be realized in 5 sec. Alternatively, the sensor-coated plate can also be used for sensing. There is a clear color contrast in the silica-coated plate adsorbed with the sensing mixture before and after ammonia exposure under the UV light source, facilitating a facile visual detection of ammonia (inset of Figure 2.11). The fluorescence intensity of the CDs was completely regained then the sensor wool was exposed to HCl gas, and the wool could be reused for detecting ammonia. Because the materials and chemicals are inexpensive, detailed studies regarding the reversibility of the sensor were not conducted. The easy design strategy, high sensitivity, and quick response makes the sensor wool superior to many of the previously described ammonia sensors (Chandra Sekhar, Manu, Govindaraj, & Rao, 2007; Widmer et al., 2014).

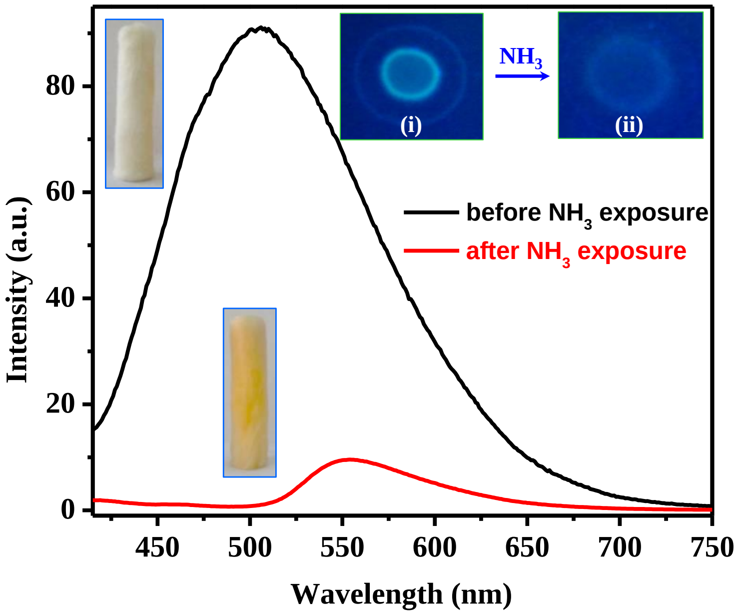

Figure 2.11. Fluorescence spectra of the sensor wool before and after ammonia vapor exposure. The ammonia concentration was 300 ppm. (i) and (ii) show the photographs of the sensor solution dried over the silica plate before and after ammonia exposure, respectively. Visible light photographs of the sensor wool before and after ammonia exposure are given alongside the corresponding spectra.

2.3.5. Selectivity of Sensor towards Ammonia against NO$_x$

Most industrial or biological processes require ammonia as the precursor gas for producing oxides of nitrogen and vice versa. Therefore, selective sensing of one over the other is critical. Several reports have emphasized the detection of reducing gases, such as ammonia, and oxidizing gases, such as NO$_x$, but the selectivity of one over the other is rarely discussed in the literature (Bekyarova et al., 2004; Y. H. Li et al., 2006). Most metal oxide-based amperometric sensors, which change the output current when the analyte molecule is adsorbed, respond equally well to the electron-donating molecules, such as ammonia, and electron-accepting gases, such as NO$_x$; this prevents selective detection. For example, a sensing device comprising a reduced graphene oxide (RGO) suspension deposited over gold interdigitated electrodes changed its electrical conductivity after NO$_2$ exposure, but the selectivity of the device towards ammonia remained unaddressed. In another report, a gas sensor comprising RGO sheets responded to both ammonia and NO$_x$ in a similar manner (Mao et al., 2011).

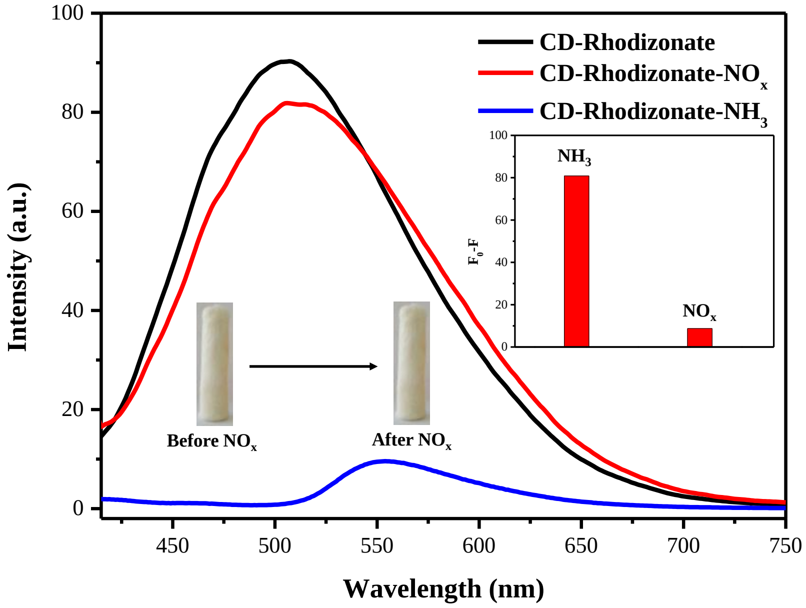

Figure 2.12. Fluorescence spectra of the sensor wool before and after exposure to NO_x gas. Fluorescence spectrum of the sensor wool exposed to ammonia is also shown for comparison (blue trace) with the corresponding photographs. Comparison of the extent of fluorescence quenching is given inset.

By contrast, our sensor wool showed a highly selective response towards ammonia over NO_x. As shown in Figure 2.12, a negligible change in the fluorescence emission of the sensor wool was observed after exposure to 350 ppm NO_x. The extent of fluorescence quenching with an equal concentration of ammonia clearly dictated the selectivity (inset of Figure 2.12). NO_x cannot change rhodizonate the dihydrate form (II) to rhodizonate (I), thus excluding the possibility of energy transfer from CDs. Hence, the emission from CDs was unaffected by NO_x exposure.

2.3.6. Selectivity of Sensor towards Ammonia against Common Organic Solvents

Ammonia is a precursor, solvent, or sometimes, a by-product of many organic syntheses. Therefore, the selectivity of the present sensor system towards ammonia over common organic solvents was an added advantage. Hence, we further extended the selectivity studies to solvents such as acetone, ethanol, toluene, diethyl ether, chloroform, and ethyl acetate. The sensor wool was exposed to the vapors of these solvents (350 ppm), and negligible changes were observed in the fluorescence emission profile (Figure 2.13). The results showed that the present sensor solution is highly selective towards ammonia over oxidizing gases, such as NO_x, and other organic solvents. Hence, the present sensor system can be exploited for industrial and laboratory applications.

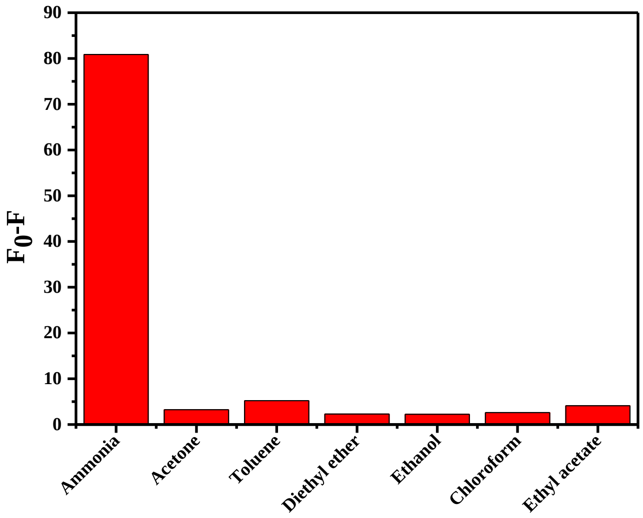

Figure 2.13. Fluorescence response of sensor wool towards NH_3 and vapors of organic solvents. Fluorescence intensity at 470 nm is plotted. Equal concentrations (350 ppm) of these vapors were exposed to the sensor system.

2.3.7. Stability of the Sensor

Several organic dyes studied for fluorescence sensing of ammonia, such as fluorescein and coumarin, are prone to photo-degradation or thermal degradation. Hence, such sensors lack reproducibility because of the fluctuations in fluorescence intensity with time or environment. Photostability experiments of the present sensor solution were performed by irradiating the sensor solution under a 360 nm UV light (lamp power: 8W) for up to 24 h. Emission spectra were recorded at different time intervals. A plot of fluorescence intensity as a function of irradiation time is shown in Figure 2.14 (a). Approximately 21% decrease in emission intensity was observed after 24 h of irradiation.

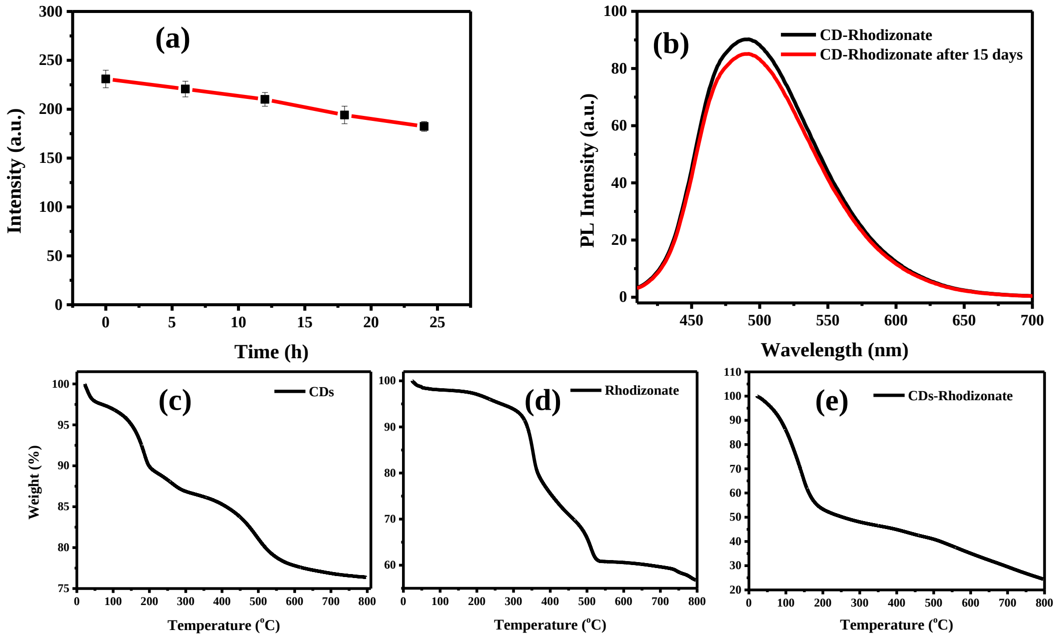

Figure 2.14. (a) Photo-stability: A plot of fluorescence intensity of sensor solution (CDs + Rhodizonate) as a function of irradiation time (360 nm UV light, lamp power: 8W) (b) Temporal stability: Fluorescence spectra of the sensor solution on Day 1 (black trace) and Day 15 (red trace). (c), (d) and (e) are the Thermogravimetric (TGA) curves of CDs, Rhodizonate, and the sensor solution, respectively.

The sensor solution was maintained at ambient condition for 15 days and checked for temporal stability. The fluorescence emission spectrum collected after 15 days is given in Figure 2.14 (b). No considerable variation in emission intensity was observed in this time frame, indicating good stability of the present sensor solution. TGA of CDs, sodium rhodizonate, and the sensor solution is showed in Figure 2.14 (c, d, e), which indicates that sensor materials are stable up to 100 °C. All these observations reflect the high stability of the present sensor material and utility for laboratory and industrial applications.

2.4. Conclusions

We successfully demonstrated a FRET-based sensing strategy for the highly selective detection of ammonia in the solution as well as vapor phases. Mechanism of the sensing process is based on the fact that resonance energy transfer between CDs and sodium rhodizonate is initiated once ammonia is introduced into the sensor solution. This leads to the quenching of the fluorescence emission of CDs; this can indirectly be used to detect and quantify ammonia. Furthermore, the sensor wool can be effectively used for the vapor phase detection of ammonia, with high selectivity over oxides of nitrogen and common organic solvents. The detection limit of the present sensor system was 3 ppm in both the solution and vapor phases. Low cost, good reversibility, high selectivity, and stability are the appealing features of the present sensor system.

CHAPTER 3

SYNTHESIS OF NITROGEN RICH CARBON DOTS, UNDERSTANDING THE LUMINESCENCE MECHANISM AND SELECTIVE SENSING OF Cu^{2+} IONS

This Chapter deals with the synthesis of nitrogen-rich carbon dots (NCDs), understanding the origin of its PL and selective sensing of Cu^{2+} *ions. The synthesis of NCDs was accomplished by treating ethylenediamine (EDA) with* P_2O_5 *in the presence of water. The NCDs showed a nearly white light emission under UV excitation. Detailed characterization studies were carried out to understand the structure and morphology of NCDs. The photophysical behaviour of NCDs was monitored with the selective interaction of* Cu^{2+} *which helped us to unfold the origin of luminescence in NCDs. Finally, a comprehensive analytical result for the* Cu^{2+} *sensing platform is presented.*

3.1. Introduction

A large number of bottom-up and top-down approaches being adopted to synthesize CDs and nitrogen doped CDs in recent times. However, many doping strategies demand long reaction time, high operating temperature and complex synthetic procedure, yet the amount of nitrogen incorporated is ineffective in many cases (Tang, Ji, Li, Teng, & Lau, 2013; Y.-Q. Zhang et al., 2012). Most of the synthetic strategies entail two or more precursors and utilize hydrothermal route which is time-consuming and often results in lower yield (L. Wang & Zhou, 2014; Z. Yang et al., 2014). A rapid and easy synthetic strategy for nitrogen doped CDs having high quantum yield and good stability is rare.

Furthermore, most of the fluorescent carbon nanoparticles in the doped and un-doped state reported so far luminesce at the blue and green portion of the visible spectrum under UV excitation and hence one needs to blend with external fluorophores to achieve white phosphor material, which is undesired (R. Liu et al., 2009). For example, Chen and co-workers recently showed the white light emission from blue emitting carbon dots and green, red emitting lanthanide composite films (Chen & Feng, 2015). A white light emission from polymeric film containing NCDs with a blue emitting InGaN were also demonstrated (Kwon et al., 2013).

Despite the various applications of CDs, the origin of photoluminescence (PL) is still blurry (H. Li et al., 2012; Lim, Shen, & Gao, 2015). Plausible reasons could be quantum confinement, size heterogeneity, and the participation of defect/trap states (Jin, Kim, Jun, Hong, & Jeon, 2013; Peng et al., 2012; Qu, Zheng, Li, Xie, & Sun, 2015; S. Zhu et al., 2015). Recently, Lie and co-workers attributed the origin of green luminescence in CDs to special edge effects controlled by edge carbon atoms and C=O functional groups (L. Wang et al., 2014). However, Peng et al. observed size-dependent PL responses from fluorescent CDs are also reported (Peng et al., 2012). Another group reported the size-dependent PL emission from phenylenediamine derived CDs (Jiang et al., 2015).

Doping provides an opportunity to tune the electronic energy levels for desired applications. Numerous synthetic strategies are available for preparing nitrogen-doped CDs from biological sources such as orange peels (Prasannan & Imae, 2013), milk,(L. Wang & Zhou, 2014) plant leaf (L. Zhu, Yin, Wang, & Chen, 2013), cucumber (C. Wang, Sun, Zhuo, Zhang, & Wang, 2014) and so on, as well as from non-biological carbon precursors such as quinolone (Z. Zhang et al., 2014), ammonium citrate (Z. Yang et al., 2014), polyacrylamide (Kwon et al., 2013), and so on. Tang et al. showed that there is a significant change in the energy level structure of CDs doped with N and thus in their photoluminescence behaviour (Tang et al., 2013). Furthermore, it is possible to tune the luminescence behaviour of nitrogen doped carbon dots by altering N-doping concentration (Y.-Q. Zhang et al., 2012). However, the effect of N on the PL behaviour of CDs remains unclear. Thus, a detailed understanding of the PL behaviour of CDs and the influence of dopants such as N is imperative in extending their scientific and technological relevance.

The electronic energy levels of the fluorophore can be tuned by the interaction with metal atoms/ions, facilitating an indirect insight into its photophysical behaviour. For instance, DFT studies show that a considerable change in the PL behaviour of anthracene derivatives is possible when it interacts with metal ions such as Hg^{2+} and Zn^{2+} due to the alteration in frontier molecular orbital structure (Lee, Hancock, & Lee, 2013). Detailed studies on the interaction of metal ions with CDs are scarce, despite many extensive studies are available with semiconductor QDs counterpart (P. Wu, Zhao, Wang, & Hou, 2014). For example, exciton band of ZnO QDs irradiated with UV light found to vary when in contact with metal islands (Wood, Giersig, & Mulvaney, 2001). Metal-CDs interactions have been widely implemented in fluorescent-based sensor applications. For example, FRET based fluorescence detection of metal ions such as Al^{3+} and K^{+} have been separately accomplished using CDs (Kim, Jang, & Lee, 2015; Wei, Xu, Ren, Xu, & Qu, 2012).

Copper is an essential element in the human body, present in numerous key enzymes including cytochrome c oxidase, superoxide dismutase, and tyrosinase. Similar to other metal ions, a surplus amount of copper in the body causes renal disorders and damages in the central nervous system. Moreover, copper is exploited in numerous industrial, environmental, and domestic processes (J. Liu, Ren, Meng, Fang, & Tang, 2013; J. Ye et al., 2015). Therefore, a simple and selective detection of Cu^{2+} is required in environmental and biological domains. Fluorescence sensors are highly sensitive, selective, and easier to operate, compared with other spectroscopic or electrochemical sensors (Basabe-Desmonts, Reinhoudt, & Crego-Calama, 2007; Carter, Young, & Palmer, 2014). Down and up-conversion fluorescence based Cu^{2+} detection using CDs has demonstrated a high sensitivity towards Cu^{2+} but this sensor lacks selectivity (Salinas-Castillo et al., 2013). Ye et al. presented the ratiometric fluorescence sensing of Cu^{2+} using a CD conjugate of a europium complex (Z. Ye et al., 2014). Graphitic carbon nitride nanosheets (Cheng et al., 2014; Tian, Liu, Asiri, Al-Youbi, & Sun, 2013), and photoluminescence polymer nanodots derived from grass (S. Liu et al., 2012) are two other representative example of carbon based fluorescent probe used in the selective detection of Cu^{2+}. In another study, a ratiometric detection of Cu^{2+} using blue luminescent graphene QDs and yellow emitting CdTe QDs was demonstrated (Sun, Liu, Wu, & Liu, 2015).

The present chapter comprises of three parts: (1) Synthesis of nearly white light emitting NCDs and its characterization. (2) Understanding the origin of PL behaviour in NCDs through the interaction with Cu^{2+} ions. (3) Selective PL sensing of Cu^{2+} ions.

3.2. Experimental Section

3.2.1. Materials

Ethylenediamine (EDA), Phosphorous pentoxide, quinine sulphate, Poly-vinyl alcohol (PVA) and dialysis bags were brought from Sigma Aldrich. Nitric acid, copper sulfate, ferric chloride, ferrous chloride, zinc sulfate, sodium chloride, potassium chloride, silver nitrate, manganese sulfate, ammonium chloride, cadmium chloride, nickel sulfate, cobalt chloride, calcium chloride, magnesium sulfate, gold chloride, glucose, glutathione and L-cysteine were purchased from Merck Specialties, India. All aqueous solutions were prepared using double distilled water.

3.2.2. Synthesis and purification of NCDs

The nitrogen-rich carbon dots were prepared by carbonizing the precursor molecule ethylenediamine using phosphorous pentoxide in the presence of water. Briefly, a mixture containing 0.6 mL of ethylenediamine and 0.5 mL of water were introduced to a beaker containing 1.25 g of P_2O_5. The spontaneous heat produced due to the exothermic reaction between P_2O_5 and H_2O subsequently boils ethylenediamine. The colour of the reaction mixture changes to dark brown in 2 min indicates the successful carbonization reaction. The dark slurry was diluted to 5 mL using distilled water. The crude NCDs were centrifuged three times (10,000 rpm) and the supernatant was dialyzed using dialysis sacks (2000 MWCO) for 24 hours and collected for further analysis. pH of the purified solution of NCDs was 2. XPS spectra of NCDs recorded before and after the purification shows a significant decrease in intensity of Phosphorous peak corresponding to the binding energy 134.5 eV, which indicates the effectiveness of the purification process.

3.2.3. Preparation of PVA-NCDs film

Solution casting technique was utilized for the preparation of PVA-NCDs film. Briefly, a known amount of PVA powder was mixed with water and heated at 60 to 80 °C. To the viscous liquid, aqueous solution of NCDs was introduced. After thorough mixing, hot solution was poured on the surface of the glass plate and dried in vacuum.

3.2.4. Characterization

All steady-state fluorescence measurements (excitation and emission) were carried out using Fluoro Max-4C Spectrofluorometer (Horiba Instruments, USA). Excitation and emission slit width was fixed at 3 nm with an integration time of 0.1 ns. Time resolved fluorescence measurements were performed using time-correlated single-photon counting (TCSPC). For TCSPC measurements, the excitation wavelength was fixed at 330 nm and decay profile was collected at 400, 450, 500 and 600 nm (laser pulse width <370 ps). QY of NCDs was calculated using quinine sulfate ($\varphi = 0.54$) as standard at 400 nm excitation according to the previously reported procedure (L. Wang et al., 2014). Photostability experiments were carried out by irradiating aqueous solution of NCDs under 360 nm UV lamp (48 W power) and fluorescence spectra of the photo-irradiated sample were recorded in the specified time interval. Raman spectral analysis were carried out using WiTec alpha 300R Confocal Raman Microscope with 785 nm laser. Transmission electron microscopy (TEM) images were recorded using JEOL 3010 UHR instrument by assembling NCDs and NCDs-Cu^{2+} on Cu grid coated with ultrathin amorphous carbon film. Atomic microscopy (AFM) images were obtained from Agilent 5500 scanning probe microscope and the obtained images were further processed using WSxM software. X-ray Photoelectron Spectroscopic (XPS) studies of NCDs and NCDs-Cu^{2+} were performed using Omicron ESCA probe spectrometer with unmonochromatised Mg Kα radiation. EUTECH instruments' pH meter was used for pH measurements. Thermogravimetric analysis (TGA) was done using TA instruments Q50. Heating rate was maintained at 10 °C/min in an inert atmosphere.

3.2.5. Calculation of QY

QY of NCDs was calculated using quinine sulfate in 0.1 M H_2SO_4 as a standard (literature quantum yield of the quinine sulphate, φo= 0.54) at the excitation wavelength 360 nm according to (Fang et al., 2012):

Table 3.1. Showing the quantum yield results of NCDs.

Exc. Λ(nm)	φ_o	A_o	I_o	η_o	A_c	I_c	η_c	Φ_c
360	0.54	0.0503	$1.7*10^8$	1.35	0.398	$7.1*10^8$	1.35	0.285

3.3. Results and Discussion

3.3.1. Characterization of NCDs

The NCDs were prepared by carbonizing EDA using P_2O_5/H_2O as a carbonizing agent according to Figure 3.1. Detailed synthesis procedure is given in experimental section. EDA can act as a nitrogenous carbon source. The heat produced due to the exothermic reaction between P_2O_5 and H_2O carbonizes the EDA precursor. Here the upper temperature of the reaction was controlled by the vaporization of EDA (boiling point of EDA is 116 °C), as the vaporization removes excess of heat produced during the reaction. Hence, vaporization of EDA also serves to restrict the size of the nanoparticles by limiting the reaction temperature. The polyphosphoric acid produced during the intermediate stage catalyzes the reaction and traps the EDA vapors (Fang et al., 2012). The crude carbonized product was diluted and centrifuged several times and the supernatant was dialysed before used for further studies. Quantum yield of purified NCDs measured using quinine sulphate as standard (Reference QY 0.54) at 360 nm excitation was 28.5%, which is superior to many of the doped and un-doped CDs (L. Wang & Zhou, 2014; Zhou, Lin, Huang, Ren, & Qu, 2012).

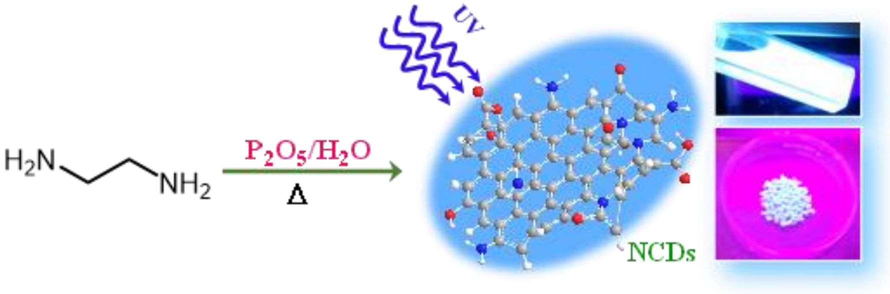

Figure 3.1. Schematic of the synthesis of NCDs.

Transmission electron microscopy (TEM) images (Figure 3.2 (A)) of NCDs show near spherical morphology with the size of the dots range from 2 to 5 nm as shown by the histogram (inset Figure 3.2 (A)). Atomic force microscopy (AFM) images of NCDs also support the formation of quasi-spherical dots with an average height ≤3 nm, indicating the thickness equivalent to ≤5 graphene layers. AFM image of NCDs and corresponding histogram (in terms of height) has shown in Figure 3.2 (B).

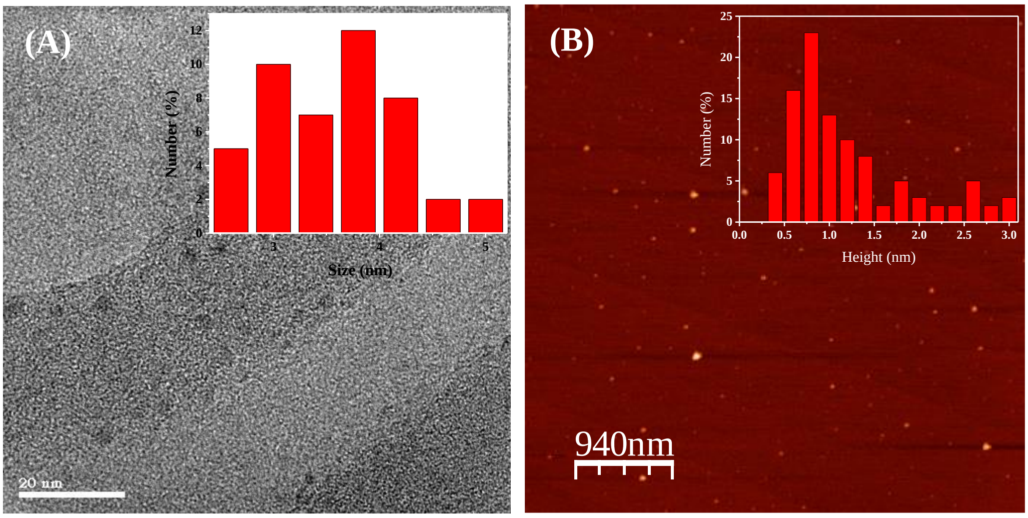

Figure 3.2. TEM (A) and AFM (B) images of NCDs, corresponding histograms are shown as an inset.

Detailed spectroscopic analysis has been carried out to explore bonding and elemental composition in NCDs. Survey scan X-ray photoelectron spectrum (XPS) of NCDs displayed P2p, C1s, N1s and O1s peaks, at 134.5, 286.0, 401.8 and 532.3 eV, respectively (Figure 3.3 (A)). The C1s peak at 286.0 eV can be deconvoluted into three peaks centered at 285.5, 287.2 and 289.1 eV which are ascribed to C–C/C–H/C–N, C–O–C/C=N and C=O bonds, respectively (Figure 3.3 (B)). High resolution N1s spectrum (Figure 3.3 (C)) shows the presence pyrrolic/N–H (400.6 eV) and graphitic (402.3 eV) nitrogen which varies the incorporation of nitrogen atoms into NCDs. Similarly, the deconvoluted O1s spectrum (Figure 3.3 (D)) depicts the presence of C–O (532.0 eV) and C=O (533.4 eV) bonds. A low intensity peak observed at 25 eV is attributed to O2s. High oxygen content shown by the XPS spectrum of NCDs compared to C and N atoms are mainly due to the adsorbed

H_3PO_4 and H_2O molecules. The peak at 134.5 eV and 191.6 eV is assigned to P atom of phosphoric acid. High resolution P2p spectrum shows only one peak centred at 134.5, which corresponds to P–O/P=O bond of H_3PO_4 (Barman, Jana, Bhattacharyya, & Patra, 2014). This ruled out the possibility of incorporation of P atoms into NCDs.

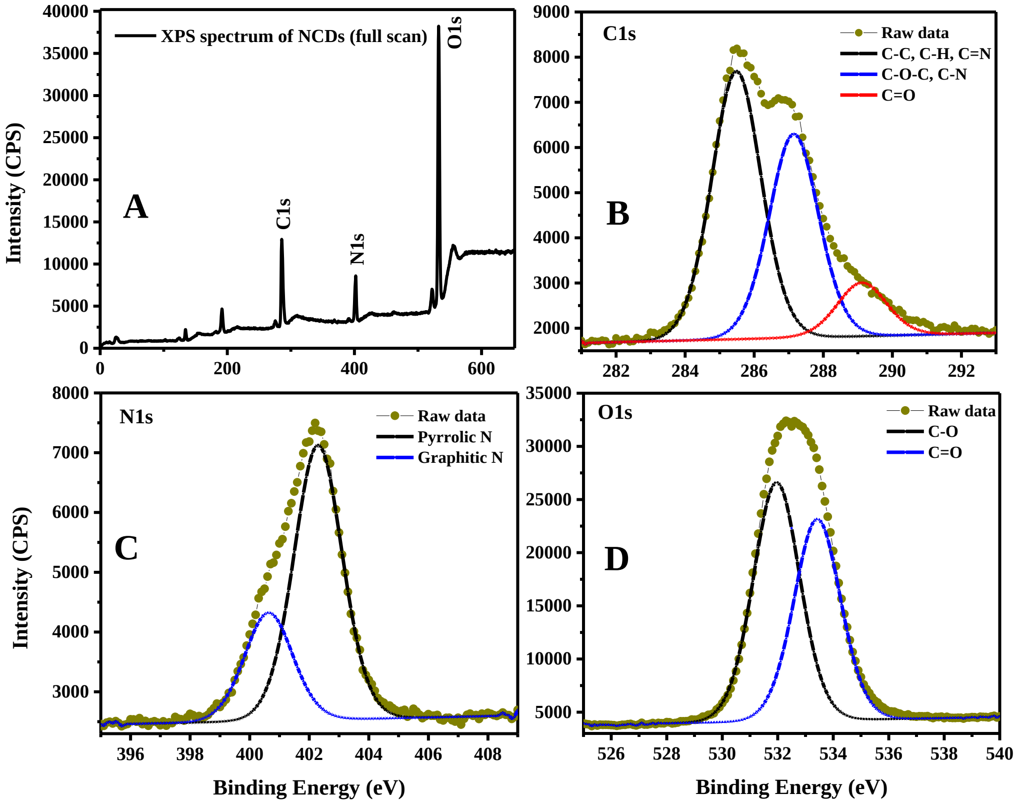

Figure 3.3. Full scan (A) and high resolution (B, C and D) XPS spectra of NCDs.

FTIR spectrum (Figure 3.4 (A)) reveals the formation of NCDs with N and O containing functional groups. The peaks at 1562/1511 and 3020 cm^{-1} due to C=C (aromatic) and C–H (aromatic), respectively suggests the formation of carbon containing ring structure. 1638 cm^{-1} and 1744 cm^{-1} bands are assigned to the stretching vibrations of C=N and C=O bonds, respectively (Y.-Q. Zhang et al., 2012). Broad vibration at 3430 cm^{-1} is indicating the presence of N–H (aromatic)/O–H groups. Bands at 1070, 1090, and 1259 cm^{-1} suggest the presence of C–O/C–N containing functional groups (Kwon et al., 2013; L. Wang & Zhou, 2014). These functional groups affirmed the excellent water solubility to NCDs. Compared to EDA, N–H bending vibration at 1595 cm^{-1} and aliphatic N–H stretching at 3278 cm^{-1} are significantly weakened in the case of NCDs, which reflects the successful carbonization of ethylenediamine (Kwon et al., 2013). Raman spectrum showed a strong D band at 1332 cm^{-1} and a weak G band centred at 1557 cm^{-1} (Figure 3.4 (B)). Weak G band is the direct result of incorporation of a large number of N atoms into the graphitic core.

3.3.2. Photophysical studies

UV-visible absorption spectrum further support the incorporation of heteroatoms into the carbon core (Figure 3.5 (A)). For NCDs, four characteristic electronic transitions around 230, 275, 335 and 385 nm were observed. The peaks at 230 and 335 nm are respectively assigned to π–π* absorption from aromatic sp^2 domains and n–π * absorption of C=O group. The latter peak is strongly red-shifted compared to the reported N-free CDs (Tang et al., 2013). The absorption at 275 nm may be due to the C=N group, similar observation is made by Tang et al. (Tang et al., 2013). Low energy absorption feature at 385 nm is possibly through J-type aggregation as reported by Tufan et al. (Ghosh & Prasad, 2015).

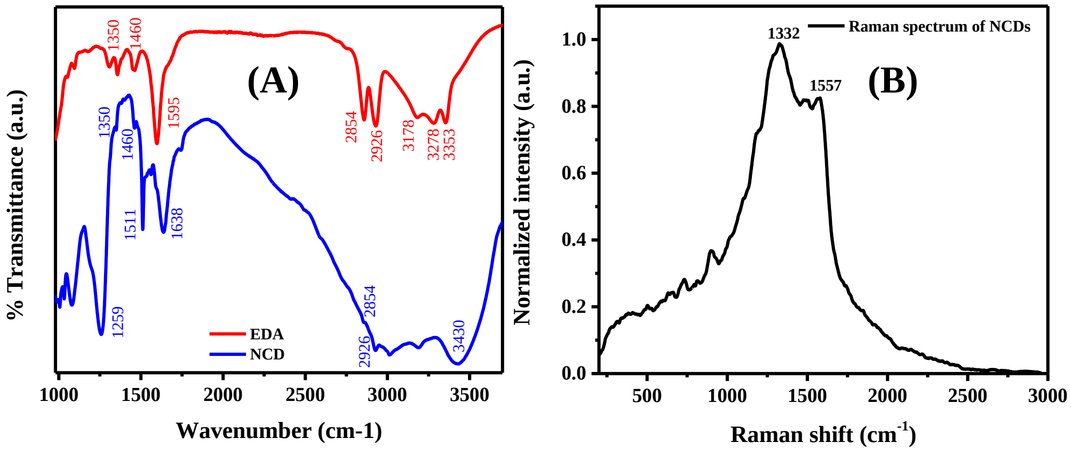

Figure 3.4. IR spectrum of NCDs (A), for comparison IR spectrum of EDA is also given, Raman (B) spectrum of NCDs.

The above microscopic and spectroscopic analysis confirms the successful synthesis of NCDs with a size around 2–5 nm and having abundant nitrogen atoms present in the core (as graphitic N and pyrrolic N) as well as at the surface (as –NH$_2$) along with oxygen containing functional groups (carboxyl and hydroxyl).

Photoluminescence excitation (PLE) spectra of NCDs at various emission wavelengths; 410 to 680 nm (Figure 3.5 (B)) have been measured. In general, PLE spectrum shows two peaks, a shoulder band around 370 nm (3.35 eV) and a longer wavelength band at 405–480 nm (3.06–2.58 eV). The latter is red-shifted when the emission wavelength is increased whereas former remains unchanged. A similar observation has been reported for N-doped CDs (Tang et al., 2013).

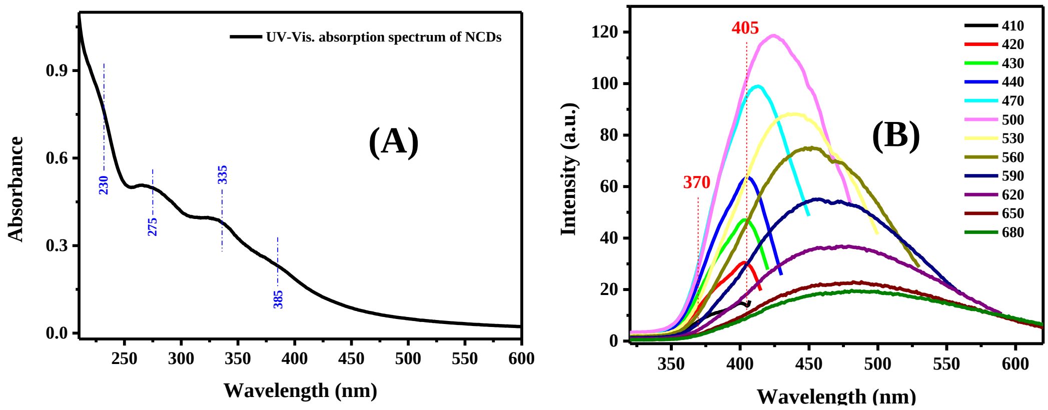

Figure 3.5. UV-visible (A) spectra of NCDs, PLE spectra of NCDs at the different excitation wavelength (B).

The emission spectra of NCDs at various excitation wavelength follows typical excitation dependent emission (Figure 3.6 (A)) which is a commonly observed phenomenon in FCNPs. As shown in Figure 3.6 (A), Fluorescence spectra of NCDs collected at various excitation wavelength spans a large portion of the visible region of the electromagnetic spectrum including blue, green, and red region, rationalizing white light emitting behaviour. Under 365 nm UV source the NCDs show white light emission. The CIE (Commission Internationale d'E' clairage) 1931 chromaticity coordinates calculated using steady-state emission spectra corresponds to the excitation wavelengths of 300, 320, 340, 360, 380 and 400 nm are found to be (0.26, 0.41), (0.25, 0.39), (0.24, 0.38), (0.22, 0.33), (0.21, 0.32), (0.22, 0.33), respectively.

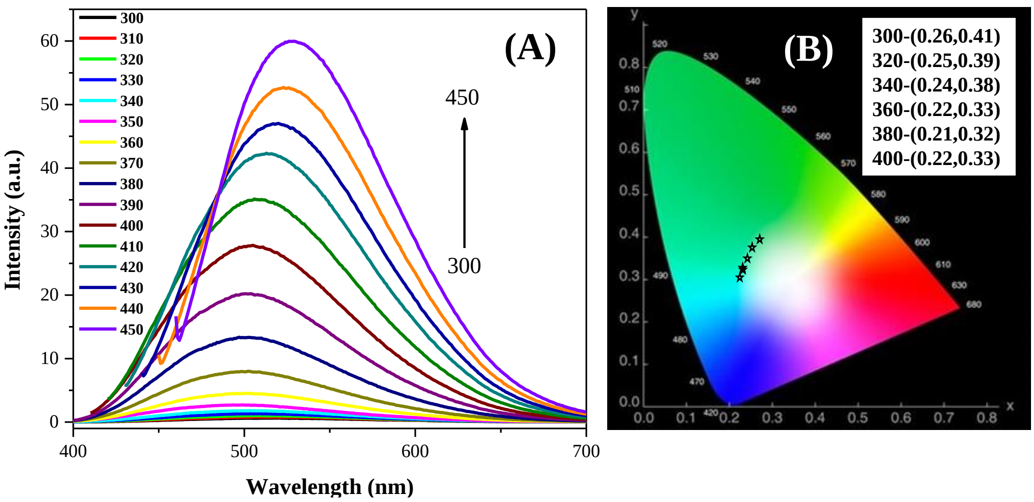

Figure 3.6. (A) Photoluminescence spectra of NCDs at various excitation wavelengths. (B) CIE chromaticity diagram showing the chromaticity coordinates at excitation wavelengths 300, 320, 340, 360, 380 and 400 nm.

These CIE coordinates are located within the breadth of white light in the chromaticity diagram shown in Figure 3.6 (B). But, due to the lack of red emission intensity compared to blue and green emission from NCDs, the CIE coordinates are away from pure white light emission coordinates (0.33, 0.33). It should be noted that solvent dependent fluorescence studies were not performed due to the lack solubility of NCDs in organic solvents. The photograph of NCDs under visible and UV light from solution and solid state is given in figure 3.7 (A-C) and 3.7 (A′-C′) respectively.

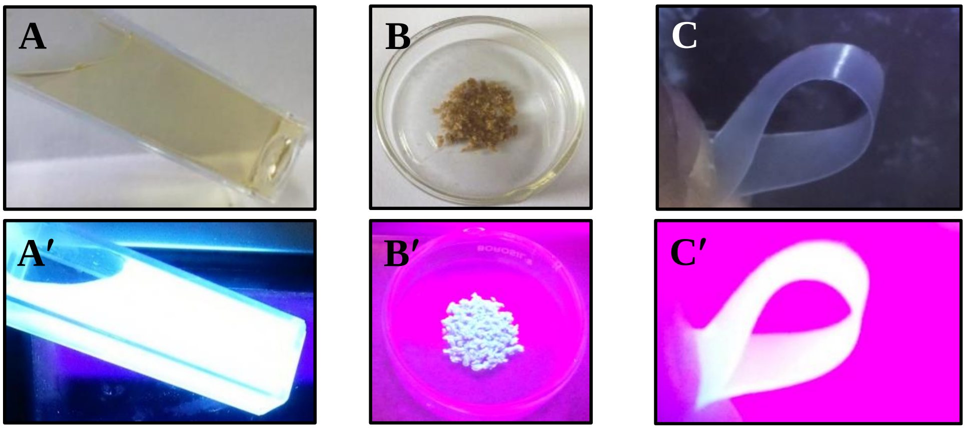

Figure 3.7. (A–C) are the visible light photographs of NCDs solution, NCDs solid powder and NCDs coated over a polymeric surface, respectively. (A′–C′) are the corresponding photographs under 365 nm UV light showing white light emission.

3.3.3. NCDs-PVA composite

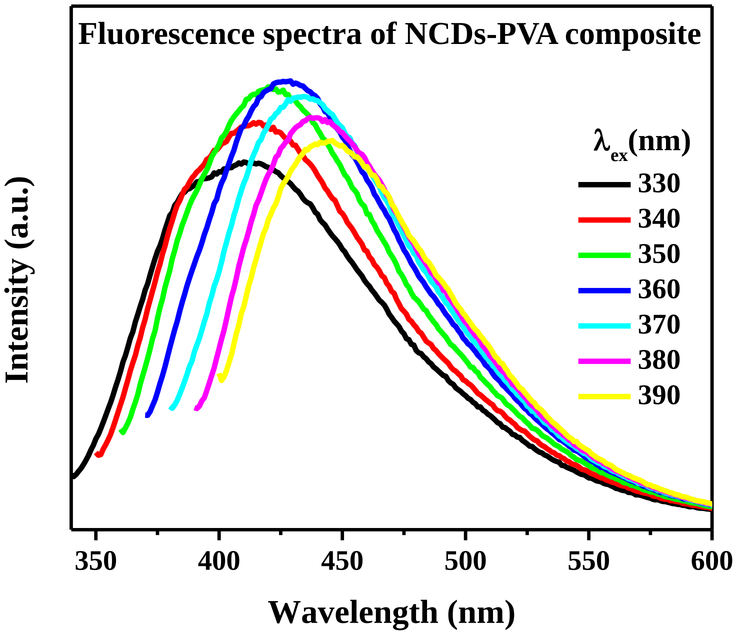

Figure 3.8. Emission spectra of PVA-NCDs film recorded at different excitation wavelength.

For solid-state device applications, fluorophore's luminescence should be retained when fabricated onto the solid surface without compromising its stability. A large number of organic molecules and semiconductor quantum dots which fluoresce strongly in solution fail to emit when coated over the solid surface due to the aggregation induced quenching (M. Yang et al., 2013; Yuan et al., 2010). Steady-state emission spectra shown in Figure 3.8 depict the emission profile of NCDs coated over the polyvinyl alcohol (PVA) films (see the photograph given in Figure 3.7 C′). Emission spectra measured at various excitation wavelength are similar to the one shown in the solution state. Hence, the ability to retain its luminescence when coated over the polymeric surface makes NCDs a highly attractive candidate for solid state device applications.

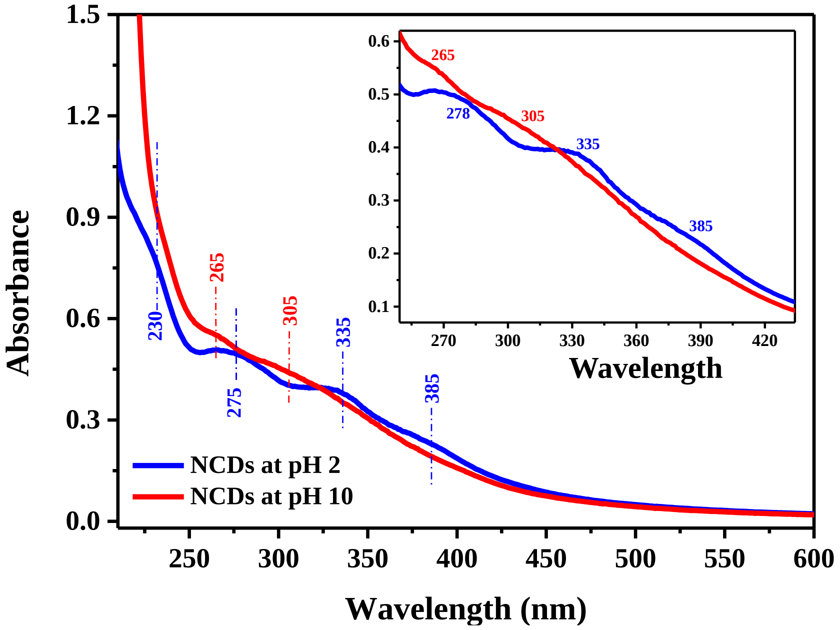

Figure 3.9. UV-visible Absorption spectra of NCDs at pH 2 (blue trace) and pH 10 (red trace). An enlarged view of 350 to 440 nm region is shown as an inset.

3.3.4. Stability of NCDs

The NCDs showed excellent stability in various optical and chemical environments. Photoluminescence intensity of NCDs under various pH were recorded and Figure 3.10 (A) shows a plot of photoluminescence intensity at 430 nm against pH. Unlike CDs and semiconductor QDs, NCDs were highly stable at extreme pH conditions. This may be due to the presence of a substantial number of N containing functional groups such as amide, amine, nitrile, etc., which are less prone to aggregation compared to carboxyl and hydroxyl functional groups as in CDs. The tendency of aggregation in CDs is found to increase with pH of the medium (Ghosh & Prasad, 2015). In the case of CDs, with the increase of pH, conversion of –COOH rich CDs to –OH rich CDs occur due to the deprotonation of –COOH. Subsequently a strong intermolecular hydrogen bonding between carboxylate and hydroxyl groups is expected. But, in the present case, a considerable number of N containing functional groups are available for NCDs. This must have reduced the extent of aggregation when the pH of NCDs solution is changed from pH 2 to pH 10. It is clear from the UV-visible absorption spectrum that the peak at 385 nm, which is due to the formation of aggregates (Ghosh & Prasad, 2015) is slightly decreased at pH 10 (Figure 3.9). Also, compared to the solution at pH 2, the peaks at 335 nm (due to carbonyl group) and 275 nm (due to N containing functional groups) are blue shifted at pH 10. At higher pH, the protonated form of C=N group converts to deprotonated form, thereby strengthening of π bond and hence an increase in $\pi - \pi^*$ absorption. This will result in a blue shift in 275 nm absorption. The change of chemical environment of N containing functional groups might have influenced the electronic transitions of C=O, which led to the blue shift in 335 nm absorption. Such influence of N containing functional groups on the C=O energy levels are reported in the literature (Tang et al., 2013).

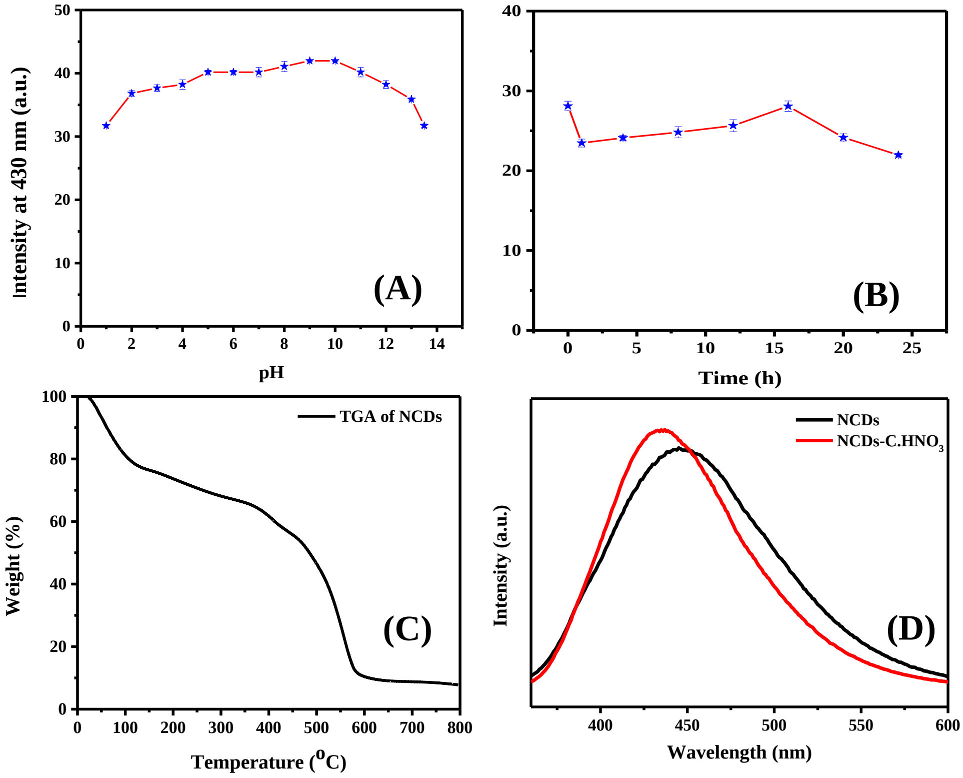

Figure 3.10. (A, B) represent the pH stability and photostability of NCDs respectively. (C) is the TGA curve of NCDs and (D) represents the oxidative stability of NCDs.

Further, the optical stability of the NCDs was tested by illuminating with 48 W power 360 nm UV light source. Emission intensity of NCDs was unchanged with continuous irradiation for 16 h, which is superior to the many carbon and semiconductor based QD fluorescent nanoparticles (Figure 3.10 (B)). Additionally, thermogravimetric analysis (TGA) reveals that NCDs are stable up to 600 °C (Figure 3.10 (C)) These observations demonstrate the excellent stability of NCDs, which is a pre-requirement for fabrication of WLED devices. Finally, to verify the stability in the oxidative environment, NCDs were subjected to react with concentrated HNO_3 and there was no appreciable change in the photoluminescence intensity (Figure 3.10 (D)).

3.3.5. Understanding the origin of luminescence via interaction with Cu^{2+} ions

To understand the luminescence mechanism in NCDs we introduced Cu^{2+} to NCDs solution considering the selective interaction between the metal ion and nitrogen-containing functional groups of NCDs. As can be seen in Figure 3.11 (A), addition of Cu^{2+} to the NCDs solution brought three notable changes in the emission spectrum. First, a large blue shift in the emission maxima (460 to 430 nm) was observed. Second, a substantial decrease was seen in the full width at half maximum (FWHM) from about 112 to 60 nm. Finally, the PL intensity of the NCDs decreased about 60% when 0.5 mg of Cu^{2+} was added to 3 mL aqueous solution of NCDs, and no changes were observed on the PL intensity with the further addition of Cu^{2+}. At this stage, the Commission Internationale de l'eclairage (CIE) coordinates of NCDs were (0.21, 0.28) and (0.15, 0.06), respectively (Figure 3.11 (B)). These values range from nearly white to blue light. Hence, the addition of Cu^{2+} also offers a facile way of tuning the white light emitting CDs to blue light emitting dots.

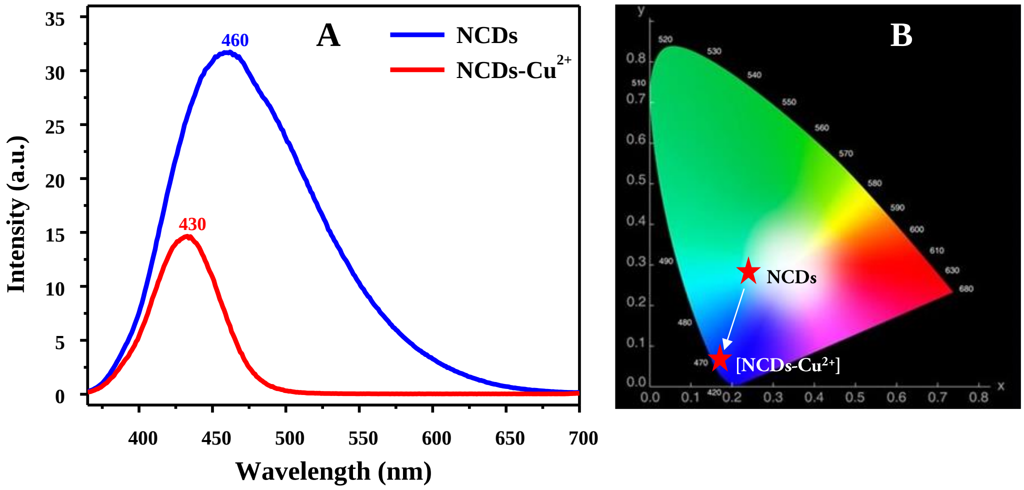

Figure 3.11. (A) Fluorescence spectra of NCDs before (blue trace) and after (red trace) adding Cu^{2+}. (B) CIE diagram showing the CIE co-ordinates of NCDs and NCDs-Cu^{2+}.

We ascribed the above observations to the selective binding of Cu^{2+} and the N atoms of NCDs that are present as pyrrolic, pyridinic and graphitic structures in the core and NH_2 surface groups. The emission at the lower energy portion of the CDs is mostly because of the involvement of defect states (L. Wang et al., 2014). In the case of NCDs, numerous defect states are occupied by N atoms, and therefore the selective quenching of lower energy portion of the emission can be attributed to the charge transfer from N to vacant orbitals of Cu^{2+}. A substantial decrease in FWHM with a blue shift after the addition of Cu^{2+} indicate that the lower energy portion of the emission band, originated from defect states is affected because of Cu^{2+} binding. The higher energy portion of the emission that is originated from the direct recombination process involving C=C core was unaffected. As already mentioned, we observed only a maximum 60% of the PL quenching. If the argument of origin of broad PL emission may be from the different sized dots was true, a complete quenching would have observed with the addition of excess Cu^{2+}. As the Cu^{2+} could bind equally to the N containing group irrespective of the size of the NCDs, decrease in FWHM with a large blue shift in the emission maxima would not be expected if the broad PL emission of NCDs stems from size heterogeneity.

To corroborate the aforementioned assumption, a systematic analysis of the NCD–Cu^{2+} system was performed. The UV/Vis absorption spectrum of the NCDs after the addition of Cu^{2+} showed two additional bands at 238 and 630 nm. These bands can be attributed to the d–d and charge-transfer absorption of the Cu^{2+}–NCD complex, respectively (Figure 3.12). The observation supports the binding of Cu^{2+} to N atoms of NCDs.

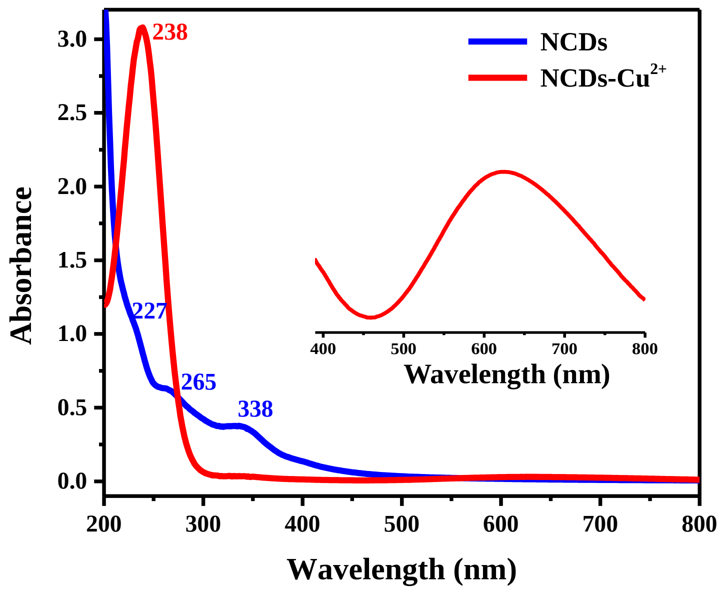

Figure 3.12. UV/Vis absorption spectra of NCDs before (blue trace) and after (red trace) the addition of Cu^{2+}. A magnified view of the charge-transfer absorption band is shown in the inset.

The Fourier-transform infrared (FTIR) spectrum of the NCDs showed a strong vibrational feature at 1638 cm^{-1}, corresponding to the stretching vibration of C=N . But this band was red-shifted to 1632 cm^{-1} after adding Cu^{2+} (see Figure 3.13). This indicates the binding of N to Cu^{2+} that weakens the C=N bond and thus vibrates at lower energy. The vibrational feature corresponding to N-H bending (1592 cm^{-1}) was reduced in Cu^{2+}-treated NCDs. In addition, the stretching vibrations of C=O and C-O of the surface COOH group at 1743 and 1259 cm^{-1}, respectively, were significantly affected after Cu^{2+} addition, which reveals the plausible involvement of the carboxylic group of NCDs along with N-containing functional groups in Cu^{2+} complexation.

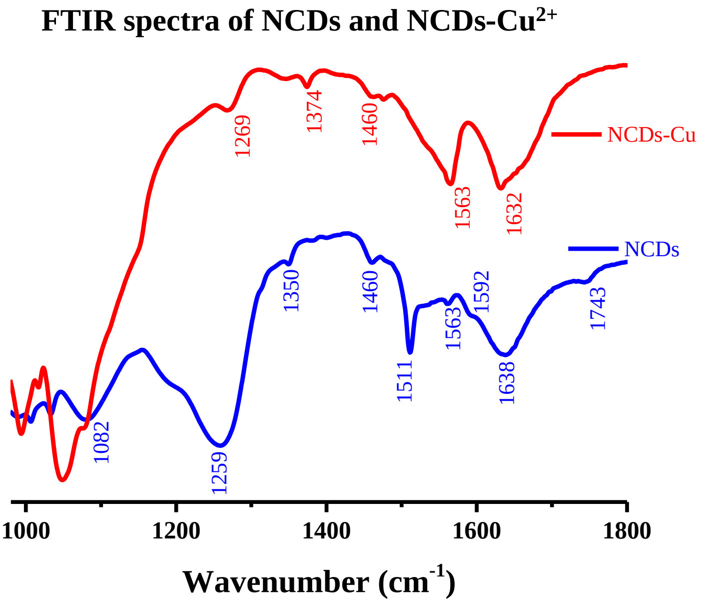

Figure 3.13. Infrared spectra of NCDs before (blue trace) and after (red trace) the addition of Cu^{2+}.

The full-scan XPS of the NCDs–Cu^{2+} system shows the presence of Cu2p$_{3/2}$ and Cu2p$_{1/2}$ along with O, N, C and Na (Figure 3.14). The Cu2p$_{3/2}$ peak at 932.6 eV was deconvoluted into three peaks, that is, 932.3, 933.1 and 934.6 eV (Figure 3.14 (A)). Also, the two peaks at 933.1 and 934.6 eV are ascribed to Cu^{2+} attached to SO_4^{2-} and OH^- ions, respectively (Othman, 2015). The lower binding energy peak at 932.3 eV reveals the increased electron density around Cu^{2+} because of the charge transfer from N atoms of NCDs to Cu^{2+}. Liu et al. and Pallavicini et al. made similar observation during the reduction of Cu^{2+} and assigned the peak to the Cu(0)/Cu(I) state. Similarly, the three deconvoluted peaks at 951.7, 953.3, and 954.1 eV observed in Cu 2p$_{1/2}$ are assigned to NCDs bound to copper (Cu(0)/Cu(I)), $CuSO_4$ and $Cu(OH)_2$, respectively (Figure 3.14 (B)) (X. Liu, Cui, Sun, & Du, 2015; Pallavicini et al., 2013). The binding energy values at 401.9, 401and 399.9 eV in N 1s XPS spectrum of NCDs was assigned to graphitic, pyrrolic and pyridinic/-NH_2 features, respectively (Figure 3.14 (C)). These peaks were shifted to higher binding energy values viz. 402.3, 401.2, and 400.3 eV, respectively, in the NCDs-Cu^{2+} system (Figure 3.14 (D)). The N1s XPS peaks also support the occurrence of charge transfer from N to Cu^{2+}, which imparts more electropositive character to N atoms and thus the core electrons experience higher binding energy. The binding energy values of O atoms present as C=O and C–O were shifted to higher energy in the

NCD-Cu^{2+} system (Figure 3.14 (F)) when compared to that of NCDs alone (Figure 3.14 (E)), indicating the participation of O atoms in the binding process. These observations indicate the binding of Cu^{2+} to NCDs via both N and O containing functional groups.

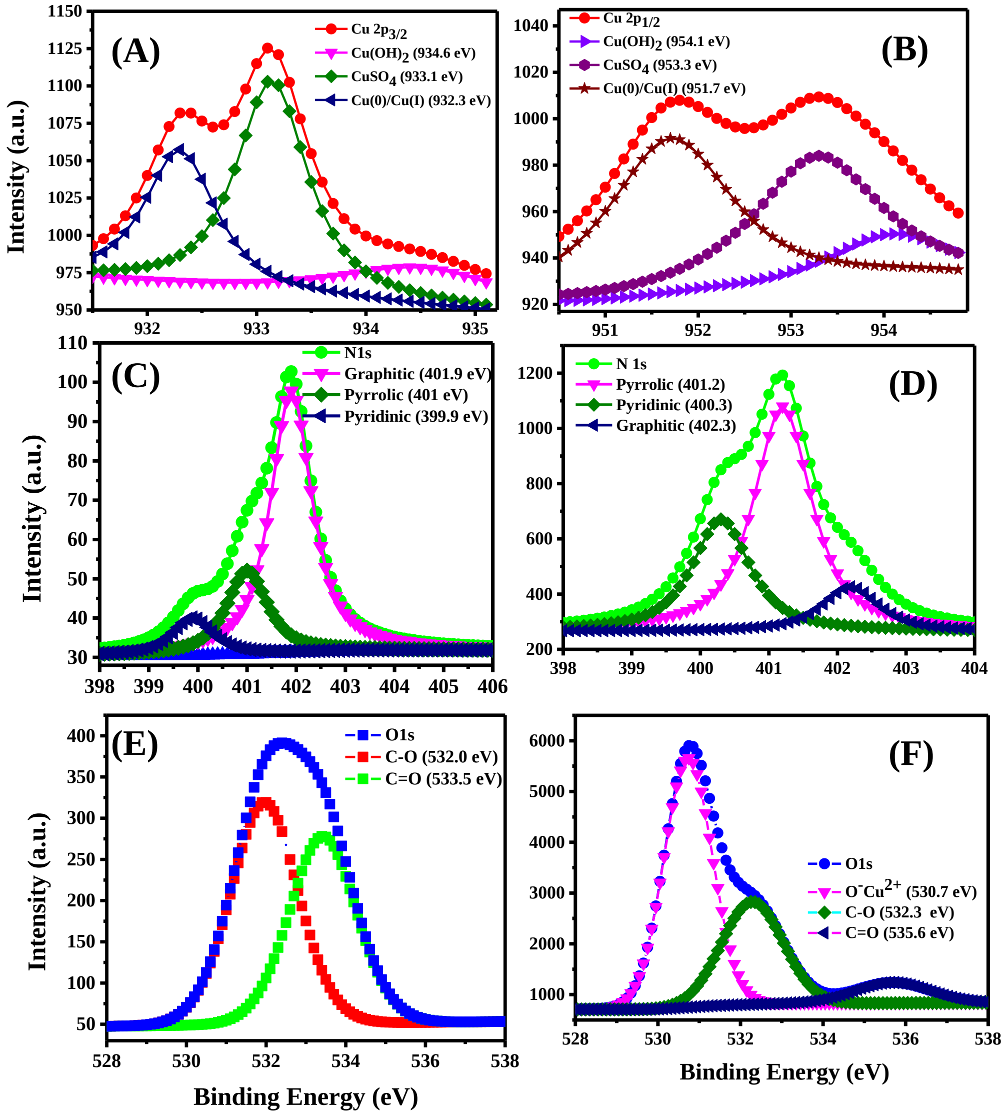

Figure 3.14. A, B, D and F represents the $Cu2p_{3/2}$, $Cu2p_{1/2}$, N1s and O1s high-resolution XPS spectra of NCDs-Cu^{2+} respectively. C and E respectively represent N1s and O1s high-resolution XPS spectra of NCDs.

Fluorescence lifetime analysis provided additional information on the PL emission behaviour of the NCDs. Time-resolved fluorescence spectra of the NCDs were collected for 400 nm (blue) and 500 nm (green) at an excitation wavelength fixed at 340 nm (Figure 3.15). Decay curves were a biexponential fit for both 400 and 500 nm emission wavelengths. Detailed lifetime parameters, such as amplitude, lifetime and CHSQ2 values of the NCDs in the absence and presence of Cu^{2+}, are given in Table 3.2. Here, the shorter component (τ_1) is attributed to the direct recombination process (intrinsic state emission) whereas the longer component (τ_2) is associated with the surface/trap states (L. Wang et al., 2014). The contribution to the average lifetime from the shorter component is higher when emission is recorded at 400 nm (A1: 54.21% and A2: 45.79%) whereas the contribution from the longer component is predominant when the emission is collected at 500 nm (A1: 31.63% and A2: 68.37 %). This, in turn, explains the increased average lifetime at 500 nm ($<\tau> = 6.59$ ns) as compared with that at 400 nm ($<\tau> = 5.21$ ns). As already stated, in the case of NCDs, a large number of defect states are occupied by N and hence the longer decay component (τ_2) is mainly controlled by N containing functional groups. If this is true, then the binding of Cu^{2+} to N should strongly influence the longer decay component (τ_2). The decay profiles of NCDs–Cu^{2+} show biexponential fits at both 400 and 500 nm emissions. However, the average lifetimes at both 400 and 500 nm collection wavelength decreased from 5.21 to 4.04 ns and 6.59 to 4.57 ns, respectively. The average lifetime of NCDs–Cu^{2+} at 400 and 500 nm collection wavelengths decreased mainly because of the large reduction in the longer lifetime component (6.30 to 4.60 ns at 400 nm and 7.18 to 4.90 ns at 500 nm) whereas the shorter decay component was not substantially affected (Table 3.2). Thus, the observed broad emission band in case of NCDs is originated from the direct recombination process (higher energy portion of the emission band) and from the defect states (lower energy portion of the emission band), which is mainly controlled by nitrogen groups. Accordingly, we proposed the energy level diagram for NCDs, which is given in Figure 3.16.

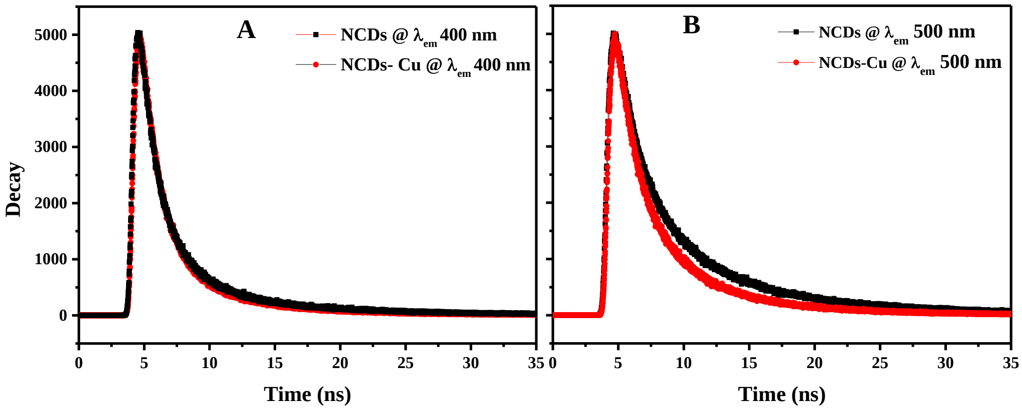

Figure 3.15. Time-resolved fluorescence spectra of NCDs and an NCD–Cu^{2+} solution at 400 (A) and 500 nm (B) emission collection. The excitation wavelength was fixed at 340 nm and the laser pulse width was <370 ps.

Table 3.2. Detailed time-resolved spectral results, where, λ_{em} is the collection wavelength, τ_1 and τ_2 are lifetime components, A_1 and A_2 are the corresponding amplitude components, and <τ> is the average lifetime.

System	λ_{em}	τ_1 (ns)	A_1 (%)	τ_2 (ns)	A_2 (%)	<τ>	χ^2
NCDs	400	1.59	54.21	6.30	45.79	5.21	1.24
NCDs	500	1.98	31.63	7.18	68.37	6.59	1.07
NCDs-Cu	400	1.05	45.00	4.60	55.00	4.04	1.27
NCDs-Cu	500	1.17	28.38	4.90	71.62	4.57	1.12

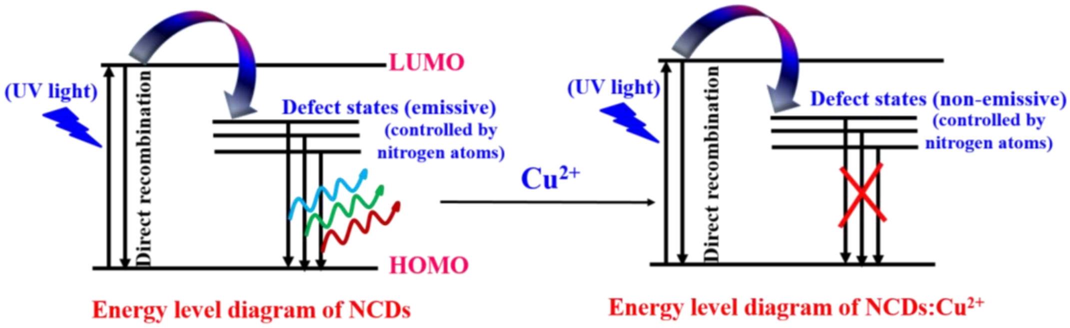

Figure 3.16. A Proposed energy level diagram of NCDs.

We attribute the PL quenching of NCDs by Cu^{2+} to the non-radiative electron transfer from NCDs to the vacant d-orbitals of Cu^{2+}. Ligand to metal charge transfer transitions are commonly observed in metals with a higher oxidation state and ligand with filled orbitals. Such transitions are well documented in semiconductor

QDs (P. Wu et al., 2014). We calculated steady-state and time-resolved fluorescence quenching efficiency at 400 and 500 nm at the maximum concentration of Cu^{2+} (0.7 mm Cu^{2+}).

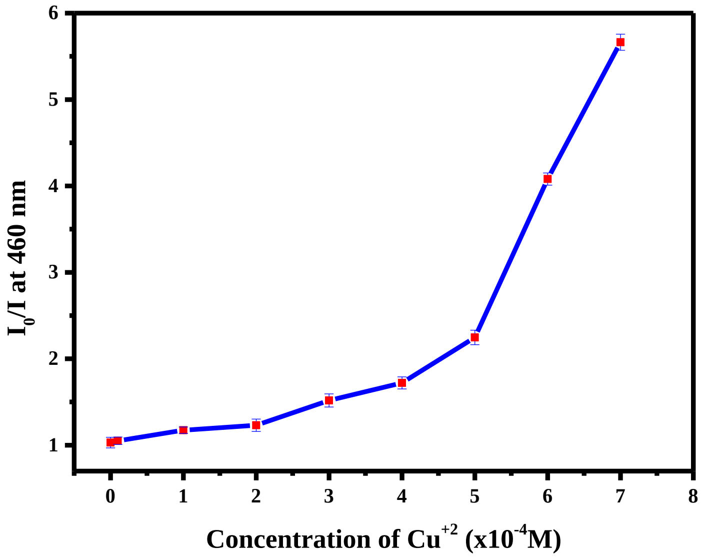

Figure 3.17. The stern-volmer plot of I_0/I vs. conc. of the quencher.

At 400 nm, the steady-state fluorescence quenching efficiency was 29% whereas the time-resolved data revealed 23% quenching. By contrast, at 500 nm, 99% steady-state PL quenching as observed whereas only 31% quenching was noticed from lifetime results. The large differences in the steady-state and time-resolved quenching efficiency at 500 nm emission are attributed to the formation of the ground-state complex between NCDs and Cu^{2+} (static quenching) because lifetime data can only unveil excited state process. Also, the Stern–Volmer quenching plot, I_0/I versus concentration of a quencher showed an upward curvature, concaved towards y-axis (Figure 3.17), which indicate the contribution from both collisional and complex formation towards the fluorescence quenching of NCDs by Cu^{2+} ions (Gore et al., 2013).

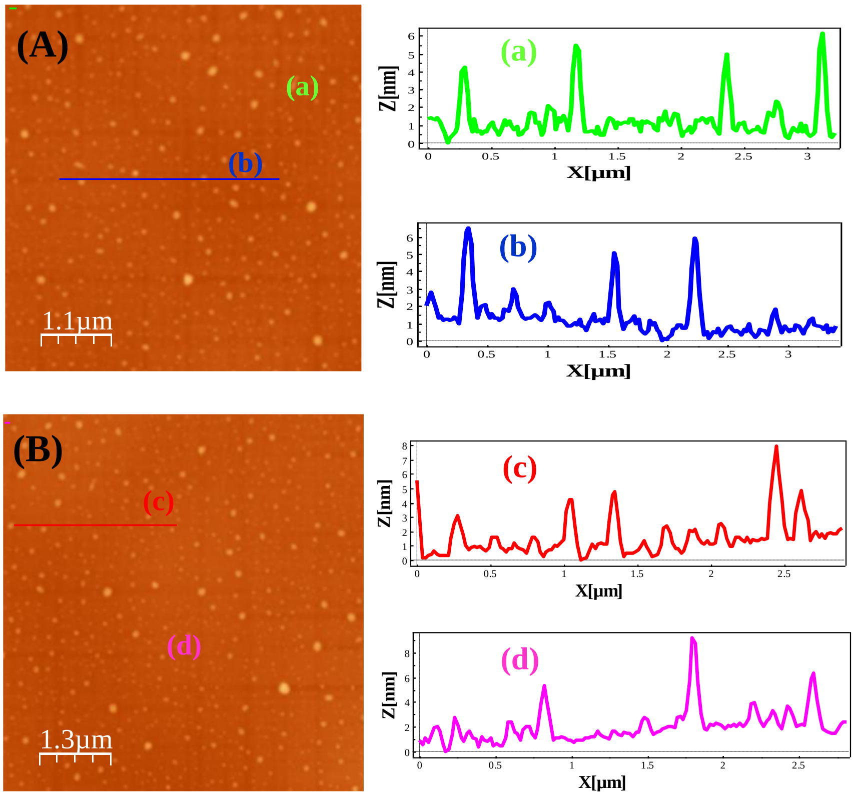

Figure 3.18. Atomic microscopy images of NCDs before (A) and after (B) the addition of Cu^{2+}. Here (a), (b), (c) and (d) are the height profiles of the corresponding line drawn in AFM images.

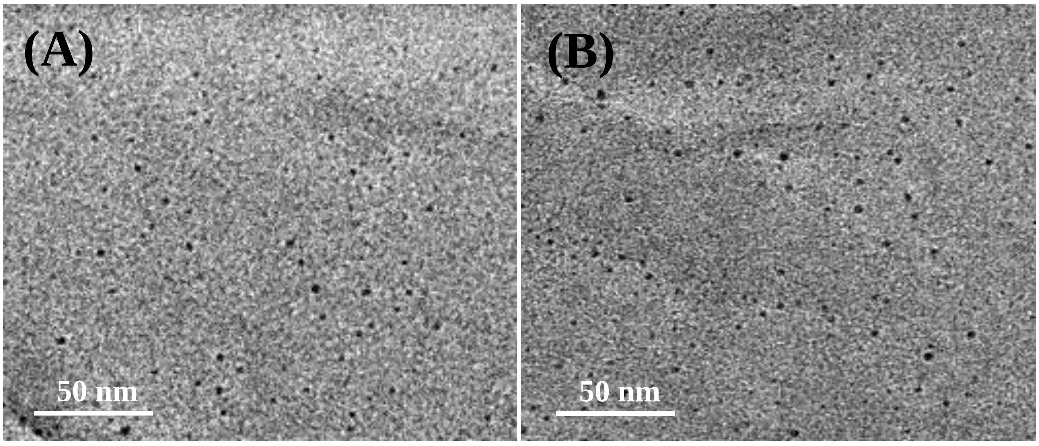

Figure 3.19. TEM images of NCDs before (A) and after (B) the addition of Cu^{2+}.

We analysed the effect of aggregation using atomic force microscopy (AFM) and transmission electron microscopy (TEM). There was no considerable change in the size of the dots before and after the addition of Cu^{2+} (see the AFM images given in Figure 3.18, and the TEM images given in Figure 3.19). Hence, we rule out the possibility of the observed fluorescence quenching of NCDs to Cu^{2+} assisted aggregation of the dots. The aggregation caused quenching (ACQ) is commonly observed in semiconductor QDs and fluorescent organic dyes (Zhao et al., 2012).

The involvement of unreacted EDA or Cu–EDA complex was studied using a freshly prepared Cu–EDA complex. The emission spectrum of the Cu-EDA complex did not show appreciable emission at 350 nm excitation (Figure 3.20 (A)). Furthermore, the Cu–EDA complex lacks absorption at 350 nm (Figure 3.20 (B)), which excluded the possibility of any inner filter effect driven fluorescence quenching of NCDs. To examine whether the NCDs can replace EDA from the Cu–EDA complex, NCDs solution was added to the Cu–EDA complex at pH 9. The PL response of this solution was identical to that of the NCDs–Cu^{2+} system, depicting the replacement of Cu^{2+} by NCDs from the Cu–EDA complex (Figure 3.20 (C)). This shows that there exists a higher chemical affinity of Cu^{2+} towards NCDs compared to simple NH_2 containing molecules. We also studied the interaction of Cu^{2+} with NCDs at various pH conditions and there was no change in the fluorescence spectra when the pH was below 9 (Figure 3.20 (D)), whereas the quenching was observed in the pH range 9–14. This is because of the existence of N- atoms in the protonated state below pH 9 and thus unable to coordinate with Cu^{2+}.

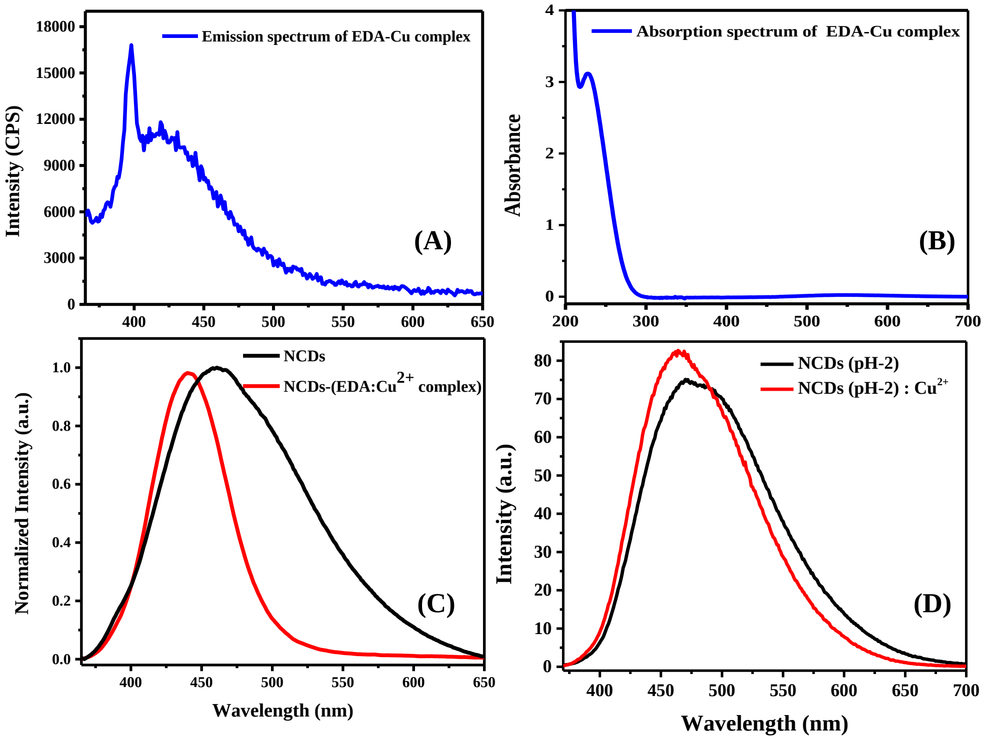

Figure 3.20. (A) The emission spectrum of EDA-Cu^{2+} complex at 350 nm excitation. (B) The absorption spectrum of EDA-Cu^{2+} complex. (C) Emission spectra of NCDs (black trace) and NCDs after the addition of EDA-Cu^{2+} complex. (D) Emission spectra of NCDs before and after the addition of Cu^{2+} at pH 2.

To further support that fluorescence quenching and the associated decrease in FWHM is due to the selective binding of Cu^{2+} with N-containing groups, we conducted similar studies with N-free CDs. CDs with carboxyl and hydroxyl functional groups were prepared by carbonizing acetic acid using P_2O_5/H_2O (Fang et al., 2012). The purified CDs were then treated with a 700 mm solution of Cu^{2+} (concentration of Cu^{+2} at which the maximum quenching of NCDs was observed) under identical conditions. No substantial change in the fluorescence intensity of the CDs was observed after adding 700 mM of a Cu^{2+} solution (Figure 3.21 (A)). Although Cu^{2+} interacts with the carboxyl and hydroxyl groups of the CDs, there was no quenching as in the case of NCDs. Although the binding of O atoms, present as carboxyl and hydroxyl functional groups in the NCDs, to Cu^{2+} is presumed, they are not directly involved in the PL quenching.

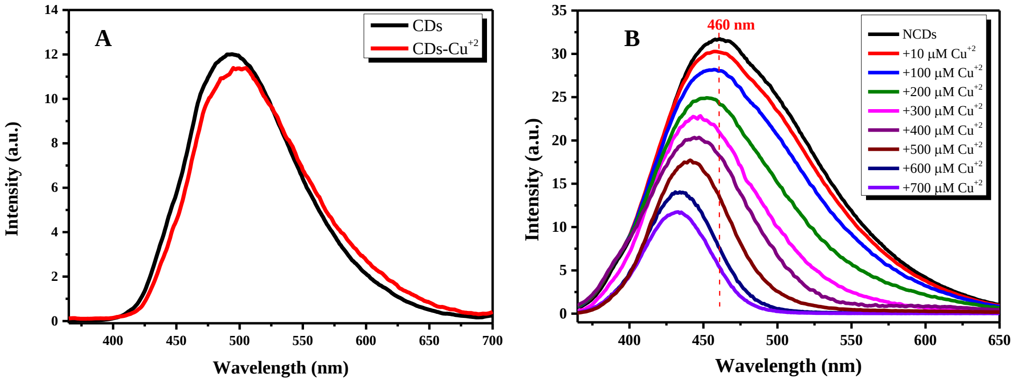

Figure 3.21. (A) The emission spectrum of CDs before (black trace) and after (red trace) addition of 700 µM of Cu^{2+}. (B) Photoluminescence spectra of NCDs at different concentrations of Cu^{2+}.

3.3.6. Cu^{2+} sensing

We exploited NCDs–Cu^{2+} interactions for the selective detection of Cu^{2+} ions. Figure 3.21 (B) represents the PL spectra of NCDs at various concentrations of Cu^{2+}. The PL intensity of NCDs without Cu^{2+} (referred as I_0) to that of the intensity of NCDs after the addition of various concentration of Cu^{2+} (referred as I) is plotted against the concentration of Cu^{2+}. The quenching of the PL intensity of NCDs along with a blue shift in emission maxima was observed till 700 mM concentration of Cu^{2+} (Figure 3.22 (A)). The dynamic range of the sensor was 10 to 400 µM (Figure 3.22 (A)). The limit of detection of the present system towards Cu^{2+} was 10 mM, because a noticeable change in the PL quenching of NCDs was observed at this concentration. The present system manifested high selectivity towards Cu^{2+} and thus it can be used in biological and environmental domains where selective sensing is highly desirable. Selectivity experiments were performed by choosing various metal cations and biomolecules such as glucose, cysteine and glutathione. Notably, the concentration of Cu^{2+} (0.7 mM) at which maximum PL quenching was observed was used for the selectivity studies. As seen in Figure 3.22 (B), the response of the aforementioned analytes was weak compared with Cu^{2+} ions toward the PL quenching of NCDs. None of the analytes showed any spectral change or a difference in the FWHM. Moreover, the visual detection of Cu^{2+} was performed using thin layer chromatography (TLC) plate coated with NCDs (inset of Figure 3.22 (B)). The nearly white light emission from NCDs remained unchanged for analytes other than Cu^{2+}. However, blue emission from the TLC plate was observed when Cu^{2+} was introduced into the NCDs, enabling easy visual detection of Cu^{2+}. Although, the sensitivity of the present sensor towards Cu^{2+} ions is weaker than many of the fluorescence based detection of Cu^{2+} using CDs reported, the present method demonstrated excellent selectivity towards large number of metal ions and biomolecules (Salinas-Castillo et al., 2013; Sun et al., 2015; Z. Ye et al., 2014).

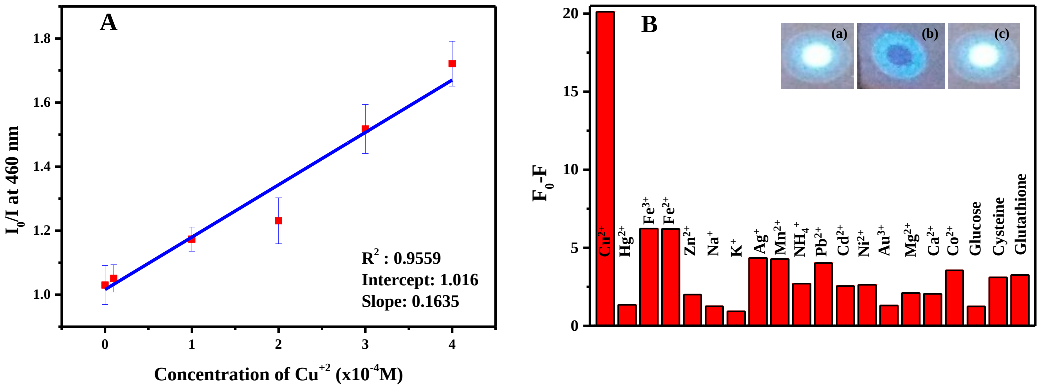

Figure 3.22. (A) The plot of I_0/I at 460 nm vs. concentration of Cu^{2+} showing the dynamic range of the sensor. B) Selectivity of the NCDs towards Cu^{2+} against various analytes. Inset: Photographs of a TLC plate (a) coated with NCDs, (b) after treating with Cu^{2+}, (c) an analyte used for selectivity studies. The photographs were taken under a UV lamp.

3.4. Conclusions

We demonstrated an easy and a rapid strategy for synthesizing NCDs under mild condition by carbonizing ethylenediamine using P_2O_5 in the presence of water. Reaction was accomplished within two minutes. An interesting property of the present material is its nearly white light emission behaviour. Presence of large number of emissive states explains the broad emission band. The effect of nitrogen on the photophysical behaviour of nitrogen containing carbon quantum dots was investigated by the interaction between NCDs and Cu^{2+}. The selective binding of Cu^{2+} to N containing functional group causes the fluorescence quenching and the concomitant spectral shift. The findings are useful in tuning the electronic energy levels of doped CDs by controlling the nature and number of doped atoms. We demonstrated that NCDs can act as a sensor for Cu^{2+} detection and their potential can be exploited in biological and environmental applications where the specificity is highly demanded. Limit of detection of the sensor system was 10 µM with a dynamic range of 10 µM to 0.4 mM.

CHAPTER 4

SYNTHESIS OF BLUE LUMINESCENT SILICON PASSIVATED CARBON DOTS POLYMERIC GEL (SiCDs gel) AND ITS APPLICATION AS Ag$^+$ SENSOR

In this chapter, we demonstrate the one-step hydrothermal synthesis of carbon dots (CDs) in polymeric gel form. The structural characterization indicates that the CDs are linked covalently to the polymeric backbone and the blue luminescence in silicon passivated carbon dots (SiCDs) gel is due to the radiative recombination of excitons in CDs. The synthesis was accomplished by the reaction of 3-aminopropyltriethoxysilane with an aqueous solution of HNO_3 *and the subsequent hydrothermal treatment at 300 °C for 2h. Detailed spectroscopic and microscopic studies used to understand the structure and morphology of SiCDs gel is given. The rheological behaviour of CD gel as well as surface area analysis is also given. Alongside, we also demonstrated the selective fluorescence sensing of* Ag^+ *using SiCDs gel. The sensor has the sensitivity and dynamic range of 85 nM and 0.4 µM - 0.1 M, respectively.*

4.1. Introduction

In recent times, gels are one of the most extensively studied soft materials because they can immobilise a large amount of solvent molecules in three-dimensional network structures and mimic biological tissues (Sangeetha & Maitra, 2005). Tissue engineering scaffolds, cell proliferation and drug delivery are the major application domains, gels have been attempted so far. Mechanical stability, biodegradability and toxicity are the major concerns in these fields (Yu, Yan, Han, & Huang, 2013). Moreover, for real time monitoring of biological process, a fluorescent signaling moiety is covalently connected to the gel network. However, the unavailability of suitable fluorophores and complicated synthetic routes often hinders this strategy. Fluorescent CDs gel could be a suitable candidate for such applications. Although, carbon based nanomaterials such as graphene oxide hydrogel composites were employed in numerous applications (Jiao et al., 2015; J. Zhang, Cao, Feng, & Wu, 2012), CDs are not often used in gel form. The gel can be advantageous in terms of a large number of surface functional groups, smaller size, and more importantly, the ability to fluoresce strongly without compromising its stability. There are reports of CDs gel prepared using gelators. For example, CDs-ionogels are prepared by combining CDs with ionic liquids within the silica gels (Y. Wang et al., 2014). Cayuela et al. achieved hybrid SiCDs gel by incorporating CDs into the low molecular weight hydrogel such as 5-aminosalicylic acid (Angelina Cayuela et al., 2015; A. Cayuela, Soriano, Kennedy, Steed, & Valcárcel, 2016). But, one step synthesis of CDs in polymeric gels form has not yet realized.

On account of industrial, biological and biomedical significance, metal ion sensors have increased steeply in recent years (Gumpu, Sethuraman, Krishnan, & Rayappan, 2015). Unless maintained within optimal levels many metal ions have adverse effects on humans as well as ecological species. Silver is a concern in the water bodies due to its widespread usage in the pharmaceutical, electrical and photographic industries and its potential use as a drinking water disinfectant (Shen, Chen, Hu, Chen, & Wang, 2013). The common analytical tools used for Ag^+ detection namely, atomic absorption spectrometry and inductively coupled mass spectrometry, need pre-concentration steps and sophisticated instrumentation (Pu & Sun, 1998). Contrarily, fluorimetric sensing platforms are simple, economical and selective (Singha, Kim, Seo, Cho, & Ahn, 2015). Fluorescent CDs are a good candidate for metal ion detection and have been shown to a good platform for Ag^+ sensing. Shen et al. developed a CDs based sensor for Ag^+ detection where the in situ formed Ag nanoparticles alter the optical properties of CDs, which enabled the effective detection of Ag^+ ions (Shen et al., 2013). A turn-on fluorescence Ag^+ sensing platform was accomplished by reducing Ag^+ to silver nanoclusters on the surface of CDs (Gao et al., 2015). Pectin derived CDs were effectively used as both colorimetric and fluorescence sensor for Ag^+ detection (Ahmed, Kumar, & Veerappan, 2016). In the present report, we further demonstrate the use of SiCDs gel in the selective and sensitive detection of Ag^+ ions.

In this chapter, we report on the direct synthesis of silicon passivated CDs (CDs) in a polymeric gel form under hydrothermal conditions. The highly luminescent SiCDs gel could be realized by the hydrothermal reaction of 3-aminopropyltriethoxysilane (APTES) in an aqueous solution of HNO_3 at 300 °C. Thermal and photo-stability of the SiCDs gel were also investigated. Notably, fluorescence lifetime of the SiCDs gel is nearly one order higher than that of many reported CDs, which is largely entailed in photocatalytic and energy storage/conversion applications. Also, our nitrogen adsorption studies have revealed that the xerogel has a high nitrogen adsorption capacity of ~322.3 m^2/g. Finally, SiCDs gel transforms Ag^+ ions to Ag nanoparticles at ambient temperature without additional reducing agents. The fluorescence quenching of SiCDs gel due to the formation of Ag nanoparticles was exploited for the selective and sensitive detection of Ag^+ ions. The limit of detection (LOD) and dynamic range of the present Ag^+ sensor was 85 nM and 0.4 µM – 0.1 M, respectively. We envisage that the present study will explore the technological domain of CDs in its soft form.

4.2. Experimental Section

4.2.1. Materials

3-aminopropyltriethoxysilane (APTES) was purchased from Sigma Aldrich, India. Nitric acid, sulphuric acid, hydrochloric acid, silver nitrate, phenol, aniline, nitrobenzene, benzoic acid, sucrose, galactose, glucose, L-cysteine, glutathione, gold(III)chloride, manganese chloride, magnesium chloride, zinc sulphate, nickel sulphate, cobalt sulphate, cadmium chloride, mercuric chloride, lead nitrate, copper sulphate, and ferrous sulphate were from Merck Chemicals, India Ltd. Double distilled water was used for all studies.

4.2.2. Characterization

All fluorescence analysis was carried out using a Fluoro Max-4C Spectrofluorometer (Horiba Instruments, USA). For steady state fluorescence measurements the slit widths (excitation and emission) were fixed at 3 nm with integration time 0.1 ns. Time-correlated single-photon counting (TCSPC) measurements of the SiCDs gel were performed by using a 340 nm LED with <1 ns pulse width. Photostability experiments were conducted by irradiating SiCDs gel at different time intervals using 365 nm UV lamp (power: 8W) and by subsequently recording the fluorescence emission spectra. UV-visible spectral measurements were done by using a Carry-100 UV-visible spectrometer. Spectrum 100T Perkin-Elmer FT-IR spectrometer in transmission mode was used for recording FT-IR spectra. X-ray Photoelectron Spectroscopic (XPS) studies were performed using Omicron ESCA probe spectrometer with unmonochromatised Mg Kα radiation.

Atomic force microscopy (AFM) images of SiCDs gel were obtained using Agilent 5500 scanning probe microscope and subsequent processing using WSxM software. The SiCDs gel were coated over mica surface, dried and used for AFM measurements. Transmission electron microscopy (TEM) images were recorded using a JEOL 3010 UHR instrument.

Anton Paar modular compact Rheometre (MCR 102) was used for performing rheological analysis of the SiCDs gel. Parallel plate geometry (25 mm diametre) was used in rheometry analysis at room temperature. Surface area and pore size distribution of the SiCDs gel was measured using surface area analyzer (Micromeritics Tristur II, USA) with N_2 as adsorbent at 77 K. Prior to the analysis, the xerogel was degassed at 100 °C for 12 h. Thermo gravimetric analysis (TGA) were done using TA instruments' Q50. Heating rate were maintained at 10 °C/min in an inert atmosphere. X-ray diffraction studies were performed using Bruker D8 discover x-ray diffractometer.

4.2.3. Synthesis of SiCDs gel

About 500 mg of APTES was introduced to the mixture of 500 µL of conc. HNO_3 and 13 mL of distilled water. The resulting solution was taken in a Teflon lined stainless steel autoclave and placed at 300 °C for 2 h (see Figure 4.1). The light-brown coloured gel was purified by constantly rinsing with distilled water.

4.2.4. Ag^+ sensor

Known concentration of Ag^+ solution was added to a specific amount of SiCDs gel. The PL quenching of SiCDs gel was completed after 3 h of Ag^+ addition. Hence all sensing experiments were carried out by recording the fluorescence spectra after 3 h of the addition of analyte solution. Xerogel was obtained by heating the purified the gel under vacuum at 40 °C.

4.3. Results and Discussion

4.3.1. Characterization of SiCDs gel

The hydrothermal reaction of APTES was carried out in the presence of HNO_3/H_2O at 300 °C (Figure 4.1). Formation of the SiCDs gel was confirmed by inversion test tube method and the crude gel was then washed several times with distilled water and used for further studies. The critical gelation concentration (CGC) was 4%.

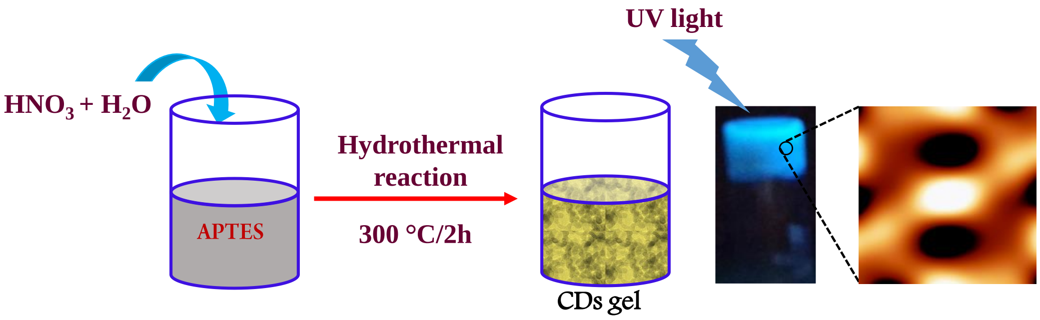

Figure 4.1. Synthesis of SiCDs gel via the hydrothermal route.

To test the role of HNO_3 for gel the formation, the hydrothermal reaction of an aqueous solution of APTES was carried out in the absence of HNO_3. A blue luminescent liquid with an emission at 430 nm was formed (Figure 4.2 (A)). The transmission electron microscopy (TEM) image depicts the formation of spherical dots of 3–4 nm size (Figure 4.2 (B)). An earlier report also shows that the organosilane functionalized CDs can be prepared by hydrothermal reaction of organosilane precursors at 300 °C (Chen, Chen, Hsu, Shih, & Chang, 2013). It is well known that the aqueous solution of HNO_3 catalyses the hydrolysis and condensation of alkoxysilanes (Parejo, Zayat, & Levy, 2006). Therefore, we presume that, in the present case, the organosilane functionalized CDs which formed initially, undergo self-condensation in the presence of HNO_3, lead to the formation of randomly cross-linked network structures.

We performed the hydrothermal reaction of APTES by replacing HNO_3 with other mineral acids such as HCl and H_2SO_4. Figure 4.2 (C) and (D), respectively demonstrate the fluorescence emission spectra of corresponding solutions. In both the cases, a blue luminescent liquid was formed but not the gel. Further, the hydrothermal reaction of APTES with HNO_3 was optimized by performing the reaction at 100, 200, 300 and 400 °C as well as various time intervals (1, 2, 3 and 4 h). The reaction performed at 200 °C (reaction time: 2h) produced a blue luminescent liquid with feeble emission indicating the incomplete growth of nanoparticles (Figure 4.2 (E)). A highly luminescent gel was obtained when the reaction temperature was maintained at or above 300 °C. The time dependent synthesis indicated that the fluorescence intensity of the formed gel remains steady after 2 h of hydrothermal reaction at 300 °C. On the contrary, despite the gel is formed after 1 h of hydrothermal treatment, only weak emission was observed (Figure 4.2 (F)). This may be due to the incomplete growth of CDs owing to the short reaction time.

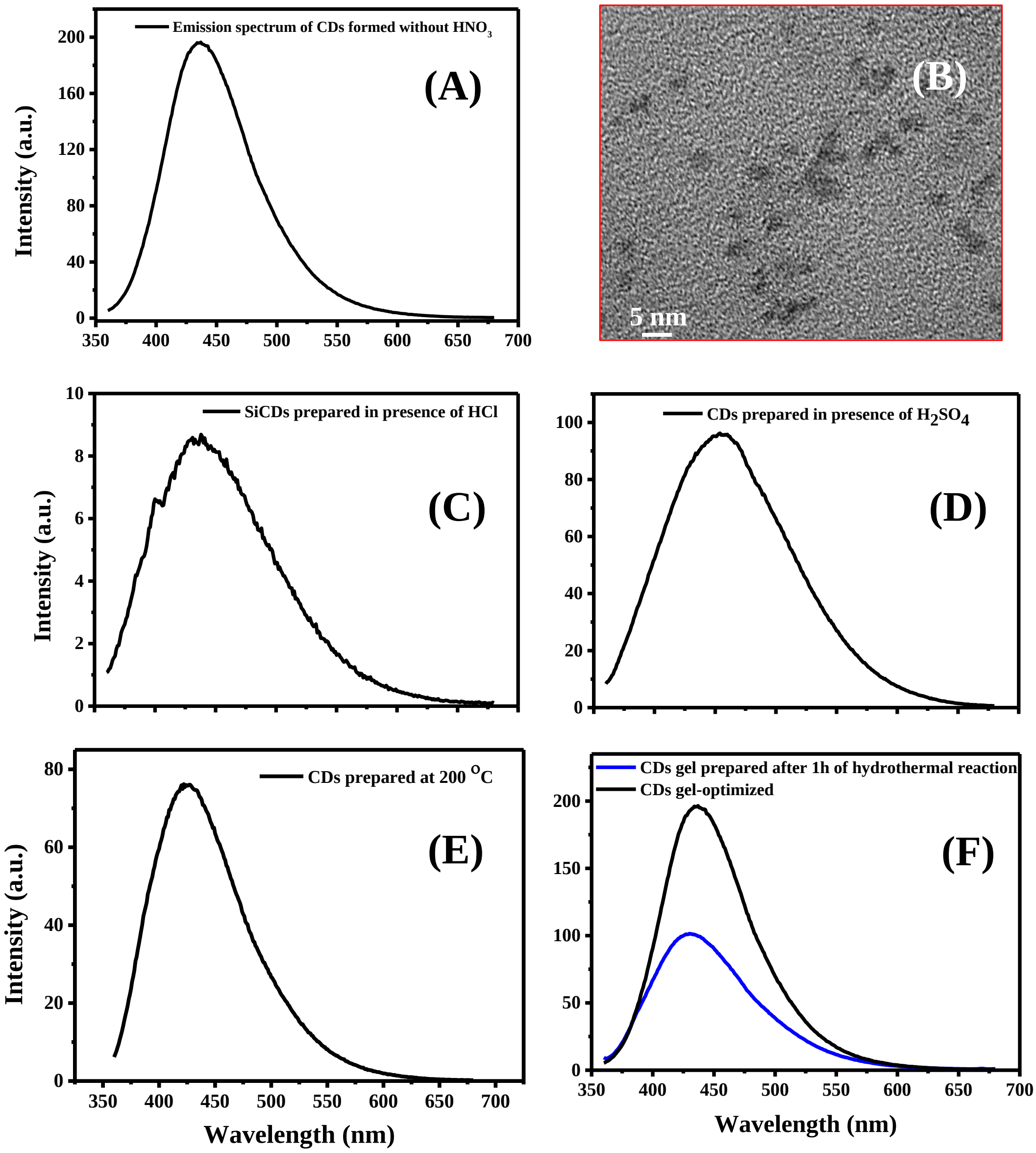

Figure 4.2. The optimization of gel formation. (A) The emission spectrum of SNCDs without the usage of Conc. HNO_3 and (B) the corresponding TEM image. The emission spectrum of SiCDs obtained using (C) HCl (D) H_2SO_4. (E) The emission spectrum of CDs obtained at 200 °C and (F) Emission spectra of CDs gel obtained after 1h and 2h (optimized) of hydrothermal treatment.

The SiCDs gel is expected to form through the following steps. In the beginning, the surface $Si(OC_2H_5)_3$ groups undergo condensation in the presence of aqueous HNO_3 to form a randomly cross-linked network structure. In the second step, the propylamine moiety of APTES undergoes bond rupture, free radical/ion generation, recombination, ring formation, aromatization and interlinking under the hydrothermal reaction conditions. The oxidation reation forms the C=C, C=N, C–OH, –COOH and C–N groups. The breaking of Si–C linkage is not presumed under present reaction condition owing to the high bond strength. The CDs thus formed is expected to contain –COOH/–OH/–NH_2/–$Si(OC_2H_5)_3$ functional groups on the surface with C=C and C=N groups at the core. Presence of these functional groups was confirmed by X-ray photoelectron spectrum (XPS) and is discussed later part of the text. The proposed structure of SiCDs gel is given in Figure 4.3.

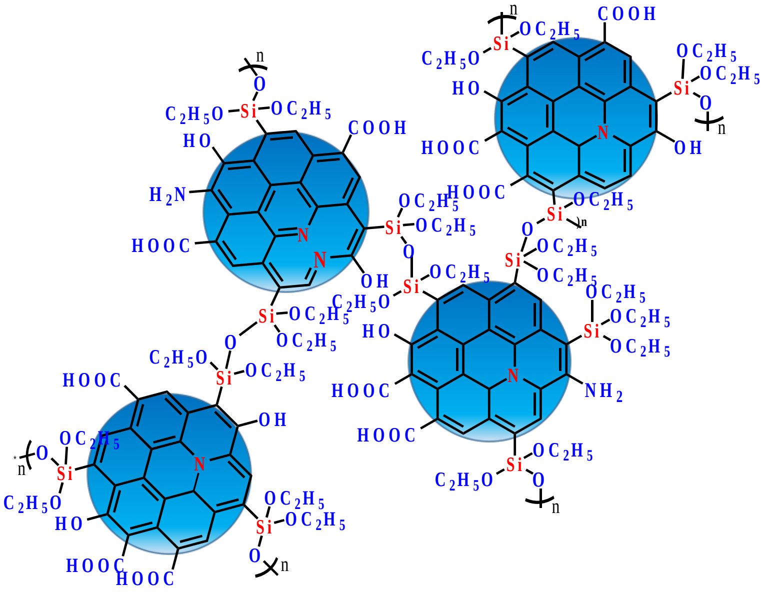

Figure 4.3. Schematic of the proposed (representative) structure of SiCDs gel.

We conducted detailed spectroscopic and microscopic analysis to understand the chemical structure/morphology of the gel and to corroborate the proposed growth mechanism.

TEM images of SiCDs gel show randomly arranged entangled network structures with a large pore size distribution (Figure 4.4 (a, b, c)). Here the SiCDs can be visualized within the network, which confirms the covalent linkage of CDs to the silicon backbone (Figure 4.4 (b and c)). The size of the dots was ~10 nm (Figure 4.4 (c)).

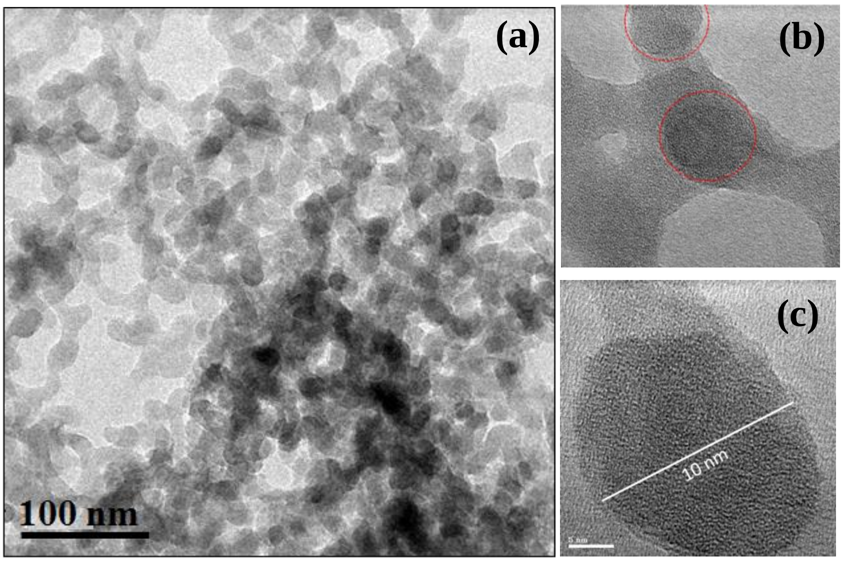

Figure 4.4. (a, b and c) represent TEM images of SiCDs gel.

Similar morphological features were also observed in the atomic force microscopy (AFM) images of the SiCDs gel (Figure 4.5 (a, c, d)). Height profile shows 0.5 to 2 nm range, which is equivalent to the thickness of 1–3 graphene layers (Figure 4.5 (b)). The direct synthesis of SiCDs gel shown here is simple, rapid and distinctive compared to the SiCDs gel glasses prepared by the post-treatment of Si doped CDs with various silane precursors (Chen et al., 2013).

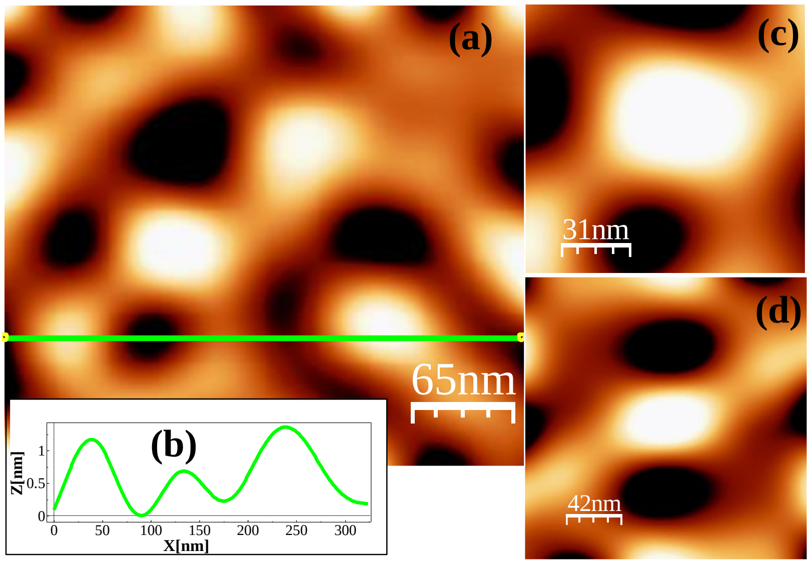

Figure 4.5. (a, c and d) are the AFM images of SiCDs gel, (b) is the height profile of the line drawn on (a).

The uv-visible spectrum of SiCDs gel shows an absorption feature centred around 265 nm, originating from π–π^* transition of CDs (Figure 4.6 (A)). Similar observations were reported for silicon doped CDs in the literature (Chen et al., 2013). In a few cases, CDs prepared from non-silicon precursors were also showed similar absorption feature (C. Zhu, Zhai, & Dong, 2012).

PL spectra of SiCDs gel, recorded at the different excitation wavelength (300-420 nm) exhibits excitation dependent emission feature (Figure 4.6 (B)). The red shift in the emission maxima with an increase in the excitation wavelength is typical of carbon based fluorescent nanomaterials. This behaviour is ascribed to the presence of various emissive states involving direct recombination/defect state emission or due to the presence of distinctly sized CDs. Similar to the emission spectra, the PL excitation spectra of SiCDs gel shows emission dependent excitation features (Figure 4.7 (A)).

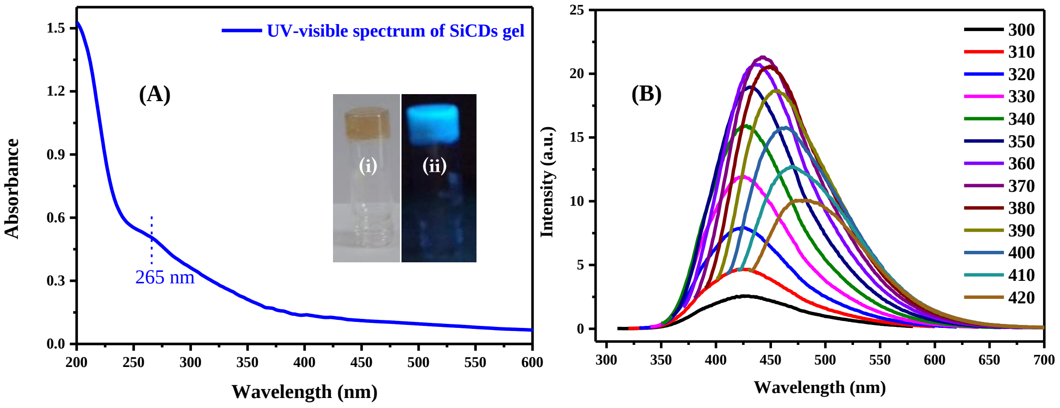

Figure 4.6. (A) UV-visible absorption spectrum of SiCDs gel, Inset: Photograph showing SiCDs gel under (i) visible and (ii) UV light. (B) Emission spectra of SiCDs gel at various excitation wavelength.

Time resolved fluorescence spectra of SiCDs gel collected at 450, 500, 550 and 600 nm wavelength is given in Figure 4.7 (B) (excitation wavelength: 340 nm). The lifetime parameters such as average lifetime, CHSQ2 (χ^2) and amplitude are given in Table 4.1. In general, all the decay curves are bi-exponential fit with shorter component ranged from 3.6 to 4.5 ns, whereas that of longer ones from 12.1 to 13.5 ns with almost equal contribution from both the lifetime components toward average lifetime.

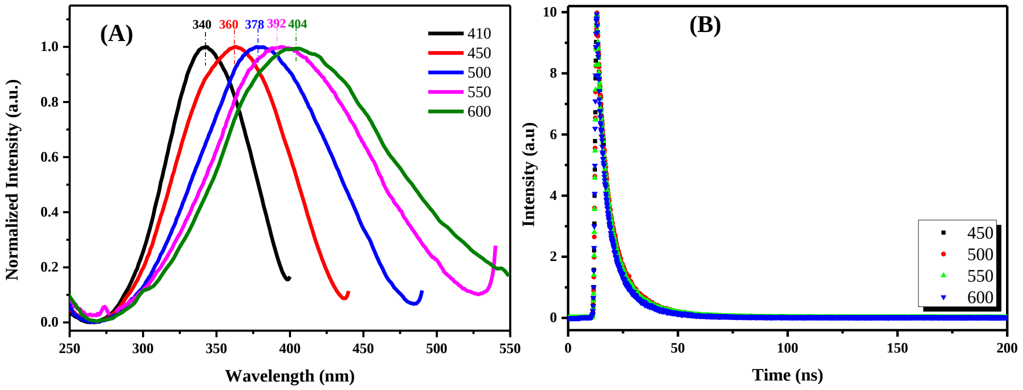

Figure 4.7. (A) Excitation spectra at the different emission wavelength. (B) Time-resolved fluorescence spectra collected at the different emission wavelengths.

There was no substantial variation in the average lifetime of SiCDs gel when the collection wavelength was shifted from 450 to 600 nm except with a decrease of 1 ns. Interestingly, the average lifetime of the SiCDs gel was higher than many reported fluorescent CDs (L. Wang & Zhou, 2014; L. Zhu, Yin, Wang, & Chen, 2013). The result presented here may indicate that the lifetime of carbon based fluorescent nanoparticles can be amplified in a gel state. The fluorophore having high lifetime is entailed in energy conversion/storage and photo/electro catalytic applications, where the electron-hole recombination is to be circumvented.

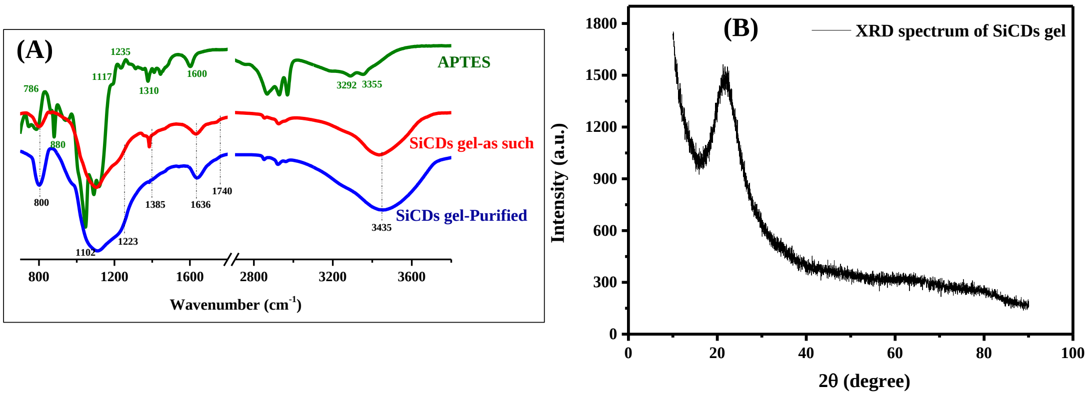

Figure 4.8. (A) FTIR spectra of SiCDs gel before and after purification, for comparison FTIR spectrum of APTES also given. (B) XRD spectrum of SiCDs gel.

Table 4.1. Time resolved fluorescence results of SiCDs gel at different collection wavelength.

$\lambda_{collection}$ (nm)	τ_1 (ns)	a_1 (%)	τ_2 (ns)	b_1 (%)	χ^2	$<\tau>$ (ns)
450	4.15	46.6	13.2	53.3	1.3	11.2
500	4.5	49.4	13.5	50.6	1.3	11.3
550	4.2	48.2	12.9	51.8	1.3	10.9
600	3.6	48.1	12.1	51.9	1.3	10.3

FTIR spectrum of purified xerogel confirms the formation of cross-linked CDs network (Figure 4.8 (A)). The features at 1636, 1740 and 3435 cm^{-1} were attributed to C=C, C=O and –OH/–NH_2 groups of the SiCDs, respectively. These features were absent in pure APTES. Compared to APTES, a significant weakening of N–H bending vibrations (1600 cm^{-1}) was observed in the case of SiCDs gel indicates a decrease of –NH_2 groups. The vibrational signatures at 1102 cm^{-1} and 1223 cm^{-1} support the formation of Si–O–Si linkage through condensation of ethoxy groups of APTES. Further, a large shift in the Si–O stretching feature of SiCDs gel (around 800 cm^{-1}) as compared to APTES (around 786 cm^{-1}) reflects the condensation of APTES molecules. The prominent band at 1385 cm^{-1} is attributed to the N–O stretching mode of nitrate anion (Abellán, Coronado, Martí-Gastaldo, Pinilla-Cienfuegos, & Ribera, 2010), which was absent in the purified gel indicating the successful removal of unreacted HNO_3. Furthermore, the presence of broad peak centred at $2\theta = 22$ degrees in the X-ray diffraction (XRD) pattern of SiCDs gel reflects the formation of disordered carbon nanomaterials (Figure 4.8 (B)).

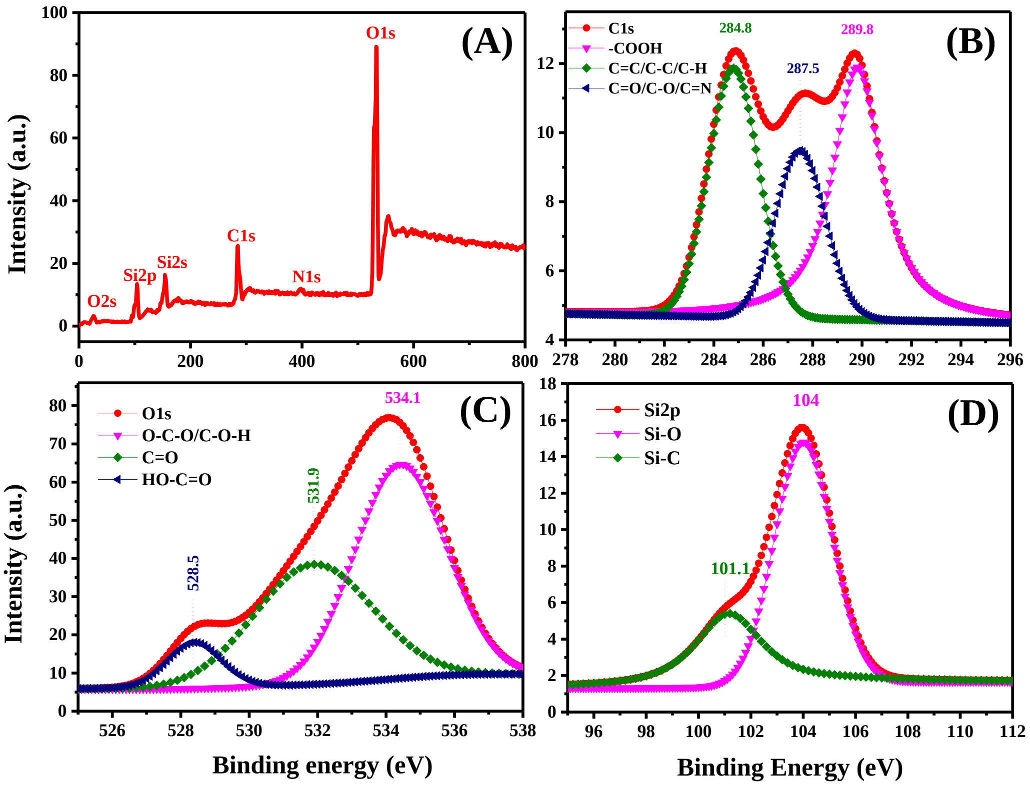

Figure 4.9. (A) The survey scan XPS spectrum of SiCDs gel. High resolution XPS spectra of C 1s, O 1s and Si 2p are given in (B), (C) and (D), respectively.

XPS of SiCDs gel depicts the presence C, O, N and Si containing functional groups. The survey scan XPS spectrum (Figure 4.9 (A)) shows C1s peak at 285 eV, N 1s peak at 398 eV, O 1s peak at 534 eV and Si 2p and Si 2s peaks at 104 and 154 eV, respectively (Qian et al., 2014; Yang et al., 2014). The high resolution spectrum of C 1s shows three peaks viz. 284.8, 287.5 and 289.8 eV, which are assigned to C=C/C–C/C-H, C=N/C=O, –COOH groups, respectively (Figure 4.9 (B)). High resolution O 1s spectrum shows the presence of –COOH (528.5 eV), –C=O (531.9 eV) and O–C–O/C–O–H (534.1 eV) groups (Figure 4.9 (C)). The presence of Si–C and Si–O bonds were observed at 101.1 and 104.0 eV, respectively (Figure 4.9 (D)). Due to the instrument limitation a high resolution XPS spectrum of N 1s is not shown as the nitrogen content was less.

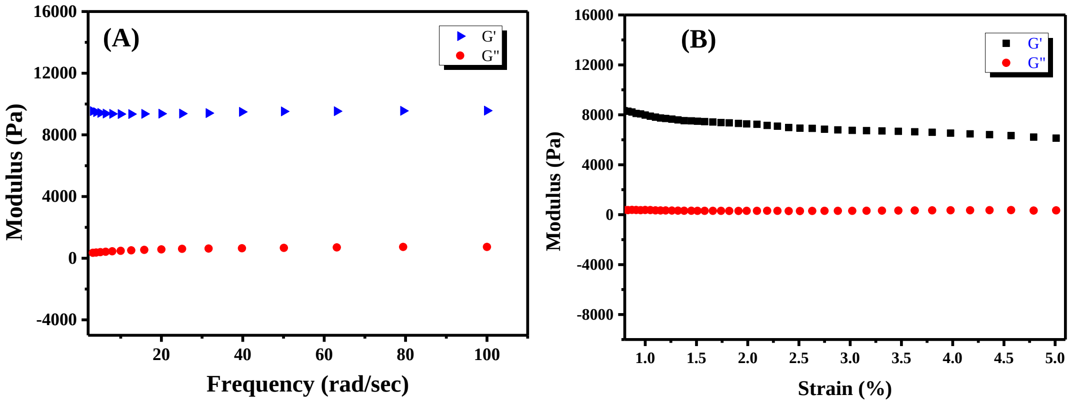

Figure 4.10. (A) Elastic modulus, G′ (▶) and viscous modulus, G″ (●) of SiCDs gel with a frequency sweep from 0.1 to 100 rad/sec at a constant strain of 2.5%, within the viscoelastic region. (B) The plot of elastic, G’ (represented as ■) and viscous, G” modulus (represented as ●) of SiCDs gel at varying strain rate from 0.5 to 5..0 %, showing the viscoelastic region.

Flow behaviour of the SiCDs gel was tested by performing rheological analysis in a parallel plate geometry. Both storage (G′) and loss modulus (G″) were found to be almost constant when a frequency sweep was conducted from 0.1 to 100 rad/s (Figure 4.10 (A)) at a constant strain of 2.5 % (within the viscoelastic region). The viscoelastic region of the gel was identified by recording G′ and G″ over a varying strain rate (%) at a constant frequency and it is linear in the strain rate of 0.5% to 5% (Figure 4.10 (B)). Most importantly, the G′ values were almost one order of magnitude higher than that of G″ over a range of frequencies, which is a characteristic feature of gels (Yu et al., 2013).

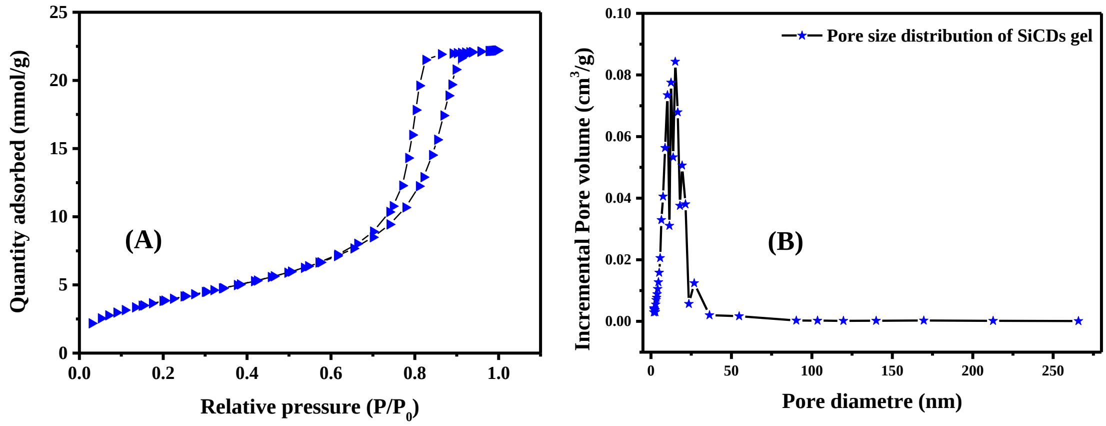

Figure 4.11 (A) Nitrogen adsorption-desorption isotherms of SiCDs gel. (B) Showing pore size distribution calculated using BJH adsorption of SiCDs gel.

Brunauer, Emmett and Teller (BET) surface area of the dried SiCDs gel measured using nitrogen sorption isotherms was 322.3 m^2/g. Presence of high porosity and smaller sized dots may be accountable for the observed high surface area of the dried gel. Nitrogen adsorption-desorption isotherms (Figure 4.11 (A)) depicted typical type (IV) isotherms (H1-like hysteresis loops and cylinder like pores) (Li, Tsai, & Kuo, 2014), indicating the mesoporous nature of the gel, having capillary condensation observed at 0.7-0.9 relative pressure. Average pore size and pore volume obtained using Barrett-Joyner-Halenda (BJH) analysis on adsorption branch of isotherms was 8.8 nm and 0.7874 cm^3/g, respectively (Figure 4.11 (B)).

4.3.2. Stability of SiCDs gel

Fluorescent nanoparticles with low photobleaching is demanded in bioimaging and light emitting diode (LED) applications. To test SiCDs photostability, the gel was subjected to UV light (365 nm, power: 8 W) irradiation for 16 h. The fluorescence spectra were measured at different irradiation time. A plot of PL intensity versus time (Figure 4.12 (A)) shows ca. 60% reduction of the PL intensity, even after 16 h, reflecting a reasonable photostability.

The thermal stability of SiCDs gel was examined by thermogravimetric analysis (TGA). About 95% of the decomposition was observed for pure SiCDs gel below 150 °C, which is attributed to the loss of water molecules in the gel (Figure 4.12 (B)). The TGA of pure SiCDs gel and the dried SiCDs gel showed a similar decomposition features in the range of 200 to 800 °C (Figure 4.12 (B) and corresponding inset). The weight loss around 200 to 500 °C can be ascribed to the decomposition of O and N containing functional groups. (Jang et al., 2015; Y. Liu, Deng, Wang, & Liu, 2012) The weight loss below 200 °C for dried SiCDs gel is due to the evaporation of surface adsorbed water molecules. Thermal behaviour of the gel indicated that 25 wt. % of the gelator is comprised of functional groups, which are decomposed in the range of 200 to 500 °C.

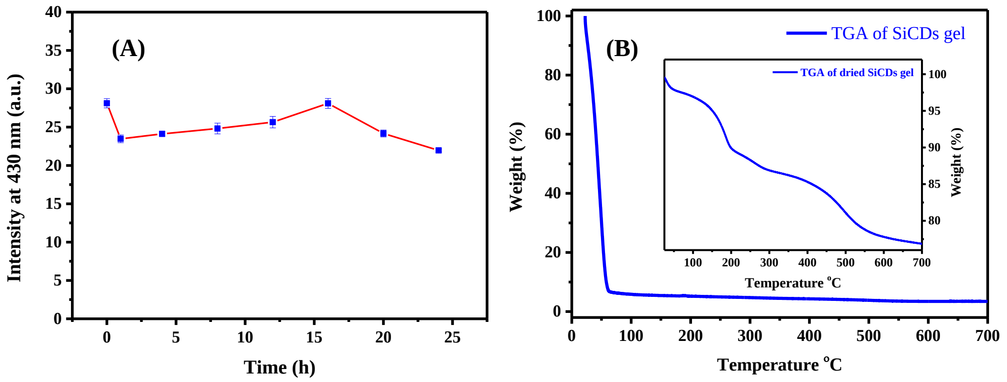

Figure 4.12. (A) Showing the variation of PL intensity of SiCDs gel at different irradiation time. (Lamp power: 8W. Wavelength: 365 nm). (B) TGA plot of pure SiCDs gel, Inset: TGA of SiCDs gel after vacuum drying (B).

4.3.3. Ag^+ Sensor

As an application point of view, we exploited SiCDs gel for the selective and sensitive fluorescence detection of Ag^+ ions. Figure 4.13, illustrates the fluorescence sensing of Ag^+ ions using SiCDs gel. Here the addition of Ag^+ to the SiCDs gel led to the quenching of the luminescence.

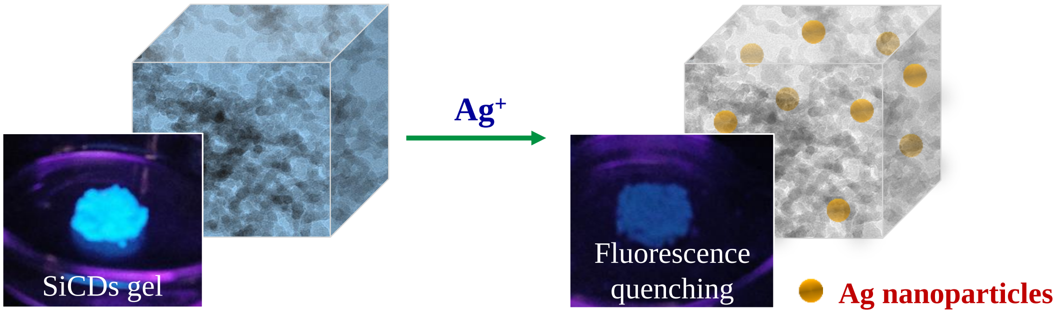

Figure 4.13. Schematic of the interaction of Ag^+ ions with SiCDs gel, which leads to the luminescence quenching of SiCDs gel.

Figure 4.14 (A), represents the fluorescence emission spectra of SiCDs gel at various concentrations of Ag^+ ions. It is to be noted that the quenching experiments were performed at an excitation wavelength of 400 nm, to avoid the plausible inner filter effect of the metal compounds or molecules used for selectivity experiments. Fluorescence quenching of SiCDs gel was observed when the concentration of Ag^+ ranged from 0.4 µM to 0.2 M. A good linearity in emission intensity was observed in the range of 0.4 µM to 0.1 M of Ag^+ ($R^2 = 0.9977$). Figure 4.14 (B) demonstrates the dynamic range of present sensing platform. F_0 and F represent the fluorescence intensity of SiCDs gel without and with various concentrations of Ag^+ ions, respectively. Detection limit calculated using the equation $3\times S_{bl}/m$ for three repetitive measurements was 0.085 µM. S_{bl} is the standard deviation of the blank and m is the slope of the linear plot (Figure 4.15 (A)).

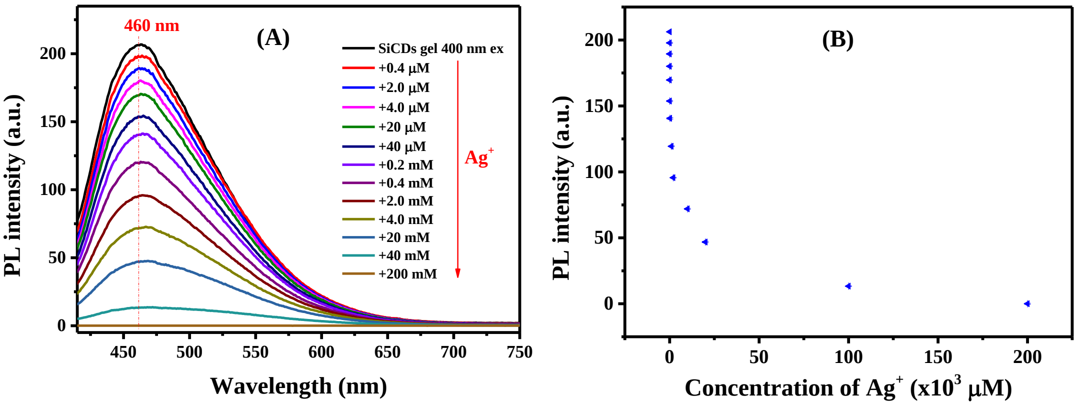

Figure 4.14 (A) PL spectra of SiCDs gel before (black trace) and after the introduction of various Ag^+ concentrations. (B) The plot of PL intensity of SiCDs gel vs concentration of Ag^+ (mM).

The UV-visible absorption spectrum of SiCDs gel treated with Ag^+ showed an additional broad absorption band centred ca. 440 nm (Figure 4.15 (B)), which is ascribed to the surface plasmon resonance (SPR) of Ag nanoparticles. A nearly transparent SiCDs gel was transformed into a dark brown coloured gel after the addition of Ag^+ (see the photographs shown in the inset of Figure 4.15 (B)).

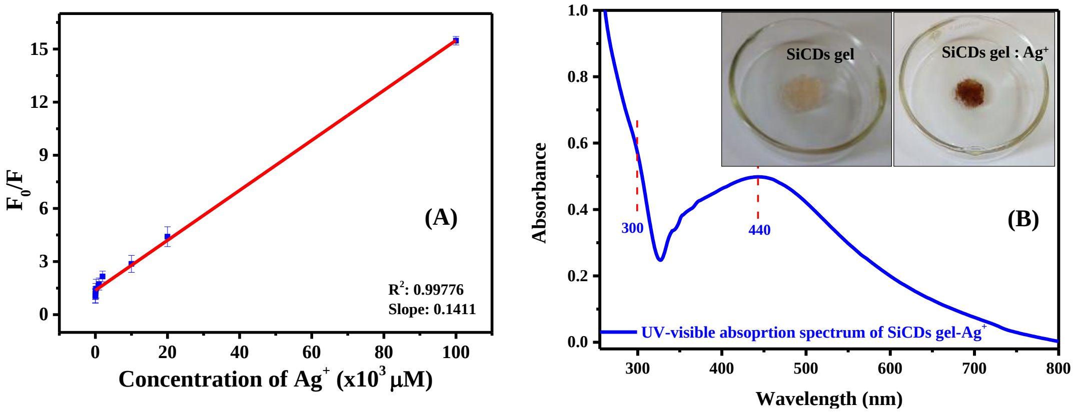

Figure 4.15 (A) showing linearity range of the sensor system (0.4 µM to 100 mM). (B) UV-visible absorption spectrum of SiCDs gel treated with Ag^+ (100 µL of 2mM $AgNO_3$ solution), recorded after 3 h of Ag^+ addition. Photographs of SiCDs gel and Ag^+ treated SiCDs gel under visible light is shown as an inset.

It was also evident from the previous report that CDs can form Ag nanoparticles, by reducing Ag^+ ions to elemental silver and subsequent stabilization (Ran, Sun, Pu, Ren, & Qu, 2013; Shen et al., 2013). The O and N containing functional groups of CDs were participated in the reduction and stabilization. A plethora of N and O containing functional groups in SiCDs gel is expected to play a similar role, as above, in the formation of Ag nanoparticle in the present study. The time required for complete formation of Ag nanoparticles was ~3 h. This was established by monitoring the PL intensity of SiCDs gel-Ag^+ mixture at different time intervals. The PL intensity was decreased steadily up to 3 h and then remained constant. Hence, all Ag^+ sensing studies were performed after 3 h of the addition of analyte.

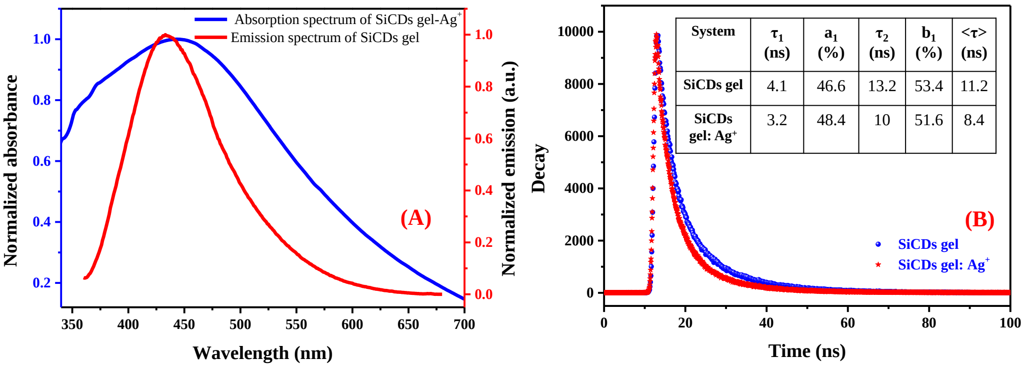

System	τ_1 (ns)	a_1 (%)	τ_2 (ns)	b_1 (%)	$<\tau>$ (ns)
SiCDs gel	4.1	46.6	13.2	53.4	11.2
SiCDs gel: Ag^+	3.2	48.4	10	51.6	8.4

Figure 4.16. (A) Show the spectral overlap between absorption spectrum of Ag^+ treated SiCDs gel and emission spectrum of SiCDs gel. (B) Time-resolved fluorescence spectra of SiCDs gel (blue trace) and Ag^+ treated SiCDs gel (red trace). Inset: Table showing the detailed lifetime parameters such as lifetime (τ), amplitude (a and b), χ^2 and average lifetime $<\tau>$. Excitation and emission wavelength were fixed respectively at 340 and 450 nm.

As mentioned above, Ag^+ ions effectively quenched the blue luminescence of SiCDs gel. The mechanism of PL quenching can be attributed to the involvement of electron and energy transfer from Ag nanoparticles to SiCDs gel. Ran et al. reported that the fluorescence of carbon based nanomaterials such as GQDs can be quenched through the electron transfer from Ag nanoparticles (Ran et al., 2013). Similarly, Yan and co-workers claimed that the palladium nanoparticles could transfer the charge to GQDs, and hence quench the fluorescence of GQDs (Yan, Li, & Li, 2012). Alongside, excited state energy transfer from SiCDs gel to Ag nanoparticles cannot be precluded owing to the considerable spectral overlap between the emission spectrum of SiCDs gel and SPR band of Ag nanoparticles (Figure 4.16 (A)). To verify the above arguement, we performed time-resolved fluorescence spectral analysis of SiCDs gel after the addition of Ag$^+$. For both SiCDs gel and Ag$^+$ treated SiCDs gel, collection wavelength was fixed at 450 nm (Figure 4.16 (B)). Decay curve of Ag$^+$ treated SiCDs gel was a bi-exponential fit with shorter lifetime component at 3.2 ns (48.38%) and the longer one at 10 ns (51.62%). Compared to pure SiCDs gel, lifetime components (both shorter and longer) were significantly lowered in this case. The average lifetime of SiCDs gel-Ag nanoparticles was 8.43 ns, whereas that of pure SiCDs gel was 11.24 ns. Decreasing the fluorescence lifetime of SiCDs gel after Ag$^+$ treatment indicated the involvement of excited state processes (energy/charge) in PL quenching of SiCDs gel by Ag nanoparticles. Moreover, the Stern-Volmer quenching plot F_0/F versus concentration of quencher was a curve which further supported the involvement of multiple quenching mechanisms.

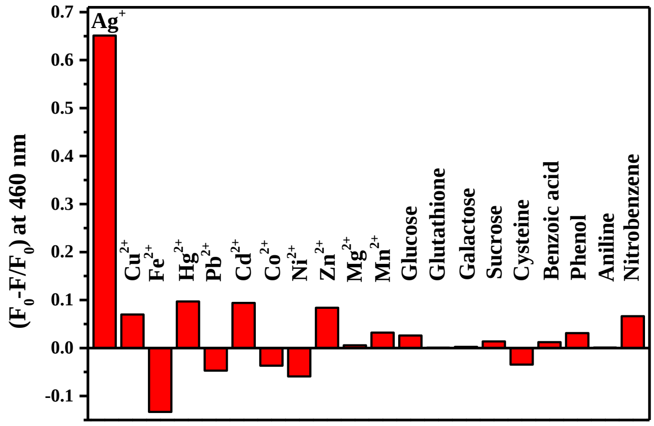

Figure 4.17. Selectivity of SiCDs gel towards Ag$^+$ against common metal ions and organic compounds.

The ability of the present sensor towards the selective screening of the target analyte was tested with a large number of metal cations, common organic molecules (benzoic acid, phenol, aniline and nitrobenzene) and small biomolecules (glutathione, cysteine, glucose, galactose and sucrose). The concentration of these analytes used for selectivity studies was 4 mM. The extent of variation in PL intensity of SiCDs gel with the various analytes is shown in Figure 4.17. Similar to the previous experiments, these measurements were also carried out after 3 h. The effect of above chemicals on the PL emission of SiCDs gel was negligible compared to Ag^+ ions. Therefore, the present fluorescence sensor is a potential tool for Ag^+ detection in environmental and biological domains where highly selective sensing is crucial. A comparison of the present Ag^+ sensor with various strategies is presented in Table 4.2. It is apparent that, the present sensing platform stands high in terms of large dynamic range, high selectivity and sensitivity.

Table 4.2. A Comparison of the analytical performance of various Ag^+ sensing methods.

Method: Brief	*LOD*	*Dynamic range*	*Selectivity*	*Reference*
Colorimetry: Simultaneous detection of heavy metal ions using a paper based strip	1.69 µM	Not specified	common metal ions	(L. Liu & Lin, 2014)
Fluorometry: Ag^+ induced fluorescence enhancement of CDs	320 nM	0–90 µM	common metal ions	(Gao et al., 2015)
Fluorescent carbon quantum dot hydrogels	0.55 µg/mL	0.8 – 20 µg/mL	common metal ions	(A. Cayuela et al., 2016)
Fluorometry: rhodanineacetic acid–pyrene based ratiometric fluorescence sensor	0.10 µM	Not specified	common metal ions	(B. Zhang et al., 2011)
Electrochemical: Metallothionein immobilized on carbon paste for electrochemical sensing	0.50 nM	Not specified	Hg (II) interfere strongly in the assay	(Trnkova, Krizkova, Adam, Hubalek, & Kizek, 2011)
Atomic absorption spectrometry (AAS): pre-concentration–	0.66 ppb	0–800 ppb	Cl^- interfere strongly in the assay	(Pu & Sun, 1998)

separation followed by Ag^+ detection using AAS				
Fluorometry	85 nM	0.4 µM–0.1 M	common metal ions, organic and biomolecule	Present study

4.4. Conclusions

In this chapter, we demonstrated the one pot direct synthesis of highly blue luminescent SiCDs gel by hydrothermal treatment of APTES in the presence of HNO_3/H_2O. To unfold the structural and morphological features of SiCDs gel, we carried out detailed spectroscopic and microscopic studies. Rheological behaviour and adsorption characteristics of SiCDs gel is also presented. The SiCDs gel was used for the selective fluorescence sensing of Ag^+ via the formation of silver nanoparticles on the surface of SiCDs gel. The detection limit and dynamic range of the sensor was 85 nM and 0.4 µM to 0.1 M, respectively. The one pot hydrothermal synthesis of SiCDs gel is useful in expanding the technological realm of carbon based fluorescent nanomaterials in the gel form.

CHAPTER 5

PHOTOPHYSICAL STUDIES OF SULFUR AND NITROGEN CO-DOPED CARBON DOTS (SNCDs) AND THE HIGHLY SELECTIVE DETECTION OF Cr(VI)

Although an exceptional progress has been observed in enhancing the quantum yield and in tuning the emission wavelength of carbon dots (CDs), the origin of photoluminescence in many types of CDs is unclear owing to the structural complexity. We performed detailed photophysical studies, including fluorescence excitation, emission and time resolved analysis to understand the observed pH dependence luminescence in S and N co-doped carbon dots (SNCDs). The SNCDs were prepared using hydrothermal carbonization of glutathione. Based on the results a comprehensive energy level diagram for SNCDs was proposed which explains the presence of multiple emissive states contributed by core, surface and edge states. A highly selective fluorescence detection strategy for the Cr(VI) was developed using the present SNCDs as a fluorophore.

5.1. Introduction

In general, CDs possess a broad, excitation dependent luminescence with emission focussed at blue part of the visible spectrum. Doping and surface passivation have been the best ways to enhance the quantum yield (QY) and to modulate the energy levels of CDs (D. Pan et al., 2011; F. Wang, Xie, Zhang, Liu, & Zhang, 2011; W.-J. Wang, Hai, Mao, Chen, & Wang, 2015). Although, adequate amount of success has been received in terms of amplifying the QY and tuning the luminescence of CDs, the rationale behind broad and excitation-dependent emission output is unclear (Ghosh et al., 2014; Gude, Das, Chatterjee, & Mandal, 2016; Lu, Cong, Zhu, Zhao, Liu, S.Tse, et al., 2016; S. Zhu et al., 2015). This is due to the complex structure of CDs in terms of the size of the core and nature of surface/edge states which differs according to the nature of synthetic strategies, dispersion media, doping, to name a few. It is demonstrated that the luminescence output of CDs derived from urea and p-phenylenediamine can be tuned by controlling the number of oxygen containing functional groups on the surface (Ding, Yu, Wei, & Xiong, 2015). By developing a model system comprising of three types of polyaromatic hydrocarbons, Fu et al. showed the origin of substantial Stokes shift and excitation dependent spectral output in CDs (Fu et al., 2015). It was shown that graphitic nitrogen doping causes variation in the PL output, whereas the presence of pyridinic, pyrrolic and amino centres do not influence its photophysical behaviour (Sarkar et al., 2016). The fluorescence at higher energy range might stem from core states whereas the emission observed at lower energy are due to surface states (Dhenadhayalan, Lin, Suresh, & Ramamurthy, 2016).

Furthermore, distinct PL response towards pH of the medium has been observed from the CDs prepared by different routes and precursors. For example, pH dependent tuneable luminescence response from amino functionalized CDs has been demonstrated (X. Liu, Pang, Xu, & Zhang, 2016). CDs prepared by the carbonization of amino acids manifested high acidophilic luminescence (Lu, Cong, Zhu, Zhao, Liu, S. Tse, et al., 2016). On the contrary, CDs synthesised by pyrolysis of ethylenediamine tetraacetic acid found to fluoresce strongly at basic pH whereas collapses its emission at acidic conditions (D. Pan et al., 2010).

Ample number industrial processes such as wood treatment, metallurgy, pigment manufacturing release Cr(VI) compounds into the environment. Although chromium in its +3 state is biologically significant in terms of activating specific enzymes in mammals, +6 state is potentially cytotoxic and carcinogenic (Babich, Schiffenbauer, & Stotzky, 1982; Fargasova, 1994). The commonly used detection strategies for Cr(VI) such as atomic absorption/emission, inductively coupled mass spectrometry, colorimetric and electrochemical methods suffer from low sensitivity and selectivity, cumbersome sample pre-treatment steps and time consuming. Hence, a fast and facile detection strategies which selectively recognizes Cr(VI) with high sensitivity is most demanded.

Here, we present a facile approach for the synthesis of nitrogen and sulphur co-doped CDs (SNCDs) using glutathione as a sole source without the use of an acid or base. The luminescence of SNCDs was found to be dependent on pH of the medium. The best emission was in acidic medium, drops steeply at neutral pH and then decreases linearly above pH 7. A comprehensive study has been carried out to understand the origin of pH dependent PL in SNCDs. The excitation, absorption and time-resolved fluorescence spectroscopic studies reveal the presence of multiple emissive states in SNCDs in which high energy emission stems from carbon core, whereas average energy emission originates from the contribution of both edge and surface states. Furthermore, we demonstrated ‘turn-off' fluorescence detection of Cr(VI), which operates via inner filter effect and FRET mechanisms, confirmed by steady state and time-resolved fluorescence spectral analysis. Here, the introduction of Cr(VI) to the solution containing SNCDs and DPC quenches the emission of SNCDs. The strong absorption of DPC-Cr(VI) complex at fluorophore's excitation wavelength and good spectral overlap between the emission of donor and absorption of the acceptor led to the efficient energy transfer from the fluorophore to the quencher. The method offers high selectivity towards Cr(VI) against most of the competing metal ions. The detection limit of this sensor was 5 nM.

5.2. Experimental Section

5.2.1. Materials

Glutathione was purchased from Sigma Aldrich, India. NaOH and HCl were from Merck Chemicals, India. Dialysis bags (MWCO: 500) was supplied by Sigma Aldrich, India. Double distilled water was used for all the studies.

5.2.2. Synthesis of SNCDs

SNCDs was prepared by hydrothermal treatment glutathione in water at 220 °C for 3h. As prepared colloidal solution of SNCDs was purified by dialysis using dialysis membrane of a molecular weight cut off 500 for 8 h. The pH of the resulting solution was around 5. The pH of the purified solution was varied using either dilute hydrochloric acid or sodium hydroxide solution and then used for all further analysis. Optimization of the hydrothermal reaction conditions was carried out by monitoring the photoluminescence and Transmission electron microscopy (TEM) images of an aqueous solution of glutathione at different temperatures such as 140, 180 and 220 °C. TEM image of hydrothermally treated glutathione at 220 °C reflects the formation of spherical dots whereas the polymeric structures and partially formed dots were obtained in case of 140 and 180 °C treated glutathione respectively. Further, the photoluminescence was found to be broad and highest for 220 °C reaction temperature. Hence, glutathione treated at 220 °C was used for all further analysis.

5.2.3. Chromium sensor

1.5 mL of purified SNCDs was mixed with 500 μL of 10^{-3} M DPC (dissolved in H_2SO_4) solution. This solution is considered as the sensor. To this, previously prepared solution of $K_2Cr_2O_7$ at various concentrations of analytes were introduced. The fluorescence spectra of all the solution were recorded at 470 nm excitation. The emission and excitation slit widths were fixed at 3.5 nm.

5.2.4. Characterization

UV-Visible spectra were collected using a Carry-100 UV-Visible spectrometer. Infrared studies were performed using a Spectrum 100T Perkin-Elmer FT-IR spectrometer. For collecting FTIR spectra, an aqueous solution of SNCDs was dried under vacuum at 50 °C and the resulting brownish semi-liquid obtained was mixed with KBr powder and palletized. The mixture was thoroughly ground, resulting fine powder was converted into a pellet. IR spectrum of the pellet was then recorded using transmission mode. All steady state fluorescence measurements (excitation and emission) were carried out using FluoroMax-4C Spectrofluorometer (Horiba Instruments USA). Both excitation and emission slit widths were fixed at 3.5 nm with an integration time of 0.1 ns. Time resolved fluorescence measurements were performed using time-correlated single-photon counting (TCSPC). TCSPC measurements excitation wavelength was fixed at 344 nm with a collection wavelength 390, 430 and 500 nm. Data analysis software (DAS) was used to fit the time resolved results and the best fit was accomplished by keeping minimal $\chi 2$ values in all the cases. X-ray Photoelectron Spectroscopic (XPS) studies of NCDs were performed using Omicron ESCA probe spectrometer with unmonochromatised Mg Kα radiation. EUTECH instruments' pH meter was used for pH measurements.

5.3. Results and Discussion

5.3.1. Characterization of SNCDs

Synthesis of SNCDs was carried out by the hydrothermal treatment of glutathione at 220 °C for 3h. After the synthesis, the light yellow coloured solution was purified by dialysis using dialysis bags of MWCO 500. The pH of the purified solution was 5 and is used for all further studies. The microscopic studies (TEM and AFM) (Figure 5.1) demonstrated the successful synthesis of spherically sized dots with the lateral size ranged from 10 to 20 nm. The thickness was ranging from 0.6 to 2.4 (AFM histogram is shown in the inset of Figure 5.1 (B)), which is equivalent to 1-4 graphene layers.

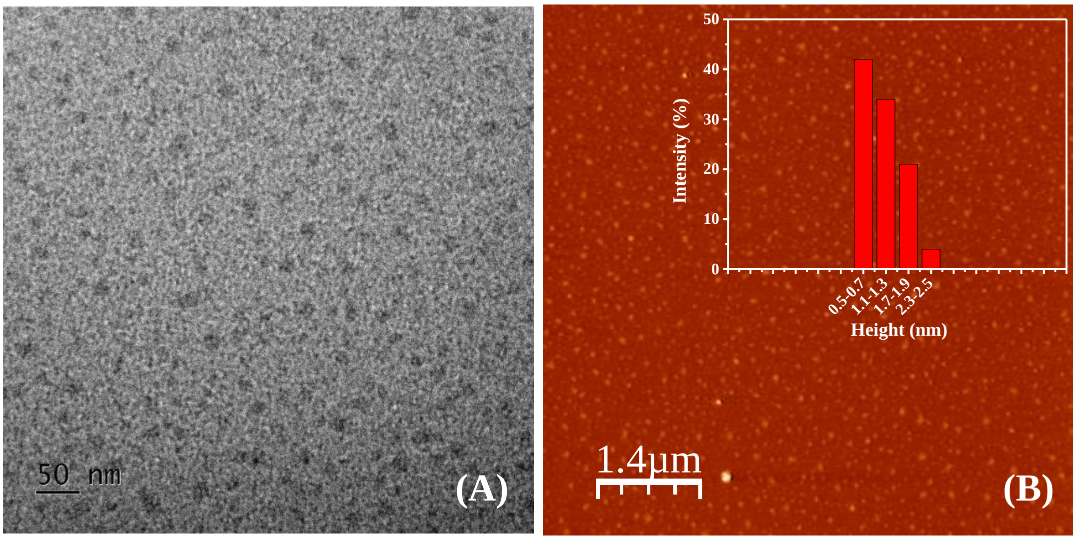

Figure 5.1. (A) TEM and (B) AFM image of SNCDs, histogram showing the size distribution is given as inset.

FTIR spectra of SNCDs and glutathione (precursor) is presented in Figure 5.2 (A). The absorption at 1730 cm^{-1} corresponds to the COOH group of SNCDs (against 1710 cm^{-1} for glutathione). A strong peak at 1668 cm^{-1} is due to the C=N vibration whereas a sharp and a strong band at 2963 cm^{-1} (absent in case of glutathione) can be attributed to the =C-H stretching vibrations. The peaks at 1403 and 805 cm^{-1} could be assigned, respectively to the C=C aromatic stretch and the

C-H bending vibration of =C–C–H. The sharp absorption at 3245 and 3340 cm^{-1} in the IR spectrum of glutathione was due to the stretching vibrations of the primary N-H groups. These features were disappeared, and a broad vibrational band at 3440 cm^{-1} due to —OH/–NH groups has appeared in case of SNCDs. The successful incorporation of S into the carbon core of SNCDs can be assumed by the disappearance of S-H vibrational feature at 2525 cm^{-1} (which was observed in case of glutathione).

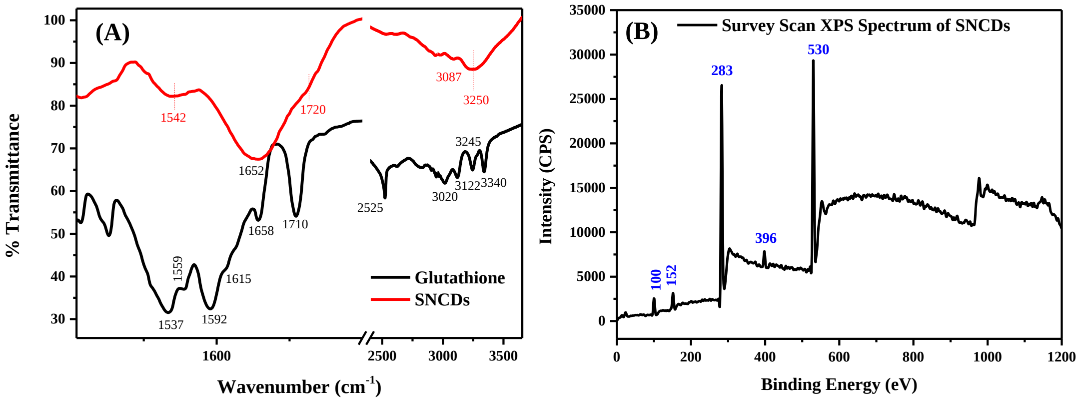

Figure 5.2. (A) FTIR spectra of SNCDs (red trace) and glutathione (black trace). (B) The survey scan XPS spectrum of SNCDs.

The XPS survey scan spectrum of SNCDs shows the presence of C, O, N and S atoms as expected (Figure 5.2 (B)). The two peaks at binding energy values 100 and 152 eV in the survey scan spectrum of SNCDs correspond to the Si 2s and Si 2p, respectively due to the SiO_2 surface used during the analysis. The deconvoluted high resolution C 1s spectrum revealed the presence of C=O (288.7 eV), C–N/C–O (286.2 eV), C–C/C=N/C–H (285..05 eV) and C=C (284.3 eV) groups (Figure 5.3 (A)). The successful incorporation of N into the carbon core was confirmed by the presence of XPS peaks corresponds to the binding energy values of graphitic, pyrrolic, pyridinic N atoms at 401.9, 400.5 and 399.5 eV, respectively (Figure 5.3 (B)). The presence of –COOH and –OH functional groups at the surface of CDs was affirmed by the high-resolution spectrum of O1s (Figure 5.3 (C)). The high-resolution S 2p peak was deconvoluted into two peaks centred at 163.5 and 164.5 eV corresponds to sulphide and thiophinic S, respectively (Figure 5.3 (D)). Based on the above spectroscopic results, a representative structure of SNCDs, comprising of carbon core with pyridinic, pyrrolic and graphitic N atoms and S in the form of thiophinic and sulphide linkages decorated with –COOH, –OH and –NH_2 functional groups at the surface was proposed (Figure 5.4). UV-visible absorption spectrum of SNCDs shows a strong absorption band ~325 nm and two shoulder bands ~370 nm and ~450 nm (Figure 5.5 (A)).

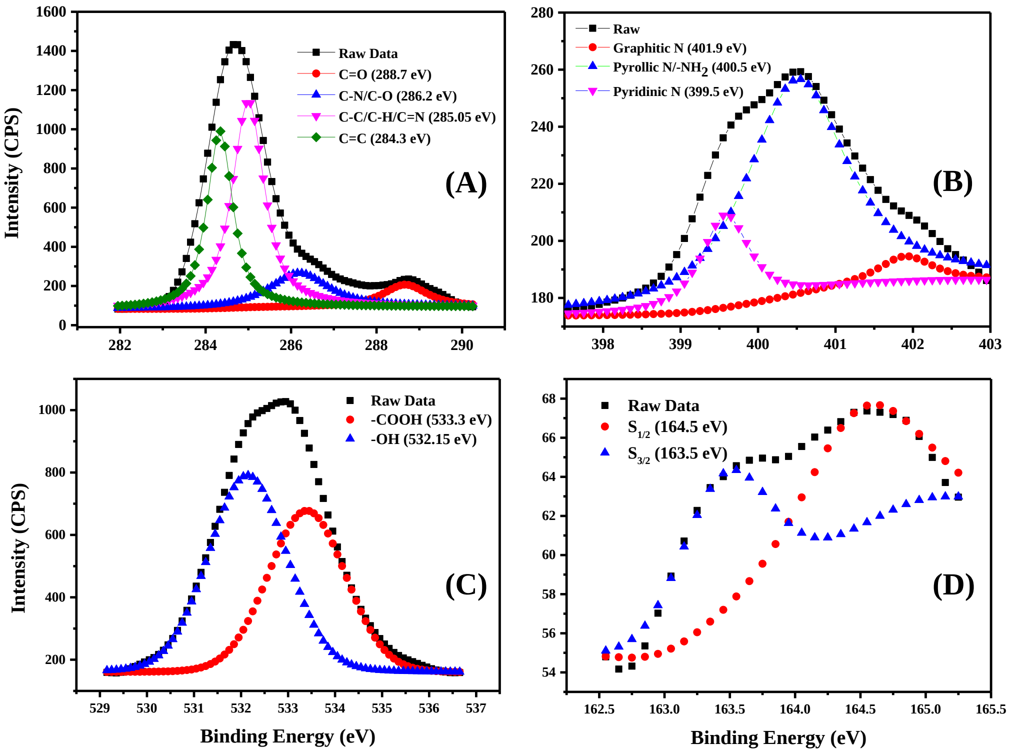

Figure 5.3. High-resolution XPS spectra of (A) C1s, (B) N1s, (C) O1s and (D) S2s peaks.

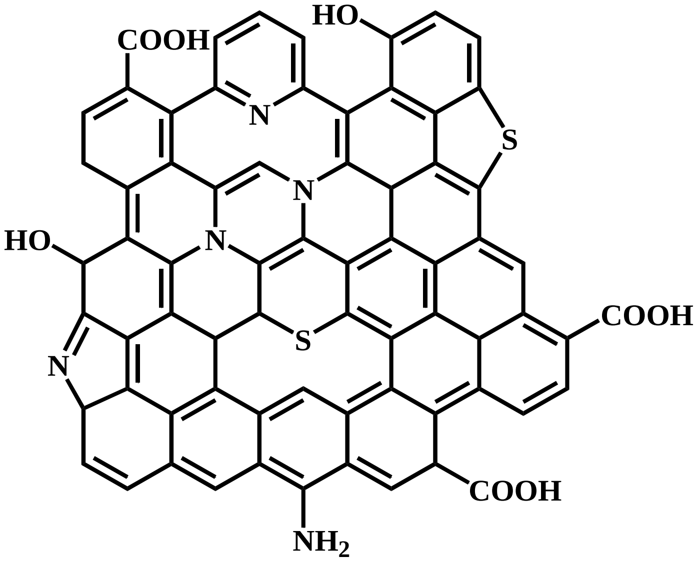

Figure 5.4. A representative structure of SNCDs proposed based on XPS and IR results.

5.3.2. pH-dependent PL response and understanding the origin of PL

The fluorescence spectra of SNCDs at different excitation wavelengths ranging from 300 to 400 nm showed interesting results. The typical emission spectra of SNCDs encompassed of three emission bands. A shoulder band around 380 nm (referred as ‘band I’) and a sharp emission around 430 nm (referred as ‘band II’) are excitation independent. An excitation-dependent emission feature observed above 430 nm (referred as ‘band III’) at ≥ 370 nm excitation (Figure 5.5 (B)). Compared to the many reported CDs, which generally manifested either excitation dependent (L. Pan et al., 2015; Sharma et al., 2016) or independent (T.-Y. Wang, Chen, Wang, Tan, & Liao, 2017) emission properties, the present CDs is atypical showing both excitation dependent and independent luminescent emission. Like emission spectrum, fluorescence excitation spectrum of SNCDs obtained for 430 nm emission wavelength was comprised of three well recognizable excitation features (inset of Figure 5.5 (B)) namely, a shoulder band at 245 nm and a strong excitation band at 430 nm and a strong and continuous excitation feature at 370 nm. The pH dependent luminescence response of band II and III specifies the involvement of the energy levels corresponding to N, S and O containing functional groups at the surface and N and S present at the core of SNCDs. Whereas, the pH independent behaviour of the band I reflect the fact that, the transition responsible for this band could be originated from SNCDs carbon core. To prove this hypothesis, we carried out a detailed photophysical studies at different pH.

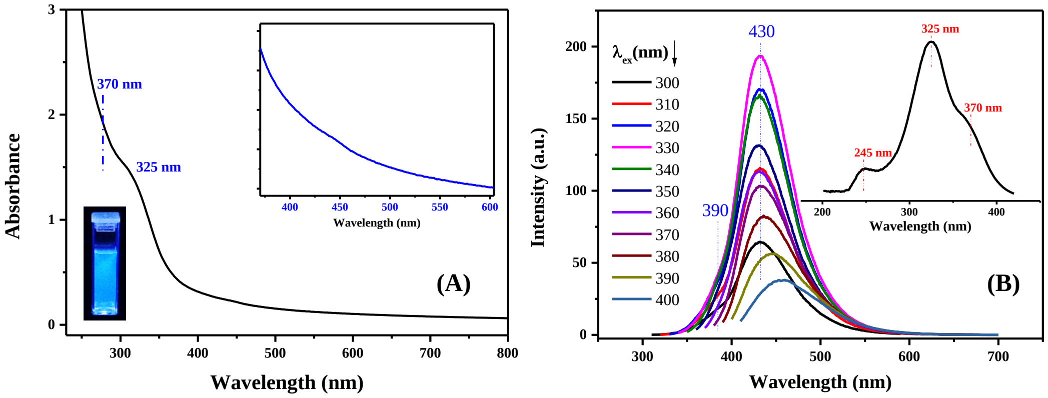

Figure 5.5 (A) UV-visible absorption spectrum of SNCDs. A magnified portion of the absorption above 380 nm and the photograph of SNCDs under UV light is given as inset. (B) Fluorescence spectra of SNCDs at different excitation wavelengths (300 to 400 nm) showing three emission bands viz., 390 nm shoulder band, emission at 430 nm and excitation dependent emission band at 430 nm and is active above 370 nm excitation. Inset is the excitation spectrum collected at 430 nm showing three excitation bands at 245, 325 and 370 nm.

The PL response of SNCDs at three pH values (2, 7 and 12) and at the different excitation wavelength (300 to 470 nm) is given in Figure 5.6. The change in the PL intensity of all three emission bands mentioned above was evaluated at different pH values. A plot of the intensity of 430 nm band with change in pH is shown in Figure 5.6 (D). The intensity variation of 390 nm band and the excitation dependent emission band versus pH of the medium is given in Figure 5.7. From these results, it is clear that the shoulder band observed at 390 nm in the emission spectrum of SNCDs has a negligible influence from the pH of the medium. However, other two bands were influenced by the pH. Both PL intensity and position of the 430 nm emission band was affected strongly by the pH.

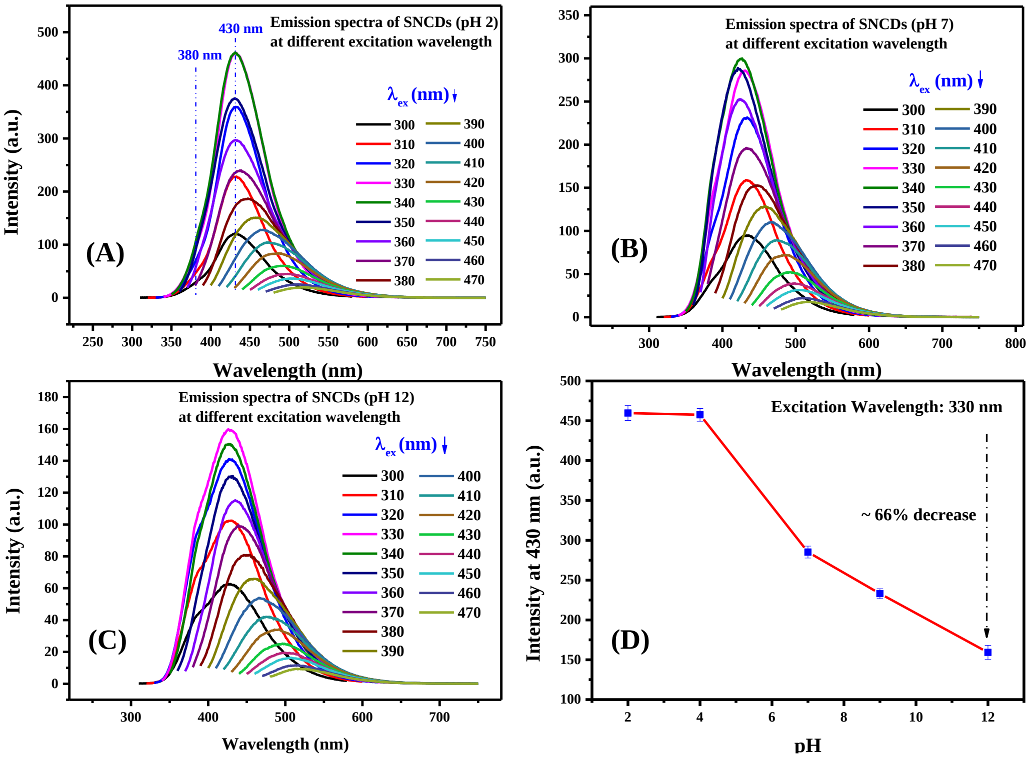

Figure 5.6. Emission spectra of SNCDs recorded at different excitation wavelengths, maintained at (A) pH 2, (B) pH 7, (C) pH 12 and (D) plot of intensity of 430 nm band verses different pH.

The PL excitation, time-resolved fluorescence and absorption measurements were carried out to shed light on the observed steady-state PL response of SNCDs at different pH conditions. UV-visible absorption features remain almost same at all pH (Figure 5.8).

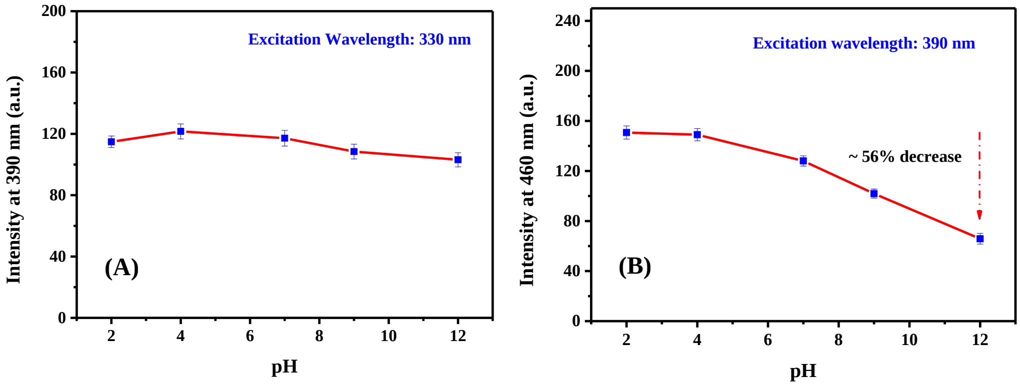

Figure 5.7. (A) Variation of PL intensity at 390 nm with pH (excitation wavelength: 330 nm) (B) Variation of intensity at 460 nm with different pH (excitation wavelength: 390 nm).

Like absorption spectra, the excitation spectra recorded at different collection wavelengths also show three excitation bands. A high energy band centered around 250 nm, a strong excitation band around 330 nm and a collection wavelength dependent low energy continuum band above 360 nm (Figure 5.9(A), (B), (C)). Similar to emission spectra, the position of the moderate energy excitation peak (330 nm) and low energy continuum (>360 nm) is highly influenced by pH of the medium whereas there is no strong influence of pH on other two excitation band. A plot of excitation intensity at 330 nm v/s pH (Figure 5.9 (D)) demonstrate the decrease of around 51% of PL intensity when the pH of the medium varied from 2 to 12.

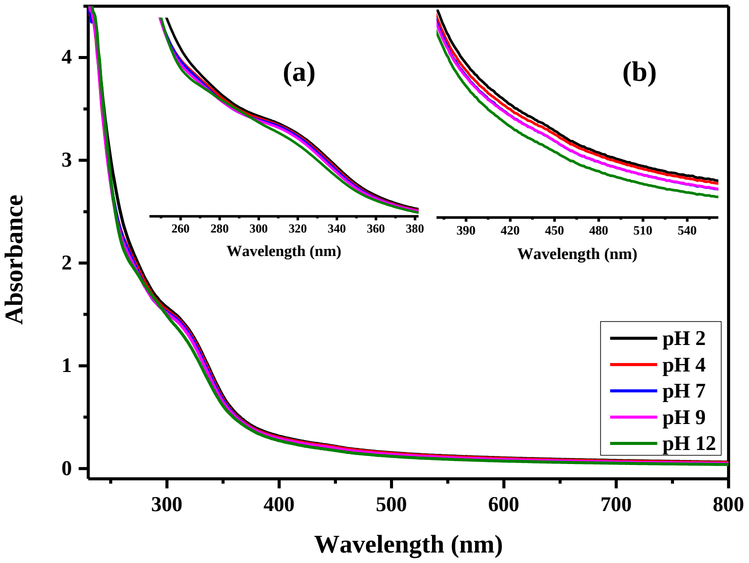

Figure 5.8. UV-visible absorption spectra of SNCDs at different pH. Figures (a) and (b) in the inset are the magnified portions of two absorption bands at 325 and 450 nm respectively.

It is reported that (Dhenadhayalan et al., 2016) the excitation feature at ~250 nm (or absorption band below 300 nm) is due to the π–π* transition of the conjugated carbon core. The excitation at this energy probably led to the ~390 nm emission (band I). Hence, the band I must be originated from the carbon core. Both peak intensity and position of the emission band was not influenced by the pH of the medium. This was supported by the fact that the carbon core is unaffected by the addition of H^+ or OH^- ions.

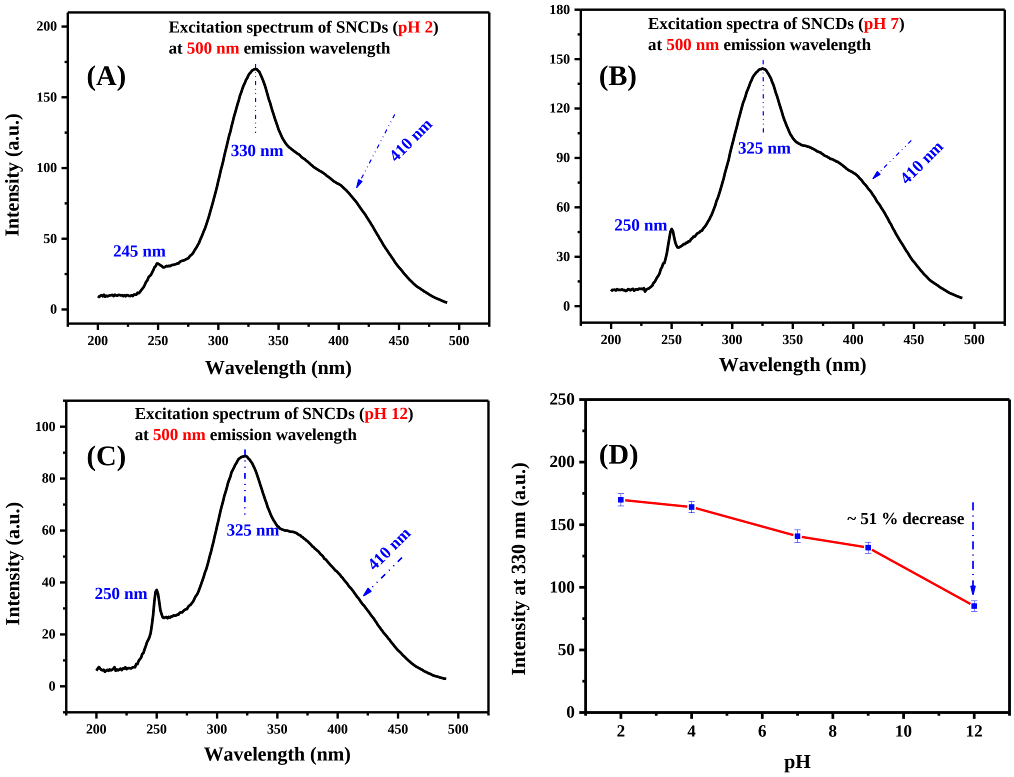

Figure 5.9. Excitation spectra of SNCDs recorded at different 500 nm emission wavelength, maintained at (A) pH 2, (B) pH 7, (C) pH 12 and (D) plot of the intensity of 330 nm band verses different pH.

We assign the strong and sharp excitation feature observed around 330 nm (or absorption band at 325 nm) to the excitation responsible for the band II found in the emission spectrum at 430 nm. This claim is supported by the fact that, both band II and its corresponding excitation peak was strongly affected by pH of the medium. The sharp excitation feature indicates the presence of a fewer number of transitions responsible for this excitation band, which in turn explains the excitation independent nature of the band II. Since the surface functional groups are expected to be affected strongly by the pH of the medium, the band II is closely related to the surface states of SNCDs. We rule out the involvement of –NH_2 for the emission at 430 as it will be affected by the protonation at acidic pH. Thus, we hypothesize that band II is due to the transition from 'n' of the edges states (S and N atoms present at core) to the π^* orbitals of emissive traps (surface functional groups stabilized C=C).

Finally, we assign the broad, and a continuous excitation band to the excitation-dependent emission band III. The broad and continuous excitation band indicates that it is composed of a large number of closely located energy states and the optical selection of these energy levels must be responsible for the strong excitation dependency of band III. The N and S atoms (present in the form of C=N and C=S) can create plenty of energy levels involving n, π and π^* orbitals depending on the chemical environment. We attribute this excitation band observed at the low energy portion of the excitation spectrum of SNCDs could be due to the transition of electrons from ‘n’ orbitals of C=N/C=S to the corresponding π^* orbitals (edge states). Since the energy gap between ‘n’ and π^* orbitals of C=N and C=S is influenced by the nature of surface functional groups and the aromatic core surrounding these edges, many discrete set of energy levels of slight difference is possible. The excitation and subsequent radiative recombination might have led to excitation dependent band III. The possibility of protonation and deprotonation of these heteroatoms explains the variation of the PL intensity of band III (around 56% decrease in PL intensity for a pH change 2 to 12) when the pH of the medium is altered. Based on the above conjecture, an energy level diagram demonstrating the origin of PL emission of SNCDs at various excitation wavelength has been given in Figure 5.10. A representative structure of SNCDs with core, surface, and edge states is given in Figure 5.11.

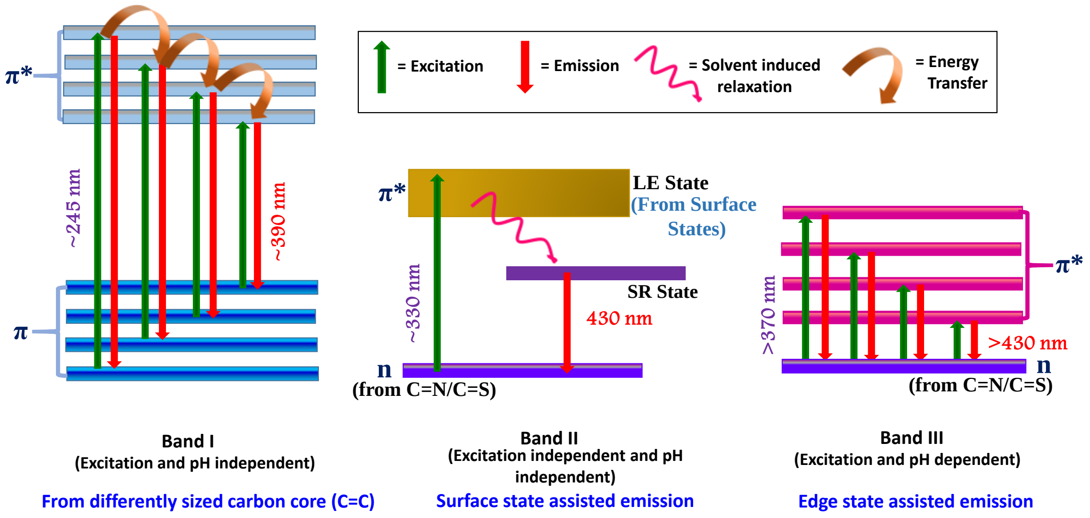

Figure 5.10. Energy level diagram of SNCDs demonstrating the origin of luminescence.

The Stokes shifts in all three bands viz. band I, II and III is explained as follows. The substantial shift (>130 nm) in the band I can be attributed to the presence of differently sized carbon core (as observed from TEM size distribution).

The emission from the larger core is assigned to the energy transfer/resonant reabsorption from small dots. The band II, manifested with a Stokes shift of ~100 nm can be easily explained by the solvent-induced relaxation of the excited fluorophore. From a locally excited state (LE state), the fluorophore relaxes to the low energy solvent induced relaxation state (SR state). Then subsequent recombination with ground state hole results in the emission at 430 nm. Because, the LE state is controlled by the polar surface functional groups which can interact strongly with surrounding water molecules before relaxing to the ground state. This solvent-induced relaxation is the most probable explanation for the observed significant Stokes shift in case of band II. Finally, the direct recombination of excited state electrons from π* orbitals of the edge states to the corresponding 'n' orbitals without involving an intersystem crossing or energy transfer would be the most likely reason for small Stokes shift in case of band III (Figure 5.10).

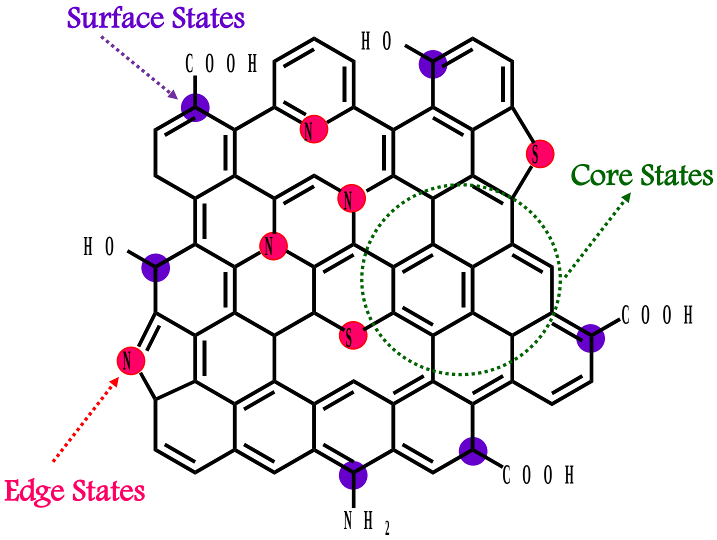

Figure 5.11. Various emissive states in SNCDs.

The decrease in PL, with pH change from acidic to neutral, could be due to the electron transfer from 'n' orbital of–NH_2 to the ground state of excited fluorophore (Figure 5.12). Such photoinduced electron transfer involving –NH_2, -OH groups leading to the luminescence quenching of fluorophore is commonly seen in case of organic fluorophores. Further decrease of luminescence in basic pH is explained as follows. At basic pH, most of the COOH groups are deprotonated. Due to the high electron withdrawing propensity of COO^-, a decrease in luminescence is envisaged as electron withdrawing groups are expected to destabilize the photo-excited state by removing the excited state electrons.

Figure 5.12. Schematic representation the PL quenching of SNCDs at neutral pH.

To support the above observations, time-resolved emission spectra of SNCDs at multiple collection wavelengths has been measured (Table 5.1). Time resolved PL decay at all collection wavelengths (390, 430 and 500 nm) and at all pH conditions is a bi-exponential decay. The shorter component was ranging from 3.6 – 5.4 ns and longer component was in 11.3 – 12.5 ns. The longer component can be attributed to the lifetime corresponds to band II emission, whereas shorter component is assigned to the band I/III. This argument is supported by the fact that, the amplitude of longer component at all pH conditions is highest when the collection wavelength was fixed at 430 nm, whereas the contribution from a shorter component is higher at other two collection wavelengths (390 and 500 nm). Also, when collection wavelength was fixed at 430 nm, the amplitude of the longer component was found to decrease continuously with the increase of pH.

Table 5.1. Time-resolved fluorescence results of SNCDs at different pH conditions. τ_1 and τ_2 are the lifetime components and A_1 and A_2 are the corresponding amplitudes, respectively. Lifetime fitting has been done using a data analysis software by keeping values of χ^2 <1.3 (best fit).

		τ_1 (ns)	A_1	τ_2 (ns)	A_2
pH 2	390	3.7	26.94	11.6	73.06
	430	4.7	8.48	11.8	91.52
	500	4.3	14.83	11.7	85.17
pH 4	390	4.3	21.57	11.3	78.43
	430	4.2	11.52	11.6	88.48
	500	4.3	18.13	11.9	81.87
pH 7	390	3.6	32.92	11.4	67.08
	430	4.9	21.83	12.1	78.17
	500	4.4	22.63	11.8	77.37
pH 9	390	4.0	18.93	11.7	81.07
	430	5.3	13.13	12.1	86.87
	500	5.4	20.28	12.5	79.72
pH 12	390	3.8	36.72	11.7	63.28
	430	3.6	28.18	11.8	71.82
	500	3.8	29.75	11.8	70.25

We conducted FTIR investigations to understand the structural changes at different pH. The asymmetric and symmetric stretching vibration of COO^- at 1590 cm^{-1} and 1465 cm^{-1}, respectively are absent in the case of SNCDs at acidic pH whereas strong shoulder band is observed in basic and neutral pH. This observation indicates the deprotonation of carboxyl groups at basic pH. A sharp peak at 1730 cm^{-1} correspond to the stretching vibration of the >C=O group of carboxyl was found at acidic pH, whereas a weak band could be discerned at neutral and basic pH ranges. A strong vibration at 1260 cm^{-1} was observed for the C–O stretching in acidic pH. At acidic pH, an additional peak at 1300 cm^{-1} was observed due to the C–O of carboxyl group. The peak at 1668 and 1632 cm^{-1}, corresponds to C=N and C=C groups respectively, which are present at all pH conditions. Peaks at 1403 cm-

1 and 805 cm^{-1}, assigned to the C=C aromatic stretch and =C-H bend, respectively. The absence of S-H stretching vibration at 2525 cm^{-1} at all pH implicates the successful incorporation of S at the carbon core of SNCDs (Figure 5.13).

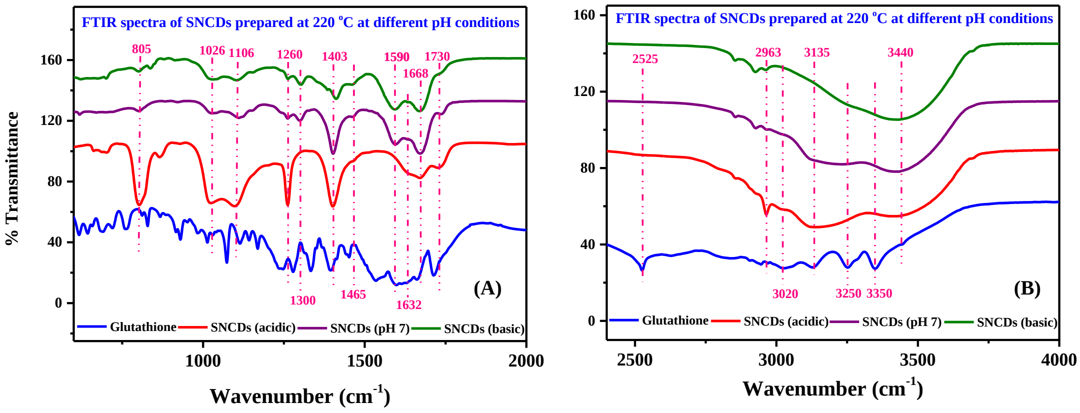

Figure 5.13. FTIR spectra of SNCDs at acidic (red trace), neutral (violet trace) and basic (green trace) pH. For comparison, IR spectrum of glutathione is also included (blue trace). From (A) 600 to 2000 cm^{-1} and (B) 2400 to 4000 cm^{-1}.

5.3.3. Chromium (VI) Sensor

Figure 5.14 represents the fluorescence quenching based sensing strategy for Cr(VI) using SNCDs–diphenylcarbazide (DPC) dyad. DPC has used an analyte specific molecule. The detection was done using a solution of the SNCDs-DPC solution at pH 2. The emission of SNCDs was not affected by the DPC. During the detection step, quenching was observed in the presence of Cr(VI). The mechanism was attributed to the combined FRET and IFE, which are activated due to the interaction of Cr(VI) with DPC. Details on the mechanism of PL quenching by Cr(VI) will be discussed in a forthcoming section.

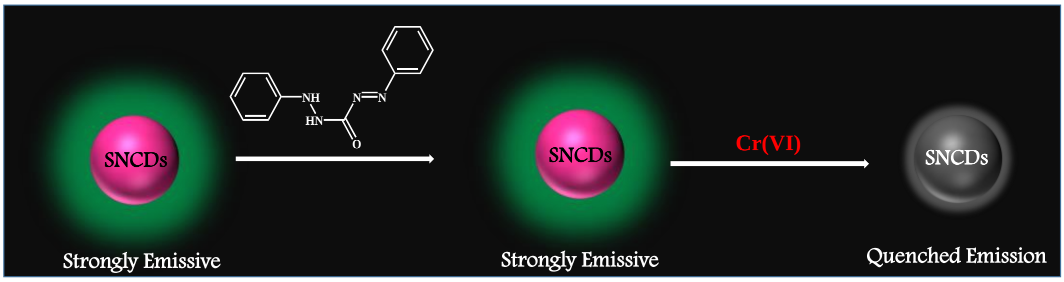

Figure 5.14. Schematic representation of Cr(VI) sensing using SNCDs.

The decrease in the PL intensity of SNCDs-DPC mixture (the sensor solution) was proportional to the amount of the Cr(VI) added (Figure 5.15 (A). A plot of the emission intensity v/s the concentration of Cr(VI) is a curve indicating the presence of multiple quenching mechanisms (Figure 5.15 (B). The minimum concentration of the quencher at which a recognizable change in the PL emission of SNCDs, the limit of detection (LOD) was 5 nM.

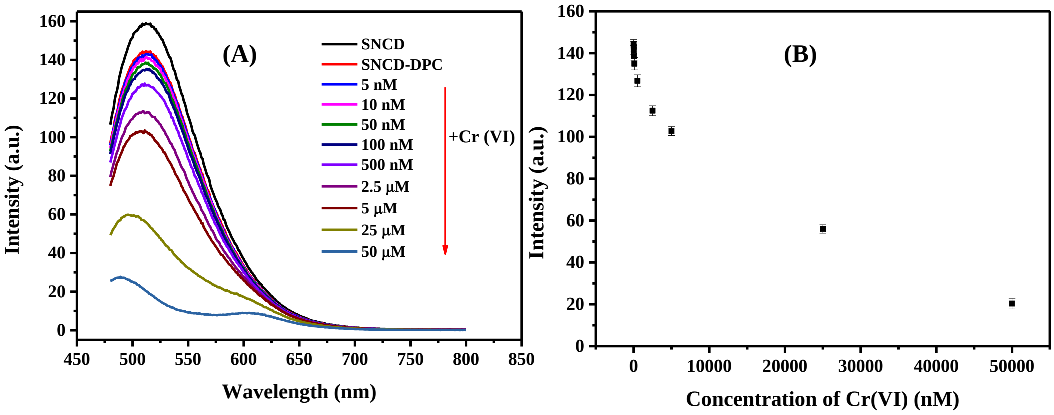

Figure 5.15. (A) Fluorescence spectra of SNCDs-DPC at different Cr(VI) concentrations. For comparison, PL spectra of pure SNCDs and the SNCDs-DPC mixture was also given (red trace). Excitation wavelength: 470 nm. (B) The plot of intensity at 500 nm versus the concentration of Cr(VI).

Specificity of SNCDs-DPC sensor solution was tested using various competing analytes such as metal ions and some commonly used organic molecules. As can be seen in Figure 5.16, the response from other analytes was least compared to the response observed from Cr(VI), which demonstrates the effectiveness of the present system as Cr(VI) sensor.

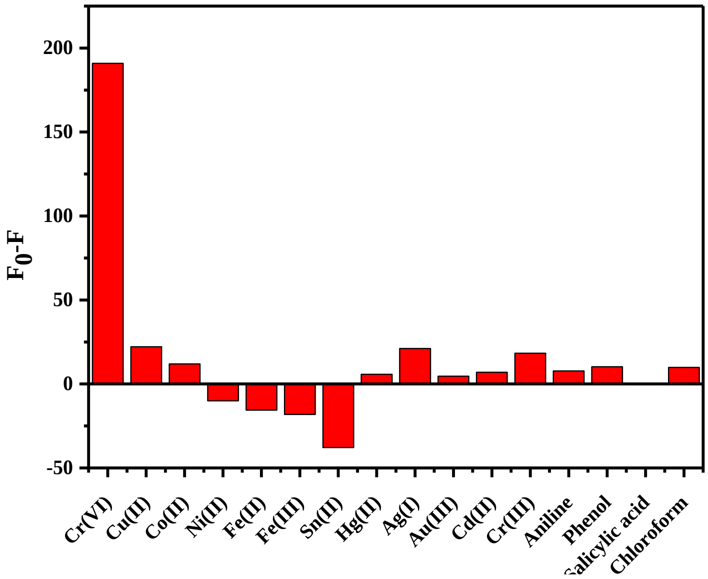

Figure 5.16. Selectivity studies. The concentration of all the analytes was kept at 50 μM (the highest concentration of Cr(VI) used).

UV-visible and time-resolved fluorescence analysis were carried out to understand the mechanism of quenching. The absorption features of both SNCDs and DPC was not affected due to the presence of SNCDs (the pH was ~2) (Figure 5.17 (A)). This observation reflects that there was no intereaction at electronic energy levels. On the contrary, strong absorption bands in the UV-visible spectrum have emerged, in the presence of Cr(VI) (Figure 5.17 (B)). These absorption bands have sufficient overlap with the emission of SNCDs. Such spectral overlap results in FRET-based quenching to operate and is the reason for decrease in PL emission of SNCDs in the presence of Cr(VI). The spectral overlap between the newly emerged band and emission spectrum of SNCDs (excited at 470 nm) is shown in Figure 5.17 (C). In addition to the spectral overlap, which is responsible for FRET, there exists a strong absorption background at 470nm (the wavelength at which SNCDs was excited) (Figure 5.17 (D)). This indicates that apart from FRET, primary IFE may also be responsible for the quenching SNCDs' emission. The results of time-resolved fluorescence spectra support our postulate. Both SNCDs and SNCDs–DPC solutions show a bi-exponential decay with shorter component at ~5 ns and a longer component at ~9 ns (excitation: 451 nm, collection: 510 nm). But in case of SNCDs–DPC–Cr(VI), a new ultrafast component with the lifetime of 0.32 ns have emerged. This component could be a non-radiative path, arises due to the excited state energy transfer from donor to acceptor. This pathway is responsible for the quenching of SNCDs emission via FRET (Table 5.2).

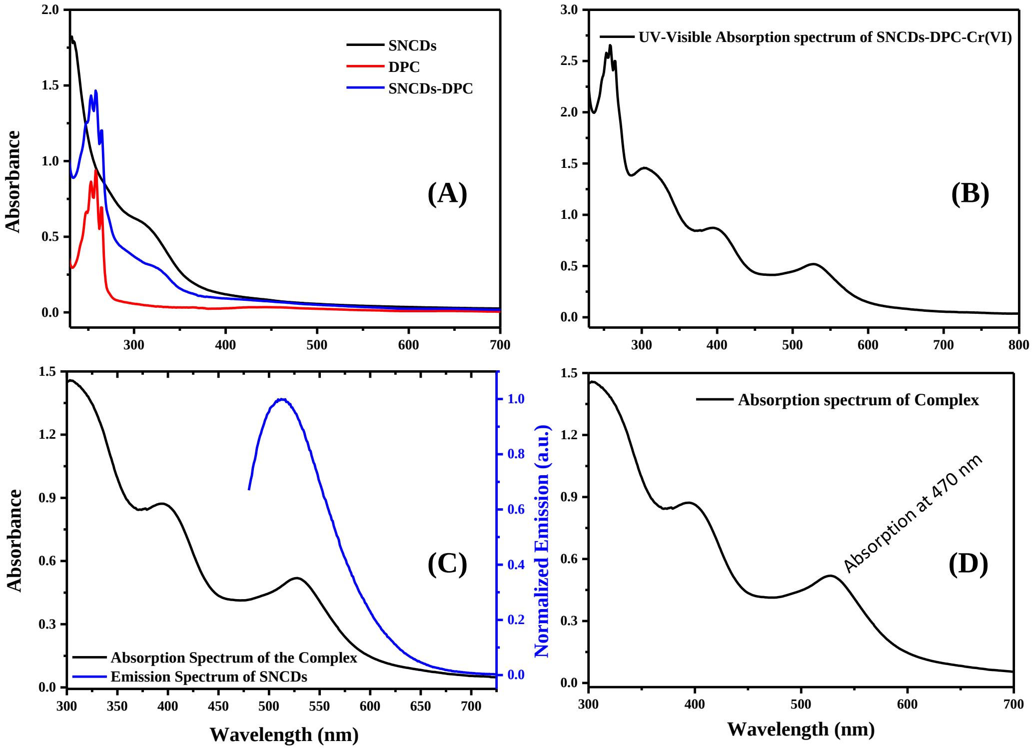

Figure 5.17. (A) UV-visible absorption spectra of SNCDs (black trace), DPC (red trace) and SNCDs-DPC (blue trace). (B) UV-visible absorption spectrum of SNCDs-DPC-Cr(VI). (C) Spectral overlap (D) Absorption spectrum of SNCDs-DPC-Cr (VI), to show the absorption of complex at 470 nm, in turn indicating the possibility of primary IFE.

Table 5.2. Time resolved fluorescence results of SNCDs, SNCDs-DPC and SNCDs-DPC-Cr(VI).

λ_{ex}: 451 nm	τ_1 (ns)	A_1 (%)	τ_2 (ns)	A_2 (%)	τ_3 (ns)	A_3 (%)
SNCDs	5..00	44.14	9.35	55..86	-	-
SNCDs-DPC	4.99	49.43	8.74	50.57	-	-
SNCDs-DPC-Cr(VI)	3.22	41.27	12.77	11.15	0.32	47.58

The new absorption band observed in presence of Cr(VI) for SNCDs–DPC solution is due to the complexation of Cr(VI) with DPC. There was an ample number of reports, which deals with the DPC–Cr(VI) complex. The strong absorption of this complex at the emission and excitation wavelength of SNCDs at acidic pH is responsible for the PL quenching of SNCDs and in turn operate during the selective detection of Cr (VI).

5.4. Conclusions

In conclusion, we demonstrated the hydrothermal synthesis of SNCDs using glutathione as the precursor for both carbon and dopants. The atypical PL emission behaviour of SNCDs, which shows both excitations dependent and independent PL response was unraveled by the detailed photophysical studies at different pH. Fluorescence emission, excitation, lifetime and UV-visible absorption spectra at five different pH demonstrate the presence of multiple energy states in SNCDs viz. core, surface and edge states. A comprehensive energy level diagram, which demonstrates the origin of PL in SNCDs was proposed based on the results. Although, further studies involving more advanced analytical tools may be required to completely understand the mechanism of photoluminescence in CDs and related luminophores, the work presented here could be a small step towards this goal. The utilization of SNCDs has been demonstrated for the selective quenching based detection of Cr(VI). The PL quenching is surmised to arise from FRET as well as IFE. The limit of detection of the present sensor was found to be 5 nM with a dynamic range, 2.5 - 50 μM.

CHAPTER 6

SYNTHESIS OF ORGANOPHILIC CARBON DOTS AND ITS APPLICATION IN SCREENING OF NITROAROMATICS

Carbon dots (CDs) are an attractive alternative to the toxic semiconductor based photoluminescent materials. However, due to the presence of a plethora of carboxyl group at the surface, CDs have a weak solubility in polar solvents, which hinders their technological possibilities. Here we demonstrate the synthesis of CDs having high solubility in non-polar environment referred as 'organophilic CDs' (OCDs) by a hydrothermal synthetic route using cyclohexane as a carbon source as well as dispersion media. The OCDs was characterized in detail using spectroscopic and microscopic tools. Further, we utilized OCDs for the selective sensing of trinitrophenol (TNP) over other structurally similar nitroaromatics (NAs), with a detection limit of ~900 nM. Detailed photophysical studies to understand the mechanism of PL quenching of OCDs by NAs were carried out. The emission of OCDs was quenched by primary inner filter effect (IFE), happens by the absorbance of NAs at the excitation wavelength of OCDs.

6.1. Introduction

Diverse synthetic strategies, encompassing top-down and bottom-up routes such as electrochemical synthesis, laser ablation, pyrolysis/carbonization of organic precursors, microwave and ultrasound assisted synthesis, etc. have been demonstrated for CDs. (Lim, Shen, & Gao, 2015; Zhang & Yu, 2016) Lab chemicals as well as naturally available materials were used as carbon sources and dopants to achieve CDs. (Ahn & Manthiram, 2017; Lim et al., 2015; Ramanan et al., 2016) During synthesis of CDs, the transformation of O and N containing precursors leads to the inception of abundant polar functional groups. The resulting CDs are 'organophobic'. Hence, any attempt to alter the nature of surface functional groups to tune the solubility of CDs is always welcome.

Nitroaromatics (NAs) are a class of organic compounds, which are extensively exploited in explosive devices and as precursors for some industrial products. On account of homeland security, environmental screening and militancy, a number of detection strategies such as electrochemical, optical and mass spectrometry based sensors were employed to identify the NAs. (Germain & Knapp, 2009; Idros et al., 2015; Song & Cooks, 2006; H. Wang et al., 2012; Yew, Ambrosi, & Pumera, 2016) Among these tools, optical sensors, in particular fluorescence based sensors are highly advantageous due to its high signal throughput, robustness and specificity. Wide range of fluorophores, particularly, fluorescent polymers (Duniho et al., 2014), metal organic frameworks,(G.-Y. Wang et al., 2014) fluorescent semiconductor QDs (Peveler, Roldan, Hollingsworth, Porter, & Parkin, 2016) and organic small molecule fluorophores (Kartha, Sandeep, Praveen, & Ajayaghosh, 2015; Stringer, Gangopadhyay, & Grant, 2010) have been scrutinized as fluorescence signalling agents for NAs. Although a significant effort has been paid to detect these molecules, the task is cumbersome due to the similarity in the chemical structure and physical properties of these NAs.

In general, NAs alter the fluorescent output of a fluorophore by electron transfer mechanism due to their high electron withdrawing propensity. (Campos et al., 2016; Yong Wang & Ni, 2014) In some cases, the energy transfer from the fluorophore to NAs are considered to be the dominant quenching mechanism as well. (Ying Wang, La, Bruckner, & Lei, 2012) Due to the strong absorption of NAs at excitation and emission wavelength of many fluorophores, the reduction in fluorescence intensity takes place as a result of inner filter effect (IFE). Hence, a comprehensive study is always imperative to fathom the underlying fluorescence sensing mechanism in these class of analytes.

The present chapter discuss the synthesis of CDs which is having high solubility in non-polar organic phase, referred as ‘organophilic CDs (OCDs)’, by solvothermal synthetic route. Cyclohexane was used as a carbon source as well as dispersion media. This is the one of the less commonly available reports in which synthesis of CDs having high solubility in non-polar phase owing to the lessened polar carboxyl group on the CDs surface is presented. A detailed fluorescence response of OCDs towards various NAs such as 2,4,6-trinitrophenol (TNP), 2,4-

dinitrophenol (DNP), o-nitrophenol (ONP), 2,4-dinitrotoluene (DNT), o-nitrotoluene (ONT) and nitrobenzene (NB) has been examined. It was observed that luminescence quenching of OCDs by TNP was the highest, as established by the selectivity factor (SF). Hence the present sensor can be used as a selective sensor for TNP over other NAs. We performed detailed photophysical studies to understand the mechanism of photoluminescence (PL) quenching of OCDs by NAs. The main pathway of quenching is IFE, which happens due to the absorption of NAs at the excitation wavelength of OCDs (350 nm), contrary to the most commonly found electron transfer based quenching.

6.2. Experimental Section

6.2.1. Synthesis of OCDs

15 mL of cyclohexane was taken in a Teflon (22 mL) lined autoclave and kept at solvothermal reaction conditions. The bright blue emitting OCDs obtained by the synthesis was purified and characterized. The purification of the OCDs was accomplished by using silica column chromatographic technique. The solution of OCDs in cyclohexane is passed through the silica bed and the various fractions generated by changing the mobile phase polarity. The purity, in terms of homogeneous size distribution was analysed by the transmission electron microscopy (TEM) images. The optimization of solvothermal synthesis parameters such as time and temperature was done by carrying out the reaction at different temperatures (140, 180, 220, 250 and 300 °C) and at different time intervals (1, 4, 8, 12, 24 h). The emission spectra of the product were recorded at different excitation wavelength without further dilution. Best emission was observed for the sample prepared at 220 °C and for 12 h. We used the OCDs obtained at this reaction condition after purification for our studies.

6.2.2. Screening of NAs

We added various concentrations of NAs dissolved in 1:1 mixture of cyclohexane and acetone to the solution of OCDs in cyclohexane. NAs used in the present study are, TNP, DNP, ONP, DNT, ONT and NB. The fluorescence spectra of OCDs in the absence and presence of various concentrations of NAs were then recorded at 350 nm excitation wavelength. A Stern-Volmer (S-V) plot was constructed using the emission intensity at 420 nm against various concentrations of NAs.

The slope of the plot was the ‘Stern-Volmer’ quenching constant and was represented as K_{sv} according to the equation, $F_0/F = 1 + [Q]K_{sv}$. Where, F_0 and F are the PL intensity of OCDs before and after the addition of NAs, respectively. $[Q]$ is the concentration of quencher. The value of K_{sv} was used for calculating the selectivity factor (SF); $SF= K_{sv(analyte)} /K_{sv(TNP)}$. The value of SF was used for evaluating the extent of selectivity towards TNP detection.

6.2.3. Quenching mechanism

The possibility of formation of ground state complex between OCDs and NAs were analysed using UV-visible absorption spectra. The concentration of various NAs in the OCDs solution was kept constant. To understand the presence of excited state electron transfer quenching, the OCDs was titrated against various NAs concentration and the fluorescence spectra were recorded at 440 nm excitation, the wavelength at which there is a minimal absorption from NAs. The S-V plot was constructed using this data. Time resolved fluorescence analysis of OCDs at different NAs concentrations (20, 40 and 60 µM) was performed using time-correlated single photon counting (TCSPC) unit.

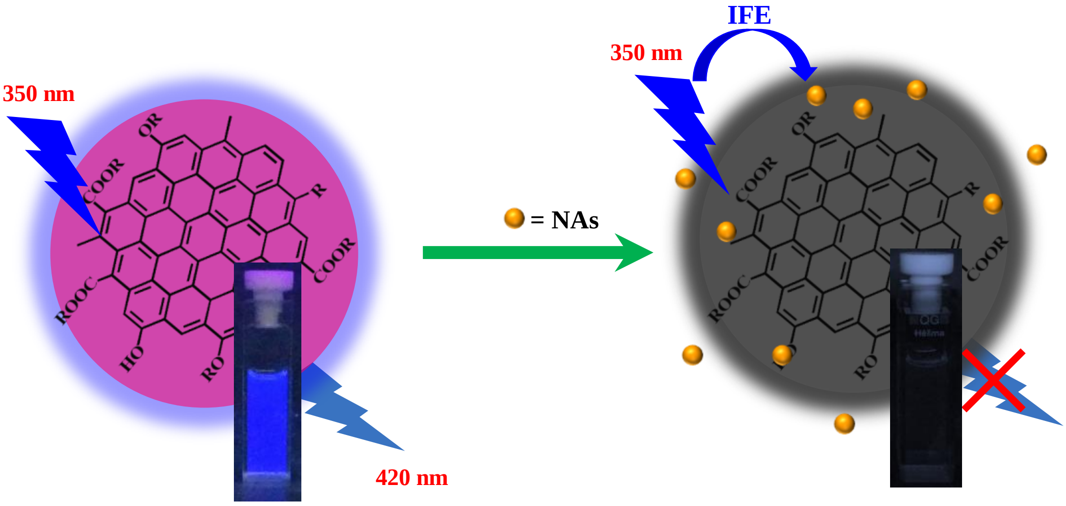

Figure 6.1. Representation of quenching of OCDs by NAs via IFE.

6.3. Results and Discussion

6.3.1. Characterization of OCDs

Ultra-small, uniformly sized, spherical particles of 3–4 nm is visible in the TEM images of the purified fraction of OCDs (Figure 6.2(A) and Figure 6.2 (B)). The OCDs were well dispersed in cyclohexane and remains stable even after several months of preparation. Addition of the polar solvents such as water, acetonitrile, ethanol, etc. to this solution unable to phase separate CDs, indicating the high non-polar nature of OCDs. Chemical nature of OCDs were understood by FTIR spectroscopy, XPS spectroscopy and ^{13}C nuclear magnetic resonance (^{13}C-NMR) spectroscopy. Vibrational signatures (see Figure 6.2 (C)) observed at 2962 cm^{-1} and 1412 cm^{-1} corresponds to =C–H stretching and bending mode of OCDs, respectively. (Nie et al., 2014) The –C=C– vibrational feature was observed at 1630 cm^{-1}, whereas stretching vibration of >C=O groups was discerned at 1710 cm^{-1}. The presence of ester/ether/epoxy groups, which imparts hydrophobicity to the OCDs was confirmed by the strong symmetric and asymmetric vibrations of C–O–C at 1022, 1098 cm^{-1}, respectively. The C–O stretching vibration was observed at 1263 cm^{-1}. The peak at 3430 cm^{-1} was attributed to the stretching vibration of –OH (Figure 6.2 (C)).

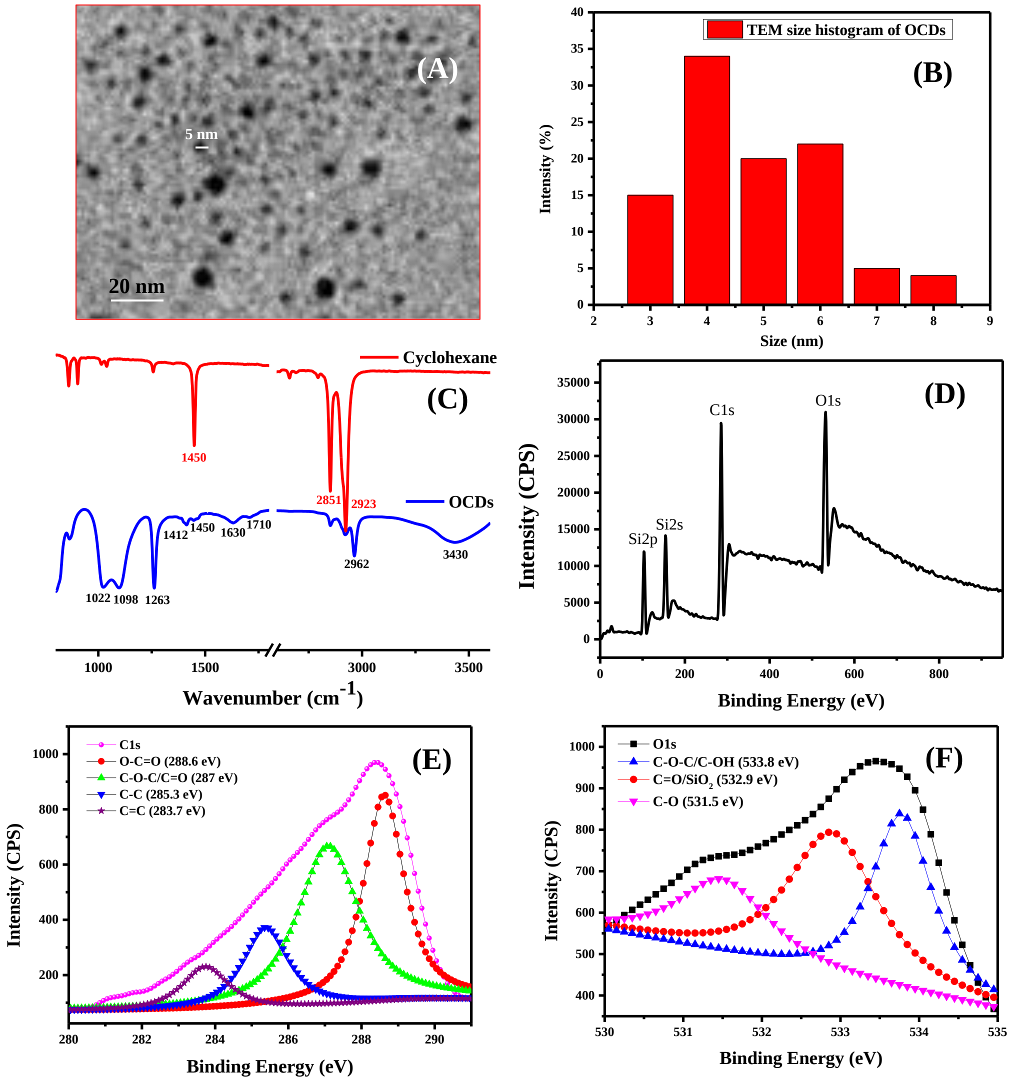

Figure 6.2. TEM image (A) and the corresponding size histogram (B). FTIR spectrum of OCDs (blue trace and cyclohexane (red trace) (C). The survey scan XPS spectrum of OCDs (D). High resolution XPS spectrum of C1s (E) and O1s (F).

Survey scan XPS shows C1s and O1s peaks at binding energy values of 285 and 532 eV, respectively (Figure 6.2 (D)). High resolution XPS spectrum of C1s peak was deconvoluted into four peaks viz. 283.7, 285.3, 287.0 and 288.6 eV, which was assigned to C=C, C–C, C–O–C/C=O and O–C=O, respectively (Figure 6.2 (E)). O1s high resolution spectrum supports the existence of C–O–C, C–OH, C=O and C–O linkages in OCDs (Figure 6.2 (F)). Further, ^{13}C NMR spectrum confirmed the presence of carbonyl carbon of ester (δ 171 and 178 ppm), aromatic nucleus (δ 157, 142, 127 and 114 ppm), sp^3 hybridized C that are directly bonded to O atoms (δ 57 to 73 ppm) and that are away from O atoms (δ 23 to 32 ppm) (Figure 6.3). All these observations confirm the formation of CDs with sp^2 hybridized aromatic nucleus feathered with an ample number of ester, ether, alkyl and hydroxyl functional groups. These groups explain the organophilic nature of the present CDs, contrary to many reports in which aqueous solubility is induced by the presence of highly polar carboxyl groups. Based on the above spectroscopic details a representative structure for OCDs is proposed and given in Figure 6.4.

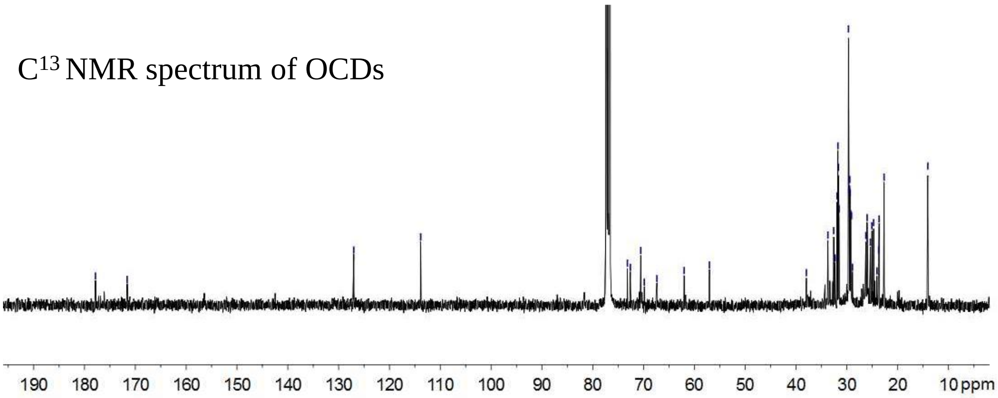

Figure 6.3. C^{13} NMR spectrum of OCDs. The strong peak around 78 ppm is due to the solvent ($CHCl_3$) and that of 12 ppm is due to the reference (TMS) used.

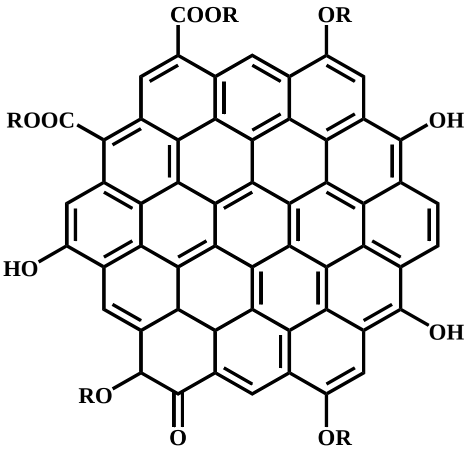

Figure 6.4. A representative structure of OCDs.

UV-visible absorption spectrum of OCDs exhibits strong absorption features corresponds to π–π^* absorption from sp^2 hybridized core (235 nm) and n–π^* absorption from C=O (280 nm) (Figure 6.5 (A)). (Nie et al., 2014) These electronic absorptions were absent in the case of cyclohexane. The PL emission spectra of CDs recorded at various excitation wavelengths, shows excitation dependent emission, typical of most of the CDs, which is attributed to the size heterogeneity, defects and the zigzag states (Figure 6.5 (B)). (Baker & Baker, 2010; Youfu Wang & Hu, 2014) Like emission spectra, excitation spectra of CDs, recorded at various collection wavelengths also depicts the emission wavelength dependent excitation, further demonstrating the contribution of various energy levels towards PL emission of CDs (figure 6.5 (C)). The decay profile obtained by recording the time-resolved fluorescence spectrum of OCDs can be best fitted by tri-exponential equation ($\chi^2 \approx 1$) verifies the presence of multiple emissive states in OCDs (Figure 6.5 (D)).

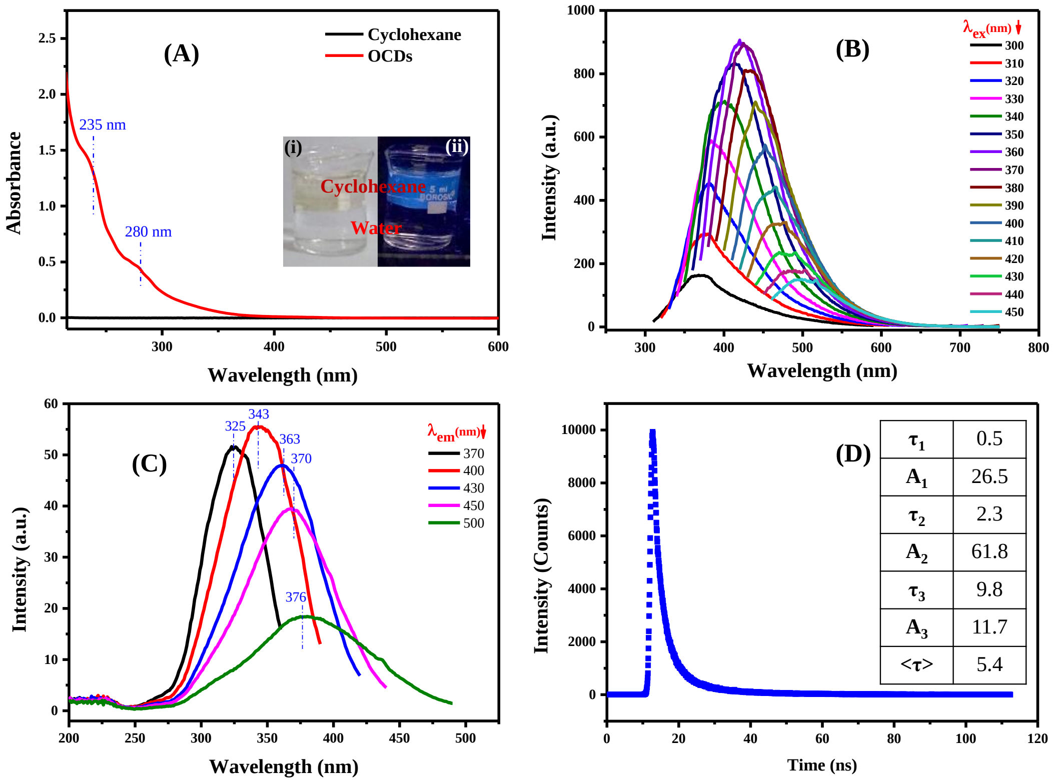

τ_1	0.5
A_1	26.5
τ_2	2.3
A_2	61.8
τ_3	9.8
A_3	11.7
$<\tau>$	5.4

Figure 6.5 (A) UV-visible absorption spectrum of OCDs (red trace) and that of cyclohexane (black trace). *Inset:* Photograph of OCDs in cyclohexane over an aqueous phase taken in (i) visible and (ii) UV light. This indicates that OCDs are dispersed in the organic phase. (B) PL spectra collected at different excitation wavelengths which demonstrate the excitation dependent emission profile. (C) Excitation spectra at different emission wavelengths. (D) Time-resolved fluorescence spectrum of OCDs (inset: lifetime results).

6.3.2. Screening of nitroaromatics

Nitroaromatics (NAs) such as nitrotoluenes and nitrophenols are the potent explosives and environmental contaminants. Due to the similarity in chemical structures and physical properties, selective detection of these NAs was always a challenge. We demonstrated a selective sensing of TNP using OCDs as a fluorophore. This is done by titrating OCDs against various concentrations of structurally similar NAs such as TNP, DNP, ONP, DNT, ONT and NB. An S-V (Stern-Volmer) plot was then constructed for each of the above analytes and the corresponding Stern-Volmer quenching constant (K_{sv}) was calculated.

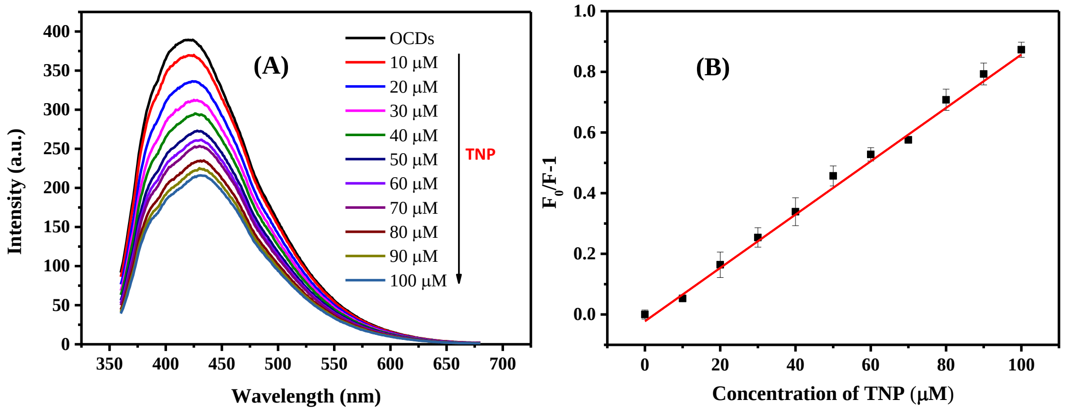

Figure 6.6. (A) PL spectra of OCDs at different TNP concentrations. (B) The stern-volmer plot, where F_0 and F represent the PL emission before and after the addition of TNP, respectively. Error bar in the S-V plot indicates the standard deviation of 3 different experiments.

From figure 6.6 (A), it is obvious that the introduction of TNP led to the fluorescence quenching of OCD solution. The quenching was linear with concentration of TNP as demonstrated by corresponding S-V plot in Figure 6.6 (B). As in the case of TNP, the same experiments were performed for other NAs and the corresponding S-V plots were plotted (Figure 6.7). The Slope (K_{sv}), R^2 and intercept obtained from the S-V plot for all these NAs have been given in Table 6.1. It is clear from the Table that, K_{sv} for TNP (8.9×10^3 M^{-1}) is much higher than that of other NAs (TNP>>DNP>DNT> ONP>NB>ONT). The ratio of K_{sv} for TNP to that of other analytes is referred as ‘selectivity factor (SF)’, which was used for calculating the selectivity of OCDs towards TNP detection. The values of SF for TNP, DNP, DNT, ONP, ONT and NB were 1.0, 0.3, 0.12, 0.09, 0.05 and 0.07, respectively (Table 6.1). The large value of SF for TNP as compared to that for other analytes display the selectivity of OCDs towards TNP detection.

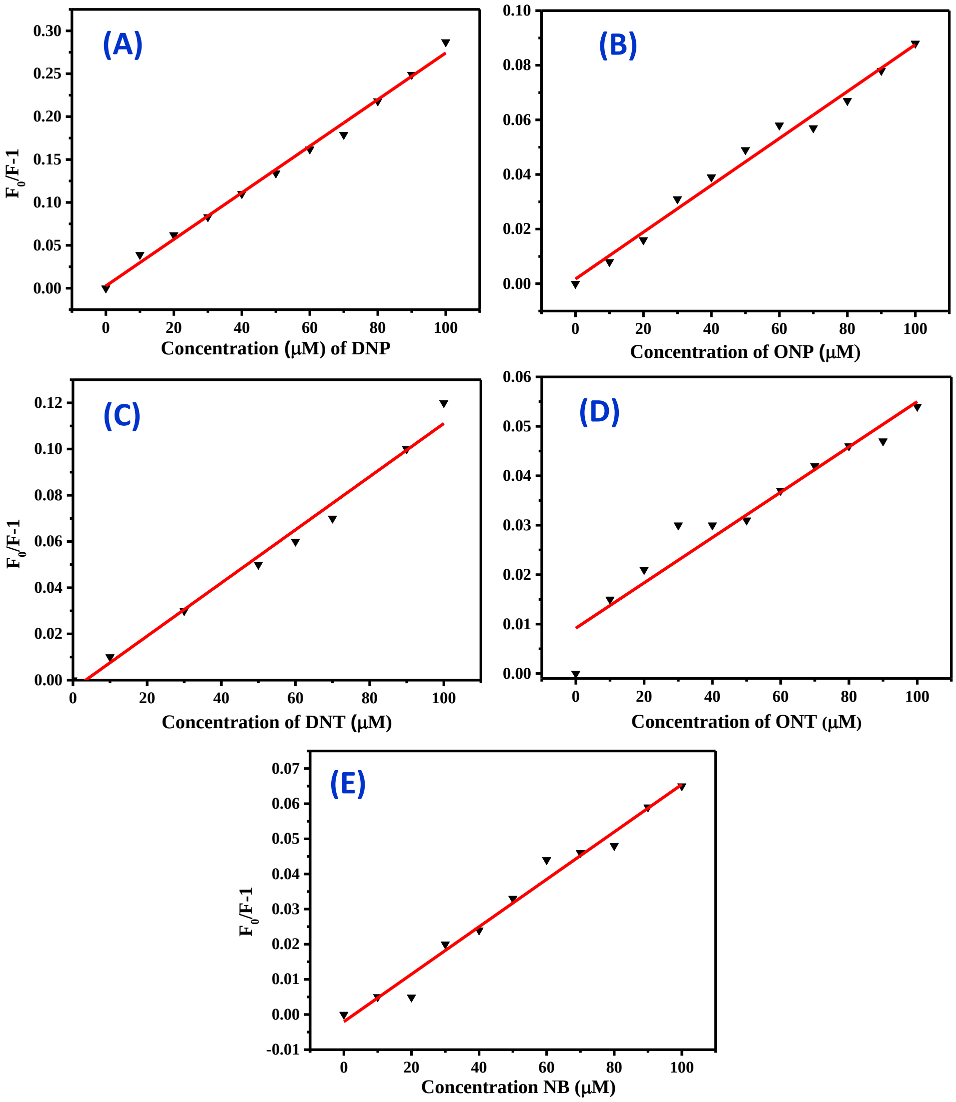

Figure 6.7. Stern-Volmer quenching plot for DNP (A), ONP (B), DNT (C), ONT (D) and NB (E). Excitation wavelength: 350 nm.

We also tested the response of OCDs towards other commonly available small organic molecules such as benzoic acid, benzaldehyde, aniline, phenol, toluene and benzene. Only a negligible variation in the emission profile of OCDs was observed after the addition of 100 μM (maximum concentration used for TNP) of these analyte species. This clearly demonstrate that the present sensor can be used to detect TNP with high specificity. A selectivity plot showing (F_0/F) versus response from TNP and all other analytes is given in Figure 6.8.

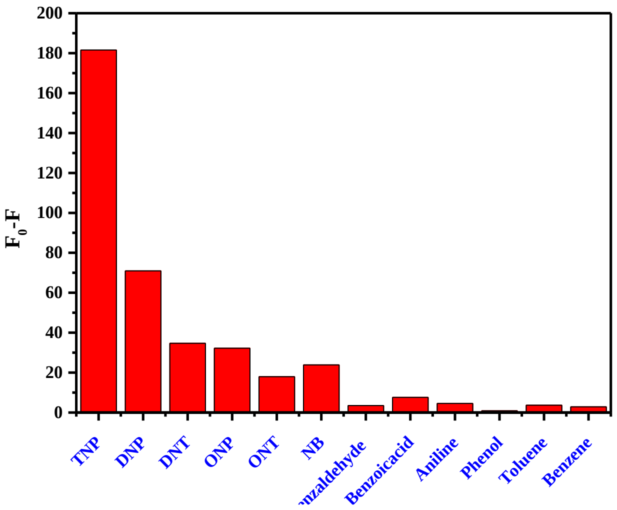

Figure 6.8. Selectivity studies. The concentration of the analytes introduced to OCDs solution was 100 µM.

The limit of detection (LOD) for TNP was calculated from S-V plot (Figure 6.6) using the equation 3σ/slope, where σ is the standard deviation of the blank measurements. The LOD for TNP was 900 nM, which is comparable to the many TNP detection strategies demonstrated earlier.

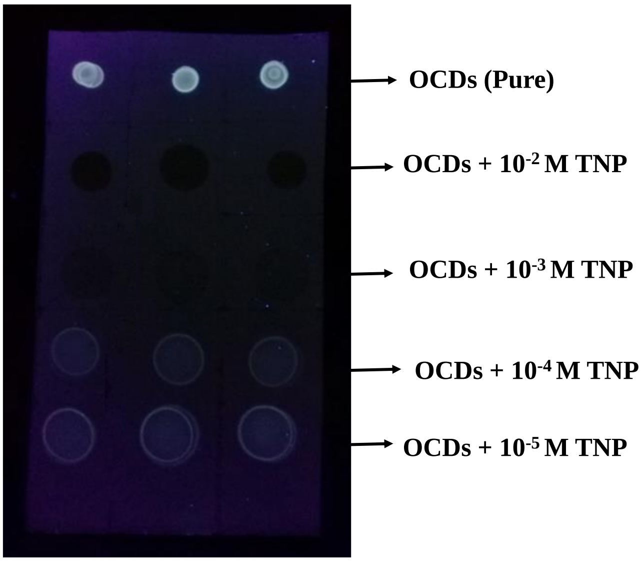

Figure 6.9. Use of test strip for the direct visual detection of TNP using OCDs.

We also established a visual method for TNP using thin layer chromatography (TLC) plate. The TLC strip was made by depositing purified OCDs followed by vacuum drying. The analyte was then drop-casted onto the dried spot of OCD on the TLC strip. The variation in luminescence was visually monitored using a UV lamp. This provided an opportunity for an easy and the visual detection of TNP. The photographs of the test strip in which fluorophore and the analyte was taken is given Figure 6.9.

Table 6.1. Summary of the results from S-V plots for various analytes. The emission intensity at 420 nm was used for the calculations.

System	K_{sv} (M^{-1})	Intercept	R^2	SF
TNP	8900	-0.0136	0.9966	1.00
DNP	2720	0.0026	0.9930	0.30
DNT	1150	-0.0039	0.9824	0.12
ONP	858	0.0017	0.9844	0.09
ONT	458	0.0092	0.9264	0.05
NB	675	-0.0020	0.9781	0.07

6.3.3. Mechanism of quenching

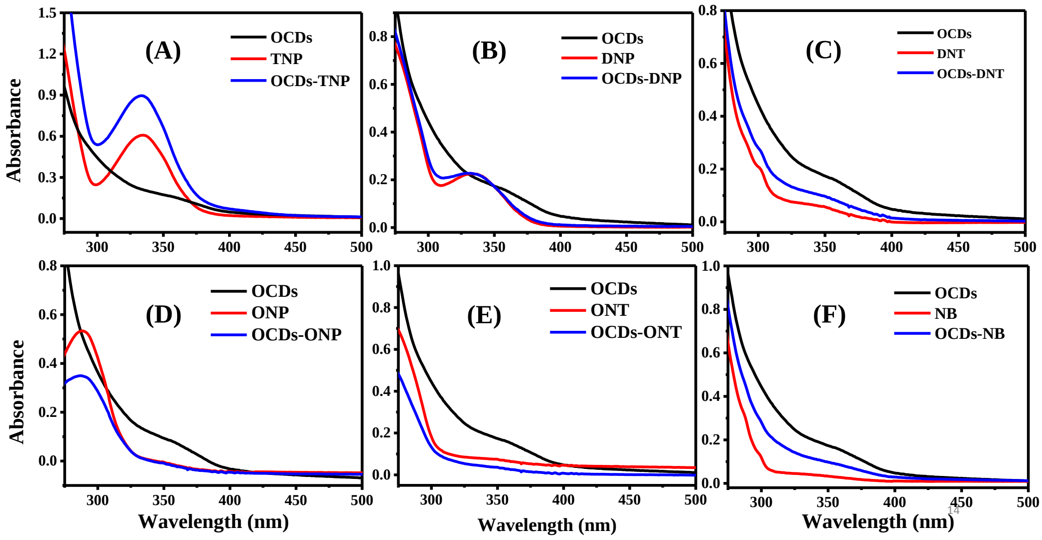

Figure 6.10. UV-Visible absorption spectra of OCDs-NAs. (A) OCDs-TNP, (B) OCDs-DNP (C) OCDs-DNT, (D) OCDs-ONP, (E) OCDs-ONT and (F) OCDs-NB.

Owing to the high propensity to withdraw the electrons by the electron withdrawing groups (EWG) attached to the benzene ring, in general, NAs quench the luminescence of a fluorophore by electron transfer mechanism. (Sadhanala & Nanda, 2015) In a few cases, the spectral overlap between NAs absorption and fluorophore's emission spectra intend to suggest energy transfer mechanism as well.(Gingras et al., 2013) Although, less explored, by virtue of strong absorption of NAs in UV and visible range, primary inner filter effect (IFE) based quenching of fluorophore’s luminescence cannot be precluded. (Chen, Liu, Zou, & Huang, 2016) To unfold the luminescence quenching of OCDs by NAs, we conducted detailed photophysical studies of OCDs-NA mixture. Absorption spectra of OCDs-NA did not show any appreciable shift in the absorption band of OCDs and NAs (Figure 6.10). This excludes the possibility of the formation of ground state complex between OCDs and NAs and hence the static type fluorescence quenching of OCDs by NAs. For comparison, absorption spectra of pure OCDs and the corresponding NAs have been given in Figure 6.10**.** To test the presence of excited state electron transfer mechanism (dynamic quenching), the quenching experiments were conducted by keeping the excitation wavelength at 440 nm, where the absorption from NAs is minimum. Electron transfer based quenching does not demand the absorption of the quencher at the excitation wavelength of the fluorophore. Therefore, we could expect similar quenching of OCDs’ emission by NAs at both 350 and 440 nm excitation if the electron transfer mechanism is predominant. Figure 6.11 is the S-V plot obtained by titrating OCDs at various concentration of NAs at 440 nm excitation wavelength. One can observe that both K_{sv} and R^2 for 440 nm excitation is significantly lower than that for 350 nm excitation wavelength. This eliminates the possibility of excited state electron transfer between OCDs and NAs.

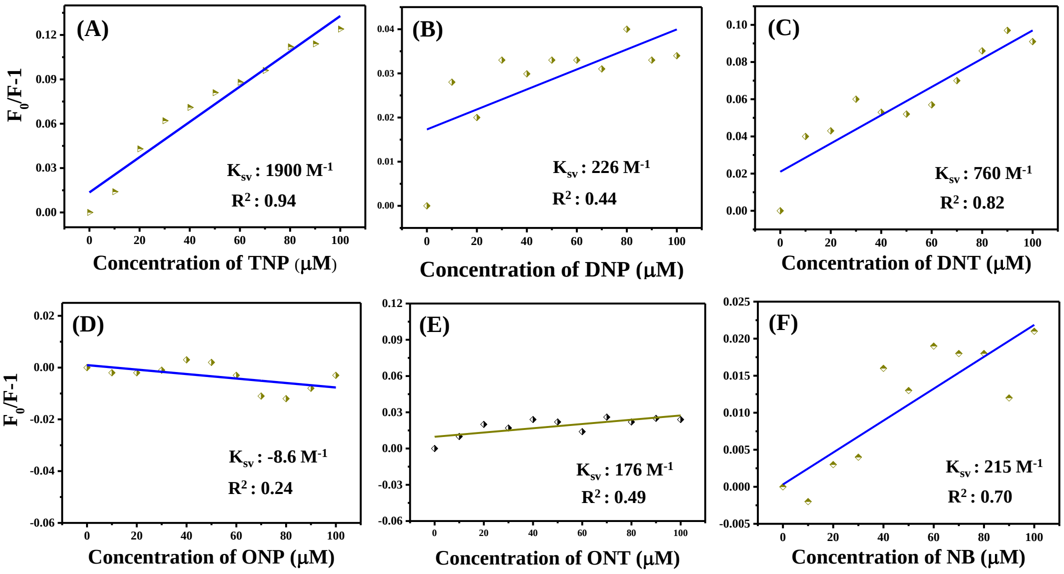

Figure 6.11. S-V plot obtained by recording the emission spectra of OCDs at different NAs concentration at 440 nm excitation wavelength. (A) OCDs-TNP (B) OCDs-DNP (C) OCDs-DNT (D) OCDs-ONT and (F) OCDs-NB. The obtained value of K_{sv} and R^2 is given in the inset of the corresponding plot.

To further corroborate this, time-resolved emission spectra of OCDs at different quencher concentration have been collected. Lifetime of the fluorophore decreases with quencher concentration if there is an excited state electron transfer between the fluorophore and quencher, owing to the emergence of new non-radiative routes. Hence, the time-resolved fluorescence analysis is an effective tool to examine the presence of any excited state quenching process. Using time-correlated single photon counting (TCSPC) technique, lifetime analysis of OCDs were performed in the absence and presence of different concentrations of quencher (Table 6.2). Lifetime analysis of OCDs-NA was performed at three different concentrations (20, 40 and 60 μM) NAs. It is clear from the Table 6.2 that, all three lifetime components of OCDs and its corresponding amplitudes remain almost same after the introduction of different concentrations of NAs. This is a direct evidence of the absence of excited state processes responsible for the PL quenching of OCDs by NAs.

Table 6.2. Results of lifetime analysis.

	τ_1 (ns)	A_1 (%)	τ_2 (ns)	A_2 (%)	τ_3 (ns)	A_3 (%)
OCDs	1.31	32.16	0.26	61.04	27.40	06.80
OCDs-20μM TNP	1.28	31.82	0.28	60.12	30.00	08.06
OCDs-40μM TNP	1.30	30.50	0.29	61.76	29.70	07.74
OCDs-60μM TNP	1.29	30.11	0.29	62.33	31.40	07.56
OCDs-20μM DNP	1.19	32.91	0.24	60.20	29.20	06.89
OCDs-40μM DNP	1.22	31.59	0.26	61.50	31.80	06.91
OCDs-60μM DNP	1.22	31.15	0.28	62.50	31.40	06.35
OCDs-20μM DNT	1.31	30.83	0.27	62.39	30.30	06.78
OCDs-40μM DNT	1.21	32.22	0.24	61.02	32.16	06.75
OCDs-60μM DNT	1.23	34.25	0.23	59.20	29.70	06.55
OCDs-20μM ONP	0.95	31.15	0.22	63.66	35.87	05.20
OCDs-40μM ONP	0.90	30.91	0.22	64.36	33.40	04.73
OCDs-60μM ONP	0.92	30.11	0.23	65.09	33.18	04.81
OCDs-20μM ONT	1.23	34.56	0.23	59.12	28.79	06.32
OCDs-40μM ONT	1.27	31.43	0.27	61.29	28.65	07.28
OCDs-60μM ONT	1.18	33.89	0.25	59.67	28.05	06.44
OCDs-20μM NB	0.97	30.95	0.24	63.84	34.35	05.21
OCDs-40μM NB	0.90	31.50	0.24	63.55	32.56	04.95
OCDs-60μM NB	0.91	31.32	0.19	63.68	33.26	04.99

Finally, the UV-visible absorption spectra of all six NAs were recorded by maintaining same concentration in all cases (Figure 6.12). The absorption of NAs at 350 nm follows the order: TNP>>DNP>>DNT>ONP>ONT≈NB, which is similar to the order of quenching observed at 350 nm excitation. This suggests that the absorption of NAs at the excitation wavelength of OCDs (primary IFE) is likely to be responsible for luminescence quenching of OCDs by NAs and precluded the existence of electron transfer between OCDs and NAs.

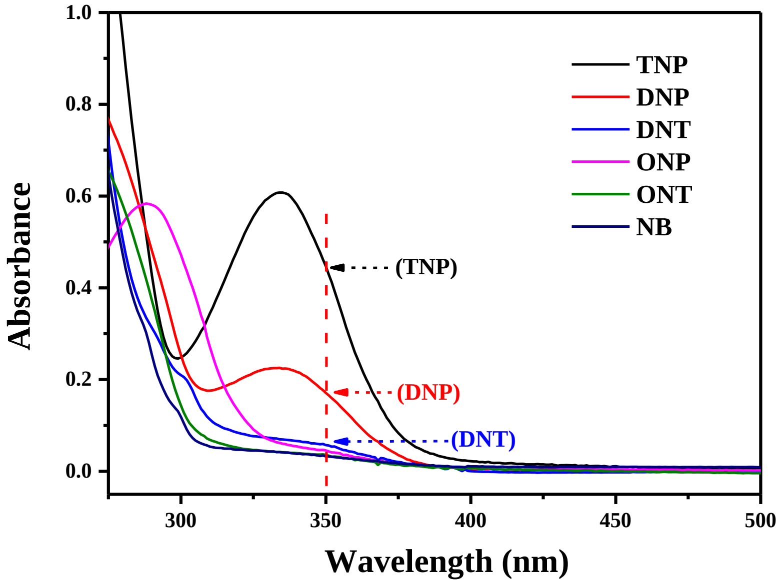

Figure 6.12. UV-visible absorption spectra of NAs (concentration was kept constant for all NAs).

6.4. Conclusions

We have shown the synthesis of OCDs which is soluble in non-polar environment. The synthesis was achieved by simple solvothermal reaction of cyclohexane as a carbon source. The OCDs was characterized in detail by various spectroscopic tools such as FTIR, XPS, NMR, UV-visible and fluorescence. We then exploited OCDs for the selective screening of TNP over other structurally similar NAs. The response of OCDs towards TNP was revealed by the high SF as compared to that of other NAs. A TLC strip was demonstrated to show the possibility of visual TNP detection. Detailed photophysical studies have been carried out to unfold the PL quenching mechanism of OCDs by NAs. The absorption of NAs at the excitation wavelength of OCDs (primary IFE) was responsible for the PL quenching. The material opens a new avenue for CDs and related materials by tuning its solubility in various solvents.

CHAPTER 7

CONCLUSIONS AND FUTURE PERSPECTIVE

7.1. Conclusions

CDs are the interesting class of carbon based fluorescent nanomaterials which attracted scientific community in the recent past because of its intriguing properties such as low-toxicity, biocompatibility, high luminescence, cheap and easy synthetic routes, a wide choice of the precursors and so on. CDs and its derivatives have been scrutinized in ample number applications which include bio and chemosensors, photo-catalysts, energy storage and conversion, bioimaging, etc. Although a variety of synthetic routes and technological possibilities of CDs have been explored over the years, there are a few issues which need further attention. (i) The quantum yield of the CDs is very low as compared to semiconductor based QDs. (ii) Most of the CDs demonstrated so far emit at the blue region of the electromagnetic spectrum when excited with UV radiation. (iii) Due to the structural complexity, the origin of the luminescence in CDs are not well understood. (iv) Most of the CDs, owing to the hydrophilic surface groups are having high solubility in the aqueous phase and less soluble in non-polar organic phase. Our work aims to address a few of the aforementioned issues and also to develop fluorescent sensors using CDs having high selectivity towards some biologically/environmentally important molecules and ions.

Chapter 1 contains introduction and literature review. It gives an overview of the present status of various synthetic routes for CDs, its general properties and its fluorescent based sensor applications. The basics of fluorescence, mechanisms of fluorescence quenching and general approaches to fluorescence sensing with a few interesting examples were highlighted in this Chapter.

A FRET based highly selective sensing of ammonia in both solution and gaseous states have been demonstrated in Chapter 2. The CDs synthesized by carbonizing acetic acid in the presence of P_2O_5/H_2O and sodium rhodizonate is used as a FRET pair for sensing ammonia. The CDs act as a fluorescent signaling agent and sodium rhodizonate binds to specifically to ammonia. The initial FRET established between CDs and sodium rhodizonate due to the spectral overlap between the two was turned off when ammonia is introduced, which in turn leads to the recovery of CDs' fluorescence and can be used to estimate ammonia. The selectivity of this FRET based sensor was tested by interacting the sensor system with oxides of nitrogen and commonly used organic solvents. It was found that there is no or weak response of sensor system towards these molecules.

The synthesis of a nearly white light emitting NCDs, their application as Cu^{2+} sensor and the origin of luminescence was detailed in Chapter 3. The synthesis was accomplished by carbonizing ethylenediamine in the presence of P_2O_5/H_2O and the detailed spectroscopic characterization of NCDs reveal the presence of graphitic, pyridinic and pyrrolic nitrogen atoms at the core of the NCDs and NH_2 group at the surface. NCDs showed broad emission profile with CIE coordinates near to white light emission. We utilized NCDs for the selective sensing of Cu^{2+} ions as Cu^{2+} selectively quenched the PL emission of NCDs directly. The nature of the interaction between NCDs and Cu^{2+} was used for the indirect understanding of the origin of luminescence in NCDs. Based on detailed time-resolved and steady-state PL results, it is deduced that the emission of NCDs at higher energy originated from carbon core whereas emission at lower energy elevated from defect states.

A hydrothermal route for the synthesis of Si passivated CDs gel using APTES as a precursor was demonstrated in Chapter 4. Microscopic analysis clearly demonstrated the formation of network structures with CDs attached to the polymeric backbone. The SiCDs gel manifested strong blue emission when excited with UV radiation. The rheological and surface area analysis of SiCDs gel showed typical a gel like characteristics. Due to the presence of large number of carboxyl and amine functional groups as well as the pore structure, SiCDs gel could transform Ag^{+} ions to Ag nanoparticles at ambient conditions without any reducing agents. The Ag nanoparticle generated on the surface of SiCDs gel quenched the emission of SiCDs gel and can be used for the detection Ag^{+} ions. The selectivity of this sensor towards Ag^{+} ions was tested by interacting SiCDs gel with various metal ions and commonly used organic molecules.

In Chapter 5 we have shown the synthesis of highly emitting S and N co-doped CDs by hydrothermal carbonization of glutathione as a source of carbon as well as S and N. The observed atypical luminescence profile and pH dependent luminescence from SNCDs triggered us to explore the origin of luminescence in doped CDs. Based on in-depth time-resolved and steady-state fluorescence analysis as well as from UV-visible studies, a comprehensive energy level diagram of SNCDs was proposed. A FRET and IFE based fluorescence sensing platform for Cr(VI) detection using SNCDs was established. Here, the emission of SNCDs was quenched due to the transfer of excited state energy from SNCDs to DPC as well as IFE after the introduction of Cr(VI), which in turn utilized for the sensing of Cr(VI).

An organophilic CDs, referred as OCDs have been synthesized using cyclohexane as a carbon source was discussed in Chapter 6. The predominance of ester, hydroxyl, ether and alkyl functional groups on the surface of OCDs was observed, which is responsible for the high solubility of OCDs in the non-polar phase. The OCDs was then interacted with various NAs to establish a sensing platform for this NAs as well as to understand the mechanism of quenching of OCDs emission by NAs. It was observed that among all the NAs studied, TNP has maximum quenching and hence the present system can be used as a selective TNP sensor. A comprehensive studies including time-resolved and steady-state fluorescence analysis were carried out to understand the mechanism of PL quenching by NAs. It reveals that NAs quench the emission of OCDs by IFE and not via commonly reported electron and energy transfer mechanism.

7.2. Future perspectives

Owing to the high absorption in the visible and near IR region as well as due to the better quantum yield of doped CDs, we propose to utilize the CDs in photocatalytic and bioimaging applications. The fluorescence response of a fluorophore in various environment is an intriguing property and one can tune the luminescence response of a fluorophore by changing the solvent environment. Hence it is interesting to study the solvotochromic behaviour of CDs synthesized by us and also to tune the solubility of our CDs by post-functionalization steps.

Although there are plenty reports on hetero atoms doped CDs, CDs doped with metals are rare. Metal doped CDs, in particular transition metal doped ones, which is envisaged to serve dual purpose viz. fluorescence and electrochemical based applications.

Energy harvesting and biological applications of CDs are yet to be explored in its capacity. The non-toxicity of CDs make them alternative to traditional heavy metal based QDs in the field of biotechnological and environmental applications. It has the propensity to be modified according to the needs. Carefully designed CDs have the potential to become next generation photovoltaic devices, bioimaging agents and chemical sensors.

REFERENCES

1. Abellán, G., Coronado, E., Martí-Gastaldo, C., Pinilla-Cienfuegos, E., & Ribera, A. (2010). Hexagonal nanosheets from the exfoliation of Ni^{2+}-Fe^{3+} LDHs: a route towards layered multifunctional materials. *Journal of materials chemistry, 20*(35), 7451-7455.

2. Ahmed, K. B. A., Kumar, S., & Veerappan, A. (2016). A facile method to prepare fluorescent carbon dots and their application in selective colorimetric sensing of silver ion through the formation of silver nanoparticles. *Journal of Luminescence, 177*, 228-234.

3. Ahn, S. H., & Manthiram, A. (2017). Direct growth of ternary Ni-Fe-P porous nanorods onto nickel foam as a highly active, robust bi-functional electrocatalyst for overall water splitting. [10.1039/C6TA10509B]. *Journal of Materials Chemistry A, 5*(6), 2496-2503. doi: 10.1039/c6ta10509b.

4. Babich, H., Schiffenbauer, M., & Stotzky, G. (1982). Comparative toxicity of trivalent and hexavalent chromium to fungi. *Bulletin of environmental contamination and toxicology, 28*(4), 452-459.

5. Baker, S. N., & Baker, G. A. (2010). Luminescent Carbon Nanodots: Emergent Nanolights. *Angewandte Chemie International Edition, 49*(38), 6726-6744. doi: 10.1002/anie.200906623.

6. Bang, J. H., & Suslick, K. S. (2010). Applications of Ultrasound to the Synthesis of Nanostructured Materials. *Advanced Materials, 22*(10), 1039-1059. doi: 10.1002/adma.200904093.

7. Bao, L., Liu, C., Zhang, Z.-L., & Pang, D.-W. (2015). Photoluminescence-Tunable Carbon Nanodots: Surface-State Energy-Gap Tuning. *Advanced Materials, 27*(10), 1663-1667. doi: 10.1002/adma.201405070.

8. Barman, M. K., Jana, B., Bhattacharyya, S., & Patra, A. (2014). Photophysical Properties of Doped Carbon Dots (N, P, and B) and Their Influence on Electron/Hole Transfer in Carbon Dots–Nickel (II) Phthalocyanine Conjugates. *The Journal of Physical Chemistry C, 118*(34), 20034-20041. doi: 10.1021/jp507080c.

9. Basabe-Desmonts, L., Reinhoudt, D. N., & Crego-Calama, M. (2007). Design of fluorescent materials for chemical sensing. [10.1039/B609548H]. *Chemical Society Reviews, 36*(6), 993-1017. doi: 10.1039/b609548h.

10. Bekyarova, E., Davis, M., Burch, T., Itkis, M. E., Zhao, B., Sunshine, S., & Haddon, R. C. (2004). Chemically Functionalized Single-Walled Carbon Nanotubes as Ammonia Sensors. *The Journal of Physical Chemistry B, 108*(51), 19717-19720. doi: 10.1021/jp0471857.

11. Bettermann, H., Dasting, I., & Wolff, U. (1997). Kinetic investigations of the laser-induced photolysis of sodium rhodizonate in aqueous solutions. *Spectrochimica Acta Part A: Molecular and Biomolecular Spectroscopy, 53*(2), 233-245. doi: https://doi.org/10.1016/S1386-1425(96)01773-8.

12. Bourlinos, A. B., Stassinopoulos, A., Anglos, D., Zboril, R., Karakassides, M., & Giannelis, E. P. (2008). Surface Functionalized Carbogenic Quantum Dots. *Small, 4*(4), 455-458. doi: 10.1002/smll.200700578.

13. Bourlinos, A. B., Zbořil, R., Petr, J., Bakandritsos, A., Krysmann, M., & Giannelis, E. P. (2012). Luminescent Surface Quaternized Carbon Dots. *Chemistry of Materials, 24*(1), 6-8. doi: 10.1021/cm2026637.

14. Cai, Q.-Y., Li, J., Ge, J., Zhang, L., Hu, Y.-L., Li, Z.-H., & Qu, L.-B. (2015). A rapid fluorescence "switch-on" assay for glutathione detection by using carbon dots–MnO_2 nanocomposites. *Biosensors and Bioelectronics, 72*(Supplement C), 31-36. doi: https://doi.org/10.1016/j.bios.2015.04.077.

15. Campos, B. B., Contreras-Cáceres, R., Bandosz, T. J., Jiménez-Jiménez, J., Rodríguez-Castellón, E., Esteves da Silva, J. C. G., & Algarra, M. (2016). Carbon dots as fluorescent sensor for detection of explosive nitrocompounds. *Carbon, 106*, 171-178. doi: https://doi.org/10.1016/j.carbon.2016.05.030

16. Carter, K. P., Young, A. M., & Palmer, A. E. (2014). Fluorescent Sensors for Measuring Metal Ions in Living Systems. *Chemical Reviews, 114*(8), 4564-4601. doi: 10.1021/cr400546e

17. Cayuela, A., Kennedy, S. R., Soriano, M. L., Jones, C. D., Valcárcel, M., & Steed, J. W. (2015). Fluorescent carbon dot–molecular salt hydrogels. *Chemical Science, 6*(11), 6139-6146.

18. Cayuela, A., Soriano, M. L., Kennedy, S. R., Steed, J. W., & Valcárcel, M. (2016). Fluorescent carbon quantum dot hydrogels for direct determination of silver ions. *Talanta, 151*(Supplement C), 100-105. doi: https://doi.org/10.1016/j.talanta.2016.01.029

19. Chae, A., Choi, Y., Jo, S., Nur'aeni, Paoprasert, P., Park, S. Y., & In, I. (2017). Microwave-assisted synthesis of fluorescent carbon quantum dots from an A_2/B_3 monomer set. [10.1039/C6RA28176A]. *RSC Advances, 7*(21), 12663-12669. doi: 10.1039/c6ra28176a

20. Chandra Sekhar, R., Manu, H., Govindaraj, A., & Rao, C. N. R. (2007). Ammonia sensors based on metal oxide nanostructures. *Nanotechnology, 18*(20), 205504.

21. Chandra, S., Pradhan, S., Mitra, S., Patra, P., Bhattacharya, A., Pramanik, P., & Goswami, A. (2014). High throughput electron transfer from carbon dots to chloroplast: a rationale of enhanced photosynthesis.

[10.1039/C3NR06079A]. *Nanoscale, 6*(7), 3647-3655. doi: 10.1039/c3nr06079a

22. Chen, B. B., Liu, Z. X., Zou, H. Y., & Huang, C. Z. (2016). Highly selective detection of 2,4,6-trinitrophenol by using newly developed terbium-doped blue carbon dots. [10.1039/C5AN02569A]. *Analyst, 141*(9), 2676-2681. doi: 10.1039/c5an02569a

23. Chen, B., & Feng, J. (2015). White-Light-Emitting Polymer Composite Film Based on Carbon Dots and Lanthanide Complexes. *The Journal of Physical Chemistry C, 119*(14), 7865-7872. doi: 10.1021/acs.jpcc.5b00208

24. Chen, D., Gao, H., Chen, X., Fang, G., Yuan, S., & Yuan, Y. (2017). Excitation-Independent Dual-Color Carbon Dots: Surface-State Controlling and Solid-State Lighting. *ACS Photonics, 4*(9), 2352-2358. doi: 10.1021/acsphotonics.7b00675

25. Chen, P.-C., Chen, Y.-N., Hsu, P.-C., Shih, C.-C., & Chang, H.-T. (2013). Photoluminescent organosilane-functionalized carbon dots as temperature probes. *Chemical Communications, 49*(16), 1639-1641.

26. Chen, S., & Sun, G. (2013). High Sensitivity Ammonia Sensor Using a Hierarchical Polyaniline/Poly(ethylene-co-glycidyl methacrylate) Nanofibrous Composite Membrane. *ACS Applied Materials & Interfaces, 5*(14), 6473-6477. doi: 10.1021/am402217s

27. Cheng, N., Jiang, P., Liu, Q., Tian, J., Asiri, A. M., & Sun, X. (2014). Graphitic carbon nitride nanosheets: one-step, high-yield synthesis and application for Cu^{2+} detection. [10.1039/C4AN00914B]. *Analyst, 139*(20), 5065-5068. doi: 10.1039/c4an00914b

28. Clare, E. R., Carl, W. B., III, Igor, L. M., & James, B. D. (2015). Intracellular FRET-based probes: a review. *Methods and Applications in Fluorescence, 3*(4), 042006.

29. Courbat, J., Briand, D., Damon-Lacoste, J., Wöllenstein, J., & de Rooij, N. F. (2009). Evaluation of pH indicator-based colorimetric films for ammonia detection using optical waveguides. *Sensors and Actuators B: Chemical, 143*(1), 62-70. doi: https://doi.org/10.1016/j.snb.2009.08.049

30. Crowley, K., O'Malley, E., Morrin, A., Smyth, M. R., & Killard, A. J. (2008). An aqueous ammonia sensor based on an inkjet-printed polyaniline nanoparticle-modified electrode. [10.1039/B716154A]. *Analyst, 133*(3), 391-399. doi: 10.1039/b716154a

31. Cui, S., Mao, S., Wen, Z., Chang, J., Zhang, Y., & Chen, J. (2013). Controllable synthesis of silver nanoparticle-decorated reduced graphene oxide hybrids for ammonia detection. [10.1039/C3AN36922F]. *Analyst, 138*(10), 2877-2882. doi: 10.1039/c3an36922f

32. Cui, S., Pu, H., Lu, G., Wen, Z., Mattson, E. C., Hirschmugl, C., . . . Chen, J. (2012). Fast and Selective Room-Temperature Ammonia Sensors Using Silver Nanocrystal-Functionalized Carbon Nanotubes. *ACS Applied Materials & Interfaces, 4*(9), 4898-4904. doi: 10.1021/am301229w

33. Dai, M.-Z., Lin, Y.-L., Lin, H.-C., Zan, H.-W., Chang, K.-T., Meng, H.-F., . . . Cheng, H. (2013). Highly Sensitive Ammonia Sensor with Organic Vertical Nanojunctions for Noninvasive Detection of Hepatic Injury. *Analytical Chemistry, 85*(6), 3110-3117. doi: 10.1021/ac303100k

34. Dang, H., Huang, L.-K., Zhang, Y., Wang, C.-F., & Chen, S. (2016). Large-Scale Ultrasonic Fabrication of White Fluorescent Carbon Dots. *Industrial & Engineering Chemistry Research, 55*(18), 5335-5341. doi: 10.1021/acs.iecr.6b00894

35. Das, R. K., & Mohapatra, S. (2017). Highly luminescent, heteroatom-doped carbon quantum dots for ultrasensitive sensing of glucosamine and targeted imaging of liver cancer cells. [10.1039/C6TB03141B]. *Journal of Materials Chemistry B, 5*(11), 2190-2197. doi: 10.1039/c6tb03141b

36. Datta, K. K. R., Qi, G., Zboril, R., & Giannelis, E. P. (2016). Yellow emitting carbon dots with superior colloidal, thermal, and photochemical stabilities. [10.1039/C6TC03452G]. *Journal of Materials Chemistry C, 4*(41), 9798-9803. doi: 10.1039/c6tc03452g

37. Dennis, A. M., Rhee, W. J., Sotto, D., Dublin, S. N., & Bao, G. (2012). Quantum Dot–Fluorescent Protein FRET Probes for Sensing Intracellular pH. *ACS Nano, 6*(4), 2917-2924. doi: 10.1021/nn2038077

38. Dhenadhayalan, N., Lin, K.-C., Suresh, R., & Ramamurthy, P. (2016). Unravelling the multiple emissive states in citric-acid-derived carbon dots. *The Journal of Physical Chemistry C, 120*(2), 1252-1261.

39. Dinda, D., Gupta, A., Shaw, B. K., Sadhu, S., & Saha, S. K. (2014). Highly Selective Detection of Trinitrophenol by Luminescent Functionalized Reduced Graphene Oxide through FRET Mechanism. *ACS Applied Materials & Interfaces, 6*(13), 10722-10728. doi: 10.1021/am5025676

40. Ding, H., Ji, Y., Wei, J.-S., Gao, Q.-Y., Zhou, Z.-Y., & Xiong, H.-M. (2017). Facile synthesis of red-emitting carbon dots from pulp-free lemon juice for bioimaging. [10.1039/C7TB01130J]. *Journal of Materials Chemistry B, 5*(26), 5272-5277. doi: 10.1039/c7tb01130j

41. Ding, H., Wei, J.-S., & Xiong, H.-M. (2014). Nitrogen and sulfur co-doped carbon dots with strong blue luminescence. [10.1039/C4NR04267K]. *Nanoscale, 6*(22), 13817-13823. doi: 10.1039/c4nr04267k

42. Ding, H., Yu, S.-B., Wei, J.-S., & Xiong, H.-M. (2016). Full-Color Light-Emitting Carbon Dots with a Surface-State-Controlled Luminescence Mechanism. *ACS Nano, 10*(1), 484-491. doi: 10.1021/acsnano.5b05406

43. Dong, Y., Pang, H., Yang, H. B., Guo, C., Shao, J., Chi, Y., . . . Yu, T. (2013). Carbon-Based Dots Co-doped with Nitrogen and Sulfur for High Quantum Yield and Excitation-Independent Emission. *Angewandte Chemie International Edition, 52*(30), 7800-7804. doi: 10.1002/anie.201301114

44. Duniho, T. L., Laughlin, B. J., Buelt, A. A., Baker, W. F., Conrad, C. A., & Smith, R. C. (2014). Conjugated polymers for the fluorescent detection of nitroaromatics: Influence of side-chain sterics and π-system electronics. *Journal of Polymer Science Part A: Polymer Chemistry, 52*(10), 1487-1492. doi: 10.1002/pola.27143

45. Edison, T. N. J. I., Atchudan, R., Shim, J.-J., Kalimuthu, S., Ahn, B.-C., & Lee, Y. R. (2016). Turn-off fluorescence sensor for the detection of ferric ion in water using green synthesized N-doped carbon dots and its bio-imaging. *Journal of Photochemistry and Photobiology B: Biology, 158*(Supplement C), 235-242. doi: https://doi.org/10.1016/j.jphotobiol.2016.03.010

46. Fang, Y., Guo, S., Li, D., Zhu, C., Ren, W., Dong, S., & Wang, E. (2012). Easy Synthesis and Imaging Applications of Cross-Linked Green Fluorescent Hollow Carbon Nanoparticles. *ACS Nano, 6*(1), 400-409. doi: 10.1021/nn2046373

47. Fargasova, A. (1994). Toxicity of metals on Daphnia magna and Tubifex tubifex. *Ecotoxicology and environmental safety, 27*(2), 210-213.

48. Fu, M., Ehrat, F., Wang, Y., Milowska, K. Z., Reckmeier, C., Rogach, A. L., . . . Feldmann, J. (2015). Carbon Dots: A Unique Fluorescent Cocktail of Polycyclic Aromatic Hydrocarbons. *Nano Letters, 15*(9), 6030-6035. doi: 10.1021/acs.nanolett.5b02215

49. Ganiga, M., & Cyriac, J. (2015). Direct synthesis of highly stable nitrogen rich carbon dots toward white light emission. [10.1039/C5RA17789H]. *RSC Advances, 5*(123), 101333-101337. doi: 10.1039/c5ra17789h

50. Gao, X., Du, C., Zhuang, Z., & Chen, W. (2016). Carbon quantum dot-based nanoprobes for metal ion detection. [10.1039/C6TC02055K]. *Journal of Materials Chemistry C, 4*(29), 6927-6945. doi: 10.1039/c6tc02055k

51. Gao, X., Lu, Y., Zhang, R., He, S., Ju, J., Liu, M., . . . Chen, W. (2015). One-pot synthesis of carbon nanodots for fluorescence turn-on detection of Ag+ based on the Ag^+-induced enhancement of fluorescence. [10.1039/C4TC02582B]. *Journal of Materials Chemistry C, 3*(10), 2302-2309. doi: 10.1039/c4tc02582b

52. Georgakilas, V., Perman, J. A., Tucek, J., & Zboril, R. (2015). Broad Family of Carbon Nanoallotropes: Classification, Chemistry, and Applications of Fullerenes, Carbon Dots, Nanotubes, Graphene, Nanodiamonds, and Combined Superstructures. *Chemical Reviews, 115*(11), 4744-4822. doi: 10.1021/cr500304f

53. Germain, M. E., & Knapp, M. J. (2009). Optical explosives detection: from color changes to fluorescence turn-on. [10.1039/B809631G]. *Chemical Society Reviews, 38*(9), 2543-2555. doi: 10.1039/b809631g

54. Ghosh, S., Chizhik, A. M., Karedla, N., Dekaliuk, M. O., Gregor, I., Schuhmann, H., . . . Schulz, O. (2014). Photoluminescence of carbon nanodots: dipole emission centers and electron–phonon coupling. *Nano letters, 14*(10), 5656-5661.

55. Ghosh, T., & Prasad, E. (2015). White-Light Emission from Unmodified Graphene Oxide Quantum Dots. *The Journal of Physical Chemistry C, 119*(5), 2733-2742. doi: 10.1021/jp511787a

56. Gingras, A., Sarette, J., Shawler, E., Lee, T., Freund, S., Holwitt, E., & Hicks, B. W. (2013). Fluorescent proteins as biosensors by quenching resonance energy transfer from endogenous tryptophan: Detection of nitroaromatic explosives. *Biosensors and Bioelectronics, 48* (Supplement C), 251-257. doi: https://doi.org/10.1016/j.bios.2013.03.076

57. Gore, A. H., Vatre, S. B., Anbhule, P. V., Han, S.-H., Patil, S. R., & Kolekar, G. B. (2013). Direct detection of sulfide ions [S2-] in aqueous media based on fluorescence quenching of functionalized CdS QDs at trace levels: analytical applications to environmental analysis. [10.1039/C3AN36825D]. *Analyst, 138*(5), 1329-1333. doi: 10.1039/c3an36825d

58. Gude, V., Das, A., Chatterjee, T., & Mandal, P. K. (2016). Molecular origin of photoluminescence of carbon dots: aggregation-induced orange-red emission. *Physical Chemistry Chemical Physics, 18*(40), 28274-28280.

59. Gui, R., An, X., Su, H., Shen, W., Zhu, L., Ma, X., . . . Wang, X. (2012). Rhodamine 6G conjugated-quantum dots used for highly sensitive and selective ratiometric fluorescence sensor of glutathione. *Talanta, 94*(Supplement C), 295-300. doi: https://doi.org/10.1016/j.talanta.2012.03.043

60. Gumpu, M. B., Sethuraman, S., Krishnan, U. M., & Rayappan, J. B. B. (2015). A review on detection of heavy metal ions in water–An electrochemical approach. *Sensors and Actuators B: Chemical, 213*, 515-533.

61. Guo, Y., Wang, Z., Shao, H., & Jiang, X. (2013). Hydrothermal synthesis of highly fluorescent carbon nanoparticles from sodium citrate and their use

for the detection of mercury ions. *Carbon, 52*(Supplement C), 583-589. doi: https://doi.org/10.1016/j.carbon.2012.10.028

62. He, H., Wang, X., Feng, Z., Cheng, T., Sun, X., Sun, Y., . . . Zhang, X. (2015). Rapid microwave-assisted synthesis of ultra-bright fluorescent carbon dots for live cell staining, cell-specific targeting and in vivo imaging. [10.1039/C5TB00570A]. *Journal of Materials Chemistry B, 3*(24), 4786-4789. doi: 10.1039/c5tb00570a

63. Heller, A., & Williams, D. L. (1970). Intramolecular proton transfer reactions in excited fluorescent compounds. *The Journal of Physical Chemistry, 74*(26), 4473-4480. doi: 10.1021/j100720a003

64. Hola, K., Bourlinos, A. B., Kozak, O., Berka, K., Siskova, K. M., Havrdova, M., . . . Zboril, R. (2014). Photoluminescence effects of graphitic core size and surface functional groups in carbon dots: COO^- induced red-shift emission. *Carbon, 70*(Supplement C), 279-286. doi: https://doi.org/10.1016/j.carbon.2014.01.008

65. Hou, Y., Lu, Q., Deng, J., Li, H., & Zhang, Y. (2015). One-pot electrochemical synthesis of functionalized fluorescent carbon dots and their selective sensing for mercury ion. *Analytica Chimica Acta, 866*(Supplement C), 69-74. doi: https://doi.org/10.1016/j.aca.2015.01.039

66. Hsu, Y.-F., Chen, Y.-H., & Chang, C.-W. (2016). The spectral heterogeneity and size distribution of the carbon dots derived from time-resolved fluorescence studies. [10.1039/C6CP05813B]. *Physical Chemistry Chemical Physics, 18*(43), 30086-30092. doi: 10.1039/c6cp05813b

67. Hu, Y., Yang, J., Tian, J., & Yu, J.-S. (2015). How do nitrogen-doped carbon dots generate from molecular precursors? An investigation of the formation mechanism and a solution-based large-scale synthesis. [10.1039/C5TB01005E]. *Journal of Materials Chemistry B, 3*(27), 5608-5614. doi: 10.1039/c5tb01005e

68. Huang, H., Li, C., Zhu, S., Wang, H., Chen, C., Wang, Z., . . . Feng, S. (2014). Histidine-Derived Nontoxic Nitrogen-Doped Carbon Dots for Sensing and Bioimaging Applications. *Langmuir, 30*(45), 13542-13548. doi: 10.1021/la503969z

69. Idros, N., Ho, M., Pivnenko, M., Qasim, M., Xu, H., Gu, Z., & Chu, D. (2015). Colorimetric-Based Detection of TNT Explosives Using Functionalized Silica Nanoparticles. *Sensors, 15*(6), 12891.

70. Jahan, S., Mansoor, F., Naz, S., Lei, J., & Kanwal, S. (2013). Oxidative Synthesis of Highly Fluorescent Boron/Nitrogen Co-Doped Carbon Nanodots Enabling Detection of Photosensitizer and Carcinogenic Dye. *Analytical Chemistry, 85*(21), 10232-10239. doi: 10.1021/ac401949k

71. Jang, S.-C., Haldorai, Y., Lee, G.-W., Hwang, S.-K., Han, Y.-K., Roh, C., & Huh, Y. S. (2015). Porous three-dimensional graphene foam/Prussian blue composite for efficient removal of radioactive 137Cs. *Scientific Reports, 5*, 17510.

72. Jia, X., Li, J., & Wang, E. (2012). One-pot green synthesis of optically pH-sensitive carbon dots with upconversion luminescence. [10.1039/C2NR31319G]. *Nanoscale, 4*(18), 5572-5575. doi: 10.1039/c2nr31319g

73. Jiang, G., Susha, A. S., Lutich, A. A., Stefani, F. D., Feldmann, J., & Rogach, A. L. (2009). Cascaded FRET in Conjugated Polymer/Quantum Dot/Dye-Labeled DNA Complexes for DNA Hybridization Detection. *ACS Nano, 3*(12), 4127-4131. doi: 10.1021/nn901324y

74. Jiang, K., Sun, S., Zhang, L., Lu, Y., Wu, A., Cai, C., & Lin, H. (2015). Red, Green, and Blue Luminescence by Carbon Dots: Full-Color Emission Tuning and Multicolor Cellular Imaging. *Angewandte Chemie International Edition, 54*(18), 5360-5363. doi: 10.1002/anie.201501193

75. Jiang, Z. C., Lin, T. N., Lin, H. T., Talite, M. J., Tzeng, T. T., Hsu, C. L., . . . Yuan, C. T. (2016). A Facile and Low-Cost Method to Enhance the Internal Quantum Yield and External Light-Extraction Efficiency for Flexible Light-Emitting Carbon-Dot Films. [Article]. *Scientific Reports, 6*, 19991. doi: 10.1038/srep19991

76. Jiao, T., Guo, H., Zhang, Q., Peng, Q., Tang, Y., Yan, X., & Li, B. (2015). Reduced Graphene Oxide-Based Silver Nanoparticle-Containing Composite Hydrogel as Highly Efficient Dye Catalysts for Wastewater Treatment. [Article]. *Scientific Reports, 5*, 11873. doi: 10.1038/srep11873

77. Jin, S. H., Kim, D. H., Jun, G. H., Hong, S. H., & Jeon, S. (2013). Tuning the Photoluminescence of Graphene Quantum Dots through the Charge Transfer Effect of Functional Groups. *ACS Nano, 7*(2), 1239-1245. doi: 10.1021/nn304675g

78. Kartha, K. K., Sandeep, A., Praveen, V. K., & Ajayaghosh, A. (2015). Detection of Nitroaromatic Explosives with Fluorescent Molecular Assemblies and π-Gels. *The Chemical Record, 15*(1), 252-265. doi: 10.1002/tcr.201402063

79. Khan, S., Gupta, A., Verma, N. C., & Nandi, C. K. (2015). Time-Resolved Emission Reveals Ensemble of Emissive States as the Origin of Multicolor Fluorescence in Carbon Dots. *Nano Letters, 15*(12), 8300-8305. doi: 10.1021/acs.nanolett.5b03915

80. Kim, T. H., White, A. R., Sirdaarta, J. P., Ji, W., Cock, I. E., St. John, J., . . . Li, Q. (2016). Yellow-Emitting Carbon Nanodots and Their Flexible and

Transparent Films for White LEDs. *ACS Applied Materials & Interfaces, 8*(48), 33102-33111. doi: 10.1021/acsami.6b12113

81. Kim, Y., Jang, G., & Lee, T. S. (2015). New Fluorescent Metal-Ion Detection Using a Paper-Based Sensor Strip Containing Tethered Rhodamine Carbon Nanodots. *ACS Applied Materials & Interfaces, 7*(28), 15649-15657. doi: 10.1021/acsami.5b04724

82. Kozák, O., Datta, K. K. R., Greplová, M., Ranc, V., Kašlík, J., & Zbořil, R. (2013). Surfactant-Derived Amphiphilic Carbon Dots with Tunable Photoluminescence. *The Journal of Physical Chemistry C, 117*(47), 24991-24996. doi: 10.1021/jp4040166

83. Krysmann, M. J., Kelarakis, A., Dallas, P., & Giannelis, E. P. (2012). Formation Mechanism of Carbogenic Nanoparticles with Dual Photoluminescence Emission. *Journal of the American Chemical Society, 134*(2), 747-750. doi: 10.1021/ja204661r

84. Kwon, W., Do, S., Lee, J., Hwang, S., Kim, J. K., & Rhee, S.-W. (2013). Freestanding Luminescent Films of Nitrogen-Rich Carbon Nanodots toward Large-Scale Phosphor-Based White-Light-Emitting Devices. *Chemistry of Materials, 25*(9), 1893-1899. doi: 10.1021/cm400517g

85. Kwon, W., Lee, G., Do, S., Joo, T., & Rhee, S.-W. (2014). Size-Controlled Soft-Template Synthesis of Carbon Nanodots toward Versatile Photoactive Materials. *Small, 10*(3), 506-513. doi: 10.1002/smll.201301770

86. Lai, C.-W., Hsiao, Y.-H., Peng, Y.-K., & Chou, P.-T. (2012). Facile synthesis of highly emissive carbon dots from pyrolysis of glycerol; gram scale production of carbon dots/mSiO_2 for cell imaging and drug release. [10.1039/C2JM32206D]. *Journal of Materials Chemistry, 22*(29), 14403-14409. doi: 10.1039/c2jm32206d

87. Lan, M., Di, Y., Zhu, X., Ng, T.-W., Xia, J., Liu, W., . . . Zhang, W. (2015). A carbon dot-based fluorescence turn-on sensor for hydrogen peroxide with a photo-induced electron transfer mechanism. [10.1039/C5CC05835J]. *Chemical Communications, 51*(85), 15574-15577. doi: 10.1039/c5cc05835j

88. Lee, H., Hancock, R. D., & Lee, H.-S. (2013). Role of Fluorophore–Metal Interaction in Photoinduced Electron Transfer (PET) Sensors: Time-Dependent Density Functional Theory (TDDFT) Study. *The Journal of Physical Chemistry A, 117*(50), 13345-13355. doi: 10.1021/jp406624p

89. Li, C.-X., Yu, C., Wang, C.-F., & Chen, S. (2013). Facile plasma-induced fabrication of fluorescent carbon dots toward high-performance white LEDs. *Journal of Materials Science, 48*(18), 6307-6311. doi: 10.1007/s10853-013-7430-6

90. Li, G., Fu, H., Chen, X., Gong, P., Chen, G., Xia, L., . . . Wu, Y. (2016). Facile and Sensitive Fluorescence Sensing of Alkaline Phosphatase Activity with Photoluminescent Carbon Dots Based on Inner Filter Effect. *Analytical Chemistry, 88*(5), 2720-2726. doi: 10.1021/acs.analchem.5b04193

91. Li, H., He, X., Liu, Y., Huang, H., Lian, S., Lee, S.-T., & Kang, Z. (2011). One-step ultrasonic synthesis of water-soluble carbon nanoparticles with excellent photoluminescent properties. *Carbon, 49*(2), 605-609. doi: https://doi.org/10.1016/j.carbon.2010.10.004

92. Li, H., Kang, Z., Liu, Y., & Lee, S.-T. (2012). Carbon nanodots: synthesis, properties and applications. [10.1039/C2JM34690G]. *Journal of Materials Chemistry, 22*(46), 24230-24253. doi: 10.1039/c2jm34690g

93. Li, H., Ming, H., Liu, Y., Yu, H., He, X., Huang, H., . . . Lee, S.-T. (2011). Fluorescent carbon nanoparticles: electrochemical synthesis and their pH sensitive photoluminescence properties. [10.1039/C1NJ20575G]. *New Journal of Chemistry, 35*(11), 2666-2670. doi: 10.1039/c1nj20575g

94. Li, H., Sun, C., Vijayaraghavan, R., Zhou, F., Zhang, X., & MacFarlane, D. R. (2016). Long lifetime photoluminescence in N, S co-doped carbon quantum dots from an ionic liquid and their applications in ultrasensitive detection of pesticides. *Carbon, 104*(Supplement C), 33-39. doi: https://doi.org/10.1016/j.carbon.2016.03.040

95. Li, J.-G., Tsai, C.-Y., & Kuo, S.-W. (2014). Fabrication and characterization of inorganic silver and palladium nanostructures within hexagonal cylindrical channels of mesoporous carbon. *Polymers, 6*(6), 1794-1809.

96. Li, J.-Y., Liu, Y., Shu, Q.-W., Liang, J.-M., Zhang, F., Chen, X.-P., . . . Tan, K.-J. (2017). One-Pot Hydrothermal Synthesis of Carbon Dots with Efficient Up- and Down-Converted Photoluminescence for the Sensitive Detection of Morin in a Dual-Readout Assay. *Langmuir, 33*(4), 1043-1050. doi: 10.1021/acs.langmuir.6b04225

97. Li, L., Wang, C., Liu, K., Wang, Y., Liu, K., & Lin, Y. (2015). Hexagonal Cobalt Oxyhydroxide–Carbon Dots Hybridized Surface: High Sensitive Fluorescence Turn-on Probe for Monitoring of Ascorbic Acid in Rat Brain Following Brain Ischemia. *Analytical Chemistry, 87*(6), 3404-3411. doi: 10.1021/ac5046609

98. Li, X., Zhao, Z., & Pan, C. (2016). Ionic liquid-assisted electrochemical exfoliation of carbon dots of different size for fluorescent imaging of bacteria by tuning the water fraction in electrolyte. [journal article]. *Microchimica Acta, 183*(9), 2525-2532. doi: 10.1007/s00604-016-1877-5

99. Li, Y. H., Zhao, Y. M., Zhu, Y. Q., Rodriguez, J., Morante, J. R., Mendoza, E., . . . Silva, S. R. P. (2006). Mechanical and NH_3 sensing properties of

long multi-walled carbon nanotube ropes. *Carbon, 44*(9), 1821-1825. doi: https://doi.org/10.1016/j.carbon.2005.12.032

100. Liang, W., Liu, S., Liu, Z., Li, D., Wang, L., Hao, C., & He, Y. (2015). Electron transfer and fluorescence "turn-off" based CdTe quantum dots for vancomycin detection at nanogram level in aqueous serum media. [10.1039/C4NJ01764A]. *New Journal of Chemistry, 39*(6), 4774-4782. doi: 10.1039/c4nj01764a

101. Liang, Z., Kang, M., Payne, G. F., Wang, X., & Sun, R. (2016). Probing Energy and Electron Transfer Mechanisms in Fluorescence Quenching of Biomass Carbon Quantum Dots. *ACS Applied Materials & Interfaces, 8*(27), 17478-17488. doi: 10.1021/acsami.6b04826

102. Liao, J., Cheng, Z., & Zhou, L. (2016). Nitrogen-Doping Enhanced Fluorescent Carbon Dots: Green Synthesis and Their Applications for Bioimaging and Label-Free Detection of Au3+ Ions. *ACS Sustainable Chemistry & Engineering, 4*(6), 3053-3061. doi: 10.1021/acssuschemeng.6b00018

103. Lim, S. Y., Shen, W., & Gao, Z. (2015). Carbon quantum dots and their applications. [10.1039/C4CS00269E]. *Chemical Society Reviews, 44*(1), 362-381. doi: 10.1039/c4cs00269e

104. Lin, F., Pei, D., He, W., Huang, Z., Huang, Y., & Guo, X. (2012). Electron transfer quenching by nitroxide radicals of the fluorescence of carbon dots. [10.1039/C2JM31191G]. *Journal of Materials Chemistry, 22*(23), 11801-11807. doi: 10.1039/c2jm31191g

105. Liu, C., Zhang, P., Tian, F., Li, W., Li, F., & Liu, W. (2011). One-step synthesis of surface passivated carbon nanodots by microwave assisted pyrolysis for enhanced multicolor photoluminescence and bioimaging. [10.1039/C1JM12744F]. *Journal of Materials Chemistry, 21*(35), 13163-13167. doi: 10.1039/c1jm12744f

106. Liu, H., He, Z., Jiang, L.-P., & Zhu, J.-J. (2015). Microwave-Assisted Synthesis of Wavelength-Tunable Photoluminescent Carbon Nanodots and Their Potential Applications. *ACS Applied Materials & Interfaces, 7*(8), 4913-4920. doi: 10.1021/am508994w

107. Liu, H., Li, M., Xia, Y., & Ren, X. (2017). A Turn-On Fluorescent Sensor for Selective and Sensitive Detection of Alkaline Phosphatase Activity with Gold Nanoclusters Based on Inner Filter Effect. *ACS Applied Materials & Interfaces, 9*(1), 120-126. doi: 10.1021/acsami.6b11920

108. Liu, J., Ren, X., Meng, X., Fang, Z., & Tang, F. (2013). Sensitive and selective detection of Hg^{2+} and Cu^{2+} ions by fluorescent Ag nanoclusters synthesized via a hydrothermal method. [10.1039/C3NR03329E]. *Nanoscale, 5*(20), 10022-10028. doi: 10.1039/c3nr03329e

109. Liu, L., & Lin, H. (2014). based colorimetric array test strip for selective and semiquantitative multi-ion analysis: simultaneous detection of Hg^{2+}, Ag^{+}, and Cu^{2+}. *Analytical Chemistry, 86*(17), 8829-8834.

110. Liu, R., Wu, D., Liu, S., Koynov, K., Knoll, W., & Li, Q. (2009). An Aqueous Route to Multicolor Photoluminescent Carbon Dots Using Silica Spheres as Carriers. *Angewandte Chemie International Edition, 48*(25), 4598-4601. doi: 10.1002/anie.200900652

111. Liu, S., Tian, J., Wang, L., Zhang, Y., Qin, X., Luo, Y., . . . Sun, X. (2012). Hydrothermal Treatment of Grass: A Low-Cost, Green Route to Nitrogen-Doped, Carbon-Rich, Photoluminescent Polymer Nanodots as an Effective Fluorescent Sensing Platform for Label-Free Detection of Cu(II) Ions. *Advanced Materials, 24*(15), 2037-2041. doi: 10.1002/adma.201200164

112. Liu, X., Cui, S., Sun, Z., & Du, P. (2015). Robust and highly active copper-based electrocatalyst for hydrogen production at low overpotential in neutral water. [10.1039/C5CC04965B]. *Chemical Communications, 51*(65), 12954-12957. doi: 10.1039/c5cc04965b

113. Liu, X., Pang, J., Xu, F., & Zhang, X. (2016). Simple Approach to Synthesize Amino-Functionalized Carbon Dots by Carbonization of Chitosan. [Article]. *Scientific Reports, 6*, 31100. doi: 10.1038/srep31100

114. Liu, X., Zhang, N., Zhou, J., Chang, T., Fang, C., & Shangguan, D. (2013). A turn-on fluorescent sensor for zinc and cadmium ions based on perylene tetracarboxylic diimide. [10.1039/C2AN36203A]. *Analyst, 138*(3), 901-906. doi: 10.1039/c2an36203a

115. Liu, Y., Deng, R., Wang, Z., & Liu, H. (2012). Carboxyl-functionalized graphene oxide–polyaniline composite as a promising supercapacitor material. *Journal of materials chemistry, 22*(27), 13619-13624.

116. Liu, Y., Wang, P., Shiral Fernando, K. A., LeCroy, G. E., Maimaiti, H., Harruff-Miller, B. A., . . . Sun, Y.-P. (2016). Enhanced fluorescence properties of carbon dots in polymer films. [10.1039/C6TC01932C]. *Journal of Materials Chemistry C, 4*(29), 6967-6974. doi: 10.1039/c6tc01932c

117. Liu, Y., Zhou, Q., Yuan, Y., & Wu, Y. (2017). Hydrothermal synthesis of fluorescent carbon dots from sodium citrate and polyacrylamide and their highly selective detection of lead and pyrophosphate. *Carbon, 115*(Supplement C), 550-560. doi: https://doi.org/10.1016/j.carbon.2017.01.035

118. Loo, A. H., Sofer, Z., Bouša, D., Ulbrich, P., Bonanni, A., & Pumera, M. (2016). Carboxylic Carbon Quantum Dots as a Fluorescent Sensing Platform for DNA Detection. *ACS Applied Materials & Interfaces, 8*(3), 1951-1957. doi: 10.1021/acsami.5b10160

119. López, C., Zougagh, M., Algarra, M., Rodríguez-Castellón, E., Campos, B. B., Esteves da Silva, J. C. G., . . . Ríos, A. (2015). Microwave-assisted synthesis of carbon dots and its potential as analysis of four heterocyclic aromatic amines. *Talanta, 132*(Supplement C), 845-850. doi: https://doi.org/10.1016/j.talanta.2014.10.008

120. Lu, S., Cong, R., Zhu, S., Zhao, X., Liu, J., S. Tse, J., . . . Yang, B. (2016). pH-Dependent Synthesis of Novel Structure-Controllable Polymer-Carbon NanoDots with High Acidophilic Luminescence and Super Carbon Dots Assembly for White Light-Emitting Diodes. *ACS Applied Materials & Interfaces, 8*(6), 4062-4068.

121. Ma, F., Sun, M., Zhang, K., & Wang, S. (2015). A ratiometric fluorescence sensor for highly selective and sensitive detection of mercuric ion. *Sensors and Actuators B: Chemical, 209*(Supplement C), 377-383. doi: https://doi.org/10.1016/j.snb.2014.11.105

122. Ma, Z., Ming, H., Huang, H., Liu, Y., & Kang, Z. (2012). One-step ultrasonic synthesis of fluorescent N-doped carbon dots from glucose and their visible-light sensitive photocatalytic ability. [10.1039/C2NJ20942J]. *New Journal of Chemistry, 36*(4), 861-864. doi: 10.1039/c2nj20942j

123. Mader, H. S., & Wolfbeis, O. S. (2010). Optical Ammonia Sensor Based on Upconverting Luminescent Nanoparticles. *Analytical Chemistry, 82*(12), 5002-5004. doi: 10.1021/ac1007283

124. Mao, S., Yu, K., Cui, S., Bo, Z., Lu, G., & Chen, J. (2011). A new reducing agent to prepare single-layer, high-quality reduced graphene oxide for device applications. [10.1039/C1NR10270B]. *Nanoscale, 3*(7), 2849-2853. doi: 10.1039/c1nr10270b

125. McCranor, B. J., Szmacinski, H., Zeng, H. H., Stoddard, A. K., Hurst, T., Fierke, C. A., . . . Thompson, R. B. (2014). Fluorescence lifetime imaging of physiological free Cu(II) levels in live cells with a Cu(II)-selective carbonic anhydrase-based biosensor. [10.1039/C3MT00305A]. *Metallomics, 6*(5), 1034-1042. doi: 10.1039/c3mt00305a

126. Ming, H., Ma, Z., Liu, Y., Pan, K., Yu, H., Wang, F., & Kang, Z. (2012). Large scale electrochemical synthesis of high quality carbon nanodots and their photocatalytic property. [10.1039/C2DT30985H]. *Dalton Transactions, 41*(31), 9526-9531. doi: 10.1039/c2dt30985h

127. Mondal, S., & Purkayastha, P. (2016). α-Cyclodextrin Functionalized Carbon Dots: Pronounced Photoinduced Electron Transfer by Aggregated Nanostructures. *The Journal of Physical Chemistry C, 120*(26), 14365-14371. doi: 10.1021/acs.jpcc.6b03145

128. Moquin, A., Hutter, E., Choi, A. O., Khatchadourian, A., Castonguay, A., Winnik, F. M., & Maysinger, D. (2013). Caspase-1 Activity in Microglia

Stimulated by Pro-Inflammagen Nanocrystals. *ACS Nano, 7*(11), 9585-9598. doi: 10.1021/nn404473g

129. Nakahara, M., & Sanada, Y. (1995). FT-IR ATR spectroscopy of the edge surface of pyrolytic graphite and its surface/PVC interface. *Journal of Materials Science, 30*(17), 4363-4368. doi: 10.1007/bf00361518

130. Nie, H., Li, M., Li, Q., Liang, S., Tan, Y., Sheng, L., . . . Zhang, S. X.-A. (2014). Carbon Dots with Continuously Tunable Full-Color Emission and Their Application in Ratiometric pH Sensing. *Chemistry of Materials, 26*(10), 3104-3112. doi: 10.1021/cm5003669

131. Othman, M. R. (2015). Electrosynthesis and characterization of $Cu(OH)_2$ nanoparticle using Cu and Cu-PVC electrodes in alkaline solution. *International Journal of Electrochemical Science, 10*(6), 4911-4921.

132. Paglia, G., Williams, J. P., Menikarachchi, L., Thompson, J. W., Tyldesley-Worster, R., Halldórsson, S., . . . Astarita, G. (2014). Ion Mobility Derived Collision Cross Sections to Support Metabolomics Applications. *Analytical Chemistry, 86*(8), 3985-3993. doi: 10.1021/ac500405x

133. Pal, A., Sk, M. P., & Chattopadhyay, A. (2016). Conducting Carbon Dot–Polypyrrole Nanocomposite for Sensitive Detection of Picric acid. *ACS Applied Materials & Interfaces, 8*(9), 5758-5762. doi: 10.1021/acsami.5b11572

134. Pallavicini, P., Dacarro, G., Grisoli, P., Mangano, C., Patrini, M., Rigoni, F., . . . Taglietti, A. (2013). Coordination chemistry for antibacterial materials: a monolayer of a Cu^{2+} 2,2[prime or minute]-bipyridine complex grafted on a glass surface. [10.1039/C2DT32607H]. *Dalton Transactions, 42*(13), 4552-4560. doi: 10.1039/c2dt32607h

135. Pan, D., Zhang, J., Li, Z., Wu, C., Yan, X., & Wu, M. (2010). Observation of pH-, solvent-, spin-, and excitation-dependent blue photoluminescence from carbon nanoparticles. [10.1039/C000114G]. *Chemical Communications, 46*(21), 3681-3683. doi: 10.1039/c000114g

136. Pan, D., Zhang, J., Li, Z., Zhang, Z., Guo, L., & Wu, M. (2011). Blue fluorescent carbon thin films fabricated from dodecylamine-capped carbon nanoparticles. *Journal of materials chemistry, 21*(11), 3565-3567.

137. Pan, L., Sun, S., Zhang, A., Jiang, K., Zhang, L., Dong, C., . . . Lin, H. (2015). Truly Fluorescent Excitation-Dependent Carbon Dots and Their Applications in Multicolor Cellular Imaging and Multidimensional Sensing. *Advanced Materials, 27*(47), 7782-7787.

138. Pandey, S., Goswami, G. K., & Nanda, K. K. (2013). Green synthesis of polysaccharide/gold nanoparticle nanocomposite: An efficient ammonia

sensor. *Carbohydrate Polymers, 94*(1), 229-234. doi: https://doi.org/10.1016/j.carbpol.2013.01.009

139. Pansare, V. J., Hejazi, S., Faenza, W. J., & Prud'homme, R. K. (2012). Review of Long-Wavelength Optical and NIR Imaging Materials: Contrast Agents, Fluorophores, and Multifunctional Nano Carriers. *Chemistry of Materials, 24*(5), 812-827. doi: 10.1021/cm2028367

140. Parejo, P. G., Zayat, M., & Levy, D. (2006). Highly efficient UV-absorbing thin-film coatings for protection of organic materials against photodegradation. *Journal of materials chemistry, 16*(22), 2165-2169.

141. Park, Y., Yoo, J., Lim, B., Kwon, W., & Rhee, S. W. (2016). Improving the functionality of carbon nanodots: doping and surface functionalization. [10.1039/C6TA04813G]. *Journal of Materials Chemistry A, 4*(30), 11582-11603. doi: 10.1039/c6ta04813g

142. Peng, H., Stich, M. I. J., Yu, J., Sun, L.-n., Fischer, L. H., & Wolfbeis, O. S. (2010). Luminescent Europium(III) Nanoparticles for Sensing and Imaging of Temperature in the Physiological Range. *Advanced Materials, 22*(6), 716-719. doi: 10.1002/adma.200901614

143. Peng, J., Gao, W., Gupta, B. K., Liu, Z., Romero-Aburto, R., Ge, L., . . . Ajayan, P. M. (2012). Graphene Quantum Dots Derived from Carbon Fibers. *Nano Letters, 12*(2), 844-849. doi: 10.1021/nl2038979

144. Peveler, W. J., Roldan, A., Hollingsworth, N., Porter, M. J., & Parkin, I. P. (2016). Multichannel Detection and Differentiation of Explosives with a Quantum Dot Array. *ACS Nano, 10*(1), 1139-1146. doi: 10.1021/acsnano.5b06433

145. Piljic, A., & Schultz, C. (2008). Simultaneous Recording of Multiple Cellular Events by FRET. *ACS Chemical Biology, 3*(3), 156-160. doi: 10.1021/cb700247q

146. Prajapati, R., Bhattacharya, A., & Mukherjee, T. K. (2016). Resonant excitation energy transfer from carbon dots to different sized silver nanoparticles. [10.1039/C6CP05451J]. *Physical Chemistry Chemical Physics, 18*(41), 28911-28918. doi: 10.1039/c6cp05451j

147. Prasannan, A., & Imae, T. (2013). One-Pot Synthesis of Fluorescent Carbon Dots from Orange Waste Peels. *Industrial & Engineering Chemistry Research, 52*(44), 15673-15678. doi: 10.1021/ie402421s

148. Privitera, A., Righetto, M., Mosconi, D., Lorandi, F., Isse, A. A., Moretto, A., . . . Franco, L. (2016). Boosting carbon quantum dots/fullerene electron transfer via surface group engineering. [10.1039/C6CP05981C]. *Physical Chemistry Chemical Physics, 18*(45), 31286-31295. doi: 10.1039/c6cp05981c

149. Pu, Q., & Sun, Q. (1998). Application of 2-mercaptobenzothiazole-modified silica gel to on-line preconcentration and separation of silver for its atomic absorption spectrometric determination. *Analyst, 123*(2), 239-243.

150. Qian, Z., Chai, L., Tang, C., Huang, Y., Chen, J., & Feng, H. (2015). Carbon Quantum Dots-Based Recyclable Real-Time Fluorescence Assay for Alkaline Phosphatase with Adenosine Triphosphate as Substrate. *Analytical Chemistry, 87*(5), 2966-2973. doi: 10.1021/ac504519b

151. Qian, Z., Ma, J., Shan, X., Feng, H., Shao, L., & Chen, J. (2014). Highly Luminescent N-Doped Carbon Quantum Dots as an Effective Multifunctional Fluorescence Sensing Platform. *Chemistry – A European Journal, 20*(8), 2254-2263. doi: 10.1002/chem.201304374

152. Qian, Z., Shan, X., Chai, L., Ma, J., Chen, J., & Feng, H. (2014). Si-doped carbon quantum dots: a facile and general preparation strategy, bioimaging application, and multifunctional sensor. *ACS Applied Materials & Interfaces, 6*(9), 6797-6805.

153. Qiao, Z.-A., Wang, Y., Gao, Y., Li, H., Dai, T., Liu, Y., & Huo, Q. (2010). Commercially activated carbon as the source for producing multicolor photoluminescent carbon dots by chemical oxidation. [10.1039/C0CC02724C]. *Chemical Communications, 46*(46), 8812-8814. doi: 10.1039/c0cc02724c

154. Qu, D., Zheng, M., Li, J., Xie, Z., & Sun, Z. (2015). Tailoring color emissions from N-doped graphene quantum dots for bioimaging applications. [Original Article]. *Light: Science &Amp; Applications, 4*, e364. doi: 10.1038/lsa.2015.137

155. Qu, K., Wang, J., Ren, J., & Qu, X. (2013). Carbon Dots Prepared by Hydrothermal Treatment of Dopamine as an Effective Fluorescent Sensing Platform for the Label-Free Detection of Iron(III) Ions and Dopamine. *Chemistry – A European Journal, 19*(22), 7243-7249. doi: 10.1002/chem.201300042

156. Ramanan, V., Thiyagarajan, S. K., Raji, K., Suresh, R., Sekar, R., & Ramamurthy, P. (2016). Outright Green Synthesis of Fluorescent Carbon Dots from Eutrophic Algal Blooms for In Vitro Imaging. *ACS Sustainable Chemistry & Engineering, 4*(9), 4724-4731. doi: 10.1021/acssuschemeng.6b00935

157. Ran, X., Sun, H., Pu, F., Ren, J., & Qu, X. (2013). Ag nanoparticle-decorated graphene quantum dots for label-free, rapid and sensitive detection of Ag^+ and biothiols. *Chemical Communications, 49*(11), 1079-1081.

158. Roy, R., Hohng, S., & Ha, T. (2008). A practical guide to single-molecule FRET. [Review Article]. *Nature Methods, 5*, 507. doi: 10.1038/nmeth.1208

159. Ruedas-Rama, M. J., Walters, J. D., Orte, A., & Hall, E. A. H. (2012). Fluorescent nanoparticles for intracellular sensing: A review. *Analytica Chimica Acta, 751*(Supplement C), 1-23. doi: https://doi.org/10.1016/j.aca.2012.09.025

160. Sadhanala, H. K., & Nanda, K. K. (2015). Boron and Nitrogen Co-doped Carbon Nanoparticles as Photoluminescent Probes for Selective and Sensitive Detection of Picric Acid. *The Journal of Physical Chemistry C, 119*(23), 13138-13143. doi: 10.1021/acs.jpcc.5b04140

161. Sahm, M., Oprea, A., Bârsan, N., & Weimar, U. (2007). Water and ammonia influence on the conduction mechanisms in polyacrylic acid films. *Sensors and Actuators B: Chemical, 127*(1), 204-209. doi: https://doi.org/10.1016/j.snb.2007.07.027

162. Salinas-Castillo, A., Ariza-Avidad, M., Pritz, C., Camprubi-Robles, M., Fernandez, B., Ruedas-Rama, M. J., . . . Capitan-Vallvey, L. F. (2013). Carbon dots for copper detection with down and upconversion fluorescent properties as excitation sources. [10.1039/C2CC36450F]. *Chemical Communications, 49*(11), 1103-1105. doi: 10.1039/c2cc36450f

163. Sangeetha, N. M., & Maitra, U. (2005). Supramolecular gels: Functions and uses. [10.1039/B417081B]. *Chemical Society Reviews, 34*(10), 821-836. doi: 10.1039/b417081b

164. Sarkar, S., Sudolska, M., Dubecký, M. s., Reckmeier, C. J., Rogach, A. L., Zboril, R., & Otyepka, M. (2016). Graphitic nitrogen doping in carbon dots causes red-shifted absorption. *The Journal of Physical Chemistry C, 120*(2), 1303-1308.

165. Sau, A., Bera, K., Mondal, P., Satpati, B., & Basu, S. (2016). Distance-Dependent Electron Transfer in Chemically Engineered Carbon Dots. *The Journal of Physical Chemistry C, 120*(47), 26630-26636. doi: 10.1021/acs.jpcc.6b08146

166. Schibilla, F., Stegemann, L., Strassert, C. A., Rizzo, F., & Ravoo, B. J. (2016). Fluorescence quenching in [small beta]-cyclodextrin vesicles: membrane confinement and host-guest interactions. [10.1039/C5PP00226E]. *Photochemical & Photobiological Sciences, 15*(2), 235-243. doi: 10.1039/c5pp00226e

167. Shangguan, J., Huang, J., He, D., He, X., Wang, K., Ye, R., . . . Tang, J. (2017). Highly Fe^{3+}-Selective Fluorescent Nanoprobe Based on Ultrabright N/P Codoped Carbon Dots and Its Application in Biological Samples. *Analytical Chemistry, 89*(14), 7477-7484. doi: 10.1021/acs.analchem.7b01053

168. Shanmugaraj, K., & Ilanchelian, M. (2016). A "turn-off" fluorescent sensor for the selective and sensitive detection of copper(ii) ions using lysozyme

stabilized gold nanoclusters. [10.1039/C6RA08325K]. *RSC Advances, 6*(59), 54518-54524. doi: 10.1039/c6ra08325k

169. Shanmugaraju, S., & Mukherjee, P. S. (2015). [small pi]-Electron rich small molecule sensors for the recognition of nitroaromatics. [10.1039/C5CC07513K]. *Chemical Communications, 51*(89), 16014-16032. doi: 10.1039/c5cc07513k

170. Sharma, A., Gadly, T., Gupta, A., Ballal, A., Ghosh, S. K., & Kumbhakar, M. (2016). Origin of excitation dependent fluorescence in carbon nanodots. *The Journal of Physical Chemistry Letters, 7*(18), 3695-3702.

171. Shen, L., Chen, M., Hu, L., Chen, X., & Wang, J. (2013). Growth and stabilization of silver nanoparticles on carbon dots and sensing application. *Langmuir, 29*(52), 16135-16140.

172. Shen, P., & Xia, Y. (2014). Synthesis-Modification Integration: One-Step Fabrication of Boronic Acid Functionalized Carbon Dots for Fluorescent Blood Sugar Sensing. *Analytical Chemistry, 86*(11), 5323-5329. doi: 10.1021/ac5001338

173. Shi, J., Lu, C., Yan, D., & Ma, L. (2013). High selectivity sensing of cobalt in HepG2 cells based on necklace model microenvironment-modulated carbon dot-improved chemiluminescence in Fenton-like system. *Biosensors and Bioelectronics, 45*(Supplement C), 58-64. doi: https://doi.org/10.1016/j.bios.2013.01.056

174. Shimizu, K.-i., Chinzei, I., Nishiyama, H., Kakimoto, S., Sugaya, S., Matsutani, W., & Satsuma, A. (2009). Doped-vanadium oxides as sensing materials for high temperature operative selective ammonia gas sensors. *Sensors and Actuators B: Chemical, 141*(2), 410-416. doi: https://doi.org/10.1016/j.snb.2009.06.048

175. Shustova, N. B., Cozzolino, A. F., Reineke, S., Baldo, M., & Dincă, M. (2013). Selective Turn-On Ammonia Sensing Enabled by High-Temperature Fluorescence in Metal–Organic Frameworks with Open Metal Sites. *Journal of the American Chemical Society, 135*(36), 13326-13329. doi: 10.1021/ja407778a

176. Singha, S., Kim, D., Seo, H., Cho, S. W., & Ahn, K. H. (2015). Fluorescence sensing systems for gold and silver species. *Chemical Society Reviews, 44*(13), 4367-4399.

177. Singla, N., Tripathi, A., Rana, M., Kishore Goswami, S., Pathak, A., & Chowdhury, P. (2015). "Turn on/off" proton transfer based fluorescent sensor for selective detection of environmentally hazardous metal ions (Zn^{2+}, Pb^{2+}) in aqueous media. *Journal of Luminescence, 165*(Supplement C), 46-55. doi: https://doi.org/10.1016/j.jlumin.2015.04.007

178. Sinha, S., Chowdhury, B., & Ghosh, P. (2016). A Highly Sensitive ESIPT-Based Ratiometric Fluorescence Sensor for Selective Detection of Al^{3+}. *Inorganic Chemistry, 55*(18), 9212-9220. doi: 10.1021/acs.inorgchem.6b01170

179. Song, Y., & Cooks, R. G. (2006). Atmospheric pressure ion/molecule reactions for the selective detection of nitroaromatic explosives using acetonitrile and air as reagents. *Rapid Communications in Mass Spectrometry, 20*(20), 3130-3138. doi: 10.1002/rcm.2714

180. Song, Y., Zhu, S., Xiang, S., Zhao, X., Zhang, J., Zhang, H., . . . Yang, B. (2014). Investigation into the fluorescence quenching behaviors and applications of carbon dots. [10.1039/C4NR00029C]. *Nanoscale, 6*(9), 4676-4682. doi: 10.1039/c4nr00029c

181. Srinivasan, K., Subramanian, K., Murugan, K., & Dinakaran, K. (2016). Sensitive fluorescence detection of mercury(ii) in aqueous solution by the fluorescence quenching effect of MoS2 with DNA functionalized carbon dots. [10.1039/C6AN00879H]. *Analyst, 141*(22), 6344-6352. doi: 10.1039/c6an00879h

182. Stringer, R. C., Gangopadhyay, S., & Grant, S. A. (2010). Detection of Nitroaromatic Explosives Using a Fluorescent-Labeled Imprinted Polymer. *Analytical Chemistry, 82*(10), 4015-4019. doi: 10.1021/ac902838c

183. Sun, H., Wu, L., Gao, N., Ren, J., & Qu, X. (2013). Improvement of Photoluminescence of Graphene Quantum Dots with a Biocompatible Photochemical Reduction Pathway and Its Bioimaging Application. *ACS Applied Materials & Interfaces, 5*(3), 1174-1179. doi: 10.1021/am3030849

184. Sun, X., Liu, P., Wu, L., & Liu, B. (2015). Graphene-quantum-dots-based ratiometric fluorescent probe for visual detection of copper ion. [10.1039/C5AN01297J]. *Analyst, 140*(19), 6742-6747. doi: 10.1039/c5an01297j

185. Suzuki, K., Malfatti, L., Carboni, D., Loche, D., Casula, M., Moretto, A., . . . Innocenzi, P. (2015). Energy Transfer Induced by Carbon Quantum Dots in Porous Zinc Oxide Nanocomposite Films. *The Journal of Physical Chemistry C, 119*(5), 2837-2843. doi: 10.1021/jp510661d

186. Takagai, Y., Nojiri, Y., Takase, T., Hinze, W. L., Butsugan, M., & Igarashi, S. (2010). "Turn-on" fluorescent polymeric microparticle sensors for the determination of ammonia and amines in the vapor state. [10.1039/B922842J]. *Analyst, 135*(6), 1417-1425. doi: 10.1039/b922842j

187. Tan, X., Li, Q., Zhang, X., Shen, Y., & Yang, J. (2015). A novel and sensitive turn-on fluorescent biosensor for the determination of thioctic acid based on Cu^{2+}-modulated N-acetyl-l-cysteine capped CdTe quantum dots.

[10.1039/C5RA05087A]. *RSC Advances, 5*(55), 44173-44182. doi: 10.1039/c5ra05087a

188. Tang, L., Ji, R., Li, X., Teng, K. S., & Lau, S. P. (2013). Energy-level structure of nitrogen-doped graphene quantum dots. [10.1039/C3TC30877D]. *Journal of Materials Chemistry C, 1*(32), 4908-4915. doi: 10.1039/c3tc30877d

189. Tantama, M., Hung, Y. P., & Yellen, G. (2011). Imaging Intracellular pH in Live Cells with a Genetically Encoded Red Fluorescent Protein Sensor. *Journal of the American Chemical Society, 133*(26), 10034-10037. doi: 10.1021/ja202902d

190. Taylor, P. R. (1982). On the origins of the blue shift of the carbonyl n-.pi.* transition in hydrogen-bonding solvents. *Journal of the American Chemical Society, 104*(19), 5248-5249. doi: 10.1021/ja00383a052

191. Tian, J., Liu, Q., Asiri, A. M., Al-Youbi, A. O., & Sun, X. (2013). Ultrathin Graphitic Carbon Nitride Nanosheet: A Highly Efficient Fluorosensor for Rapid, Ultrasensitive Detection of Cu^{2+}. *Analytical Chemistry, 85*(11), 5595-5599. doi: 10.1021/ac400924j

192. Timmer, B., Olthuis, W., & Berg, A. v. d. (2005). Ammonia sensors and their applications: a review. *Sensors and Actuators B: Chemical, 107*(2), 666-677. doi: https://doi.org/10.1016/j.snb.2004.11.054

193. Trnkova, L., Krizkova, S., Adam, V., Hubalek, J., & Kizek, R. (2011). Immobilization of metallothionein to carbon paste electrode surface via anti-MT antibodies and its use for biosensing of silver. *Biosensors and Bioelectronics, 26*(5), 2201-2207.

194. Vinci, J. C., Ferrer, I. M., Seedhouse, S. J., Bourdon, A. K., Reynard, J. M., Foster, B. A., . . . Colón, L. A. (2013). Hidden Properties of Carbon Dots Revealed After HPLC Fractionation. *The Journal of Physical Chemistry Letters, 4*(2), 239-243. doi: 10.1021/jz301911y

195. Wang, C., Sun, D., Zhuo, K., Zhang, H., & Wang, J. (2014). Simple and green synthesis of nitrogen-, sulfur-, and phosphorus-co-doped carbon dots with tunable luminescence properties and sensing application. [10.1039/C4RA10885J]. *RSC Advances, 4*(96), 54060-54065. doi: 10.1039/c4ra10885j

196. Wang, C., Xu, Z., & Zhang, C. (2015). Polyethyleneimine-Functionalized Fluorescent Carbon Dots: Water Stability, pH Sensing, and Cellular Imaging. *ChemNanoMat, 1*(2), 122-127. doi: 10.1002/cnma.201500009

197. Wang, C.-I., Wu, W.-C., Periasamy, A. P., & Chang, H.-T. (2014). Electrochemical synthesis of photoluminescent carbon nanodots from glycine for highly sensitive detection of hemoglobin.

[10.1039/C3GC42325E]. *Green Chemistry, 16*(5), 2509-2514. doi: 10.1039/c3gc42325e

198. Wang, F., Chen, Y.-h., Liu, C.-y., & Ma, D.-g. (2011). White light-emitting devices based on carbon dots' electroluminescence. [10.1039/C0CC05391K]. *Chemical Communications, 47*(12), 3502-3504. doi: 10.1039/c0cc05391k

199. Wang, F., Xie, Z., Zhang, H., Liu, C. y., & Zhang, Y. g. (2011). Highly luminescent organosilane-functionalized carbon dots. *Advanced Functional Materials, 21*(6), 1027-1031.

200. Wang, G.-Y., Song, C., Kong, D.-M., Ruan, W.-J., Chang, Z., & Li, Y. (2014). Two luminescent metal-organic frameworks for the sensing of nitroaromatic explosives and DNA strands. [10.1039/C3TA14199C]. *Journal of Materials Chemistry A, 2*(7), 2213-2220. doi: 10.1039/c3ta14199c

201. Wang, H., Xu, X., Lee, C., Johnson, C., Sohlberg, K., & Ji, H.-F. (2012). Highly Selective Sensing of Nitroaromatics Using Nanomaterials of Ellagic Acid. *The Journal of Physical Chemistry C, 116*(7), 4442-4448. doi: 10.1021/jp2106549

202. Wang, J., Wang, C.-F., & Chen, S. (2012). Amphiphilic Egg-Derived Carbon Dots: Rapid Plasma Fabrication, Pyrolysis Process, and Multicolor Printing Patterns. *Angewandte Chemie International Edition, 51*(37), 9297-9301. doi: 10.1002/anie.201204381

203. Wang, L., & Zhou, H. S. (2014). Green Synthesis of Luminescent Nitrogen-Doped Carbon Dots from Milk and Its Imaging Application. *Analytical Chemistry, 86*(18), 8902-8905. doi: 10.1021/ac502646x

204. Wang, L., Zhu, S.-J., Wang, H.-Y., Qu, S.-N., Zhang, Y.-L., Zhang, J.-H., . . . Sun, H.-B. (2014). Common Origin of Green Luminescence in Carbon Nanodots and Graphene Quantum Dots. *ACS Nano, 8*(3), 2541-2547. doi: 10.1021/nn500368m

205. Wang, Q., Liu, X., Zhang, L., & Lv, Y. (2012). Microwave-assisted synthesis of carbon nanodots through an eggshell membrane and their fluorescent application. [10.1039/C2AN36059D]. *Analyst, 137*(22), 5392-5397. doi: 10.1039/c2an36059d

206. Wang, Q., Zhang, S., Ge, H., Tian, G., Cao, N., & Li, Y. (2015). A fluorescent turn-off/on method based on carbon dots as fluorescent probes for the sensitive determination of Pb^{2+} and pyrophosphate in an aqueous solution. *Sensors and Actuators B: Chemical, 207*(Part A), 25-33. doi: https://doi.org/10.1016/j.snb.2014.10.096

207. Wang, R., Lu, K.-Q., Tang, Z.-R., & Xu, Y.-J. (2017). Recent progress in carbon quantum dots: synthesis, properties and applications in photocatalysis. [10.1039/C6TA08660H]. *Journal of Materials Chemistry A, 5*(8), 3717-3734. doi: 10.1039/c6ta08660h

208. Wang, T.-Y., Chen, C.-Y., Wang, C.-M., Tan, Y. Z., & Liao, W.-S. (2017). Multicolor Functional Carbon Dots via One-Step Refluxing Synthesis. *ACS Sensors, 2*(3), 354-363. doi: 10.1021/acssensors.6b00607

209. Wang, W.-J., Hai, X., Mao, Q.-X., Chen, M.-L., & Wang, J.-H. (2015). Polyhedral oligomeric silsesquioxane functionalized carbon dots for cell imaging. *ACS Applied Materials & Interfaces, 7*(30), 16609-16616.

210. Wang, X., Cheng, J., Yu, H., & Yu, J. (2017). A facile hydrothermal synthesis of carbon dots modified g-C_3N_4 for enhanced photocatalytic H_2-evolution performance. [10.1039/C7DT00773F]. *Dalton Transactions, 46*(19), 6417-6424. doi: 10.1039/c7dt00773f

211. Wang, X., Qu, K., Xu, B., Ren, J., & Qu, X. (2011). Microwave assisted one-step green synthesis of cell-permeable multicolor photoluminescent carbon dots without surface passivation reagents. [10.1039/C0JM02963G]. *Journal of Materials Chemistry, 21*(8), 2445-2450. doi: 10.1039/c0jm02963g

212. Wang, Y., & Hu, A. (2014). Carbon quantum dots: synthesis, properties and applications. [10.1039/C4TC00988F]. *Journal of Materials Chemistry C, 2*(34), 6921-6939. doi: 10.1039/c4tc00988f

213. Wang, Y., & Ni, Y. (2014). Molybdenum Disulfide Quantum Dots as a Photoluminescence Sensing Platform for 2,4,6-Trinitrophenol Detection. *Analytical Chemistry, 86*(15), 7463-7470. doi: 10.1021/ac5012014

214. Wang, Y., Kalytchuk, S., Zhang, Y., Shi, H., Kershaw, S. V., & Rogach, A. L. (2014). Thickness-Dependent Full-Color Emission Tunability in a Flexible Carbon Dot Ionogel. *The Journal of Physical Chemistry Letters, 5*(8), 1412-1420. doi: 10.1021/jz5005335

215. Wang, Y., La, A., Bruckner, C., & Lei, Y. (2012). FRET- and PET-based sensing in a single material: expanding the dynamic range of an ultra-sensitive nitroaromatic explosives assay. [10.1039/C2CC34492K]. *Chemical Communications, 48*(79), 9903-9905. doi: 10.1039/c2cc34492k

216. Wei, W., Xu, C., Ren, J., Xu, B., & Qu, X. (2012). Sensing metal ions with ion selectivity of a crown ether and fluorescence resonance energy transfer between carbon dots and graphene. [10.1039/C2CC16481G]. *Chemical Communications, 48*(9), 1284-1286. doi: 10.1039/c2cc16481g

217. Wen, Z.-H., & Yin, X.-B. (2016). Excitation-independent carbon dots, from photoluminescence mechanism to single-color application.

[10.1039/C5RA27172J]. *RSC Advances, 6*(33), 27829-27835. doi: 10.1039/c5ra27172j

218. Widmer, S., Dorrestijn, M., Camerlo, A., Urek, S. K., Lobnik, A., Housecroft, C. E., . . . Scherer, L. J. (2014). Coumarin meets fluorescein: a Forster resonance energy transfer enhanced optical ammonia gas sensor. [10.1039/C4AN00061G]. *Analyst, 139*(17), 4335-4342. doi: 10.1039/c4an00061g

219. Wood, A., Giersig, M., & Mulvaney, P. (2001). Fermi Level Equilibration in Quantum Dot−Metal Nanojunctions. *The Journal of Physical Chemistry B, 105*(37), 8810-8815. doi: 10.1021/jp011576t

220. Wu, P., Zhao, T., Wang, S., & Hou, X. (2014). Semicondutor quantum dots-based metal ion probes. [10.1039/C3NR04628A]. *Nanoscale, 6*(1), 43-64. doi: 10.1039/c3nr04628a

221. Wu, Z. L., Zhang, P., Gao, M. X., Liu, C. F., Wang, W., Leng, F., & Huang, C. Z. (2013). One-pot hydrothermal synthesis of highly luminescent nitrogen-doped amphoteric carbon dots for bioimaging from Bombyx mori silk - natural proteins. [10.1039/C3TB20418A]. *Journal of Materials Chemistry B, 1*(22), 2868-2873. doi: 10.1039/c3tb20418a

222. Xiang, L., & Tang, J. (2017). QD-aptamer as a donor for a FRET-based chemosensor and evaluation of affinity between acetamiprid and its aptamer. [10.1039/C6RA26118C]. *RSC Advances, 7*(14), 8332-8337. doi: 10.1039/c6ra26118c

223. Xu, J., Zhang, L., Shi, R., & Zhu, Y. (2013). Chemical exfoliation of graphitic carbon nitride for efficient heterogeneous photocatalysis. [10.1039/C3TA13188B]. *Journal of Materials Chemistry A, 1*(46), 14766-14772. doi: 10.1039/c3ta13188b

224. Xu, J.-L., Liu, Y.-H., Gao, X., Sun, Y., Shen, S., Cai, X., . . . Wang, S.-D. (2017). Embedded Ag Grid Electrodes as Current Collector for Ultraflexible Transparent Solid-State Supercapacitor. *ACS Applied Materials & Interfaces, 9*(33), 27649-27656. doi: 10.1021/acsami.7b06184

225. Xu, S., Xu, S., Zhu, Y., Xu, W., Zhou, P., Zhou, C., . . . Song, H. (2014). A novel upconversion, fluorescence resonance energy transfer biosensor (FRET) for sensitive detection of lead ions in human serum. [10.1039/C4NR03092C]. *Nanoscale, 6*(21), 12573-12579. doi: 10.1039/c4nr03092c

226. Xu, X., Ray, R., Gu, Y., Ploehn, H. J., Gearheart, L., Raker, K., & Scrivens, W. A. (2004). Electrophoretic Analysis and Purification of Fluorescent Single-Walled Carbon Nanotube Fragments. *Journal of the American Chemical Society, 126*(40), 12736-12737. doi: 10.1021/ja040082h

227. Xu, Z., Wang, C., Jiang, K., Lin, H., Huang, Y., & Zhang, C. (2015). Microwave-Assisted Rapid Synthesis of Amphibious Yellow Fluorescent Carbon Dots as a Colorimetric Nanosensor for Cr(VI). *Particle & Particle Systems Characterization, 32*(12), 1058-1062. doi: 10.1002/ppsc.201500172

228. Yan, X., Li, Q., & Li, L.-s. (2012). Formation and stabilization of palladium nanoparticles on colloidal graphene quantum dots. *Journal of the American Chemical Society, 134*(39), 16095-16098.

229. Yan, Z., Shu, J., Yu, Y., Zhang, Z., Liu, Z., & Chen, J. (2015). Preparation of carbon quantum dots based on starch and their spectral properties. *Luminescence, 30*(4), 388-392. doi: 10.1002/bio.2744

230. Yang, M., Xu, D., Xi, W., Wang, L., Zheng, J., Huang, J., . . . Tian, Y. (2013). Aggregation-Induced Fluorescence Behavior of Triphenylamine-Based Schiff Bases: The Combined Effect of Multiple Forces. *The Journal of Organic Chemistry, 78*(20), 10344-10359. doi: 10.1021/jo401719c

231. Yang, W., Ni, J., Luo, F., Weng, W., Wei, Q., Lin, Z., & Chen, G. (2017). Cationic Carbon Dots for Modification-Free Detection of Hyaluronidase via an Electrostatic-Controlled Ratiometric Fluorescence Assay. *Analytical Chemistry, 89*(16), 8384-8390. doi: 10.1021/acs.analchem.7b01705

232. Yang, X., Wang, Y., Shen, X., Su, C., Yang, J., Piao, M., . . . Lin, Q. (2017). One-step synthesis of photoluminescent carbon dots with excitation-independent emission for selective bioimaging and gene delivery. *Journal of Colloid and Interface Science, 492*(Supplement C), 1-7. doi: https://doi.org/10.1016/j.jcis.2016.12.057

233. Yang, Z., Xu, M., Liu, Y., He, F., Gao, F., Su, Y., . . . Zhang, Y. (2014). Nitrogen-doped, carbon-rich, highly photoluminescent carbon dots from ammonium citrate. [10.1039/C3NR05380F]. *Nanoscale, 6*(3), 1890-1895. doi: 10.1039/c3nr05380f

234. Ye, J., Zhao, L., Bogale, R. F., Gao, Y., Wang, X., Qian, X., . . . Ning, G. (2015). Highly Selective Detection of 2,4,6-Trinitrophenol and Cu^{2+} Ions Based on a Fluorescent Cadmium–Pamoate Metal–Organic Framework. *Chemistry – A European Journal, 21*(5), 2029-2037. doi: 10.1002/chem.201405267

235. Ye, Z., Tang, R., Wu, H., Wang, B., Tan, M., & Yuan, J. (2014). Preparation of europium complex-conjugated carbon dots for ratiometric fluorescence detection of copper(ii) ions. [10.1039/C4NJ00966E]. *New Journal of Chemistry, 38*(12), 5721-5726. doi: 10.1039/c4nj00966e

236. Yew, Y. T., Ambrosi, A., & Pumera, M. (2016). Nitroaromatic explosives detection using electrochemically exfoliated graphene. [Article]. *6*, 33276. doi: 10.1038/srep33276

237. Yu, C., Li, X., Zeng, F., Zheng, F., & Wu, S. (2013). Carbon-dot-based ratiometric fluorescent sensor for detecting hydrogen sulfide in aqueous media and inside live cells. [10.1039/C2CC37329G]. *Chemical Communications, 49*(4), 403-405. doi: 10.1039/c2cc37329g

238. Yu, G., Yan, X., Han, C., & Huang, F. (2013). Characterization of supramolecular gels. [10.1039/C3CS60080G]. *Chemical Society Reviews, 42*(16), 6697-6722. doi: 10.1039/c3cs60080g

239. Yu, H., Li, X., Zeng, X., & Lu, Y. (2016). Preparation of carbon dots by non-focusing pulsed laser irradiation in toluene. [10.1039/C5CC08384B]. *Chemical Communications, 52*(4), 819-822. doi: 10.1039/c5cc08384b

240. Yu, P., Wen, X., Toh, Y.-R., & Tang, J. (2012). Temperature-Dependent Fluorescence in Carbon Dots. *The Journal of Physical Chemistry C, 116*(48), 25552-25557. doi: 10.1021/jp307308z

241. Yuan, F., Wang, Z., Li, X., Li, Y., Tan, Z. a., Fan, L., & Yang, S. (2017). Bright Multicolor Bandgap Fluorescent Carbon Quantum Dots for Electroluminescent Light-Emitting Diodes. *Advanced Materials, 29*(3), 1604436-n/a. doi: 10.1002/adma.201604436

242. Yuan, L., Lin, W., Zheng, K., & Zhu, S. (2013). FRET-Based Small-Molecule Fluorescent Probes: Rational Design and Bioimaging Applications. *Accounts of Chemical Research, 46*(7), 1462-1473. doi: 10.1021/ar300273v

243. Yuan, W. Z., Lu, P., Chen, S., Lam, J. W. Y., Wang, Z., Liu, Y., . . . Tang, B. Z. (2010). Changing the Behavior of Chromophores from Aggregation-Caused Quenching to Aggregation-Induced Emission: Development of Highly Efficient Light Emitters in the Solid State. *Advanced Materials, 22*(19), 2159-2163. doi: 10.1002/adma.200904056

244. Zhang, B., Sun, J., Bi, C., Yin, G., Pu, L., Shi, Y., & Sheng, L. (2011). A highly selective ratiometric fluorescent chemosensor for Ag^+ based on a rhodanineacetic acid–pyrene derivative. *New Journal of Chemistry, 35*(4), 849-853.

245. Zhang, J., & Yu, S.-H. (2016). Carbon dots: large-scale synthesis, sensing and bioimaging. *Materials Today, 19*(7), 382-393. doi: https://doi.org/10.1016/j.mattod.2015.11.008

246. Zhang, J., Cao, Y., Feng, J., & Wu, P. (2012). Graphene-Oxide-Sheet-Induced Gelation of Cellulose and Promoted Mechanical Properties of Composite Aerogels. *The Journal of Physical Chemistry C, 116*(14), 8063-8068. doi: 10.1021/jp2109237

247. Zhang, L., Han, Y., Zhu, J., Zhai, Y., & Dong, S. (2015). Simple and Sensitive Fluorescent and Electrochemical Trinitrotoluene Sensors Based

on Aqueous Carbon Dots. *Analytical Chemistry, 87*(4), 2033-2036. doi: 10.1021/ac5043686

248. Zhang, L., Wang, D., Huang, H., Liu, L., Zhou, Y., Xia, X., . . . Liu, X. (2016). Preparation of Gold–Carbon Dots and Ratiometric Fluorescence Cellular Imaging. *ACS Applied Materials & Interfaces, 8*(10), 6646-6655. doi: 10.1021/acsami.5b12084

249. Zhang, X., Zhang, Y., Wang, Y., Kalytchuk, S., Kershaw, S. V., Wang, Y., . . . Rogach, A. L. (2013). Color-Switchable Electroluminescence of Carbon Dot Light-Emitting Diodes. *ACS Nano, 7*(12), 11234-11241. doi: 10.1021/nn405017q

250. Zhang, X.-L., Zheng, C., Guo, S.-S., Li, J., Yang, H.-H., & Chen, G. (2014). Turn-On Fluorescence Sensor for Intracellular Imaging of Glutathione Using g-C3N4 Nanosheet–MnO_2 Sandwich Nanocomposite. *Analytical Chemistry, 86*(7), 3426-3434. doi: 10.1021/ac500336f

251. Zhang, Y.-Q., Ma, D.-K., Zhuang, Y., Zhang, X., Chen, W., Hong, L.-L., . . . Huang, S.-M. (2012). One-pot synthesis of N-doped carbon dots with tunable luminescence properties. [10.1039/C2JM32973E]. *Journal of Materials Chemistry, 22*(33), 16714-16718. doi: 10.1039/c2jm32973e

252. Zhang, Z., Shi, Y., Pan, Y., Cheng, X., Zhang, L., Chen, J., . . . Yi, C. (2014). Quinoline derivative-functionalized carbon dots as a fluorescent nanosensor for sensing and intracellular imaging of Zn2+. [10.1039/C4TB00677A]. *Journal of Materials Chemistry B, 2*(31), 5020-5027. doi: 10.1039/c4tb00677a

253. Zhao, D., Li, J., Yang, T., & He, Z. (2014). “Turn off–on” fluorescent sensor for platinum drugs-DNA interactions based on quantum dots. *Biosensors and Bioelectronics, 52*(Supplement C), 29-35. doi: https://doi.org/10.1016/j.bios.2013.08.031

254. Zhao, Q., Li, K., Chen, S., Qin, A., Ding, D., Zhang, S., . . . Tang, B. Z. (2012). Aggregation-induced red-NIR emission organic nanoparticles as effective and photostable fluorescent probes for bioimaging. [10.1039/C2JM31368E]. *Journal of Materials Chemistry, 22*(30), 15128-15135. doi: 10.1039/c2jm31368e

255. Zhao, Q.-L., Zhang, Z.-L., Huang, B.-H., Peng, J., Zhang, M., & Pang, D.-W. (2008). Facile preparation of low cytotoxicity fluorescent carbon nanocrystals by electrooxidation of graphite. [10.1039/B812420E]. *Chemical Communications*(41), 5116-5118. doi: 10.1039/b812420e

256. Zheng, H., Wang, Q., Long, Y., Zhang, H., Huang, X., & Zhu, R. (2011). Enhancing the luminescence of carbon dots with a reduction pathway. [10.1039/C1CC14741B]. *Chemical Communications, 47*(38), 10650-10652. doi: 10.1039/c1cc14741b

257. Zhou, L., Lin, Y., Huang, Z., Ren, J., & Qu, X. (2012). Carbon nanodots as fluorescence probes for rapid, sensitive, and label-free detection of Hg^{2+} and biothiols in complex matrices. [10.1039/C2CC16791C]. *Chemical Communications, 48*(8), 1147-1149. doi: 10.1039/c2cc16791c

258. Zhou, X.-H., Li, L., Li, H.-H., Li, A., Yang, T., & Huang, W. (2013). A flexible Eu(iii)-based metal-organic framework: turn-off luminescent sensor for the detection of Fe(iii) and picric acid. [10.1039/C3DT51081F]. *Dalton Transactions, 42*(34), 12403-12409. doi: 10.1039/c3dt51081f

259. Zhu, C., Zhai, J., & Dong, S. (2012). Bifunctional fluorescent carbon nanodots: green synthesis via soy milk and application as metal-free electrocatalysts for oxygen reduction. *Chemical Communications, 48*(75), 9367-9369.

260. Zhu, L., Yin, Y., Wang, C.-F., & Chen, S. (2013). Plant leaf-derived fluorescent carbon dots for sensing, patterning and coding. [10.1039/C3TC30701H]. *Journal of Materials Chemistry C, 1*(32), 4925-4932. doi: 10.1039/c3tc30701h

261. Zhu, S., Song, Y., Zhao, X., Shao, J., Zhang, J., & Yang, B. (2015). The photoluminescence mechanism in carbon dots (graphene quantum dots, carbon nanodots, and polymer dots): current state and future perspective. *Nano Research, 8*(2), 355-381. doi: 10.1007/s12274-014-0644-3

LIST OF PUBLICATIONS BASED ON THE THESIS

International Journals

1. Manjunatha Ganiga and Jobin Cyriac (2015). Direct synthesis of highly stable nitrogen rich carbon dots toward white light emission. *RSC Advances*, 5, 101333-101337.
2. Manjunatha Ganiga and Jobin Cyriac (2016). FRET based ammonia sensor using dots. *Sensors and Actuators B: Chemical*, 225, 522-528.
3. Manjunatha Ganiga and Jobin Cyriac (2016). Understanding the photoluminescence mechanism of nitrogen doped carbon dots by selective interaction with copper ions. *ChemPhysChem*, 17, 2315–2321. (*Accepted as back cover page article*)
4. Manjunatha Ganiga and Jobin Cyriac (2017). Direct one pot synthesis of blue luminescent polymeric carbon dots gel and their application for selective detection of Ag^+ ions. *Soft Materials*, 15(4), 331-340.
5. Manjunatha Ganiga and Jobin Cyriac (2018). Synthesis of organophilic carbon dots, selective screening of trinitrophenol and a comprehensive understanding of luminescence quenching mechanism. *ChemistrySelect*, 3 (17), 4663-4668.
6. Manjunatha Ganiga and Jobin Cyriac. A comprehensive understanding of multiple emissive states in S and N doped Carbon dots (*Under Revision*).

Other Publications

1. Manjunatha Ganiga and Jobin Cyriac (2015). Detection of PETN and RDX using a FRET-based fluorescence sensor system' *Analytical Methods*, 7, 5412-5418.
2. Manjunatha Ganiga and Jobin Cyriac (2016). An ascorbic acid sensor based on cadmium sulphide quantum dots. *Analytical Bioanalytical Chemistry*, 408, 3699-3706.
3. K Jalaja, S Bhuvaneshwari, Manjunatha Ganiga, R Divyamol, S Anup and Jobin Cyriac and Benny K George (2017). Effective SERS detection using a flexible wiping substrate based on electrospun polystyrene nanofibers. *Analytical Methods* 9 (26), 3998-4003.
4. Neema Pallikkarathodi Mani, Manjunatha Ganiga, Jobin Cyriac (2017). Synthesis of MoS_2 Quantum Dots Uniformly Dispersed on Low

Dimensional MoS_2 Nanosheets and Unravelling its Multiple Emissive States. *ChemistrySelect*, 2 (21), 5942-5949.

5. Neema P M, Manjunatha Ganiga and Jobin Cyriac (2018), "MoS_2 nanohybrid as a fluorescence sensor for highly selective detection of dopamine", *Analyst* 143 (7), 1691-1698.

CONFERENCES/SEMINARS

Talks

1. Manjunatha Ganiga and Jobin Cyriac, 'Highly selective FRET based detection of PETN and RDX', *Materials Research Society of India; Thiruvananthapuram Chapter, January 30, (2015).*
2. Manjunatha Ganiga and Jobin Cyriac. Synthesis of Blue luminescent carbon dot polymeric gel for the selective sensing of Ag^+ ions; *NIIST Thiruvananthapuram, December 20, (2016).*

Poster Presentations

1. Manjunatha Ganiga and Jobin Cyriac.A Wiping Substrate for SERS detection; *NCMST, IIST Thiruvananthapuram, July 10-12, (2013).*
2. Manjunatha Ganiga and Jobin Cyriac. SERS detection of Rhodamine 6G using wiping substrate; *9th International High Energy Materials Conference, Thiruvananthapuram, February 13-15, (2014).*
3. Manjunatha Ganiga and Jobin Cyriac. FRET based highly selective detection of PETN and RDX; *8th Asian Photochemistry Conference, Thiruvananthapuram, November 10-13, (2014).*
4. Manjunatha Ganiga and Jobin Cyriac. Detection of PETN and RDX; *Bangalore India Nano, Bangalore, December 6-8, (2014).*
5. Manjunatha Ganiga and Jobin Cyriac. Synthesis of nitrogen doped carbon dots and understanding its luminescence behaviour through the interaction with Cu^{2+}; *International Symposium on clusters, cluster-assemblies and Nanomaterials, Thiruvananthapuram, March 9-12, (2016).*
6. Manjunatha Ganiga and Jobin Cyriac. Synthesis and understanding the luminescence behaviour in S and N doped carbon dots; *CRSI-ACS joint symposium, IICT, Hyderabad, July 13-15 (2017).*